UNITED STATES DEPARTMENT OF COMMERCE
HARRY L. HOPKINS, Secretary
NATIONAL BUREAU OF STANDARDS
Lyman J. Briggs, Director

✦

Journal of Research

of the

National Bureau of Standards

✦

Volume 24, Number 6
June 1940

[Published with approval of the Director of the Budget]

UNITED STATES
GOVERNMENT PRINTING OFFICE
WASHINGTON : 1940

For sale by the Superintendent of Documents, Washington, D. C. - - - - - - Price 30 cents
$3.50 per year on subscription

The prices of the separate Research Papers appearing in this JOURNAL are given on the front cover page. If 100 or more copies of any separate are ordered, a discount of 25 percent is allowed. Those who desire copies of separate Research Papers should send their orders and remittances without delay to the Superintendent of Documents, U. S. Government Printing Office, Washington, D. C. This will aid him to determine the number of copies to be printed for sale. Research Papers are not printed from electrotypes, and usually no more reprints can be had when the first and only printing is exhausted.

U. S. DEPARTMENT OF COMMERCE NATIONAL BUREAU OF STANDARDS

RESEARCH PAPER RP1302

Part of Journal of Research of the National Bureau of Standards, Volume 24, June 1940

THEORY OF A SINGLE-LAYER, BIFILAR, ABSOLUTE STANDARD OF MUTUAL INDUCTANCE

By Chester Snow

ABSTRACT

A formula is derived for the mutual inductance of two helical wires wound bifilarly upon the same cylindrical form. This aims at a precision sufficient for use in absolute electrical measurements, so that terms are retained which, compared with the principal term, are relatively small quantities of the order of the square of the ratio of pitch to cylindrical radius. Nominally the two helical windings consist of wires of equal diameters, equally spaced, with equal cylindrical radii, but allowance is made for the case where these three equalities are not quite attained. The axial lengths are assumed to be equal, so that, since their pitch must be the same, the total number of turns is the same. The latter is considered to be integral, which permits of the two return currents being carried each by a straight wire parallel to a generator of the cylindrical form and close to it. The effect of these lead wires is included in the formula. The azimuth angle between these generators is assumed to lie between $-\pi$ and π, so that the point of current entrance for the primary is on a turn adjacent to that of the secondary. Allowance is made for a general type of current distribution.

CONTENTS

		Page
I.	Introduction	597
II.	Mutual inductance, M, of the wires as an integral over their sections	598
III.	Mutual inductance, m, of two elementary helical filaments	603
	1. Formula for m in terms of the ω-functions	603
	2. Principal term, $\omega_\theta\ (l)$	606
	3. Small term, $\omega_\theta\ (\lambda)$	607
	4. Axial-current term, $\omega_z\ (l)$	608
	5. Azimuth term, ω_a	608
	6. Second-order approximation for m	621
IV.	Mutual inductance, M, of the helical wires	624
V.	Effect of lead wires	630
VI.	Modification required when the reference sections are not quite circular	630
VII.	Summary	637
VIII.	List of symbols	638

I. INTRODUCTION

Mutual inductors are now being constructed as single-layer, bifilar windings on a circular, cylindrical form. The dimensions may be measured as precisely as those of a self inductor. However, a formula for computing the mutual inductance between bifilar windings is not available. The object of this paper is to supply that need.

II. MUTUAL INDUCTANCE, *M*, OF THE WIRES AS AN INTEGRAL OVER THEIR SECTIONS

The helical wires, w_1 and w_2, have the pitch $2\pi p$. The two full circles of figure 1 with diameters d_1 and d_2 are their generating circles, for these circles sweep through the volume of the wires when the plane of the paper is given an angular velocity, $d\theta/dt$, about the x axis, together with a translational velocity, $pd\theta/dt$, in the x-direction. The same definition applies to a helical wire with any generating section, such as an ellipse or rectangle. The modifications necessary to extend the formulas to wires with general types of cross section will be indi-

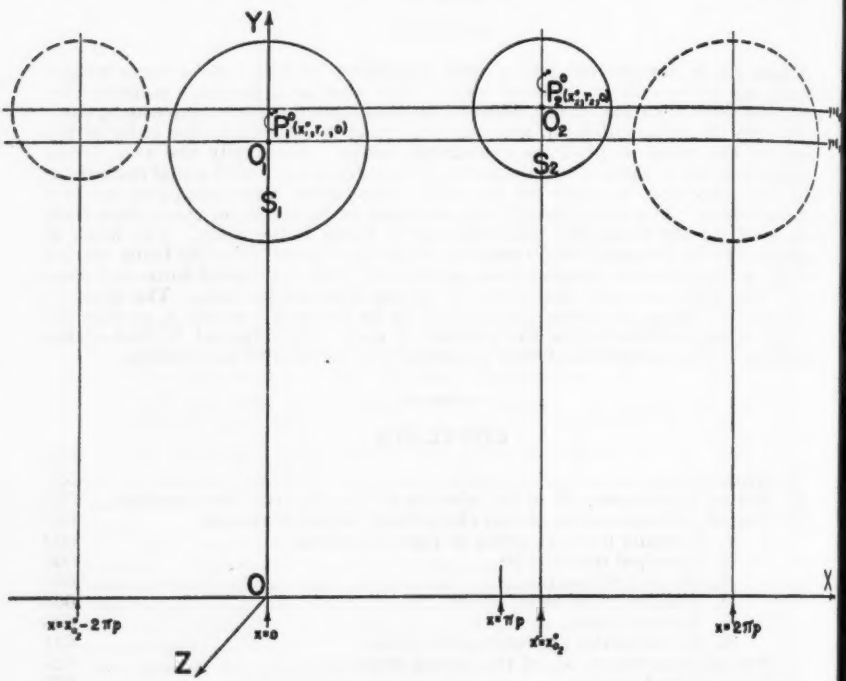

FIGURE 1.—*Reference circles which generate the two helical wires.*

cated later. The center of the first circle is at $x=0$, $y=a_1$, $z=0$, that of the second at $x=x_{0_2}^0$, $y=a_2$, $z=0$. In the actual construction, the attempt will be made to have the two wires equally spaced ($x_{0_2}^0=\pi p$) and to give them the same mean cylindrical radii ($a_1=a_2$). As neither of these conditions may be attainable with sufficient precision, we consider the more general $x_{0_2}^0$, and assume a_1-a_2 small compared to the pitch. The two adjacent circular sections bounded by full circles in figure 1 may be designated as the "reference sections" of the wires, to distinguish them from the initial or end sections, where the current enters or leaves the wires. However, the first of these sections, S_1, may be considered the initial section, S_{i_1}, of wire w_1, but the second, S_2, is in general not the initial section, S_{i_2}, of wire w_2. The initial

section, S_{i_2}, is the circular section in which w_2 is cut by a plane which passes through the x axis and makes a given angle, α, with the plane XOY, where $-\pi \leq \alpha < \pi$.

If x, y, z are rectangular coordinates and x, r, θ the cylindrical coordinates with the axis, as shown in figure 1, then the azimuth of the initial section, S_{i_1}, of w_1 is $\theta=\theta_{i_1}=0$, and that of the end section, S_{e_1}, is $\theta=\theta_{e_1}=2\pi N$, where N is a (large) given positive integer, the total number of complete turns. The initial and end sections thus being in the same plane, the lead wires for the return current may be made to consist mainly of a straight wire parallel to a generator of the cylindrical form and close to it. Similarly, for wire w_2 the initial azimuth is $\theta=\theta_{i_2}=\alpha$, and the end azimuth is $\theta_{e_2}=\alpha+2\pi N$; so a similar lead wire in the plane $\theta=\alpha$ may be used. These are shown, together with the central helical filaments of w_1 and w_2, in figure 2, which is drawn for the case where the wires are equally spaced ($x^0_{0_2}=\pi p$), and where the azimuthal angle is $\alpha=-\pi$ (as explained below).

To designate any particular helix, h_1, of the helical wire, w_1, it suffices to assign the two coordinates, x_1^0 and r_1, of the point P_1^0 in the reference plane of figure 1, through which this helix passes. Then, if x_1, y_1, z_1 are the rectangular coordinates of any point P_1 on this helix, the equations of the helix, h_1, are

$$\left.\begin{aligned} x_1&=x_1^0+p\theta_1 \\ y_1&=r_1\cos\theta_1 \\ z_1&=r_1\sin\theta_1 \end{aligned}\right\}, \text{ where } 0\leq\theta_1\leq 2\pi N. \tag{1}$$

It is understood that x_1^0 and r_1 are constant (as well as p), and that as the line parameter, θ_1, ranges over the prescribed interval, the point P_1 moves along the helix. The pair of constants (x_1^0, r_1) may have any values subject to the limitation

$$x_1^{0^2}+(r_1-a_1)^2\leq\left(\frac{d_1}{2}\right)^2.$$

The particular pair, $x_1^0=0$, $r_1=a_1$, corresponds to the central helix of wire w_1. Its equations are

$$\left.\begin{aligned} x_1&=p\theta_1 \\ y_1&=a_1\cos\theta_1 \\ z_1&=a_1\sin\theta_1 \end{aligned}\right\}, \text{ where } 0\leq\theta_1\leq 2\pi N.$$

Similarly, any helix, h_2, of wire w_2, may be specified by assigning the coordinates of x_2^0 and r_2 of the point P_2^0 in the reference plane of figure 1, through which this helix passes or would pass if continued outside the range which limits the line parameter, θ_2. The equations of h_2 are

$$\left.\begin{aligned} x_2&=x_2^0+p\theta_2=x_{i_2}+p(\theta_2-\alpha) \\ y_2&=r_2\cos\theta_2 \\ z_2&=r_2\sin\theta_2 \end{aligned}\right\}, \text{ where } \leq\theta_2\leq\alpha+2\pi N. \tag{2}$$

This helix passes through the point in the initial section, S_{i_2}, whose cylindrical coordinates are (x_{i_2}, r_2, α), where $x_2^0=x_{i_2}-p\alpha$. The pair

of constants (x_2^0, r_2) which characterize h_2 are subject to the inequality

$$(x_2^0-x_{0_2}^0)^2+(r_2-a_2)^2\leqq\left(\frac{d_2}{2}\right)^2.$$

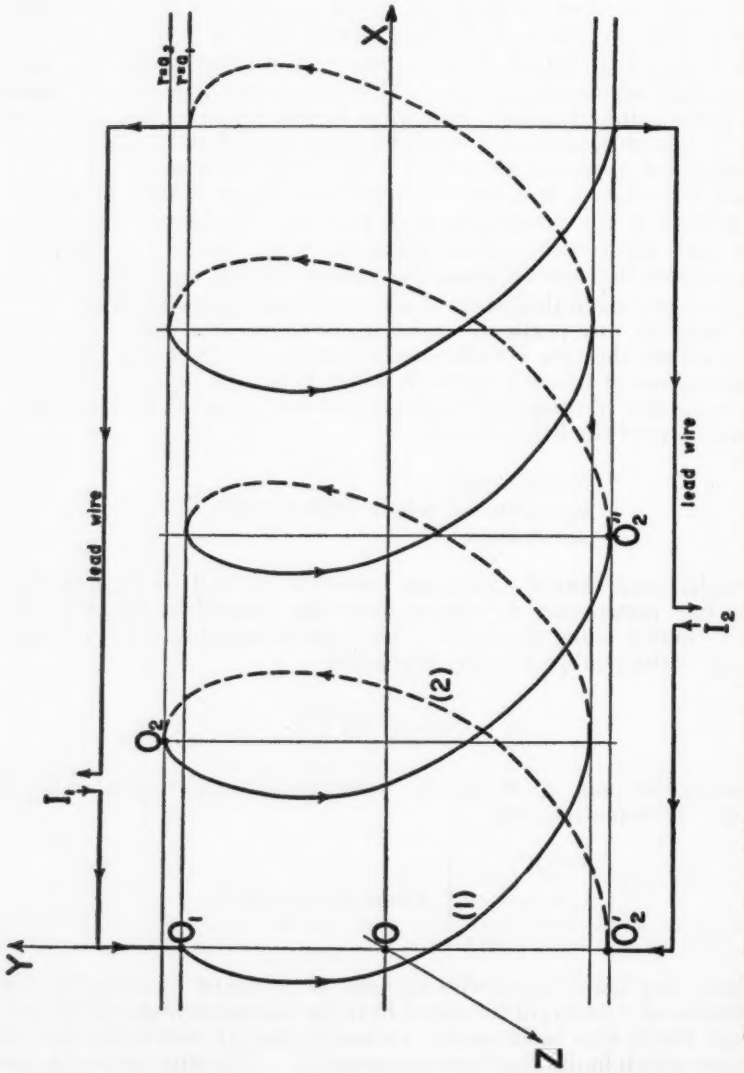

FIGURE 2.—*Central filaments of the two wires when the lead wires are on opposite sides of the cylindrical form (azimuth* $\alpha=-\pi$*).*

The particular pair, $x_2^0=x_{0_2}^0$ and $r_2=a_2$, correspond to the central helix whose equations are

$$\left.\begin{aligned}x_2&=x_{0_2}^0+p\theta_2\\ y_2&=a_2\cos\theta_2\\ z_2&=a_2\sin\theta_2\end{aligned}\right\},\ \text{where}\ \alpha\leqq\theta_2\leqq\alpha+\pi N.$$

In the special case where the helices are equally spaced, ($x^0_{02}=\pi p$), the central helix passes through the point in its initial section, S_{i_2}, whose cylindrical coordinates are ($p(\pi+\alpha)$, a_2, α) which, for the case $\alpha=-\pi$, becomes (0, a_2, $-\pi$).

This is the point $0_2'$ in figure 2. The two wires then have the same mean end planes. In the general case, if $-\pi<\alpha<0$, the point $0_2'$ would be moved toward 0_2 along this helix. If $0<\alpha<\pi$, it would fall between 0_2 and $0_2''$.

Every helix in either wire has the same axial length, $l=2\pi pN$. Every helix, h_1, in the wire w_1 has the same initial azimuth, $\theta_{i_1}=0$, and end azimuth, $\theta_{e_1}=2\pi N$. They differ in their cylindrical radii, r_1, and in the initial and end planes. Thus the helix h_1 lies between the initial plane, $x=x_{i_1}=x^0_1$, and the end plane, $x=x_{e_1}=x^0_1+l$, these limiting planes being 0 and l for the central helix.

Every helix, h_2, of wire w_2 has the initial azimuth, $\theta_{i_2}=\alpha$, and the end azimuth, $\theta_{e_2}=\alpha+2\pi N$. The helix h_2 lies between the initial plane, $x=xi_2=x^0_2+p\alpha$, and the end plane, $x=x_{e2}=x_{i2}+l$, these limiting planes for the central filament being x^0_{02} and $x^0_{02}+l$.

It is assumed that l and a_1 (or a_2) are finite quantities of the same order of magnitude, and that the pitch, $2\pi p$, is a small quantity of the first order compared with a_1 or a_2. A formula for the mutual inductance of the two wires will be obtained which neglects terms that are smaller, relative to the principal part, than the square of this infinitesimal compared with one. It is evident that the diameters of the wires must be small quantities of the same order as the pitch.

In the formula to be obtained, the principal term is proportional to a_1a_2/p^2, so that a term proportional to $\sqrt{a_1a_2}/p$ would be (relatively) a first-order small quantity, the proportionality factors being "finite" functions. Hence a finite function would be relatively of second order. Such terms are not quite negligible, but they need not be evaluated with great precision. In fact the principal term must be of the order of magnitude of 10 mh (10^7 cm) or larger, if the coil is to be of value in absolute electrical measurements, so that in the "finite", or smallest terms, retained in the formula, an error of $a/2$ is tolerable. The mutual inductance of a bifilar coil is practically equal to the self inductance of one of the windings. In the case of a coil of 500 turns, 100 cm long with radius 14 cm, the total self inductance is 17 $(10)^6$ cm, so that $a/2$ is 7 cm, or about 4 parts in 10 million. For a shorter coil, 27 cm long, 135 turns with a larger radius, 22 cm, the self inductance is 7 $(10)^6$ cm, so that $a/2=11$ cm is about 4 parts in 3 million. This is the basis for replacing certain expressions defined as infinite series or as definite integrals by simpler expressions in closed form, which are sufficiently close approximations.

Concerning the distribution of the steady current in the wires, we make the assumption that the vector-current density at any point, P_1, of wire w_1 has the direction of helix h_1 passing through that point, and its magnitude remains constant as the point moves along this helix, so that it is some function, $u_1(x^0_1, r_1)=u(x_1-p\theta_1, r_1)$. The current density will then be a solenoidal vector. Similar assumptions as to the current density in w_2 make its magnitude some function, $u_2(x^0_i, r_2)$.

Any axial plane (θ=constant) cuts the wire w_1 in a circular section of diameter d_1. If dS_1 is an element of area of this section, a helical tube of current, whose (oblique) section is dS_1, carries the current

$$dI_1=\frac{u_1(x_1^0, r_1)dS_1}{\sqrt{1+p^2/r_1^2}},$$

since $[1+p^2/r_1^2]^{-\frac{1}{2}}$ is the cosine of the angle between the normal to dS_1 and the direction of flow. The total current carried by the wire is unity, so that

$$\int\int\frac{u_1(x_1^0, r_1)dS_1}{\sqrt{1+p^2/r_1^2}}=1, \tag{3}$$

where the integration may be taken over *any* section of the wire made by the plane θ=constant.

A precisely similar equation applies to the unit current in wire w_2. It will be convenient in these integrals, and in those over the same sections which are to be encountered presently, to consider them as taken over the circular reference sections in the plane of figure 1, even though in the case of the section S_2, this may not be an actual section of the wire w_2.

If the wires were of rectangular section, it would be appropriate to take $dS_1=dx_1^0dr_1$ and $dS_2=dx_2^0dr$, but since they are circular, it is more natural to use plane polar coordinates (ρ_1, ϕ_1) for points in S_1 and (ρ_2, ϕ_2) for points in S_2, where

$$x_1^0=\rho_1\cos\phi_1 \text{ and } r_1-a_1=\rho_1\sin\phi_1$$

while

$$x_2^0-x_{0_2}^0=\rho_2\cos\phi_2 \text{ and } r_2-a_2=\rho_2\sin\phi_2,$$

so that

$$dS_1=\rho_1d\rho_1d\phi_1 \text{ and } dS_2=\rho_2d\rho_2d\phi_2,$$

where

$$S_1=\frac{\pi d_1^2}{4} \text{ and } S_2=\frac{\pi d_2^2}{4}$$

If $m_\alpha(x_1^0, r_1; x_2^0, r_2)$ denotes the mutual inductance (Neumann's line integral) of the two helices, h_1 and h_2, then the mutual inductance, M_α, of the two helical wires, w_1 and w_2, is

$$M_\alpha=\int\int\frac{u_1(x_1^0, r_1)dS_1}{\sqrt{1+p^2/r_1^2}}\int\int\frac{m_\alpha(x_1^0, r_1; x_2^0r_2)u_2(x_2^0, r_2)}{\sqrt{1+p^2r_2^2}}dS_2. \tag{4}$$

We shall obtain an expression eq 52 for m_α, whose principal part is constant; so this term contributes its own value to M_α when used in eq 4, as shown by eq 3 for any shape of wire section. The smallest terms of m (second order) may then be evaluated by taking

$$\frac{u_1}{\sqrt{1+p^2/r_1^2}}=\frac{1}{S_1} \text{ and } \frac{u_2}{\sqrt{1+p^2/r_2^2}}=\frac{1}{S_2},$$

where these terms are concerned in the integration of eq 4. This is also valid for any shape of the sections. For the small terms of the first order we use (when the sections are circular) the Taylor expansions

$$\frac{u_1(x_1^0, r_1)}{\sqrt{1+p^2/r_1^2}} = \frac{1}{S_1}\left\{1 + c_{x_1}\rho_1 \cos\phi_1 + c_{r_1}\rho_1 \sin\phi_1\right\}$$
$$\frac{u_2(x_2^0, r_2)}{\sqrt{1+p^2/r_2^2}} = \frac{1}{S_2}\left\{1 + c_{x_2}\rho_2 \cos\phi_2 + c_{r_2}\rho_2 \sin\phi_2\right\}, \tag{5a}$$

where the constants c_{x_1} and c_{r_1} are the values, at the central filament of

$$c_{x_1} = \frac{1}{u_1} D_{x_1^0} u_1 \text{ and } c_{r_1} = \frac{1}{u_1} D_{r_1} u_1 \tag{5b}$$

with similar expressions for c_{x_2} and c_{r_2}. In the case of most practical importance, the two wires will be of the same diameter and will have received the same treatment, so that $c_{x_1} = c_{x_2} \equiv c_x$ and $c_{r_1} = c_{r_2} \equiv c_r$. In this case it will be found that the variation with x^0 is unimportant, as the effect in one wire cancels the effect in the other, so that c_x need not be known. The radial variation, however, has some terms which cancel and some which add, giving a term of second order involving c_r. It may be noted that c_r is zero if the current is uniformly distributed over the cross section of the wire. In the "natural" distribution where the current density varies inversely as the cylindrical radius (that is inversely as the length of helical filament), the value of c_r is $-1/a$, where a is the radius of the central filament. If the conductivity of the wire were uniform, it can be shown that the distribution would be "natural."

It may be noted that the integrations in eq 4 are taken over the plane reference sections of figure 1. The equation is valid for wires with the most general type of cross section. If the sections are not circular, the second members of the two eq 5a must be replaced by other first-order approximations with other variables of integration which are more suitable for the particular type of sections considered. These equations are only necessary for use with the small correction terms which are of first order.

We leave eq 4 at this point and, in section III, digress with tedious detail in pursuit of an approximation for m which may be used in the eq 4. The results are collected in eq 53. After that, in section IV, it is relatively easy (with circular sections) to evaluate the fundamental integral given in eq 4.

III. MUTUAL INDUCTANCE, m, OF TWO ELEMENTARY HELICAL FILAMENTS

1. FORMULA FOR m IN TERMS OF THE ω-FUNCTIONS

The general formula for m has been developed in a recent paper,[1] in which the small correction terms depending upon the azimuthal angle were reduced to a practicable form by limiting the application to cases where the two helices were nowhere close to each other.

[1] C. Snow, *Mutual inductance and force between coaxial helical wires.* J. Research NBS 22, 239 (1939) RP1178.

These terms require a different treatment in the present problem of the bifilar inductor, but for all other terms we merely quote the results of that paper. For brevity, this will be referred to as paper I.

It is first necessary to place here for reference the function of the modulus k denoted by $\phi_n(k)$, which is in fact equal to $\pi^{-1}Q_{n-\frac{1}{2}}$ with argument $(2-k^2)/k^2$, where Q is Legendre's function of the second kind. Since $0<k<1$, it is defined for $n=0, 1, 2, 3 * * *$ by the hypergeometric function

$$\phi_n(k)=\frac{k^{2n+1}\Gamma^2(n+\frac{1}{2})}{2\pi\Gamma(2n+1)}F(n+\tfrac{1}{2}, n+\tfrac{1}{2}, 2n+1; k^2) \tag{6}$$

or in terms of the complementary modulus $k'=(1-k^2)^{\frac{1}{2}}$.

$$\phi_n(k)=-\frac{k^{2n+1}}{\pi}\Big\{F(n+\tfrac{1}{2}, n+\tfrac{1}{2}, 1; k^2)\log k'$$

$$+\frac{1}{\Gamma^2(n+\frac{1}{2})}\sum_{s=0}^{\infty}k'^{2s}\frac{\Gamma^2(s+n+\frac{1}{2})}{\Gamma^2(s+1)}[\psi(s+n+\tfrac{1}{2})-\psi(s+1)]\Big\}, \tag{7}$$

where $\psi(z)$ is $\Gamma'(z)/\Gamma(z)$. The first two functions are given in terms of the complete elliptic integrals

$$\pi\phi_0(k)=kK(k) \text{ and } \pi\phi_1(k)=\frac{2}{k}[K(k)-E(k)]-kK(k). \tag{8}$$

When k_x is a function of x, r_1, and r_2 given by

$$k_x^2=\frac{4r_1r_2}{x^2+(r_1+r_2)^2} \text{ or } k_x'^2=\frac{x^2+(r_2-r_1)^2}{4r_1r_2+x^2+(r_2-r_1)^2}, \tag{9}$$

then

$$\phi_n(k_x)=\sqrt{r_1r_2}\int_0^{\infty}e^{-|x|s}J_n(r_1s)J_n(r_2s)ds, \tag{10a}$$

where J_n is Bessel's function.

Also when k is given by eq 9, $\phi_n(k)$ is a solution of the partial differential equation

$$\left\{D_x^2+D_{r_1}^2+\frac{1-2\alpha}{r_1}D_{r_1}+\frac{\alpha^2-n^2}{r_1^2}\right\}r_1^{\alpha-\frac{1}{2}}\phi_n(k)=0, \tag{10b}$$

where α is any constant. The same equation holds when r_1 is replaced by r_2.

The function $\phi_n(k)$ is the coefficient in the following Fourier's series:

$$\frac{k}{4\sqrt{1-k^2\cos^2\theta}}=\frac{1}{2}\phi_0(k)+\sum_{n=1}^{\infty}\phi_n(k)\cos 2n\theta.$$

In the following, it will be assumed that k_x and k_x' are the functions of x, r_1 and r_2 defined in eq 9. When x is merely replaced by x_1, this

is indicated by k_1; when x is l, by k_l; and when x is zero, by k_0; similarly, k_λ, when $x=\lambda$. The fundamental equation is eq 13 of paper 1.

$$m=\omega(x_{e_2}-x_{i_1})-\omega(x_{e_2}-x_{e_1})+\omega(x_{i_2}-x_{e_1})-\omega(x_{i_2}-x_{i_1}), \tag{11}$$

where the subscripts i and e indicate initial and end planes, and $\omega(x)$ is written in place of $\omega(x, r_1, r_2; \alpha)$. This function was there resolved into three constituents, as follows:

$$\omega(x)=\omega_\theta(x)+\omega_x(x)+\omega_a(x,\alpha). \tag{12}$$

The term ω_a was called the azimuthal ω-function, as it is the only one depending upon α. All three functions depend upon r_1 and r_2.

The associated current sheet of the helix, h_1, is defined as the circular cylindrical surface coaxial with it, having the same radius, r_1, and end planes, x_{i_1}, x_{e_1}, on which surface the linear density of current has the angular component, $j_\theta=1/2\pi p=n=$the number of turns per centimeter. The axial component of current is $j_x=1/2\pi r_1$, so that the unit current in the x direction is uniformly distributed over the sheet. The two terms, $\omega_\theta(x)+\omega_x(x)$, when used in eq 11 give the mutual inductance of the two current sheets which are associated with the helical filaments, h_1 and h_2. The first, $\omega_\theta(x)$, is that due to their angular or θ components of current, and this contributes the principal part to m. The second, $\omega_x(x)$, is relatively a second-order infinitesimal, representing the effect of the axial components of current. Each of these functions is an even function of its x-argument, vanishing with it. This property used in eq 11 gives the following interpretation of these functions.

Let the helices have the same end planes, $x_{i_1}=x_{i_2}$ and $x_{e_1}=x_{e_2}$. Then, if $x=x_{i_1}-x_{e_1}$, the function $2\omega_\theta(x)+2\omega_x(x)$, or explicitly $2\omega_\theta(x, r_1, r_2)+2\omega_x(x, r_1, r_2)$, represents the mutual inductance of two coaxial circular cylindrical current sheets of axial length x and radii r_1 and r_2, when they have the same end planes.

The integral definitions of these functions are

$$\omega_\theta(x)=\frac{\sqrt{r_1r_2}}{p^2}\int_0^x dx_2\int_0^{x_2}\phi_1(k_1)dx_1 \tag{13a}$$

$$\omega_x(x)=\frac{1}{\sqrt{r_1r_2}}\int_0^x dx_2\int_0^{x_2}\phi_0(k_1)dx_1 \tag{13b}$$

The azimuthal function, $\omega_a(x, \alpha)$, is written

$$\omega_a(x, \alpha)=\sum_{n=1}^{\infty}\omega_n(x, \alpha), \tag{13c}$$

where

$$\omega_n(x, \alpha)=\frac{\sqrt{r_1r_2}}{p^2}\int_0^x dx_2\int_0^{x_2}[\phi_{n-1}(k_1)+\phi_{n+1}(k_1)]\cos\frac{n}{p}(x_1-x+p\alpha)dx_1. \tag{13d}$$

It will be found that ω_a is also infinitesimal compared with the principal term ω_θ but, unlike ω_x, it contains first-order terms.

If, for brevity, we define the small quantity λ by

$$\lambda \equiv x_{i_2} - x_{i_1} = x_2^0 - x_1^0 + p\alpha, \tag{14}$$

the fundamental eq 11 becomes

$$m = \omega_\theta(l+\lambda) + \omega_\theta(l-\lambda) - 2\omega_\theta(\lambda) + 2\omega_x(l) + \omega_a(l+\lambda, \alpha) + \omega_a(-l+\lambda, \alpha) - 2\omega_a(\lambda, \alpha).$$

Since λ is small, this becomes

$$m = 2\omega_\theta(l) - 2\omega_\theta(\lambda) + 2\omega_x(l) + 4\sqrt{r_1 r_2}\left(\frac{\lambda}{2\pi p}\right)^2 \pi^2 \phi_1(k_l) + \omega_a(l+\lambda, \alpha) + \omega_a(-l+\lambda, \alpha) - 2\omega_a(\lambda, \alpha). \tag{15}$$

In the evaluation of these ω-functions which follows, frequent use will be made of the results and methods of an earlier paper,[2] which will be referred to as paper 2. Reference will also be made to paper 3.[3]

2. PRINCIPAL TERM, $\omega_\theta(l)$

The principal term, $2\omega_\theta(l)$, in eq 15 represents the mutual inductance of two coaxial current sheets of radii r_1 and r_2, which have common end planes and axial length, l. It is due to their angular component of current only. When $r_2 \to r_1$, this becomes the self inductance of the circular cylindrical sheet.

Since $r_2 - r_1$ is small, it will be appropriate to express this term as a self inductance corresponding to the cylindrical radius a, which is the arithmetic mean of the radii a_1 and a_2 of the two central filaments.

The self inductance of the current sheet of length, l, and this radius a is

$$L_s = \frac{4\pi N^2}{3}\sqrt{l^2+D^2}\left[K - E + \frac{D^2}{l^2}(E-k)\right], \tag{16}$$

where the modulus k is now given by

$$k^2 = \frac{D^2}{l^2+D^2} \text{ and } D = 2a = a_1 + a_2. \tag{17}$$

In eq 19 of appendix 3 of paper 2 is given an expansion which, to the second order inclusive, is, by a slight change in notation, equivalent to the following equation:

$$2\omega_\theta(l) = L_s - l\frac{|r_2-r_1|\sqrt{r_1 r_2}}{p^2} - 2\pi a\left(\frac{r_2-r_1}{2\pi p}\right)^2 \log\left(\frac{r_2-r_1}{8a}\right)^2 + 32\pi a\left\{A_1\left(\frac{a}{2\pi p}\right)\left(\frac{r_1-a+r_2-a}{2\pi p}\right) + A_3\left(\frac{r_1-a}{2\pi p}\right)\left(\frac{r_2-a}{2\pi p}\right) + A_4\left(\frac{r_2-r_1}{2\pi p}\right)^2\right\}, \tag{18}$$

[2] C. Snow, *Formula for the self inductance of a helix made with wire of any section*, BS Sci. Pap. **21**, 431 (1926–27) S537.

[3] C. Snow, *A simplified precision formula for the inductance of a helix with corrections for the lead-in wires*, BS J. Research **9**, 419 (1932) RP479.

where the constants A_1, A_3, and A_4 are functions of the modulus, k, which was defined in eq 17, as follows:

$$\left.\begin{aligned} A_1&=\frac{1}{2}\left[\frac{E}{k}-1\right] \\ A_3&=\frac{1}{2k}[2E-(1-k^2)K]-1 \\ A_4&=\frac{1}{8}\left[\frac{4E-(2-k^2)K}{k}-\frac{5}{2}\right] \end{aligned}\right\}. \tag{19}$$

It is evident that in the fourth term of eq 15 we may place $\sqrt{r_1r_2}=a$ and $\phi_1(k_1)=\phi_1(k)$, since this term is of the smallest order retained (second order).

3. SMALL TERM, $\omega_\theta(\lambda)$

To simplify the term $-2\omega_\theta(\lambda)$ (on account of the fact that λ is small), we write, by eq 15 and 13a,

$$-2\omega_\theta(\lambda)=-\frac{2\sqrt{(r_1r_2}}{p^2}\int_0^\lambda(\lambda-x_1)\phi_1(k_1)dx_1.$$

But since λ is small, x_1 is small throughout the range of this integration. Also r_2-r_1 is small, so that by eq 9 k_1' is small. Therefore, in this integral we may use eq 7, which gives

$$\begin{aligned} -2\phi_1(k_1)&=\frac{2}{\pi}\left[\log k_1'+\psi\left(\frac{3}{2}\right)-\psi(1)\right]+\text{infinitesimals} \\ &=\frac{2}{\pi}[\log k_1'+2-2\log 2] \\ &=\frac{1}{\pi}\left\{4-2\log 8\sqrt{r_1r_2}+\log[x_1^2+(r_2-r_1)^2]\right\}. \end{aligned}$$

Hence $\omega_\theta(\lambda)$ is an even function of λ, which differs infinitesimally from the following integral:

$$-2\omega_\theta(\lambda)=\frac{\sqrt{r_1r_2}}{\pi p^2}\int_0^\lambda(\lambda-x_1)\left\{4-2\log 8\sqrt{r_1r_2}+\log[x_1^2+(r_2-r_1)^2]\right\}dx_1.$$

The result of this integration and of others which are to follow may be abbreviated by introducing the complex variables

$$z\equiv i[\lambda+i(r_2-r_1)]=-(r_2-r_1)+i(x_2^0-x_1^0+p\alpha). \tag{20}$$

and

$$z'\equiv|r_2-r_1|+i|\lambda|. \tag{20'}$$

Then $\omega_\theta(\lambda)$ is a relatively small term of second order, given by the real part of

$$-2\omega_\theta(\lambda)=\pi a\left\{\left(\frac{\lambda}{2\pi p}\right)^2\left[2-4\log\frac{8a}{2\pi p}\right]+2\left(\frac{r_2-r_1}{2\pi p}\right)^2\log\left(\frac{r_2-r_1}{2\pi p}\right)^2 -4\left(\frac{z}{2\pi p}\right)^2\log\left(\frac{z}{2\pi p}\right)\right\} \tag{21}$$

4. AXIAL-CURRENT TERM, $\omega_x(l)$

This term of second order may be treated as a constant. It may be computed by

$$2\omega_x(l)=2l\omega_x'(l)-\frac{4D}{\pi}\left(\frac{E}{k}-1\right), \tag{22}$$

where, by eq 43 of paper 1,

$$\omega_x'(l)=\log\frac{l+\sqrt{l^2+D^2}}{D}+\frac{l}{\sqrt{l^2+D^2}}\log 2. \tag{23}$$

This approximation was derived on the assumption (here adopted) that terms in the ω-functions of order of magnitude $.1D$ are negligible (3 parts in 10^7).

In paper 3 (eq 8) an approximation was used which is equivalent to

$$2\omega_x'(l)=P\left(\frac{k'}{k}\right)=\frac{k^2}{4k'^2}+2\log\frac{4k'}{k}, \text{ if } k'>k$$

$$=\frac{3k'}{k}-\frac{k'}{k}\log\frac{k'}{k}, \text{ if } k'<k. \tag{23'}$$

Either eq 23 or 23′ is adequate for computing this relatively small term. The former has the advantage of a single form, and is one which blends naturally with the corresponding terms representing the effect of the lead wires (eq 62, below).

5. AZIMUTH TERM, ω_n

In paper 1, pages 255–258, it is shown that instead of the integral 13d for ω_n we may take

$$\frac{n^2\omega_n(x,\alpha)}{\pi\sqrt{r_1r_2}}=-\frac{\sqrt{r_1r_2}\cos n\alpha}{\pi}\int_0^\infty\frac{1-\left(\frac{ps}{n}\right)^2}{\left[1+\left(\frac{ps}{n}\right)^2\right]^2}e^{-|x|s}J(n_1s)ds$$

$$\pm\left\{\left[\frac{nx}{\pi p}\cos n\left(\alpha-\frac{x}{p}\right)+\left(\frac{1}{\pi}+\frac{n|r_2-r_1|}{\pi p}\right)\sin n\left(\alpha-\frac{x}{p}\right)\right]e^{\frac{-n|r_2-r_1|}{p}}\right.$$

$$\left.-\sin n\alpha\frac{2p\sqrt{r_1r_2}}{\pi n}\int_0^\infty\frac{se^{-|x|s}J(n,s)}{\left[1+\left(\frac{ps}{n}\right)^2\right]^2}ds\right\}, \tag{24}$$

where for brevity

$$J(n,s)\equiv J_{n-1}(r_1s)J_{n-1}(r_2s)+J_{n+1}(r_1s)J_{n+1}(r_2s). \tag{25}$$

The upper or lower of the ambiguous signs is to be taken according as x is positive or negative, the quantity affected with the $\pm$ sign being

zero when x is zero. This expression 24 is not equal to the integral definition of ω_n given in eq 13d. It is, however, effectively the same since terms have been discarded which cancel out of eq 11. Such a procedure is allowable if we make eq 24 the basis for simplifying the function $\omega_n(k)$ both in the case where x is small and when it is finite, so that the terms in question actually are discarded from each of the four ω-functions occurring in eq 11.

The simplification of eq 24 depends upon the fact that we may neglect all terms in this equation which are infinitesimals of higher order than the second in comparison with ω_θ, which contains the factor $1/p^2$.

When x is finite, the second integral in eq 24 is negligible, and the first may be replaced by

$$\int_0^\infty e^{-|x|s} J(n, s)ds = \frac{1}{\sqrt{r_1 r_2}}[\phi_{n-1}(k) + \phi_{n+1}(k)],$$

as shown by eq 10. This is an even function of x.
Hence

$$\omega_a(l+\lambda, \alpha) + \omega_a(l-\lambda, \alpha) =$$

$$= \pi\sqrt{r_1 r_2}\left\{\frac{2l}{\pi p}\sum_{n=1}^{\infty}\frac{1}{n}e^{\frac{-n|r_3-r_1|}{p}}\cos\frac{n(x_2^0-x_1^0)}{p} - \frac{2}{\pi}\sum_{n=1}^{\infty}[\phi_{n-1}(k_l)+\phi_{n+1}(k_s)]\frac{\cos n\alpha}{n^2}\right\}$$

$$= -\pi\sqrt{r_1 r_2}\left\{\frac{2l}{\pi p}\log\left[1-e^{-\left(\frac{|r_3-r_1|+i(x_2^0-x_1^0)}{p}\right)}\right]\right.$$

$$\left. + \frac{2}{\pi}\sum_{n=1}^{\infty}\frac{[\phi_{n-1}(k_l)+\phi_{n+1}(k_l)]}{n^2}\cos n\alpha\right\}, \qquad (26)$$

where the real part is to be taken.

The logarithmic term containing the factor l/p is the most important correction term. The series in $\cos n\alpha$ is the smallest order of magnitude retained (second order relative to ω_θ). It is shown in eq 57 of paper 1 that an approximation in finite form sufficient in all cases is given by

$$\frac{2}{\pi}\sum_{n=1}^{\infty}\left[\frac{\phi_{n-1}(k)+\phi_{n+1}(k)}{n^2}\right]\cos n\alpha = \frac{2\pi}{3}\phi_1(k) + \frac{1}{k}\sqrt{1-k^2\cos^2\frac{\alpha}{2}}$$

$$-\left(\frac{k'}{k}\right)^2\left(\cos\frac{\alpha}{2}\right)\sin^{-1}\left(k\cos\frac{\alpha}{2}\right) - \frac{1}{k^2}\sin\frac{\alpha}{2}\log\left[\frac{k\sin\frac{\alpha}{2}+\sqrt{1-k^2\cos^2\frac{\alpha}{2}}}{k'}\right] \qquad (27)$$

(By a misprint the logarithm had the factor $1/k$ instead of $1/k^2$ in eq 57, but this was used correctly in the equations depending upon it.)

The derivation of eq 27 depends upon the fact that the continuous, even function of θ, $f(\theta)$, which is never negative and is a periodic function of θ with period 2π, defined for all real values of θ by the series

$$f(\theta)=\frac{2}{3}-\frac{4}{\pi^2}\sum_{n=1}^{\infty}\frac{\cos n\theta}{n^2} \tag{28}$$

is represented approximately, for all values of θ, by

$$f(\theta)\approx\left|\sin\frac{\theta}{2}\right|. \tag{28'}$$

The exact expression for $f(\theta)$ is

$$f(\theta)=4\left(\frac{\theta}{2\pi}\right)\left(1-\frac{\theta}{2\pi}\right) \text{ for the range } 0\leqslant\theta\leqslant 2\pi \tag{28''}$$

or

$$f(\theta)=4\left[\left|\frac{\theta}{2\pi}\right|-\left(\frac{\theta}{2\pi}\right)^2\right] \text{ for the range } -2\pi<\theta<2\pi. \tag{28'''}$$

The graph of $f(\theta)$ is a continuous curve represented by a succession of parabolic arcs. Its slope is discontinuous at $\theta=0$ or $2\pi n$.

Using eq 27, we find that expression 26 becomes

$$\begin{aligned}&\omega_a(l+\lambda,\alpha)+\omega_a(l-\lambda,\alpha)\\&=-\pi\sqrt{r_1r_2}\left\{\frac{2l}{\pi p}\log\left[1-e^{-\left(\frac{|r_2-r_1|+i(x_2^0-x_1^0)}{p}\right)}\right]\right.\\&\quad+\frac{2\pi}{3}\phi_1(k_l)+\frac{1}{k_l}\sqrt{1-k_l^2\cos^2\frac{\alpha}{2}}\\&\quad-\left(\frac{k_l'}{k_l}\right)^2\cdot\left(\cos\frac{\alpha}{2}\right)\sin^{-1}\left(k_l\cos\frac{\alpha}{2}\right)\\&\quad\left.-\frac{1}{k_l^2}\sin\frac{\alpha}{2}\cdot\log\left[\frac{k_l\sin\frac{\alpha}{2}+\sqrt{1-k_l^2\cos^2\frac{\alpha}{2}}}{k_l'}\right]\right\}.\end{aligned} \tag{29}$$

We next consider the last term in eq 15, which is $-2\omega_a(\lambda,\alpha)$. Since λ is small, we must now consider all the terms in eq 24 in order to obtain valid expressions for $\omega_n(\lambda,\alpha)$. Considering λ as an infinitesimal of the same order as the pitch or smaller, it is evident that the ratio, λ/p, may be infinitesimal, but in general may have a finite value positive or negative.

Reference to eq 10*a* shows that we may write

$$-\frac{\sqrt{(r_1r_2}}{\pi}\int_0^\infty \frac{1-\left(\frac{ps}{n}\right)^2}{\left[1+\left(\frac{ps}{n}\right)^2\right]^2}\, e^{-|\lambda|s}J(n,\, s)ds = -\frac{1}{\pi}[\phi_{n-1}(k_\lambda)+\phi_{n+1}(k_\lambda)]$$

$$+\frac{\sqrt{r_1r_2}}{\pi}\int_0^\infty\left(\frac{ps}{n}\right)^2\left\{\frac{2}{\left[1+\left(\frac{ps}{n}\right)^2\right]^2}+\frac{1}{1+\left(\frac{ps}{n}\right)^2}\right\}e^{-|\lambda|s}J(n,\, s)ds, \quad (30)$$

where the last integral is no longer infinitesimal with p, because λ is also infinitesimal. In fact, the substitution $s=nt/p$ gives

$$I\equiv\frac{\sqrt{r_1r_2}}{\pi}\int_0^\infty\left(\frac{ps}{n}\right)^2\left\{\frac{2}{\left[1+\left(\frac{ps}{n}\right)^2\right]^2}+\frac{1}{1+\left(\frac{ps}{n}\right)^2}\right\}e^{-|\lambda|s}Jn,\, s)ds$$

$$=\frac{n\sqrt{r_1r_2}}{\pi p}\int_0^\infty t^2\left\{\frac{2}{[1+t^2]^2}+\frac{1}{1+t^2}\right\}e^{-\left|\frac{n}{p}\right|t}\, J\left(n,\frac{nt}{p}\right)dt, \quad (31)$$

which shows the integral is a function of the finite ratio, $|\lambda/p|$. Referring to eq 25, we find

$$J\left(n,\frac{nt}{p}\right)=J_{n-1}\left(\frac{nr_1}{p}t\right)J_{n-1}\left(\frac{nr_2}{p}t\right)+J_{n+1}\left(\frac{nr_1}{p}t\right)J_{n+1}\left(\frac{nr_2}{p}t\right),$$

in which the argument, ntr/p, of the Bessel's function is large (even in the case $n=1$), except when t is small, but in that case the factor t^2 in the integrand of eq 31 renders its values of little or no importance in the initial range of the variable t. (Also all the Bessel's functions involved vanish with t except J_0). We make an infinitesimal error in I by introducing in place of $J\left(n,\frac{nt}{p}\right)$ the principal term of its asymptotic expansion, which is

$$\frac{n}{p}\sqrt{r_1r_2}J\left(n,\frac{nt}{p}\right)\approx\frac{2}{\pi t}\left[\cos\frac{n}{p}(r_2-r_2)t-(-1)^n\sin\frac{n}{p}(r_2+r_1)t\right]. \quad (32)$$

Reference to tabular values of Bessel's functions shows that this is exceedingly accurate for arguments greater than 10. In this case, if the pitch, $2\pi p$, is 0.1 cm, and $r_1=15$ cm, the argument nr_1t/p is $300\pi nt$, or $t(10)^3$, even in the case $n=1$. Hence the asymptotic expansion is good if t is as small as .01, in which case the factor t^2 of the integrand in eq 31 is not greater than $(10)^{-4}$.

Hence, if λ, r_2-r_1, and p are all infinitesimals, the integral I of eq 31 may be shown by use of eq 32 to differ by an infinitesimal amount from the following:

$$I=\frac{2}{\pi^2}\int_0^\infty\left[\frac{2t}{(1+t^2)^2}+\frac{t}{1+t^2}\right]e^{-n|\frac{\lambda}{p}|t}\cos\frac{n}{p}(r_2-r_1)tdt$$

$$=\frac{2}{\pi^2}+\frac{2}{\pi^2}\int_0^\infty\frac{e^{-\frac{n}{p}|\lambda|t}}{1+t^2}\left[(t-\frac{n}{p}|\lambda|)\cos\frac{n}{p}(r_2-r_1)t-\frac{n}{p}(r_2-r_1)\sin\frac{n}{p}(r_2-r_1)t\right]dt.$$

This is equivalent to

$$I=\frac{2}{\pi^2}+\frac{2}{\pi^2}\int\frac{s+\frac{inz'}{p}}{1+s^2}e^{\frac{inz'}{p}s}ds, \tag{33}$$

where the real part is to be taken and z' is defined by eq 20′. The detailed justification of this process of deriving eq 33 is given in appendix 5 of paper 2. In appendix 8 of the same paper, it is also shown by deforming the path of the integral that

$$\frac{2}{\pi^2}\int_0^\infty\frac{s+\frac{inz'}{p}}{1+s^2}e^{\frac{inz'}{p}s}ds=\frac{i}{\pi}\left(1+\frac{nz'}{p}\right)e^{\frac{-nz'}{p}}+\frac{2}{\pi^2}\int_0^\infty\frac{\left[t\cos nt-n\left(\frac{z'}{p}\right)^2\sin nt\right]}{t^2+\left(\frac{z'}{p}\right)^2}dt. \tag{34}$$

Hence eq 30 becomes

$$-\frac{\sqrt{r_1r_2}}{\pi}\int_0^\infty\frac{1-\left(\frac{ps}{n}\right)^2}{\left[1+\left(\frac{ps}{n}\right)^2\right]^2}e^{-|\lambda|s}J(n,s)ds=-\frac{1}{\pi}[\phi_{n-1}(k_\lambda)+\phi_{n+1}(k_\lambda)]$$

$$+\frac{2}{\pi^2}+\frac{i}{\pi}\left(1+\frac{nz'}{p}\right)e^{-\frac{nz'}{p}}+\frac{2}{\pi^2}\int_0^\infty\frac{t\cos nt-n\left(\frac{z'}{p}\right)^2\sin nt}{t^2+\left(\frac{z'}{p}\right)^2}dt. \tag{35}$$

By the same process it is found that

$$-\frac{2p\sqrt{r_1r_2}}{n\pi}\int_0^\infty\frac{se^{-|\lambda|s}J(n,s)}{\left[1+\left(\frac{ps}{n}\right)^2\right]^2}ds=-\frac{2}{\pi^2}\int_0^\infty\frac{1-\frac{inz'}{p}s}{1+s^2}e^{\frac{inz'}{p}s}ds$$

$$=-\frac{1}{\pi}\left(1+\frac{nz'}{p}\right)e^{-\frac{nz'}{p}}-\frac{2iz}{\pi^2p}\int_0^\infty\frac{\sin nt-nt\cos nt}{t^2+\left(\frac{z'}{p}\right)^2}dt. \tag{36}$$

Now, by eq 13c

$$\frac{\omega_a(\lambda, \alpha)}{\pi\sqrt{r_1 r_2}} = \frac{1}{\pi\sqrt{r_1 r_2}} \sum_{n=1}^{\infty} \omega_n(\lambda, \alpha),$$

where ω_n is given by eq 24 and where the two integrals of eq 24 are given by eq 35 and 36. Hence

$$\frac{\omega_a(\lambda, \alpha)}{\pi\sqrt{r_1 r_2}} = \sum_{n=1}^{\infty} \frac{\cos n\alpha}{n^2} \left\{ -\frac{1}{\pi}[\phi_{n-1}(k_\lambda) + \phi_{n+1}(k_\lambda)] + \frac{2}{\pi^2} + \right.$$

$$\left. + \frac{i}{\pi}\left(1 + \frac{nz'}{p}\right) e^{\frac{-nz'}{p}} + \frac{2}{\pi^2} \int_0^{\infty} \frac{t \cos nt - n\left(\frac{z'}{p}\right)^2 \sin nt}{t^2 + \left(\frac{z'}{p}\right)^2} dt \right\}$$

$$\pm \sum_{n=1}^{\infty} \frac{1}{n^2} \left\{ \left[\frac{n\lambda}{\pi p} \cos n\left(\alpha - \frac{\lambda}{p}\right) + \left(\frac{1}{\pi} + \frac{n|r_2 - r_1|}{\pi p}\right) \sin n\left(\alpha - \frac{\lambda}{p}\right) \right] e^{\frac{-n|r_2 - r_1|}{p}} \right.$$

$$\left. - \frac{1}{\pi}\left(1 + \frac{nz'}{p}\right) e^{\frac{-nz'}{p}} \sin n\alpha - \frac{2iz \sin n\alpha}{\pi^2 p} \int_0^{\infty} \frac{\sin nt - nt \cos nt}{t^2 + \left(\frac{z'}{p}\right)^2} dt \right\},$$

where the real part is to be taken, z' being given by eq 20′. The upper or lower of the ambiguous signs belongs with λ positive or negative, respectively.

Making some cancelations, this gives

$$\frac{\omega_a(\lambda, \alpha)}{\pi\sqrt{r_1 r_2}} = \frac{2}{\pi^2} \sum_{n=1}^{\infty} \frac{\cos n\alpha}{n^2} - \frac{1}{\pi} \sum_{n=1}^{\infty} [\phi_{n-1}(k_\lambda) + \phi_{n+1}(k_\lambda)] \frac{\cos n\alpha}{n^2}$$

$$+ \frac{1}{\pi^2} \int_0^{\infty} \frac{dt}{t^2 + \left(\frac{z'}{p}\right)^2} \left\{ t \sum_{n=1}^{\infty} \frac{2 \cos nt \cos n\alpha}{n^2} - \left(\frac{z'}{p}\right)^2 \sum_{n=1}^{\infty} \frac{2 \sin nt \cos n\alpha}{n} \right.$$

$$\left. \pm \frac{iz'}{p} \left[\sum_{n=1}^{\infty} \frac{2 \sin nt \sin n\alpha}{n^2} - t \sum_{n=1}^{\infty} \frac{2 \cos nt \sin n\alpha}{n} \right] \right\}. \quad (37)$$

It is now easy to see, by taking the real part of this equation, that the ambiguous sign $\pm$ may be avoided, for we obtain the same real part if we replace z' by z in eq 37 and take the upper of the double sign $\mp$. We thus return to the complex variable z of eq 20 and have no more need for z'.

It is necessary to evaluate eq 37 for the case where $-2\pi < \alpha < 2\pi$.

Writing $2 \cos nt \cos n\alpha = \cos n(t+\alpha) + \cos n(t-\alpha)$, and then making the substitution $t' = t + \alpha$ and $t' = t - \alpha$, respectively, we obtain integrals

over the infinite range, in which the integrand contains either the factor

$$\pi^{-2}\sum_{1}^{\infty}n^{-2}\cos nt$$

or

$$\pi^{-2}\sum_{1}^{\infty}n^{-1}\sin nt,$$

both of which are periodic functions of t with period 2π, the first being an even function of t, which is equal to

$$\left(\frac{t}{2\pi}\right)^2-\frac{t}{2\pi}+\frac{1}{6}$$

for the positive range, $0\leqq t\leqq 2\pi$; the second an odd function, which is equal to

$$-\frac{1}{2\pi}\left[2\left(\frac{t}{2\pi}\right)-1\right]$$

for this range.

Hence, writing

$$\int_0^{\infty}(\ldots)dt=\sum_{n=0}^{\infty}\int_{2\pi n}^{2\pi(n+1)}(\ldots)dt,$$

and taking account of the periodicity of the series, we find (for the case $0\leqq|\alpha|<2\pi$).

$$I_1\equiv\frac{1}{\pi^2}\int_0^{\infty}\frac{dt}{t^2+\frac{z^2}{p^2}}\left\{t\sum_{1}^{\infty}\frac{2\cos nt\cos n\alpha}{n^2}-\frac{z^2}{p^2}\sum_{1}^{\infty}\frac{2\sin nt\cos n\alpha}{n}\right\}$$

$$=-2\int_0^{\frac{|\alpha|}{2\pi}}\frac{\left(t-\frac{|\alpha|}{2\pi}\right)\left(t^2-t+\frac{1}{6}\right)+\left(\frac{z}{2\pi p}\right)^2(2t-1)}{\left(t-\frac{|\alpha|}{2\pi}\right)^2+\left(\frac{z}{2\pi p}\right)^2}dt$$

$$+\sum_{n=0}^{\infty}\int_0^1 dt\left\{\frac{\left(t+n+\frac{\alpha}{2\pi}\right)\left(t^2-t+\frac{1}{6}\right)+\left(\frac{z}{2\pi p}\right)^2(2t-1)}{\left(t+n+\frac{\alpha}{2\pi}\right)^2+\left(\frac{z}{2\pi p}\right)^2}\right.$$

$$+\frac{\left(t+n-\frac{\alpha}{2\pi}\right)\left(t^2-t+\frac{1}{6}\right)+\left(\frac{z}{2\pi p}\right)^2(2t-1)}{\left(t+n-\frac{\alpha}{2\pi}\right)^2+\left(\frac{z}{2\pi p}\right)^2}\Bigg\} \tag{38}$$

and

$$I_2\equiv\frac{-iz}{\pi^2 p}\int_0^\infty \frac{dt}{t^2+\frac{z^2}{p^2}}\left\{\sum_1^\infty \frac{2\sin nt\sin n\alpha}{n^2}-t\sum_1^\infty\frac{\cos nt\sin n\alpha}{n}\right\}$$

$$=\pm 2i\left(\frac{z}{2\pi p}\right)\int_0^{\frac{|\alpha|}{2\pi}}\frac{t^2-t+\frac{1}{6}-\left(t-\frac{|\alpha|}{2\pi}\right)(2t-1)}{\left(t-\frac{|\alpha|}{2\pi}\right)^2+\left(\frac{z}{2\pi p}\right)^2}dt$$

$$-2i\left(\frac{z}{2\pi p}\right)\sum_{n=0}^\infty\int_0^1 dt\Bigg\{\frac{t^2-t+\frac{1}{6}-\left(t+n+\frac{\alpha}{2\pi}\right)(2t-1)}{\left(t+n+\frac{\alpha}{2\pi}\right)^2+\left(\frac{z}{2\pi p}\right)^2}$$

$$-\frac{t^2-t+\frac{1}{6}-\left(t+n-\frac{\alpha}{2\pi}\right)(2t-1)}{\left(t+n-\frac{\alpha}{2\pi}\right)^2+\left(\frac{z}{2\pi p}\right)^2}\Bigg\}, \tag{39}$$

where the upper sign of the $\mp$ is to be taken when α is positive and the lower when α is negative.

Hence

$$I_1+I_2=-2\int_0^{\frac{\alpha}{2\pi}}\frac{t^2-|t|+\frac{1}{6}-\left(\frac{iz}{2\pi p}\right)(2t\mp 1)}{t-\frac{p\alpha+iz}{2\pi p}}dt$$

$$+\sum_{n=0}^\infty\int_0^1 dt\Bigg\{\frac{t^2-t+\frac{1}{6}+\left(\frac{iz}{2\pi p}\right)(2t-1)}{t+n+\frac{p\alpha+iz}{2\pi p}}$$

$$+\frac{t^2-t+\frac{1}{6}-\left(\frac{iz}{2\pi p}\right)(2t-1)}{t+n-\frac{p\alpha+iz}{2\pi p}}\Bigg\} \tag{40}$$

or

$$I_1+I_2=-2\int_0^{\alpha/2\pi}\left[t\mp 1+\frac{\alpha}{2\pi}-\frac{iz}{2\pi p}+\frac{\frac{1}{6}\mp\frac{\alpha}{2\pi}+\left(\frac{\alpha}{2\pi}\right)^2+\left(\frac{z}{2\pi p}\right)^2}{t-\frac{p\alpha+iz}{2\pi p}}\right]dt$$

$$+\sum_{n=0}^{\infty}\int_0^1 dt\left\{2t-2n-2+\frac{n(n+1)+\frac{1}{6}+(2n+1)\frac{\alpha}{2\pi}+\left(\frac{\alpha}{2\pi}\right)^2+\left(\frac{z}{2\pi p}\right)^2}{t+n+\frac{p\alpha+iz}{2\pi p}}\right.$$

$$\left.+\frac{n(n+1)+\frac{1}{6}-(2n+1)\frac{\alpha}{2\pi}+\left(\frac{\alpha}{2\pi}\right)^2+\left(\frac{z}{2\pi p}\right)^2}{t+n-\frac{p\alpha+iz}{2\pi p}}\right\}. \tag{41}$$

At this point it is convenient to introduce the complex quantity

$$z_{12}\equiv x_2^0-x_1^0+i(r_2-r_1)=-(p\alpha+iz). \tag{42}$$

Then for brevity let

$$t_0\equiv-\frac{z_{12}}{2\pi p}=\frac{\alpha}{2\pi}+i\left(\frac{z}{2\pi p}\right) \tag{43}$$

Then $|t_0|<1$, since the absolute value, $|z_{12}|$, is the distance between the two points, P_1^0 and P_2^0, in the reference sections, through which the helices h_1 and h_2 pass. The terms of the series in eq 41 may therefore be expanded before integrating. This gives

$$I_1+I_2=-1-\frac{\alpha}{\pi}\left[\frac{3\alpha}{4\pi}-\frac{iz}{2\pi p}\mp 1\right]-2\left[\frac{1}{6}\mp\frac{\alpha}{2\pi}+\left(\frac{\alpha}{2\pi}\right)^2+\left(\frac{z}{2\pi p}\right)^2\right]\int_0^{\alpha/2\pi}\frac{dt}{t-t_0}$$

$$+\left[\frac{1}{6}+\frac{\alpha}{2\pi}+\left(\frac{\alpha}{2\pi}\right)^2+\left(\frac{z}{2\pi p}\right)^2\right]\int_0^1\frac{dt}{t+t_0}$$

$$+\left[\frac{1}{6}-\frac{\alpha}{2\pi}+\left(\frac{\alpha}{2\pi}\right)^2+\left(\frac{z}{2\pi p}\right)^2\right]\int_0^1\frac{dt}{t-t_0}$$

$$-\sum_{n=1}^{\infty}\left\{2n+1-\left[\frac{1}{6}+n(n+1)\right]\log\left(\frac{n+1}{n}\right)^2\right\}$$

$$+\left[\frac{1}{6}+\left(\frac{\alpha}{2\pi}\right)^2+\left(\frac{z}{2\pi p}\right)^2\right]\sum_{n=1}^{\infty}\sum_{s=1}^{\infty}\frac{t_0^{2s}}{s}\left[\frac{1}{n^{2s}}-\frac{1}{(n+1)^{2s}}\right]$$

$$-\frac{\alpha}{\pi}\sum_{n=1}^{\infty}\left\{(2n+1)\sum_{s=1}^{\infty}\frac{t_0^{2s-1}}{2s-1}\left[\frac{1}{n^{2s-1}}-\frac{1}{(n+1)^{2s-1}}\right]-t_0\log\left(\frac{n+1}{n}\right)^2\right\}$$

$$+\sum_{n=1}^{\infty}\left\{n(n+1)\sum_{s=1}^{\infty}\frac{t_0^{2s}}{s}\left[\frac{1}{n^{2s}}-\frac{1}{(n+1)^{2s}}\right]-t_0^2\log\left(\frac{n+1}{n}\right)^2\right\}. \qquad (44)$$

The first series in this equation is purely numerical and has the value .004, which is negligible, as are terms 10 times as large.

The term containing the next series is found (by summing first with respect to n) to be

$$-\left[\frac{1}{6}+\left(\frac{\alpha}{2\pi}\right)^2+\left(\frac{z}{2\pi p}\right)^2\right]\log(1-t_0^2).$$

To transform the next series in eq 44, we expand $\log\left(\frac{n+1}{n}\right)^2$ and write

$$\sum_{s=1}^{\infty}\frac{t_0^{2s-1}}{2s-1}B_{n,\,s}=(2n+1)\sum_{s=1}^{\infty}\frac{t_0^{2s-1}}{2s-1}\left[\frac{1}{n^{2s-1}}-\frac{1}{(n+1)^{2s-1}}\right]-t_0\log\left(\frac{n+1}{n}\right)^2,$$

where

$$B_{n,\,1}\equiv-\frac{1}{n(n+1)}+2\left[\frac{1}{2n^2}-\frac{1}{3n^3}+\frac{1}{4n^4}-\frac{1}{5n^5}+\ldots\right]$$

and

$$B_{n,\,s}=2\left[\frac{1}{n^{2s-2}}-\frac{1}{(n+1)^{2s-2}}\right]+\frac{1}{n^{2s-1}}+\frac{1}{(n+1)^{2s-1}},\ \text{if } s>1.$$

Hence

$$\sum_{n=1}^{\infty}B_{n,\,s}=1+2\sum_{n=1}^{\infty}\frac{1}{n^{2s-1}},\ \text{if } s>1.$$

$$=.154\ldots,\ \text{if } s=1.$$

Hence introducing Riemann's zeta function

$$\zeta(s)\equiv\sum_{n=1}^{\infty}\frac{1}{n^s}\ \text{for } s>1, \qquad (45)$$

then the next to last series in eq 44 is

$$\frac{\alpha}{\pi}\left\{.846t_0+\frac{1}{2}\log\left(\frac{1-t_0}{1+t_0}\right)-2\sum_{s=2}^{\infty}\frac{\zeta(2s-1)}{2s-1}\cdot t_0^{2s-1}\right\}.$$

Similarly, to transform the last series in eq 44, we write

$$\sum_{s=1}^{\infty}\frac{t_0^{2s}}{s}C_{n,\,s}=n(n+1)\sum_{s=1}^{\infty}\frac{t_0^{2s}}{s}\left[\frac{1}{n^{2s}}-\frac{1}{(n+1)^{2s}}\right]-t_0^2\log\left(\frac{n+1}{n}\right)^2,$$

where $C_{n,\,1}=B_{n,\,1}$ and

$$C_{n,\,s}=\frac{1}{n^{2s-2}}-\frac{1}{(n+1)^{2s-2}}+\frac{1}{n^{2s-1}}+\frac{1}{(n+1)^{2s-1}},\text{ if } s>1.$$

Hence

$$\sum_{n=1}^{\infty}C_{n,\,s}=2\sum_{n=1}^{\infty}\frac{1}{n^{2s-1}}=2\zeta(2s-1),\text{ if } s>1$$
$$=.154,\text{ if } s=1.$$

The last series in eq 44 is therefore

$$.154t_0^2+2\sum_{s=2}^{\infty}\frac{\zeta(2s-1)}{s}t_0^{2s}.$$

Hence eq 44 becomes

$$\begin{aligned}I_1+I_2=&-1+\frac{|\alpha|}{\pi}\left(1-\frac{|\alpha|}{2\pi}\right)-\frac{\alpha}{2\pi}\left[\frac{\alpha}{2\pi}-\frac{2iz}{2\pi p}\right]\\&-2\left[\frac{1}{6}-\frac{|\alpha|}{2\pi}+\left(\frac{\alpha}{2\pi}\right)^2+\left(\frac{z}{2\pi p}\right)^2\right]\cdot\left[\log\left(\frac{z}{2\pi pt_0}\right)+i\frac{\pi}{2}\right]\\&+\left[\frac{1}{6}+\frac{\alpha}{2\pi}+\left(\frac{\alpha}{2\pi}\right)^2+\left(\frac{z}{2\pi p}\right)^2\right]\cdot[\log(1+t_0)-\log t_0]\\&+\left[\frac{1}{6}-\frac{\alpha}{2\pi}+\left(\frac{\alpha}{2\pi}\right)^2+\left(\frac{z}{2\pi p}\right)^2\right]\cdot[\log(1-t_0)-\log t_0+i\pi]\\&-\left[\frac{1}{6}+\left(\frac{\alpha}{2\pi}\right)^2+\left(\frac{z}{2\pi p}\right)^2\right]\log(1-t_0^2)+\frac{\alpha}{2\pi}\log\frac{1-t_0}{1+t_0}\\&+[1-.154]\frac{\alpha t_0}{\pi}+.154t_0^2-\frac{2\alpha}{\pi}\sum_{s=2}^{\infty}\frac{\zeta(2s-1}{2s-1}\cdot t_0^{2s-1}+2\sum_{s=2}^{\infty}\frac{\zeta(2s-1)}{s}\cdot t_0^{2s},\end{aligned}$$

where imaginary terms are to be discarded.

This reduces to

$$\begin{aligned}I_1+I_2=&-1-\frac{3\alpha^2}{4\pi^2}+\frac{|\alpha|}{\pi}\left(1-\frac{|\alpha|}{\pi}\right)+1.85\frac{\alpha}{\pi}t_0+.154t_0^2\\&+\left[\frac{|\alpha|}{\pi}\left(1-\frac{|\alpha|}{2\pi}\right)-\frac{1}{3}-2\left(\frac{z}{2\pi p}\right)^2\right]\log\frac{z}{2\pi p}\\&-\frac{|\alpha|}{\pi}\log t_0-2\frac{\alpha}{\pi}\sum_{s=2}^{\infty}\frac{\zeta(2s-1)}{2s-1}t_0^{2s-1}+2\sum_{s=2}^{\infty}\frac{\zeta(2s-1)}{s}t_0^{2s}.\end{aligned}\qquad(46)$$

The definitions of I_1 and I_2 in eq 38 and 39 show that eq 37 is

$$\frac{\omega_s(\lambda,\,\alpha)}{\pi\sqrt{r_1r_2}}=\frac{2}{\pi^2}\sum_{n=1}^{\infty}\frac{\cos n\alpha}{n^2}-\frac{1}{\pi}\sum_{n=1}^{\infty}[\phi_{n-1}(k_\lambda)+\phi_{n+1}(k_\lambda)]\frac{\cos n\alpha}{n^2}+I_1+I_2.\qquad(47)$$

Since we are considering the case where $-2\pi<\alpha<2\pi$ for which eq 46 applies, it is evident by reference to eq 28 and 28″ that

$$\frac{2}{\pi^2}\sum_{n=1}^{\infty}\frac{\cos n\alpha}{n^2}=\frac{1}{3}-\frac{|\alpha|}{\pi}\left(1-\frac{|\alpha|}{2\pi}\right). \tag{48}$$

Also since λ is small, as well as r_2-r_1, it is evident that k'_λ is small, so that by eq 27, neglecting infinitesimals

$$-\frac{1}{\pi}\sum_{n=1}^{\infty}[\phi_{n-1}(k_\lambda)+\phi_{n+1}(k_\lambda)]\frac{\cos n\alpha}{n^2}=-\frac{\pi}{3}\phi_1(k_\lambda)-\frac{1}{2}\left|\sin\frac{\alpha}{2}\right|\cdot\left(1-\log\frac{2\left|\sin\frac{\alpha}{2}\right|}{k'_\lambda}\right)$$

$$=\frac{2}{3}+\frac{1}{3}\log\frac{k'_\lambda}{4}-\frac{1}{2}\left|\sin\frac{\alpha}{2}\right|\cdot\left(1-\log\frac{2\left|\sin\frac{\alpha}{2}\right|}{k'_\lambda}\right)$$

$$=\frac{2}{3}-\frac{1}{2}\left|\sin\frac{\alpha}{2}\right|\left(1-\log\frac{1}{2}\left|\sin\frac{\alpha}{2}\right|\right)+\left[\frac{1}{3}-\frac{1}{2}\left|\sin\frac{\alpha}{2}\right|\right]\log\left(\frac{z}{8\sqrt{r_1r_2}}\right).$$

By eq 28′ and 28″ we may place

$$\frac{1}{2}\left|\sin\frac{\alpha}{2}\right|=\frac{|\alpha|}{\pi}\left(1-\frac{|\alpha|}{2\pi}\right)$$

so that

$$-\frac{1}{\pi}\sum_{n=1}^{\infty}[\phi_{n-1}(k_\lambda)+\phi_{n+1}(k_\lambda)]\frac{\cos n\alpha}{n^2}=\frac{2}{3}-\frac{|\alpha|}{\pi}\left(1-\frac{|\alpha|}{2\pi}\right)\left[1-\log\frac{|\alpha|}{\pi}\left(1-\frac{|\alpha|}{2\pi}\right)\right]$$

$$+\left[\frac{1}{3}-\frac{|\alpha|}{\pi}\left(1-\frac{|\alpha|}{2\pi}\right)\right]\log\frac{z}{8\sqrt{r_1r_2}}. \tag{49}$$

Using eq 46, 48, and 49, the eq 47 becomes

$$\frac{\omega_\alpha(\lambda,\alpha)}{\pi\sqrt{r_1r_2}}=1.85\frac{\alpha}{\pi}t_0+.15t_0^2-\frac{|\alpha|}{\pi}\log t_0$$

$$+2\sum_{s=2}^{\infty}\frac{\zeta(2s-1)}{s}t_0^{2s}-2\frac{\alpha}{\pi}\sum_{s=2}^{\infty}\frac{\zeta(2s-1)}{2s-1}t_0^{2s-1}$$

$$-\frac{3\alpha^2}{4\pi^2}-2\left(\frac{z}{2\pi p}\right)^2\log\frac{z}{2\pi p}$$

$$-\frac{|\alpha|}{\pi}\left(1-\frac{|\alpha|}{2\pi}\right)\left[1-\log\frac{|\alpha|}{\pi}\left(1-\frac{|\alpha|}{2\pi}\right)\frac{4\sqrt{r_1r_2}}{\pi p}\right]-\frac{1}{3}\log\frac{4\sqrt{r_1r_2}}{\pi p}.$$

On replacing t_0 by its value $-\frac{z_{12}}{2\pi p}$ and $\sqrt{r_1r_2}$ by a, this gives

$$-\frac{2\omega_a(\lambda,\alpha)}{\pi a}=3.7\left(\frac{\alpha}{\pi}\right)\left(\frac{z_{12}}{2\pi p}\right)-\cdot 3\left(\frac{z_{12}}{2\pi p}\right)^2+2\frac{|\alpha|}{\pi}\log\frac{z_{12}}{2\pi p}$$

$$-4\sum_{s=2}^{\infty}\frac{\zeta(2s-1)}{s}\left(\frac{z_{12}}{2\pi p}\right)^{2s}-4\frac{\alpha}{\pi}\sum_{s=2}^{\infty}\frac{\zeta(2s-1)}{2s-1}\left(\frac{z_{12}}{2\pi p}\right)^{2s-1}+4\left(\frac{z}{2\pi p}\right)^2\log\left(\frac{z}{2\pi p}\right)$$

$$+\frac{3\alpha^2}{2\pi^2}+\frac{2|\alpha|}{\pi}\left(1-\frac{|\alpha|}{2\pi}\right)\left\{1-\log\left[\frac{|\alpha|}{\pi}\left(1-\frac{|\alpha|}{2\pi}\right)\left(\frac{8a}{2\pi p}\right)\right]\right\}+\frac{2}{3}\log\frac{8a}{2\pi p}. \quad (50)$$

The imaginary part is to be discarded. This equation is valid for $|z_{12}|<2\pi p$ and for $-2\pi<\alpha<2\pi$. It shows that $\omega_a(\lambda, \alpha)$ contributes a correction term which is of the smallest order of magnitude retained.

To express the first logarithmic term in eq 29 in terms of the variable z_{12} defined in eq 42, we first let $v=|r_2-r_1|+i(x_2^0-x_1^0)$, so that, as in appendix 7 of paper 2

$$-\log\,(1-e^{-\frac{v}{p}})=\frac{v}{2p}-\log\frac{v}{p}+\sum_{s=1}^{\infty}\frac{\zeta(2s)}{s}\left(\frac{iv}{2\pi p}\right)^{2s}, \text{ if } |v|<2\pi p.$$

Since the real part of this is to be taken (this logarithm contains a real factor in eq 29), we may place

$$\log|v|=\log|z_{12}| \text{ and } \mathscr{R}\,(iv)^{2s}=\mathscr{R}\,(z_{12}{}^{2s},)$$

$$\text{since } \mathscr{R}\,(iv)^{2s}=\mathscr{R}\,[-(x_2^0-x_1^0)+i|r_2-r_1|]^{2s},$$

and this contains only even powers of $-(x_2^0-x_1^0)$ and $|r_2-r_1|$. The eq 29 therefore becomes

$$\omega_a(l+\lambda,\alpha)+\omega_a(-l+\lambda,\alpha)=\frac{l|r_2-r_1|\sqrt{r_1r_2}}{p^2}$$

$$-4\pi Na\left[\log\frac{z_{12}}{p}-\sum_{s=1}^{\infty}\frac{\zeta(2s)}{s}\left(\frac{z_{12}}{2\pi p}\right)^{2s}\right]\cdot\left[1+\frac{r_1-a+r_2-a}{2a}\right]$$

$$-\pi a\left[\frac{2\pi}{3}\phi_1(k)+\frac{1}{k}\sqrt{1-k^2\cos^2\frac{\alpha}{2}}\right.$$

$$\left.-\left(\frac{k'}{k}\right)^2\left(\cos\frac{\alpha}{2}\right)\sin^{-1}\left(k\cos\frac{\alpha}{2}\right)-\frac{1}{k^2}\sin\frac{\alpha}{2}\log\left[\frac{k\sin\frac{\alpha}{2}+\sqrt{1-k^2\cos^2\frac{\alpha}{2}}}{k'}\right]\right], \quad (51)$$

where k_i has been replaced by k and $\sqrt{r_1r_2}$ by a in those terms which are of second order. In the term multiplied by $4\pi N$, we have replaced $\sqrt{r_1r_2}$ by $a\left[1+\frac{r_1-a+r_2-a}{2a}\right]$.

6. SECOND-ORDER APPROXIMATION FOR m

By use of eq 18, 21, 50, and 51 in the eq 15, we obtain the second-order approximation to m as the real part of eq 53 below. In this equation, we have placed

$$z_{12}=z_2-z_1, \text{ where } \left\{\begin{matrix} z_1=x_1^0+i(r_1-a_1) \\ z_2=x_2^0+i(r_2-a_1) \end{matrix}\right\}. \tag{52}$$

The complex quantities, z_1 and z_2, will be found to be the most appropriate ones with respect to integration over the sections of the wires. They are both referred to the centroid, 0_1, of section S_1 as origin, but could equally well have been defined with reference to any other point, such as 0_2. As shown by figure 1, the position of any point $P_1(x_1^0, r_1)$ in section S_1 is represented by the vector or complex variable z_1, and the position of any point $P_2(x_2^0, r_2)$ in section S_2 by the vector or complex variable z_2 with reference to the same origin. Since P_1 and P_2 are in different wires, it is evident that $|z_2-z_1|/2\pi p$ is less than 1.

The equation for m takes the form

$$m_a(x_1^0, r_1; x_2^0, r_2)=L_s+2\omega_x(l)$$

$$+2\pi a\left\{C_a+C_1\left(\frac{x_2^0-x_1^0}{2\pi p}\right)+C_2\left(\frac{x_2^0-x_1^0}{2\pi p}\right)^2+C_3\left(\frac{r_2-r_1}{2\pi p}\right)^2+\frac{|\alpha|}{\pi}\log\left(\frac{z_2-z_1}{2\pi p}\right)\right.$$

$$+16A_1\left(\frac{a}{2\pi p}\right)\left(\frac{r_1-a_1+r_2-a_2}{2\pi p}\right)+16A_3\left(\frac{r_1-a_1}{2\pi p}\right)\left(\frac{r_2-a_2}{2\pi p}\right)$$

$$\left.-2N\left(1+\frac{r_1-a_1+r_2-a_2}{2\pi p}\right)f\left(\frac{z_2-z_1}{2\pi p}\right)+f_1\left(\frac{z_2-z_1}{2\pi p}\right)+\frac{\alpha}{\pi}f_2\left(\frac{z_2-z_1}{2\pi p}\right)\right\}, \tag{53}$$

where

$$C_1=\frac{\alpha}{\pi}\left[2.85+2\pi\phi_1-2\log\frac{4a}{\pi p}\right] \tag{53a}$$

$$C_2=.85+2\pi\phi_1-2\log\frac{4a}{\pi p} \tag{53b}$$

$$C_3=.15+16A_4+2\log\frac{4a}{\pi p}. \tag{53c}$$

The constants A_1, A_3, A_4, and ϕ_1 are functions of k, which are defined in eq 19 and 8, respectively.

$$C_a=\frac{|\alpha|}{\pi}\left(1-\frac{|\alpha|}{2\pi}\right)\left[1-\log\frac{|\alpha|}{\pi}\left(1-\frac{|\alpha|}{2\pi}\right)\right]+\frac{\alpha^2}{\pi^2}\left(1+\frac{\pi\phi_1}{2}\right)$$

$$-\frac{\pi}{3}\phi_1-\frac{1}{2k}\sqrt{1-k^2\cos^2\frac{\alpha}{2}}+\frac{1}{2}\left(\frac{k'}{k}\right)^2\left(\cos\frac{\alpha}{2}\right)\sin^{-1}\left(k\cos\frac{\alpha}{2}\right)$$

$$+\left(\frac{1}{3}-\frac{|\alpha|}{\pi}\right)\log\left(\frac{4a}{\pi p}\right)+\frac{\sin\frac{\alpha}{2}}{2k^2}\log\left[\frac{k\sin\frac{\alpha}{2}+\sqrt{1-k^2\cos^2\frac{\alpha}{2}}}{k'}\right], \tag{53d}$$

where $-\pi<\alpha<\pi$.

The real part of the complex terms in eq 53 is to be taken, so that the principal branch of the multiple-valued function log (z_2-z_1) may be understood, since this is indeterminate only to the extent of an additive constant which is a multiple of $2\pi i$. With this understanding, this term and all the three other functions of $(z_2-z_1)/2\pi p$ are single-valued, analytic functions of either variable z_1 or z_2 in a region including the respective sections S_1 or S_2. To define the other functions with general argument z (where z is later to be replaced by $(z_2-z_1)/2\pi p$), we have the following series:

$$f(z) \equiv \log 2\pi z - \sum_{s=1}^{\infty} \frac{\zeta(2s)}{s} z^{2s}, \text{ when } |z|<1, \tag{53e}$$

where log $2\pi z$ denotes the principal branch (which is real when z is positive).

$$f_1(z) \equiv -2\sum_{s=2}^{\infty} \frac{\zeta(2s-1)}{s} z^{2s}, \text{ when } |z|<1 \tag{53f}$$

$$f_2(z) \equiv -2\sum_{s=2}^{\infty} \frac{\zeta(2s-1)}{2s-1} z^{2s-1}, \text{ when } |z|<1. \tag{53g}$$

Obviously,

$$f_1'(z)=2zf_2'(z), \tag{53h}$$

so that

$$f_1(z)=2\int_0^z z'f_2(z')dz'=2zf_2(z)-2\int_0^z f_2(z')dz'. \tag{53i}$$

For integrating over sections not closely resembling circles, it will in general be more convenient to use these functions in the form of series. For circular sections, the use of the series for f and f_2 may be avoided, as these are summable in terms of known functions as follows:

Taking the logarithm of both sides of the equation

$$\frac{\sin \pi z}{\pi z}=\prod_{n=1}^{\infty}\left(1-\frac{z^2}{n^2}\right)$$

gives

$$\log \frac{\sin \pi z}{\pi z}=\sum_{n=1}^{\infty}\log\left(1-\frac{z^2}{n^2}\right).$$

Since we are here concerned with the case $|z|<1$, we may place

$$\log\left(1-\frac{z^2}{n^2}\right)=-\sum_{s=1}^{\infty}\frac{z^{2s}}{s}\cdot\frac{1}{n^{2s}},$$

so that

$$\log \frac{\sin \pi z}{\pi z}=-\sum_{n=1}^{\infty}\sum_{s=1}^{\infty}\frac{z^{2s}}{s}\frac{1}{n^{2s}}=-\sum_{s=1}^{\infty}\frac{z^{2s}}{s}\sum_{n=1}^{\infty}\frac{1}{n^{2s}},$$

the inversion of the order of summation of the double series being valid because it is absolutely convergent. Since the zeta-function of Riemann is defined by

$$\zeta(s)=\sum_{n=1}^{\infty}\frac{1}{n^s}, \text{ (when) } s>1,$$

this becomes

$$\log\frac{\sin \pi z}{\pi z}=-\sum_{s=1}^{\infty}\frac{\zeta(2s)}{s}z^{2s}, \text{ when } |z|<1.$$

Comparing this with eq 53e shows that if the logarithm denotes that branch which is real when its subject is positive,

$$f(z)=\log 2 \sin \pi z. \tag{53j}$$

Similarly, we find that

$$f_2(z)=2\gamma z+\log\frac{\Gamma(1+z)}{\Gamma(1-z)}, \tag{53k}$$

where $\gamma=0.577216$=Euler's constant.

This may be found by taking the logarithm of the infinite product which represents the reciprocal of the gamma-function

$$\frac{1}{\Gamma(z+1)}=e^{\gamma z}\prod_{n=1}^{\infty}\left(1+\frac{z}{n}\right)e^{-\frac{z}{n}}.$$

This gives

$$\gamma z+\log\Gamma(z+1)=-\sum_{n=1}^{\infty}\left[\log\left(1+\frac{z}{n}\right)-\frac{z}{n}\right].$$

When

$$|z|<1, \quad -\left[\log\left(1+\frac{z}{n}\right)-\frac{z}{n}\right]=\sum_{s=2}^{\infty}\frac{(-1)^s z^s}{sn^s},$$

so that

$$\begin{aligned}\gamma z+\log\Gamma(z+1)&=\sum_{s=2}^{\infty}\frac{(-1)^s\zeta(s)}{s}z^s\\&=\sum_{s=1}^{\infty}\frac{\zeta(2s)}{2s}z^{2s}-\sum_{s=2}^{\infty}\frac{\zeta(2s-1)}{2s-1}z^{2s-1}\\&=-\frac{1}{2}\log\frac{\sin \pi z}{\pi z}+\frac{1}{2}f_2(z)\\&=+\frac{1}{2}\log\Gamma(1+z)+\frac{1}{2}\log\Gamma(1-z)+\frac{1}{2}f_2(z)s\end{aligned}$$

since $\Gamma(1+z)\ \Gamma(1-z)=\pi z/\sin \pi z$. This proves eq 53k.

The principal term in eq 53 is the term L_s, representing the self inductance of a cylindrical current sheet, for as shown by eq 16, it contains the large factor N^2 or $l^2/(2\pi p)^2$. The correction terms of first order are two terms within the braces, the first being $-2Nf$ on account of the large factor N. The second is the term containing A_1 with the large factor $a/2\pi p$. All other terms are of second order. The modulus, k, (complementary modulus k') is computed in terms of $l=2\pi pN$ and $D=2a$, by $k^2=D^2/(l^2+D^2)$. The cylindrical radius a will be taken as the mean of the two mean cylindrical radii of the wires in the sense that a_1 and a_2 are the distances of the centroids of the reference sections from the axis.

However, it is important to notice that eq 53 represents the mutual inductance, m_α $(x_1^0\, r_1; x_2^0, r_2)$, of any two helices, h_1 and h_2, with relative azimuth α, when the pair of coordinates (x_1^0, r_1) and (x_2^0, r_2), which serve to specify h_1 and h_2 are such that $|x_2^0-x_1^0|<2\pi p$, $|\alpha|<\pi$ and $|r_2-r_1|$ is of the order of magnitude of $2\pi p$. More precisely $|z_2-z_1|<2\pi p$. It, of course, contains no reference to wire sections. Hence the constant a is, within certain small limits, still at our disposal. The constants a_1 and a_2 occur only in the first-order terms of eq 53, and there they appear in the sum, a_1+a_2, which is $2a$.

The only thing that has been assumed concerning a in obtaining the approximations in eq 53 is that r_1-a and r_2-a are of the order of magnitude of the pitch. It is conceivable that for example the mean radius a_1 of the first wire section might be measurable with greater precision than a_2. It might then suit our purpose to take $a=a_1$, which would then be used in determining the modulus k upon which all the constants L_s, $2w_x(l)$, C_a, C_1, etc. depend.

On placing $\alpha=0$ in eq 53, it is found to be equivalent to the equation which was used in paper 3 for the self inductance of a helical wire (neglecting $D/4$, which, as indicated above, is in general less than 1 part in a million).

IV. MUTUAL INDUCTANCE, M_a, OF THE HELICAL WIRES

In evaluating the integral of eq 4, which gives M_a, there is an enormous saving of labor in adhering to the compex form until the integrations have been performed. Accordingly, we introduce the complex constant, z_0, which represents the vector from the centroid 0_1 of the reference section S_1 to the centroid 0_2 of reference section S_2. Its axial component is seen to be x_{02}^0 of figure 1, which may now be designated by x_0. Its radial component is a_2-a_1.
Hence

$$z_0=x_0+i(a_2-a_1)=qe^{i\beta}, \text{ where } -\pi<\beta<\pi, \tag{54a}$$

so that $q=|z_0|=\sqrt{x_0^2+(a_2-a_1)^2}$, and $\beta=\tan^{-1}[(a_2-a_1)/x_0]$. The points of integration, P_1 and P_2, are fixed respectively by the vectors z_1 and z_2, both drawn from 0_1 as origin. The eq 53 then give

$$\left.\begin{aligned} z_1&=x_1^0+i(r_1-a_1)=\rho_1 e^{i\phi_1}\\ z_2&=x_2^0+i(r_2-a_1)=z_0+\rho_2 e^{i\phi_2}\end{aligned}\right\}. \tag{54b}$$

Since each wire carries unit current, as implied by eq 3, it is evident that the constant terms in eq 53, namely, $L_s+2w_x(l)+2\pi aC_\alpha$, when used in the integral 4 are merely multiplied by unity, whatever the shape of the sections S_1 and S_2.

All of the terms of eq 53, which are of second order, are then to be averaged first over one section, and this result then averaged over the other section. Since the points 0_1 and 0_2 are centroids of the reference sections, it is evident that the average value of x_1^0 over S_1 is zero, and the average value of x_2^0 over S_2 is x_0. The average of $(x_1^0)^2$ over S_1 may be denoted by k_{xx}, and that of $(x_2^0-x_0)^2$ over S_2 by k'_{xx}. Also the average of r_1-a_1 over S_1 is zero, as is the average of r_2-a_2 over S_2. We may denote by k_{yy} the average of $(r_1-a_1)^2$ over S_1, and by k'_{yy} the average of $(r_2-a_2)^2$ over S_2. These averages multiplied by the area of the section represent its moment of inertia. For the products of inertia, we use the similar notation, where k_{xy} denotes the average over S_1 of $x_1^0(r_1-a_1)$ and k'_{xy} the average over S_2 of $(x_2^0-x_0)(r_2-a_2)$.

Then k_{xx}, k_{yy}, k_{xy}, etc. are all of the order of magnitude of $(2\pi p)^2$ or x_0^2.

The terms of first order in eq 53 must be treated more carefully. They are the two terms in 53 affected by the factors $A_1a/2\pi p$ and $-2N$, respectively. For these we use the expressions 5a, and for the formulation in the case of general shapes of section we prefer to use rectangular rather than polar coordinates in harmony with the definitions adopted for k_{xx}, etc.

The formula for the mutual inductance, M_α, of two helical wires with general shape of reference section may then be written.

$$M_\alpha=L_s+2\omega_x(l)$$
$$+2\pi a\Big\{C_\alpha+C_1\Big(\frac{x_0}{2\pi p}\Big)+C_2\frac{x_0^2+k_{xx}+k'_{xx}}{(2\pi p)^2}+C_3\frac{k_{yy}+k'_{yy}}{(2\pi p)^2}$$
$$+16A_1a\Big[\frac{c_{x_1}k_{xy}+c_{x_2}k'_{xy}+c_{r_1}k_{yy}+c_{r_2}k'_{yy}}{(2\pi p)^2}\Big]$$
$$-2N\bar{\bar{f}}+\bar{\bar{f}}_1+\frac{\alpha}{\pi}\bar{\bar{f}}_2+\frac{|\alpha|}{\pi}\overline{\overline{\log}}\Big(\frac{z_2-z_1}{2\pi p}\Big)$$
$$-2N\int\int\frac{dS_1}{S_1}\int\int\frac{dS_2}{S_2}f\Big(\frac{z_2-z_1}{2\pi p}\Big)\Big[c_{x_1}x_1^0+c_{x_2}(x_2^0-x_0)$$
$$+\Big(c_{r_1}+\frac{1}{2\pi p}\Big)(r_1-a_1)+\Big(c_{r2}+\frac{1}{2\pi p}\Big)(r_2-a_2)\Big]\Big\}, \qquad (55)$$

where $\bar{\bar{f}}$, etc. denotes the double average taken in succession over the one section and then over the other, of the function of $(z_2-z_1)/2\pi p$.

The principal correction term comes from $-2N\bar{\bar{f}}$, since this is the only term of first order in eq 55.

In the case of circular reference sections $k_{xy}=0$ and $k_{xx}=k_{yy}=d_1^2/16$ so this becomes

$$M_\alpha=L_s+2\omega_x(l)+2\pi a\Big\{C_\alpha+\frac{2\alpha}{\pi}\Big(\frac{x_0}{2\pi p}\Big)$$
$$+\Big(\frac{x_0}{2\pi p}\Big)\Big(\frac{x_0+2p\alpha}{2\pi p}\Big)\Big[.85+2\pi\phi_1-2\log\Big(\frac{4a}{\pi p}\Big)\Big]+$$

$$+\frac{1}{4}\left(\frac{E}{k}-1\right)\left[(1+2ac_{r1})\left(\frac{d_1}{2\pi p}\right)^2+(1+2ac_{r2})\left(\frac{d_2}{2\pi p}\right)^2\right]$$

$$-2N\bar{f}+\bar{f}_1+\frac{\alpha}{\pi}\bar{f}_2+\frac{|\alpha|}{\pi}\overline{\log}\left(\frac{z_2-z_1}{2\pi p}\right)$$

$$-2N\int\int\frac{dS_1}{S_1}\int\int\frac{dS_2}{S_2}f\left(\frac{z_2-z_1}{2\pi p}\right)\left[c_{x_1}\rho_1\cos\phi_1+\left(c_{r1}+\frac{1}{2\pi p}\right)\rho_1\sin\phi_1\right.$$

$$\left.+c_{x_2}\rho_2\cos\phi_2+\left(c_{r2}+\frac{1}{2\pi p}\right)\rho_2\sin\phi_2\right], \quad (56)$$

where $dS_1=\rho_1 d\rho_1 d\phi_1$ and $S_1=\frac{\pi d_1^2}{4}$.

To perform the remaining integrations, consider the line average taken around any circular arc $\rho_1=$const., of any monogenic function of z_1, multiplied by $e^{in\phi_1}$. Considering n an integer, positive, negative, or zero,

$$\frac{1}{2\pi}\int_{-\pi}^{\pi}e^{in\phi_1}F(z_1)d\phi_1=\frac{1}{2\pi i}\int_{-\pi}^{\pi}\frac{e^{in\phi_1}F(z_1)}{\rho_1 e^{i\phi_1}}d(\rho_1 e^{i\phi_1})$$

$$=\frac{{\rho_1}^{-n}}{2\pi i}\oint z_1^{n-1}F(z_1)dz_1, \text{ since } z_1=\rho_1 e^{i\phi_1}$$

This is a contour integral around a circle in the z_1-plane, which encloses the point $z_1=0$. Hence by Cauchy's theorem

$$\frac{1}{2\pi}\int_{-\pi}^{\pi}e^{in\phi_1}F(z_1)d\phi_1=0, \text{ if } n \text{ is a positive integer}$$

$$=F(0), \text{ if } n=0.$$

and

$$\frac{1}{2\pi}\int_{-\pi}^{\pi}e^{-in\phi_1}F(z_1)d\phi_1=\frac{{\rho_1}^n F^{(n)}(0)}{n!}, \text{ if } n \text{ is a positive integer,}$$

where

$$F^{(n)}(0)=\left[\frac{d^n}{dz_1^n}F(z_1)\right]_{z_1=0}.$$

Hence

$$\frac{1}{\pi}\int_{-\pi}^{\pi}F(z_1)d\phi_1=2F(0) \quad (57a)$$

$$\left.\begin{aligned}\frac{1}{\pi}\int_{-\pi}^{\pi}\cos\ n\phi_1 F(z_1)d\phi_1&=\frac{\rho_1{}^n F^{(n)}(0)}{n!}\\ \frac{1}{\pi}\int_{-\pi}^{\pi}\sin\ n\phi_1 F(z_1)d\phi_1&=\frac{i\rho_1{}^n F^{(n)}(0)}{n!}\end{aligned}\right\}\text{, if } n \text{ is a positive integer} \tag{57b, 57c}$$

Multiplying 57a by $\rho_1 d\rho_1$, and integrating from $\rho_1=0$ to $\rho_1=d_1/2$, gives, on dividing by $d_1^2/4$,

$$\int\int\frac{dS_1}{S_1}F(z_1)d\phi_1=F(0). \tag{5a}$$

Similarly, from 57b and 57c, we find

$$\left.\begin{aligned}\int\int\frac{dS_1}{S_1}\rho_1\cos\ n\phi_1 F(z_1)d\phi_1&=\frac{1}{n+3}\left(\frac{d_1}{2}\right)^{n+1}\frac{F^{(n)}(0)}{n!}\\ \int\int\frac{dS_1}{S_1}\rho_1\sin\ n\phi_1 F(z_1)d\phi_1&=\frac{i}{n+3}\left(\frac{d_1}{2}\right)^{n+1}\frac{F^{(n)}(0)}{n!}\end{aligned}\right\}\text{, if } n \text{ is a positive integer.} \tag{58b, 58c}$$

Taking $F(z_1)=f\left(\frac{z_2-z_1}{2\pi p}\right)$, it is evident that the first average over the circle S_1 is

$$\bar{f}\left(\frac{z_2-z_1}{2\pi p}\right)=f\left(\frac{z_2}{2\pi p}\right)=f\left(\frac{z_0+\rho_2 e^{i\phi_2}}{2\pi p}\right).$$

Letting z_2' denote $\rho_2 e^{i\phi_2}$, the same theorem applies for averaging over the second circle, S_2.

Consequently, the four functions in eq 56, which are twice averaged, give

$$-2N\bar{\bar{f}}+\bar{\bar{f}}_1+\frac{\alpha}{\pi}\bar{\bar{f}}_2+\frac{|\alpha|}{\pi}\bar{\bar{\log}}\left(\frac{z_2-z_1}{2\pi p}\right)=$$

$$=-2Nf\left(\frac{z_0}{2\pi p}\right)+f_1\left(\frac{z_0}{2\pi p}\right)+\frac{\alpha}{\pi}f_2\left(\frac{z_0}{2\pi p}\right)+\frac{|\alpha|}{\pi}\log\left(\frac{z_0}{2\pi p}\right).$$

Similarly, the formulas 58b and 58c suffice for evaluating the last integral in eq 56.

The eq 56 then becomes

$$M_a=L_s+2\omega_x(l)+\pi D\Big\{C_a+\frac{2\alpha}{\pi}\left(\frac{x_0}{2\pi p}\right)$$

$$+\left(\frac{x_0}{2\pi p}\right)\left(\frac{x_0+2p\alpha}{2\pi p}\right)\left[.85+2\pi\phi_1-2\log\left(\frac{2D}{\pi p}\right)\right]$$

$$+\frac{1}{4}\left(\frac{E}{k}-1\right)\left[(1+Dc_{r_1})\left(\frac{d_1}{2\pi p}\right)^2+(1+Dc_{r_2})\left(\frac{d_2}{2\pi p}\right)^2\right]$$

$$-2Nf\left(\frac{z_0}{2\pi p}\right)+f_1\left(\frac{z_0}{2\pi p}\right)+\frac{\alpha}{\pi}f_2\left(\frac{z_0}{2\pi p}\right)+\frac{|\alpha|}{\pi}\log\left(\frac{z_0}{2\pi p}\right)$$

$$+\frac{l}{16}\left[\left(c_{x_1}+i\left(c_{r_1}+\frac{1}{2\pi p}\right)\right)\left(\frac{d_1}{2\pi p}\right)^2-\left(c_{x_2}+i\left(c_{r_2}+\frac{1}{2\pi p}\right)\right)\left(\frac{d_2}{2\pi p}\right)^2\right]f'\left(\frac{z_0}{2\pi p}\right)\Bigg|, \tag{59}$$

where the real part is to be taken and

$$z_0=x_0+i(a_2-a_1)=qe^{i\beta}.$$

Referring to eq 53, we find

$$\mathscr{R}f\left(\frac{z_0}{2\pi p}\right)=\mathscr{R}\log\left(2\sin\frac{z_0}{2p}\right)=\mathscr{R}\log 2\sin\left[\frac{x_0+i(a_2-a_1)}{2p}\right]$$

$$=\frac{1}{2}\log 2\left[\cosh\left(\frac{a_2-a_1}{p}\right)-\cos\frac{x_0}{p}\right] \tag{59a}$$

$$f'\left(\frac{z_0}{2\pi p}\right)=\pi\cot\frac{z_0}{2p}=\frac{\pi\left[\sin\frac{x_0}{p}-i\sinh\left(\frac{a_2-a_1}{p}\right)\right]}{\cosh\left(\frac{a_2-a_1}{p}\right)-\cos\frac{x_0}{p}} \tag{59b}$$

$$\mathscr{R}f_1\left(\frac{z_0}{2\pi p}\right)=-2\sum_{s=2}^{\infty}\frac{\zeta(2s-1)}{s}\left(\frac{q}{2\pi p}\right)^{2s}\cos 2s\beta \tag{59c}$$

$$\mathscr{R}f_2\left(\frac{z_0}{2\pi p}\right)=-2\sum_{s=2}^{\infty}\frac{\zeta(2s-1)}{2s-1}\left(\frac{q}{2\pi p}\right)^{2s-1}\cos(2s-1)\beta=\frac{2\gamma x_0}{2\pi p}$$

$$+\log\left|\frac{\Gamma\left(1+\frac{z_0}{2\pi p}\right)}{\Gamma\left(1-\frac{z_0}{2\pi p}\right)}\right|. \tag{59d}$$

Using these real values in eq 59 gives the general formula for M_α when the wires are circular. For practical purposes, this may be simplified, since any single-layer, bifilar winding which is to be used as an absolute standard of mutual inductance could be given the following characteristics.

A. The two wires have practically the same diameter and the same treatment, so that the terms of eq 59 which contain the factor f' will cancel each other ($c_{x_1}=c_{x_2}$ and $c_{r_1}=c_{r_2}$).

B. The mean radii a_1 and a_2 are approximately equal, so that we may place $z_0=x_0$ in all except the principal correction term of first order, which is $-2Nf\ (z_0/2\pi\rho)$.

C. The helical windings are nearly equally spaced, so that $z_0=x_0=\pi p$ in all terms except the principal correction term.

In this case, by eq 59d,

$$f_2\left(\frac{z_0}{2\pi p}\right)=f_2\left(\frac{1}{2}\right)=\gamma+\log\frac{\Gamma\left(1+\frac{1}{2}\right)}{\Gamma\left(1-\frac{1}{2}\right)}=\gamma-\log 2=-.116$$

$$\log\frac{z_0}{2\pi p}=-\log 2=-.693, \text{ and from } =53f$$

$$f_1\left(\frac{z_0}{2\pi p}\right)=f_1\left(\frac{1}{2}\right)=-2\sum_{s=2}^{\infty}\frac{\zeta(2s-1)}{s4^s}=-2\left[\sum_{s=2}^{\infty}\frac{1}{s4^s}+\sum_{s=2}^{\infty}\left(\frac{\zeta(2s-1)-1}{s4^s}\right)\right]$$

$$=\frac{1}{2}+2\log\frac{3}{4}-2\sum_{s=2}^{\infty}\left[\frac{\zeta(2s-1)-1}{s4^s}\right]=-.087$$

The eq 59 then becomes

$$M_a=L_s+2\omega_x(l)+\pi D\Big\{C_\alpha+.12+1.31\frac{\alpha}{\pi}-.693\frac{|\alpha|}{\pi}$$
$$+\left(\frac{1}{2}+\frac{\alpha}{\pi}\right)\left(\pi\phi_1-\log\frac{2D}{\pi p}\right)-N\log 2\left(\cosh\frac{a_2-a_1}{p}-\cos\frac{x_0}{p}\right)$$
$$+\frac{1}{2}\left(\frac{E}{k}-1\right)\left(1+Dc_r\right)\left(\frac{d}{2\pi p}\right)^2\Big\}. \quad (60)$$

It may be noticed that the term $1+Dc_r$ is $+1$ or -1, according as the current distribution is uniform or "natural." The approximate value of the principal correction term within the brace is $-N\log 4=-1.38629\,N$.

When the initial sections of both wires are in the same axial plane, $\alpha=0$, the special case of eq 60 then is

$$M_0=L_s+2\omega_x(l)-\pi D\Big\{-.12+\frac{1}{6}\log\left(\frac{2D}{\pi p}\right)-\frac{\pi\phi_1}{6}+\frac{k'}{2k}\left(1-\frac{k'}{k}\sin^{-1}k\right)$$
$$-\frac{1}{2}\left(\frac{E}{k}-1\right)\left(1+Dc_r\right)\left(\frac{d}{2\pi p}\right)^2+N\log 2\left(\cosh\frac{a_2-a_1}{p}-\cos\frac{x_0}{p}\right)\Big\}. \quad (60a)$$

When $\alpha=-\pi$, the special case of eq 60 is

$$M_{-\pi}=L_s+2\omega_x(l)-\pi D\Big\{\frac{1}{6}\log\left(\frac{2D}{\pi p}\right)+\frac{\pi\phi_1}{3}+\frac{1}{2k}-\frac{1}{4k^2}\log\left(\frac{1+k}{1-k}\right)$$
$$-\frac{1}{2}\left(\frac{E}{k}-1\right)(1+Dc_r)\left(\frac{d}{2\pi p}\right)^2+N\log 2\left(\cosh\frac{a_2-a_1}{p}-\cos\frac{x_0}{p}\right)\Big\}. \quad (60b)$$

In this equation the lead wires may be taken in the same axial plane but on opposite sides of the cylindrical form, as shown in figure 2. As a guide in computing, it may be useful to remember that terms smaller than $D/4$ have been neglected in the derivation of formula 60. This corresponds to an uncertainty of about 0.1 in the value of all the terms within the brace which has the factor πD.

For the sake of comparison, the self inductance, L, of either of the two equal helical wires (paper 3) may be put in the form

$$L=L_s+2\omega_z(l)$$
$$+\pi D\left\{2N\left[\log\frac{2\pi p}{D}-.89473\right]+\frac{1}{3}\log\frac{D}{2p}\right.$$
$$+\frac{1}{2}\left(\frac{E}{k}-1\right)(1+Dc_r)\left(\frac{d}{2\pi p}\right)^2$$
$$\left.-\frac{\pi\phi_1}{3}-\frac{k'}{2k}\left(1-\frac{k'}{k}\sin^{-1}k\right)\right\}, \tag{61}$$

where $\omega_z(l)$ in this equation and in eq 55, 56, 60a and 60b is computed by eq 22.

V. EFFECT OF LEAD WIRES

When the lead wires are each parallel and close to a generator of the cylindrical form, it is simpler to use, in eq 60, instead of the term $2\omega_z(l)$, the term $2\bar{\omega}_z(l, \alpha)$, which takes account of *all* axial currents in lead wires and helices together. In paper 1 eq 42 to 46 are given the relations which in the case $r_1=r_2=D/2$ are equivalent to

$$2\bar{\omega}_z(l,\alpha)=2\left\{\frac{2D}{\pi}\left(\frac{E}{k}-1\right)+R(\alpha)-\sqrt{l^2+R^2_{(\alpha)}}\right.$$
$$\left.\frac{-l^2}{\sqrt{l^2+D^2}}\log 2+l.\log\frac{D[l+\sqrt{l^2+R^2_{(\alpha)}}]}{R(\alpha)[l+\sqrt{l^2+D^2}]}\right\}, \tag{62}$$

where

$$R^2(\alpha)=r_{l1}^2-2r_{l_1}r_{l_2}\cos\alpha+r_{l_2}^2 \tag{63}$$

the distance of the lead wires from the axis of the cylindrical form being r_{l_1} and r_{l_2}, where $r_{l_1}-a$ and $r_{l_2}-a$ are small, so that when $\alpha=\pm\pi$, $R(\pm\pi)$ is practically the same as the mean diameter, D, of the coils.

The term $2\varpi_z(l, \alpha)$ is to be substituted for (not added to) the term $2\omega_z(l)$ in eq 60 and its special cases.

VI. MODIFICATION REQUIRED WHEN THE REFERENCE SECTIONS ARE NOT QUITE CIRCULAR

In this case, we first find the position of the centroids of the sections, thus determining a_1, a_2, and x_0, so that the points 0_1 and 0_2 are determined. With these points as centers, we describe two circles whose diameters, d_1 and d_2 are determined by

$$\pi\left(\frac{d_1}{2}\right)^2=S_1 \text{ and } \pi\left(\frac{d_2}{2}\right)^2=S_2. \tag{64a}$$

The equations of the boundary curves of S_1 and S_2 may then be put in the form

$$\rho_1=\frac{d_1}{2}[1+\epsilon_1(\phi_1)] \text{ and } \rho_2=\frac{d_2}{2}[1+\epsilon_2(\phi_2)], \tag{64b}$$

where ϵ_1 and ϵ_2 are functions of ϕ_1 and ϕ_1, which must take on positive and negative values. We assume that the order of magnitude of $|\epsilon_1|$ and $|\epsilon_2|$ is not greater than that of p/a.

We may at first consider S_2 to be exactly circular. The section S_1 differs from the area of a circle of diameter d_1 by the area of a narrow strip whose radial breadth is

$$\frac{d_1}{2}\epsilon_1(\phi_1).$$

Since the centroid of circle is at O_1, and also the centroid of S_1 is at O_1, it follows that the centroid of this narrow strip is at O_1. Hence we have imposed four conditions upon the small function $\epsilon_1(\phi_1)$.

Since the element of area of the strip is $\left(\frac{d_1}{2}\right)^2\epsilon_1(\phi_1)d\phi_1$, these four conditions are

$$|\epsilon_1(\phi_1)|\leq C\frac{p}{a}, \text{ (where } C \text{ is of the order of magnitude of unity)} \tag{65a}$$

$$\int_{-\pi}^{\pi}\epsilon_1(\phi_1)d\phi_1=0 \tag{65b}$$

$$\int_{-\pi}^{\pi}\epsilon_1(\phi_1)\cos\phi_1 d\phi_1=0 \tag{65c}$$

$$\int_{-\pi}^{\pi}\epsilon_1(\phi_1)\sin\phi_1 d\phi_1=0 \tag{65d}$$

The eq 65b states that d_1 has been so chosen that the area of the noncircular section, S_1, is $\pi\left(\frac{d_1}{2}\right)^2$

Equations 65c and 65d state that O_1 is the centroid of the section S_1 and also of the circle.

The function ϵ_1 must be a periodic function with period 2π. Hence it is developable in a Fourier's series in the form

$$\epsilon_1(\phi_1)=\sum_{n=2}^{\infty}(C_n\cos n\phi_1+D_n\sin n\phi_1), \tag{66}$$

where the term $n=1$ must be absent because of eq 65c and 65d. The constant term is absent because of condition 65b.

As explained in the derivation of eq 59, the only effect of this deviation of S_1 from exact circularity will consist in a correction (of second order) that must be made to the principal correction term of eq 59, which is the term $-2Nf(z_0/2\pi p)$ within the brace.

Instead of the term $f(z_0/2\pi p)$ in eq 59, we must place

$$\int\int\frac{dS_1}{S_1}\int\int\frac{dS_2}{S_2}f\left(\frac{z_2-z_1}{2\pi p}\right)=\int\int\frac{dS_1}{S_1}f\left(\frac{z_0-z_1}{2\pi p}\right),$$

where the integral is now taken over the section S_1, whose boundary curve is given by eq 64b. When this same integral was taken over the circular section, its value was found to be $f(z_0/2\pi p)$. Hence the correction term to be added to eq 59 is equal to $1/S_1$ times the integral of $f(z_0-z_1)/2\pi p)$ taken over the area of the narrow strip. This gives, since ϵ_1 is small, the correction

$$\Delta_1=\frac{1}{\pi}\int_{-\pi}^{\pi}\epsilon_1(\phi_1)f\left(\frac{z_0-z_1}{2\pi p}\right)d\phi_1, \tag{67}$$

where the integral is taken around the circle $\rho_1=d_1/2$. When Δ_1 is found, the term $-2Nf(z_0/2\pi p)$ in eq 59 must be replaced by $-2N\left[\Delta_1+f\left(\frac{z_0}{2\pi p}\right)\right]$. This will make a change in the formula 59 by an amount which cannot be larger than a second-order term.

If, in eq 67, we insert the series 66 and make use of eq 57b and 57c, we find

$$\Delta_1=\sum_{n=2}^{\infty}\frac{(-1)^n(C_n+iD_n)}{n.'}\left(\frac{d_1}{4\pi p}\right)^n f^{(n)}\left(\frac{z_0}{2\pi p}\right). \tag{68a}$$

Similarly,

$$\Delta_2=\sum_{n=2}^{\infty}\frac{(-1)^n(C_n'+cD)_n'}{n.'}\left(\frac{d_2}{4\pi p}\right)^n f^{(n)}\left(\frac{z_0}{2\pi p}\right) \tag{68b}$$

when the boundary curve of S_2 is of the type of eq 64b and

$$\epsilon_2(\phi_2)=\sum_{n=2}^{\infty}(C_n' \cos n\phi_2+D_n' \sin n\phi_2).$$

Therefore, the correction is made to eq 59, 60, 60a, and 60b by adding within the brace which is multiplied by πD, the term $-2N(\Delta_1+\Delta_2)$.

Perhaps the case of most practical interest is the elliptic section

$$\frac{x_1^2}{A_1^2}+\frac{(r_1-a_1)^2}{B_1^2}=1, \tag{69}$$

or in polar coordinates

$$\rho_1=\frac{A_1B_1}{\sqrt{\frac{A_1^2+B_1^2}{2}-\left(\frac{A_1^2-B_1^2}{2}\right)\cos 2\phi_1}}.$$

If $(A_1-B_1)/A_1$ is small, this becomes, neglecting $(A-B_1)^2/A^2$,

$$\rho_1=\sqrt{A_1B_1}\left[1+\frac{A_1-B_1}{2A_1}\cos 2\phi_1\right].$$

The diameter, d_1, of a circle whose area is equal to the area πA_1B_1 of the ellipse is given by $d_1/_2=\sqrt{A_1B}$, hence the boundary curve is

$$\rho_1=\frac{d_1}{2}\left[1+\frac{A_1-B_1}{d_1}\cos 2\phi_1\right], \tag{70a}$$

so that, on reference to eq 64b, we find

$$\epsilon_1(\phi_1)=\frac{A_1-B_1}{d_1}\cos 2\phi_1. \tag{70b}$$

The only Fourier's coefficient in eq 66 which is not zero is C_2, which is equal to $(A_1-B_1)/d_1$. Hence, by eq 68a,

$$\Delta_1=\frac{1}{2}\left(\frac{A_1-B_1}{d_1}\right)\left(\frac{d_1}{4\pi p}\right)^2 f^{(2)}\left(\frac{z_0}{2\pi p}\right).$$

From eq 53j, we find . . . . $f^{(2)}\left(\frac{z_0}{2\pi p}\right)=-\frac{\pi^2}{\sin^2\frac{z_0}{2p}}$.

Taking the real part

$$Rf^{(2)}\left(\frac{z_0}{2\pi p}\right)=-\pi^2\frac{\cosh\left(\frac{a_2-a_1}{2p}\right)-\cos\frac{x_0}{2p}}{\cosh\left(\frac{a_2-a_1}{2p}\right)+\cos\left(\frac{x_0}{2p}\right)},$$

so that

$$\Delta_1=-\frac{1}{2}\left(\frac{A_1-B_1}{d_1}\right)\left(\frac{d_1}{2p}\right)^2\frac{\cosh\left(\frac{a_2-a_1}{2p}\right)-\cos\frac{x_0}{2p}}{\cosh\frac{a_2-a_1}{2p}+\cos\frac{x_0}{2p}}$$

The correction, Δ_2, by change of subscripts, takes account of the fact that the reference section of the second wire is an ellipse, as in eq 69, with semiaxes A_2 and B_2. In these equations A_1 may be greater or less than B_1. Hence with both wires of elliptic sections the correction to be added to eq 59 within the brace is the real quantity

$$-2N(\Delta_1+\Delta_2)$$

$$=N\left[\left(\frac{A_1-B_1}{\alpha_1}\right)\left(\frac{d_1}{2p}\right)^2+\left(\frac{A_2-B_2}{d_2}\right)\left(\frac{d_2}{2p}\right)^2\right]\frac{\cosh\frac{a_2-a_1}{2p}-\cos\frac{x_0}{2p}}{\cosh\frac{a_2-a_1}{2p}+\cos\frac{x_0}{2p}}. \qquad (71)$$

Since, by hypothesis, the order of magnitude of $(A_1-B_1)/d_1$, etc., is not greater than that of p/a, it is evident that the correction term 71 is not greater than second order. If $(A-_1B_1)/d_1$ is of the order of magnitude of p^2/a^2, the correction for ellipticity is entirely negligible in the formulas 59 to 60b.

In the eq 60 and its special cases 60a and 60b we have placed $x_0=\pi p$ and $a_2-a_1=0$ in the second-order terms of eq 59. Hence for the eq 60, 60a, and 60b, the correction term 71 reduces to

$$-2N(\Delta_1+\Delta_2)=N\left[\left(\frac{A_1-B_1}{d_1}\right)\left(\frac{d_1}{2p}\right)^2+\left(\frac{A_2-B_2}{d_2}\right)\left(\frac{d_2}{2p}\right)^2\right]. \qquad (71a)$$

We have idealized the actual helical wire, w_1, as one which is cut in a circular section by a plane through the axis of the cylindrical form. This is the circle shown in the reference plane, or xy plane, of figure 1. However, a more natural view of the wire is one which is cut in a circular section by a plane normal to its central filament. The reference section of such a wire would be slightly elliptical. If its semiaxes are A_1 and B_1, it will be shown that the ratio $(A_1-B_1)/d_1$ is equal to $p^2/2a^2$, so that by eq 71 the correction is of third order and is therefore not to be made to the formula here given, since we have neglected an unknown number of terms of third order.

To examine this second view of the helical wire, consider the three eq 1, which may be written (dropping subscripts)

$$\left.\begin{aligned} x&=x^0+p\,\theta \\ y&=r\cos\theta \\ z&=r\sin\theta \end{aligned}\right\},\ \text{where}\ \left\{\begin{aligned} -2\pi p<x^0<2\pi p \\ -\infty<\theta<\infty \\ 0<r<\infty \end{aligned}\right\}. \tag{72}$$

Since the assignment of the values of x^0, r, and θ uniquely determines the position of a point in space, they constitute a system of space coordinates which are not orthogonal. With this specification of their ranges, they are uniquely determined when x, y, and z are given. Any equation of the form $x^0=\phi(r, \theta)$ represents a surface. In particular, the equation independent of θ

$$x^0=\phi(r) \tag{73}$$

represents the surface of a helicoidal wire. This surface cuts the cylinder r=constant in a helix whose equations would be given by eq 72 on replacing x^0 by $\phi(r)$, and holding r constant, while θ is varied.

The curve in which the surface of eq 73 is cut by a plane, $\theta=c$=constant, is congruous with the curve in which the surface is cut by any other plane, $\theta=c_1$=constant. The two curves may be made to coincide by giving one a translation in the x direction, followed by a rotation about the x axis.

Taking as a representative cutting plane, the plane $\theta=0$ gives a curve whose rectangular equations are by eq 72

$$x=\phi(y) \tag{74a}$$

$$z=0. \tag{74b}$$

Hence if we have the equation of the surface of any helical wire in the form of eq 73, we may find the curve bounding its reference section of figure 1 by replacing x^0 by x and r by y in eq 73.

Next, suppose the equations of any closed space curve are given in rectangular coordinates in the form

$$f_1(x, y, z)=0 \tag{75a}$$

$$f_2(x, y, z)=0. \tag{75b}$$

Let it be required to find the equation of the surface of a helical wire which passes through this assigned curve.

Writing the equations of the given curve in helicoidal coordinates x^0, r, and θ, they are, by eq 72,

$$f_1(x^0+p\theta, r\cos\theta, r\sin\theta)=0 \tag{76a}$$

$$f_2(x^0+p\theta, r\cos\theta, r\sin\theta)=0. \tag{76b}$$

Eliminating θ between these two equations, we obtain a relation between x^0 and r, which, if solved for x^0, takes the form of eq 73. It is therefore the required equation of the surface of the helicoidal wire but expressed in helicoidal coordinates. Its reference section is found by placing $x^0=x$, $r=y$, as in eq 74.

Such elimination of θ is seldom possible, so that the reference section may be considered as a curve defined in parametric form

by placing $x^0=x$ and $r=y$ in the two eq 76a and 76b. The variable line parameter is θ.

Consider next another rectangular system of coordinates obtained by rotating the x, y, z system of figure 1 about the y axis, through a positive angle, γ. Any point, P, in space has the rectangular coordinates x, y, z, in the old system and x', y', z', in the new, where

$$x'=x\cos\gamma-z\sin\gamma$$

$$y'=y$$

$$z'=x\sin\gamma+z\cos\gamma. \tag{77}$$

Suppose that we desire the equation of the surface of a helical wire whose section by the plane $z'=0$ is a circle of diameter d with center at $x'=0$, $y'=a$, $z'=0$. The equations of this circle (as a space curve) are

$$x'^2+(y'-a)^2=\frac{d^2}{4} \tag{78a}$$

$$z'=0 \tag{78b}$$

or by eq 77

$$(x\cos\gamma-z\sin\gamma)^2+(y-a)^2=\frac{d^2}{4} \tag{79a}$$

$$x\sin\gamma+z\cos\gamma=0. \tag{79b}$$

The two latter correspond to eq 75a and 75b. In helicoidal coordinates, these become

$$[(x^\circ+p\theta)\cos\gamma-r\sin\theta\sin\gamma]^2+(r\cos\theta-a)^2-\frac{d^2}{4}=0 \tag{80a}$$

$$(x^\circ+p\theta)\sin\gamma+r\sin\theta\cos\gamma=0, \tag{80b}$$

which are special cases of the general eq 76a and 76b. The relation between x^0 and r resulting from the elimination of θ between 80a and 80b would be the equation of the surface of a helicoidal wire which is cut by the plane $z'=0$ (i. e. $z=-x$ tau γ) in the circular section defined by 78a and 78b. Instead of attempting to eliminate θ, it is better to retain it as a parameter. The equations of the boundary curve of the reference section of this wire is found, as explained above, by replacing x^0 by x and r by y. They are

$$[(x+p\theta)\cos\gamma-y\sin\theta\sin\gamma]^2+(y\cos\theta-a)^2-\frac{d^2}{4}=0 \tag{81a}$$

$$(x+p\theta)\sin\gamma+y\sin\theta\cos\gamma=0 \tag{81b}$$

(together with $z=0$).

The second view of the wire corresponds to

$$\cos\gamma=\frac{a}{\sqrt{a^2+p^2}}\text{ and }\sin\gamma=\frac{p}{\sqrt{a^2+p^2}}, \tag{82}$$

which, as shown by 72, makes the plane $z'=0$ normal to the central filament of the wire at $x=0$, $y=a$, $z=0$. Using eq 82, eq 81 may be written

$$x=-p\theta-y\left(\frac{a\sin\theta}{p}\right) \tag{83a}$$

$$(a^2\sin^2\theta+p^2)y^2-2p^2a\cos\theta.y+p^2\left(a^2-\frac{d^2}{4}\right)=0, \tag{83b}$$

which are the parametric equations of the boundary curve of the reference section of the wire. The last was obtained by eliminating x between 81a and 81b. On solving this equation for y, we obtain the following parametric equations for the boundary of the reference section of this wire:

$$x=-p\theta-y\left(\frac{a\sin\theta}{p}\right) \tag{84a}$$

$$y=\frac{1}{1+\left(\frac{a\sin\theta}{p}\right)^2}\left[a\cos\theta\pm\sqrt{\rho^2-(a^2+p^2-\rho^2)\left(\frac{a\sin\theta}{p}\right)^2}\right], \tag{84b}$$

where $\rho=d/2$.
From this we find

$$\frac{dy}{dx}=-\frac{ay\sin\theta}{p(a\cos\theta-y)}.$$

The section is a closed curve symmetrical with respect to the line $x=0$.

The real values of y correspond to values of the parameter θ in the range $-\theta_0<\theta<\theta_0$,

where

$$\theta_0=\sin^{-1}\frac{p\rho}{a\sqrt{a^2+p^2-\rho^2}}$$

If we now introduce the facts that p/a and $\rho/a(=d/2a)$ are small, it is found that

$$\theta_0=\frac{pd}{2a^2}\left[1+Zero\left(\frac{p^2}{a^2}\right)\right]$$

Hence in eqs 83a and 83b we may expand $\sin\theta$ and $\cos\theta$ in powers of θ This gives, neglecting terms smaller than p^2/a^2,

$$x=-\frac{a\theta}{p}\left(1+\frac{p^2}{a^2}\right)y$$

$$(y-a)^2+\left(\frac{a\theta}{p}\right)^2y^2=\frac{d^2}{4}.$$

On eliminating θ between these equations, we find for the boundary of the reference section, the equation

$$\frac{x^2}{A^2}+\frac{(y-a)^2}{B^2}=1,$$

where

$$A=\frac{d}{2}\left(1+\frac{p^2}{a^2}\right) \text{ and } B=\frac{d}{2},$$

so that

$$\frac{A-B}{d}=\frac{p^2}{2a^2},$$

as stated above.

Since terms smaller than second order have been neglected, the formula here obtained for the mutual inductance of the two helical wires has the same validity for either of the two modes of defining the helical wire. This applies to formulas for mutual inductance and selfinductance obtained in the earlier papers quoted above. The conclusion is important because the absolute determinations of the ohm and of the ampere which have been made at this Bureau during the last decade are based upon the use of these formulas, in which the terms of second order have not been negligible. However, if the wire is found to have an elliptic section whose ellipticity is a small quantity of the first order, then the correction 71 must be applied.

VII. SUMMARY

The formula for the mutual inductance of the two helical wires of wire diameter d, which are wound bifilarly in a single layer on a circular cylindrical form is given by eq 60. In this formula the azimuthal angle, α between the initial ends of wires w_1 and w_2 lies between $-\pi$ and π, inclusive. When $\alpha=-\pi$, the central filament of wire $w_2$begins at $0_2'$ in figure 2; when $\alpha=0$, it begins at 0_2; and when $\alpha=+\pi$, at $0_2''$; the central filament of wire w_1 beginning at 0_1 in all cases. The total number of turns in each helix is N. The cylindrical radii, a_1 and a_2, of the central filaments are considered so nearly equal that $a_2-a_1/2\pi p$ is small where $2\pi p$ is the pitch of the windings, the axial length, l, being $2\pi pN$. The principal term of eq 60 is L_s, which represents the self inductance of a circular cylindrical current sheet of length l and radius $a=(a_1+a_2)/2=D/2$. This sheet has angular component of current only.

The term $2\omega_x(l)$ in eq 60 represents the effect of axial components of current in the helices. It is a relatively small term of second order which may be computed by eq 22, but which should be replaced by $2\bar{\omega}_x(l)$ given by eq 62 when the lead wires are close to a generator of the cylinder, as this takes into account the effect of axial currents in lead wires and helices together.

The principal correction term in eq 60 contains the large factor, N. In this term, x_0 is the (positive) axial component of the line from 0_1 to 0_2 in figure 1. In all other correction terms, x_0 has been placed equal to πp and a_2-a_1 equal to zero, but allowance is made in this term for the possibility that measurements will show slight deviations from these values. The value $x_0=\pi p$ corresponds to the fact that the windings of one wire are equally spaced between those of the other.

In section VI, a modification of the formula is given to apply when the reference sections of the wires are only approximately circular.

VIII. LIST OF SYMBOLS

a_1=mean radius of primary wire, w_1.
a_2=mean radius of secondary wire, w_2.
d_1=diameter of wire w_1.
d_2=diameter of wire w_2.
$2\pi p$=the pitch of each winding.
N=number of turns in each winding.
$l=2\pi pN$=the axial length of each winding.
$x_0=x_0^0$ of figure 1=axial distance from center of wire w_1 to center of wire w_2, both centers lying in a plane through the x axis. When windings of one are midway between those of the other, $x_0=\pi p$. It is assumed that x_0 is near πp. q and β defined by $z_0\equiv x_0+i(a_2-a_1)\equiv qe^{i\beta}$, where $-\pi/2<\beta<\pi/2$.
α=the difference in azimuth of the initial points of wires w_1 and w_2, both wires having the same end planes when $\alpha=-\pi$. It is assumed that $|\alpha|<\pi$.

c_{x_1}, c_{r_1}, c_{x_2}, c_{r_2}=partial derivatives of the logarithm of the magnitude of the current density, for points on the respective central filaments (eq 5b). For uniform current distribution they are zero; for the natural distribution
$c_{x_1}=c_{x_2}=0$ and $c_{r_1}=-1/a_1$, $c_{r_2}-1/a_2$.
$D=2a=a_1+a_2$.

$$k^2=\frac{D^2}{l^2+D^2} \text{ and } k'^2=1-k^2.$$

K and E are the complete elliptic integrals with modulus k.
L_s=the self inductance of a current sheet of length l and diameter D (eq 16).
M=the mutual inductance of the helical wires, w_1 and w_2.

$$\zeta(2s-1)=\sum_{n=1}^{\infty}\frac{1}{n^{2s-1}}(=45).$$

$$\pi\phi_1=\frac{2}{k}[K-E]-kK\ (=8).$$

C_a defined in eq 53d.
Conditions A, B, and C preceding eq 60 give the assumptions by which eq 60 becomes a special case of eq 59.

The term $2\omega_x(l)$ in eq 59, 60, 60a, and 60b, may be computed by eq 22 and 23. It represents the effect of the axial components of current in the two helical wires, w_1 and w_2. The term $2\overline{\omega}_x(l, \alpha)$ may be computed by eq 62 and 63. When the lead wires are close to the cylindrical form, as shown in figure 2, the term $2\overline{\omega}_x(l, \alpha)$ should replace $2\omega_x(l)$ in eq 59 to 60 to take account of all axial components of current in helices and lead wires together.

The "helical wire" is assumed to be built up of helical filaments (all with the same pitch) in such a manner that any plane through the x axis cuts the wire in circular sections.

WASHINGTON, December 19, 1939.

U. S. DEPARTMENT OF COMMERCE NATIONAL BUREAU OF STANDARDS

RESEARCH PAPER RP1303

Part of Journal of Research of the National Bureau of Standards, Volume 24, June 1940

EQUIPMENT FOR CONDITIONING MATERIALS AT CONSTANT HUMIDITIES AND AT ELEVATED TEMPERATURES

By James G. Wiegerink [1]

ABSTRACT

Equipment is described for the study of the moisture relations of materials in air of controlled relative humidities at elevated temperatures. The air is brought to the desired relative humidity and temperature by an arrangement including a saturator and automatically controlled heaters, and then passed through a working chamber in which the materials to be studied can be weighed rapidly and accurately. Provision is made for measuring the rate of flow of air and for accurately determining the relative humidity in the working chamber.

The equipment has been used at temperatures from 96° to 300° F, at relative humidities from 10 to 90 percent for temperatures up to 212° F, and up to the maximum relative humidities obtainable at atmospheric pressure for temperatures between 212° and 300° F. The temperature in the working chamber can be maintained constant within ±0.4° F and the relative humidity within ±1-percent relative humidity for experimental runs of several days' duration.

Data are given illustrating the performance of the equipment.

CONTENTS

	Page
I. Introduction	639
II. Description of equipment	640
1. General	640
2. Saturator	641
3. Working chamber	642
4. Sampling unit	643
III. Constancy of relative humidity and temperature	644

I. INTRODUCTION

The first step in an investigation of the drying of textiles, cooperatively undertaken by the National Bureau of Standards and the United States Institute for Textile Research, was to design and build equipment in which samples could be dried under known conditions of atmospheric humidity, temperature, and airflow. Since the equipment was planned for a study of eight or more different kinds of textiles, it was decided to provide sufficient capacity to condition 18 samples simultaneously under each drying condition. It was necessary for the equipment to be large enough to accommodate various sizes of samples and to provide a relatively large ratio of volume of chamber to volume of samples in order to insure uniform treatment of each sample. It was particularly desirable to be able to weigh the samples rapidly and conveniently while they were in the

[1] Research Associate at the National Bureau of Standards, representing the United States Institute for Textile Research. The establishment of this research associateship was made possible by funds contributed by 57 individual manufacturers.

apparatus. Temperatures up to 300° F and the relative humidities corresponding to a water-vapor pressure equal to 90 percent of normal atmospheric pressure can be maintained in the conditioning chamber.

The construction and operation of the equipment are described in this paper. The equipment has been in use for 2 years and has been found to be very satisfactory.

II. DESCRIPTION OF EQUIPMENT

1. GENERAL

The four principal parts of the equipment are shown in figure 1. Air enters the apparatus at *A*, is heated to a predetermined tempera-

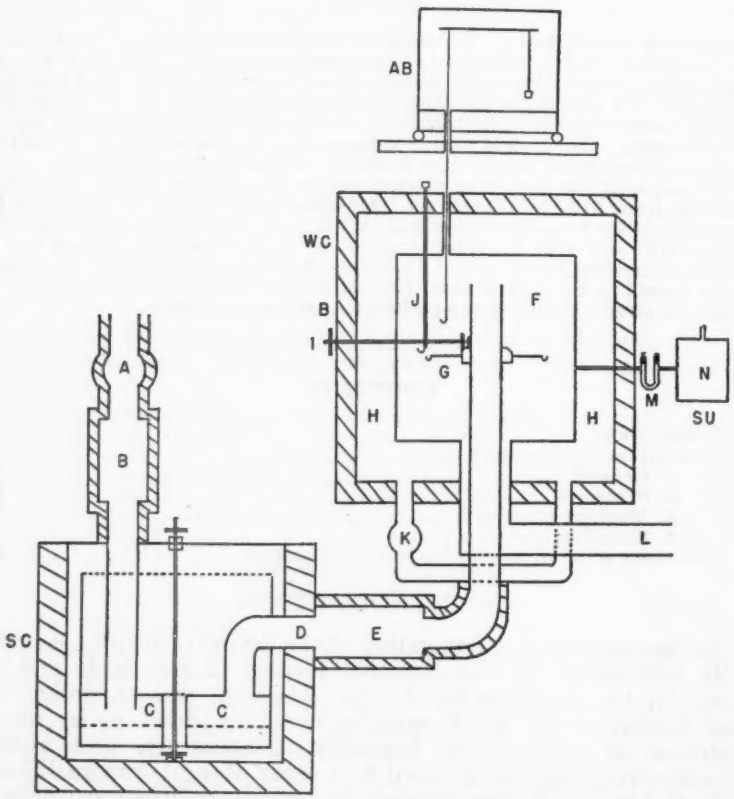

FIGURE 1.—*Diagrammatic sketch of equipment for conditioning materials at constant humidities and at elevated temperatures.*

SC, saturation chamber; *WC*, working chamber; *AB*, analytical balance; *SU*, sampling unit.

A. Air propeller.
B. First preheater.
C. Water chamber; water kept at 3-in. depth; equipped with series of baffles for directing air through definite path.
D. Air outlet from conditioner.
E. Second preheater.
F. Working chamber.
G. Sample support (there are 18 of these arranged radially).
H. Air chamber.
I. Drive for rotating sample supports.
J. Mechanism for transferring sample from support to balance hook.
K. Air circulator.
L. Air outlet from working chamber.
M. Drying tube.
N. Wet test meter.

ture in the pipe heater, *B*, and enters a saturating chamber, *SC*, where it passes over the surface of water maintained at this temperature by a surrounding oil bath. This air, after prolonged recirculation, becomes saturated to a constant degree with water vapor at this temperature and is delivered to the working chamber, *WC*, maintained at some higher temperature. The textile samples exposed to this air in *WC* are weighed from time to time while approaching equilibrium, using the analytical balance, *AB*. *SU* is a sampling unit for gravimetrically determining the relative humidity in *WC*. Provision is made for the adjustment and automatic control of temperatures in *SC* and *WC*, and for insulating the duct, *E*, between these two chambers to prevent condensation of moisture. The relation between the vapor pressure of water in the bath, *SC*, to that of water at the temperature of *WC* approximately determines the relative humidity of the air in this chamber, modified to some extent by the rate at which air flows through *SC*. The exact humidity maintained in *WC* depends upon the temperature control of both *SC* and *WC*, together with the air flow.

2. SATURATOR

The air intake, *A*, is through the blower shown at the top center of figure 2. The rate of airflow through the equipment is kept constant by a blower driven by a 220-v, a-c, 1/20-hp, synchronous motor. The airflow may be changed by adjustment of the dampers in the inlet and outlet sides of the blower. For most of the experimental runs, a constant airflow of about 2½ ft^3/min was used. At this rate, the air in the working chamber changes about every minute, which removes the water practically as fast as it is given off by the samples.

The large section, *B*, of the insulated vertical pipe for preheating the air is shown in figure 2. This brass pipe is 3 in. in diameter at the inlet and 6 in. in diameter where the heaters are located. The pipe contains two electric heaters, each with a maximum capacity of 330 w. The temperature of the air leaving this preheater is regulated to approximate the temperature of the oil bath. This condition is checked by comparing the thermocouple in the preheater with the thermocouple in the oil bath. The air then passes downward into the chamber, *C*, which is set in the oil bath.

The oil bath shown in figure 2, 22 in. in diameter and 20 in. high, is cylindrical, made of heavy-gage tinned copper, and is insulated with 4 inches of fiberboard. The outside covering of the oil bath is made of heavy-gage sheet iron. This bath is heated by means of two 500-w immersion heaters. One of these is connected with an automatic control system consisting of a mercury thermoregulator and relay. The other auxiliary heater is for quickly heating the bath to a desired temperature. The oil is circulated in the bath by a motor-driven propeller in such a manner that the oil is pulled down into the center of the bath and pushed over the side walls of the submerged water chamber. The control of the oil temperature is within $\pm 0.1°$ F.

An annular water chamber, 16 in. in outside diameter and 5 in. high, which is made of heavy-gage tinned copper, is set in the oil bath. This chamber, with a water layer 3 in. deep, contains a series of baffles so constructed that the air takes a spiral path as it travels over the water surface. A reservoir of 1-gallon capacity, and a

constant-leveling device set in the bath maintain the water supply. The 1-gallon oilcan mounted on the bath is for filling the reservoir, which is below it, without interfering with the operation of the leveling mechanism.

The air passes from the saturating equipment at *D* and then through the horizontal insulated pipe, *E*, shown under the working chamber in figure 3. This pipe contains two electric heaters, each with a maximum capacity of 500 w, and one electric heater with a maximum capacity of 1,000 w. This last heating unit is seldom used except for quickly raising the temperature to that desired. The air is heated in this preheater to the temperature at which it is to be used and passes upward to the interior of the working chamber.

3. WORKING CHAMBER

The inside of the working chamber, *WC*, is shown in figure 4. The cylindrical inner chamber, about 18-in. in diameter and 18-in. high, is made of heavy-gage copper and provided with a door containing a window. The samples under test hang from Nichrome rings at the ends of 18 horizontal rods, *G*, which are arranged radially about the air-inlet pipe and revolve around it four times a minute. The motor for rotating the sample supports may be seen on the top left-hand side of the working chamber in figure 3.

Air of the desired temperature and relative humidity enters the inner chamber, *F*, at the top through the central vertical standpipe, passes downward over the samples, *G*, and out through a passage around the intake pipe, *L*. Recirculation is provided by a connection between *L* and *A*.

The inner chamber is surrounded by an air jacket, *H*, as shown in figure 4. This air jacket is surrounded by ½-in. of Transite and 2-in. of fiberboard, the exterior surface being made of heavy-gage sheet iron. The working chamber is rectangular, 26 by 26 by 26-in. inside dimensions. It is supported by the angle-iron base shown in figure 3.

The air jacket is heated by three sets of electric plug-in heaters placed respectively at the bottom, center, and top (fig. 4). The bottom and center heaters each consist of two 660-w plug-in units connected in series to consume a maximum of 330 w. The top heaters, with a maximum of 330 w, are connected with the automatic control system, consisting of a mercury thermoregulator and relay. During an experimental run, sufficient heat is applied to the air jacket by the bottom and center heaters to bring the temperature within a few degrees of the temperature desired, the remaining amount of heat being supplied by the automatic control system. The air in this jacket, *H*, is circulated by withdrawing it from one side by means of the blower, *K*, shown at the bottom in figure 3, and then blowing it into the other side. The air returns over a partition which separates the two sides and extends to within a few inches of the top of the air jacket.

The temperature of the working chamber can be controlled within ±0.4° F for the range 96° to 300° F. Thermocouples are placed at the top and bottom of the working chamber to indicate any changes of temperature. The temperature of the air is recorded continuously during a test by a resistance-type recording thermometer, not shown.

FIGURE 2.—*Air-saturating equipment.*

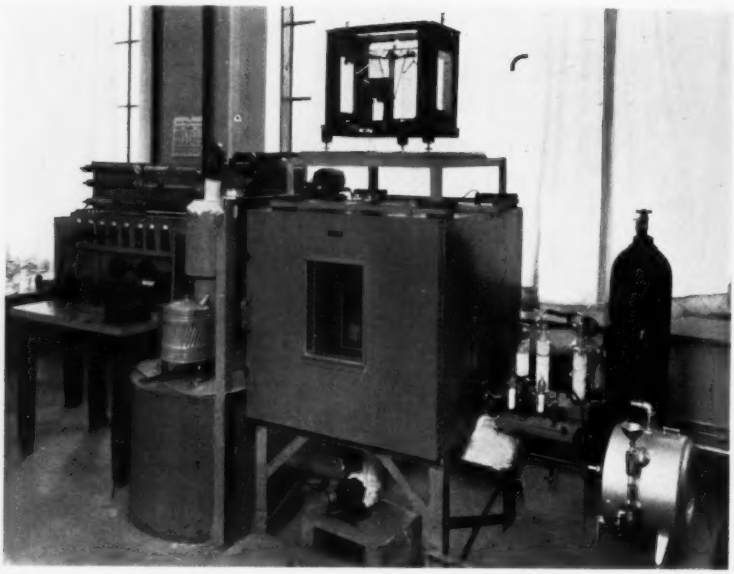

FIGURE 3.—*General view of the equipment.*

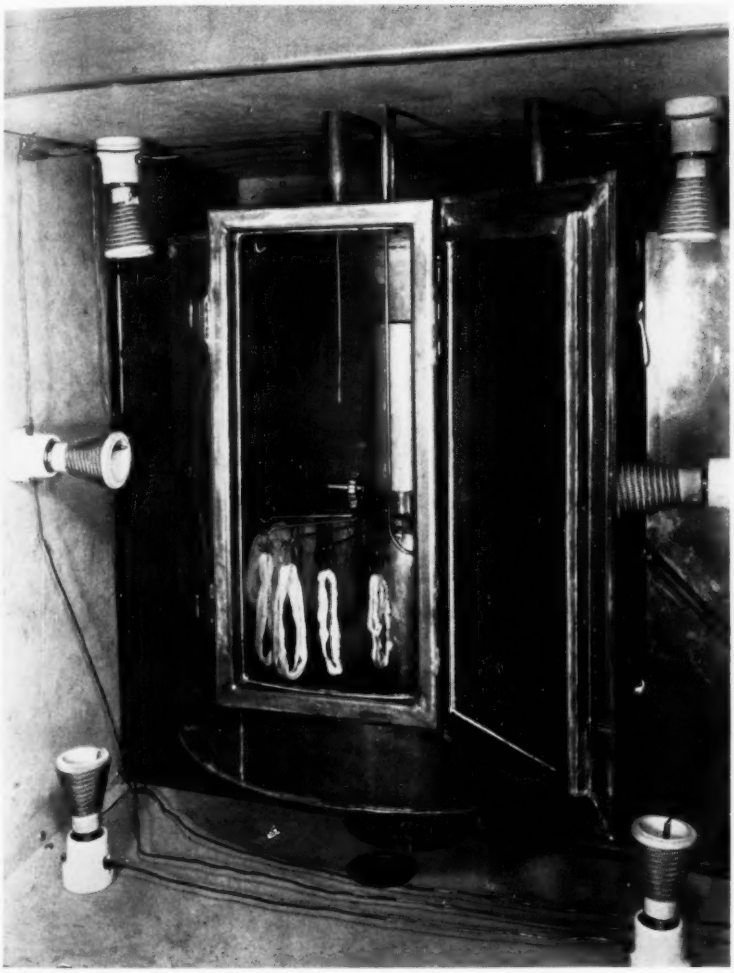

FIGURE 4.—*Inside of working chamber.*

UNIV. OF MICH.

Windows in the inner and outer chambers make it possible to see the samples when transferring them by means of *J* from the supports to a Nichrome wire which extends into the working chamber from the bottom of the balance pan. This wire passes downward from the balance through a heated glass cylinder, through which dry air is passed, and through an iris diaphragm. When a weighing is to be made, the rotation of the samples is stopped, the sample is transferred to the rod, and weighed. This takes only 10 to 15 seconds with the magnetically damped balance provided. With the above arrangement, no difficulty was experienced from the rise of warm air about the wire or from the condensation of moisture on it.

The air from the inner chamber passes out through *L*, to which a wet test meter may be attached when flow measurements are desired. However, if the air is not recirculated, relative humidities above 65 percent at temperatures up to 212° F are not practicable. By recirculating the air from the outlet, *L*, of the working chamber to the blower, *A*, it is possible to obtain approximately a relative humidity of 90 percent at 212° F with an airflow of 2½ ft^3/min. It was necessary to provide proper insulation and a heater for this return duct in order to reduce condensation of moisture to a minimum. This return duct is not shown in any of the figures. It is located behind the working chamber.

On the table at the left in figure 3 are the switchboard and the electric control equipment. Four variable transformers for regulating some of the heating circuits are also mounted on the table. To the right of the transformers are a galvanometer and a standard resistance box for reading thermocouples. Above the transformers are two relays which are in the automatic temperature-control circuits. Above the switches are slide-wire resistors for the manual regulation of some of the heaters and motors.

4. SAMPLING UNIT

The relative humidity in the working chamber may be determined gravimetrically by means of a sampling unit, *SU*, shown to the right of the working chamber in figure 3. Air containing moisture is withdrawn from the working chamber, the moisture being adsorbed by the $Mg(ClO_4)_2.3H_2O$ in the drying tubes. The amount of moisture is determined, and the relative humidity is calculated from a knowledge of the temperature in the working chamber, the weight of the moisture, and the volume and temperature of the air analyzed. The volume of air is measured by means of a wet-test meter, *N*, of ¼-ft^3 capacity per revolution, with an accuracy of 0.5 percent. The temperature of the air varies from 70° to 80° F (room temperature). This gravimetric method gives the relative humidity to within ±0.5-percent relative humidity.

It was found necessary to provide a means of driving over into the drying tubes any moisture that may condense between the equipment and the drying tubes, particularly at the higher temperatures and higher relative humidities. This was done by placing a glass trap between the equipment and the drying tubes. After a run is made, this condensed water was then driven into the $Mg(ClO_4)_2.3H_2O$ with dry air. The dry air is produced by taking compressed air from a tank and passing it over sulfuric acid, $Mg(ClO_4)_2.3H_2O$ and P_2O_5.

III. CONSTANCY OF RELATIVE HUMIDITY AND TEMPERATURE

The constancy of the relative humidity in the working chamber under operating conditions may be judged from table 1. These results are typical of the experiments that have been made with the equipment while in operation for the past 2 years.

TABLE 1.—*Constancy of relative humidity*

Time	Relative humidities at 96° F, with recirculation	Time	Relative humidities at 96° F, without recirculation
	Percent		*Percent*
Beginning	92.3	Beginning	62.9
End of 24 hr	92.3	End of 12 hr	63.3
End of 48 hr	92.1	End of 24 hr	63.0
End of 72 hr	92.5	End of 36 hr	63.2
End of 96 hr	92.3	End of 60 hr	63.1
Average	92.3	Average	63.1
Time	Relative humidities at 219° F, with recirculation	Time	Relative humidities at 219 F, without recirculation
	Percent		*Percent*
Beginning	79.2	Beginning	15.8
End of 4 hr	79.0	End of 4 hr	16.2
End of 8 hr	79.4	End of 8 hr	16.0
End of 24 hr	79.0	End of 24 hr	16.4
Average	79.2	Average	16.1

Acknowledgment is made to A. C. Walker, chairman, and Frederic Bonnet, member, Administration Committee for Drying Research, United States Institute for Textile Research, and to W. D. Appel, of the National Bureau of Standards, for valuable suggestions in the development of the constant-humidity and constant-temperature equipment.

WASHINGTON, March 14, 1940.

U. S. DEPARTMENT OF COMMERCE NATIONAL BUREAU OF STANDARDS

RESEARCH PAPER RP1304

Part of Journal of Research of the National Bureau of Standards, Volume 24, June 1940

MOISTURE RELATIONS OF TEXTILE FIBERS AT ELEVATED TEMPERATURES

By James G. Wiegerink [1]

ABSTRACT

The moisture contents of 10 kinds of textile fibers in the form of specially prepared yarns were determined when the fibers were in equilibrium with air for a series of relative humidities and temperatures. Data were obtained for both "desorption" and "adsorption," the yarns being brought to equilibrium from a wet condition and a dry condition, respectively. The fibers studied were raw cotton, "purified" cotton, mercerized cotton, clothing wool, carpet wool, viscose rayon, cuprammonium rayon, raw silk, degummed silk, and cellulose acetate. The temperatures ranged from 96° to 302° F, and the relative humidities ranged from 5 to 90 percent for temperatures below 212° F and up to the maximum obtainable at atmospheric pressure above 212° F.

The results are given in the form of graphs showing moisture content against relative humidity and also in the form of graphs in which the logarithms of the moisture contents at given relative humidities are plotted against the reciprocals of the corresponding absolute temperatures. The last show straight-line relationships with changes in the slopes of the lines between 200° and 220° F.

CONTENTS

		Pag
I.	Introduction	645
II.	Materials	648
III.	Procedure	649
IV.	"Dry" weight of the fibers	650
V.	Results and conclusions	652

I. INTRODUCTION

As part of a program of investigation of the drying of textiles, the moisture contents of 10 kinds of textile fibers were determined when the fibers were in equilibrium with air at different relative humidities and temperatures ranging from 96° to 302° F. Equilibrium was approached from both the wet state (desorption) and from the dry state (adsorption). The desorption data, of importance in the drying of textiles, include measurements at nine temperatures and at as many relative humidity values at each temperature as were considered necessary or expedient. Since an analysis of the desorption data revealed a linear relationship between the logarithm of the moisture content and the reciprocal of the absolute temperature from which intermediate values could be obtained, the adsorption data, of importance in the reconditioning of textiles, were obtained for only five temperatures. Below the boiling point of water at atmospheric

[1] Research Associate at the National Bureau of Standards, representing the United States Institute for Textile Research. The establishment of this research associateship was made possible by funds contributed by 57 individual manufacturers.

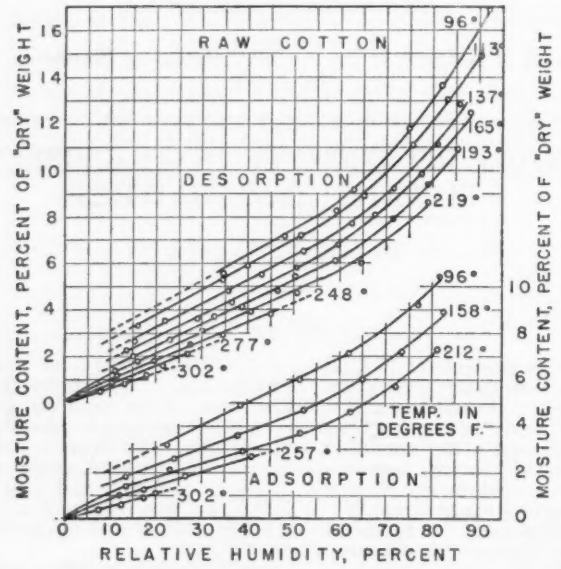

FIGURE 1.—*Equilibrium moisture content of raw cotton yarn at different relative humidities and temperatures.*

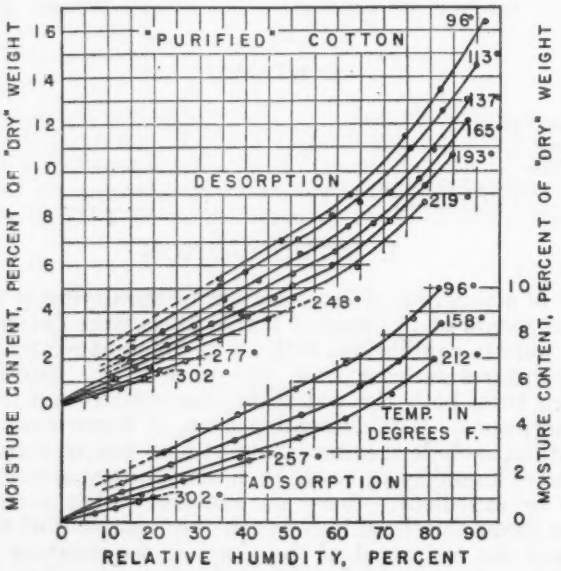

FIGURE 2.—*Equilibrium moisture content of "purified" cotton yarn at different relative humidities and temperatures.*

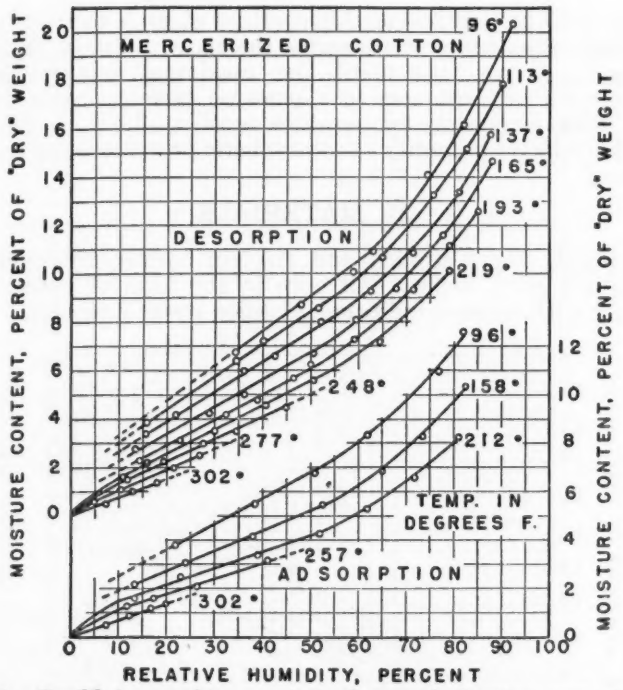

FIGURE 3.—*Equilibrium moisture content of mercerized cotton yarn at different relative humidities and temperatures.*

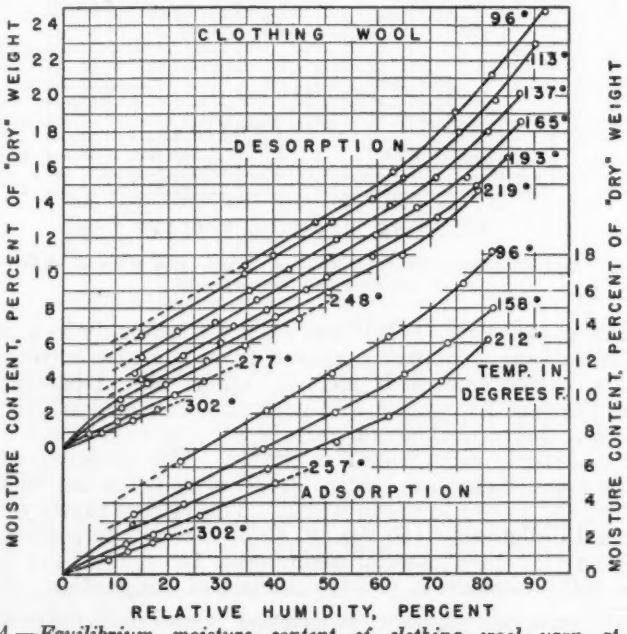

FIGURE 4.—*Equilibrium moisture content of clothing wool yarn at different relative humidities and temperatures.*

pressure, 6 to 10 relative-humidity values at each temperature were considered sufficient to characterize the range between dryness and saturation. Above this point the maximum relative humidity attainable without recourse to a pressure system progressively decreases with increasing temperature until at 302° F, the highest attainable relative humidity at atmospheric pressure is approximately 20 percent.

II. MATERIALS

The textile fibers studied and the purification treatments they received are given below. All were in the form of yarns. Where treatment with water is indicated, distilled water was used.

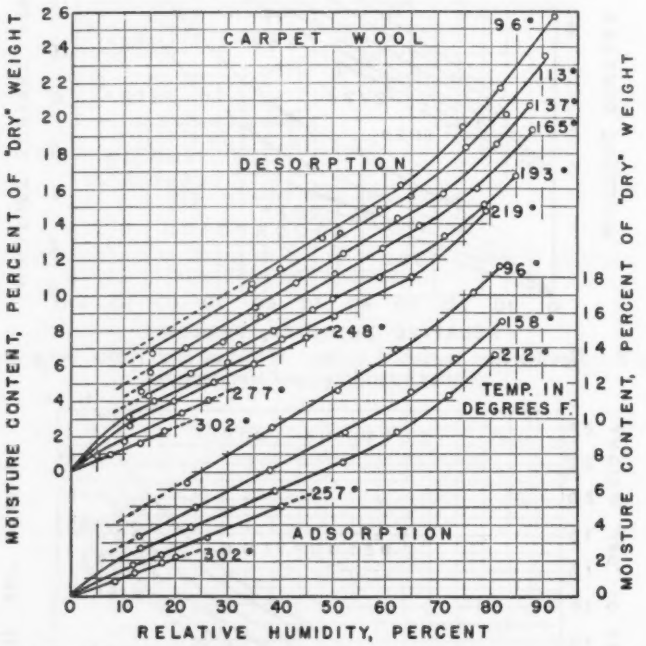

FIGURE 5.—*Equilibrium moisture content of carpet wool yarn at different relative humidities and temperatures.*

The raw cotton yarn (1/24)[2] was washed thoroughly in water. The "purified" cotton yarn was prepared from the raw cotton yarn by successive extractions with alcohol, ether, and 1-percent NaOH solution, followed by rinsing in 5-percent acetic acid solution and in water. The mercerized cotton yarn (2/25) was washed in a 5-percent NH_4OH solution, then rinsed in water. The clothing wool yarn (2/2.3) and the carpet wool yarn (3/1.2) were extracted with alcohol and ether, and rinsed in warm water. The viscose rayon yarn (1/30; commercial designation 150 denier, 40 filament), the cuprammonium rayon yarn (1/30; commercial designation 150 denier, 112 filament), and the cellulose acetate (1/30; commercial designation 150 denier,

[2] The typp system for designating sizes of yarns is employed. The first number (1 in the case of the raw cotton yarn) indicates the number of units of which the yarn is composed, that is, the ply. The second number given (24 in the case of the raw cotton yarn) indicates the number of thousands of yards in 1 pound.

46 filament) were washed in a warm 1-percent NH_4OH solution, then rinsed in warm water. The raw silk yarn (1/300; commercial designation 13–15 denier) was washed in water at room temperature. The degummed silk was prepared from the raw silk yarn by degumming with an olive oil soap solution, followed by rinsing in warm water.

III. PROCEDURE

The equipment used for this investigation is described in detail in a previous paper.[3] It consists of equipment for controlling the temperature and relative humidity of air, for passing a stream of this air

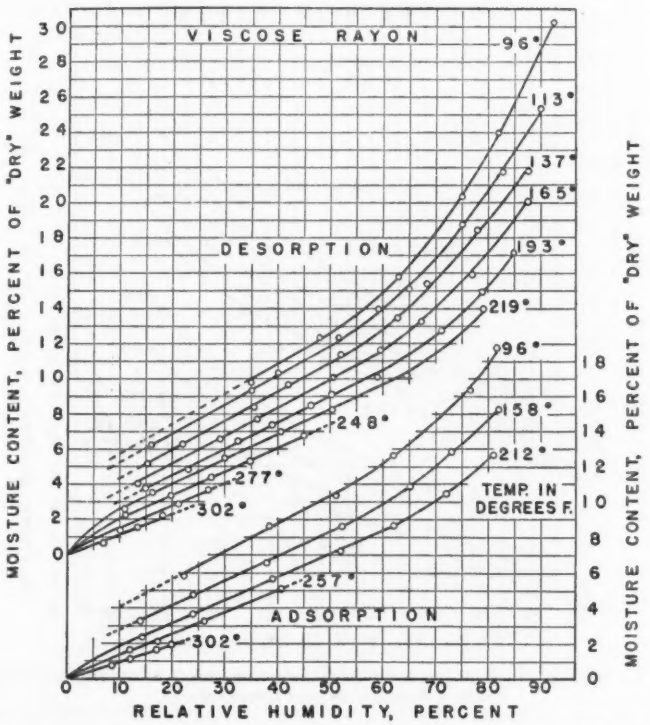

FIGURE 6.—*Equilibrium moisture content of viscose rayon yarn at different relative humidities and temperatures.*

through a working chamber at a known rate, for exposing the samples in this chamber to the air stream and weighing them in it conveniently and rapidly; and for sampling the air in the working chamber and accurately determining its relative humidity, by a gravimetric measurement of the moisture content. The temperature in the working chamber was maintained constant within $\pm 0.4°$ F and the relative humidity within ± 1-percent relative humidity throughout each test run. Some of the runs were 24 hours or more in duration.

[3] J. G. Wiegerink, *Equipment for conditioning materials at constant humidities and elevated temperatures*, J. Research NBS **24**, 639 (1940) RP 1303.

The samples for the desorption experiments were conditioned by soaking them overnight in distilled water. Then the excess water was removed by gently squeezing the samples until the weights of squeezed yarns were about twice that of dry weights, and the samples were then placed in the working chamber at the temperature and the initial high humidity of the test condition. They were brought to equilibrium at a series of progressively decreasing relative-humidity values, weighings being made at suitable intervals until no change in weight was found over a period of approximately 12 hours. The

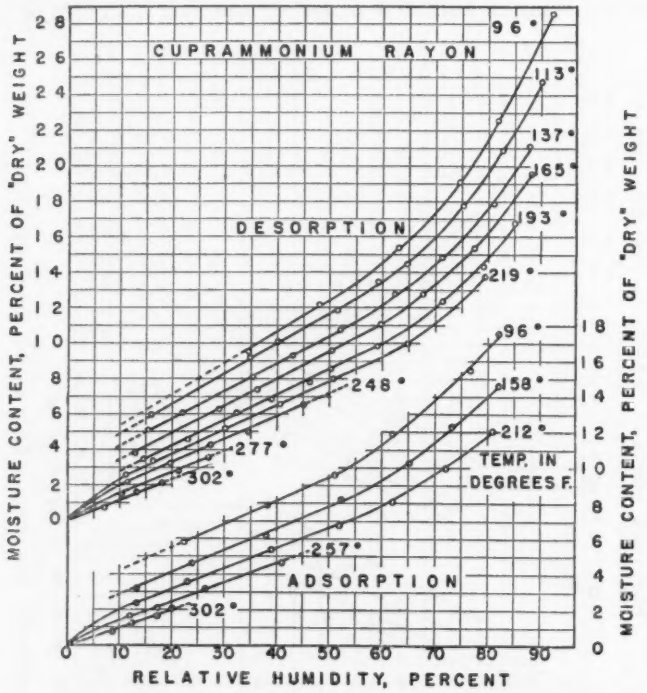

FIGURE 7.—*Equilibrium moisture content of cuprammonium rayon yarn at different relative humidities and temperatures.*

adsorption samples were conditioned by drying over $Mg(ClO_4)_2 \cdot 3H_2O$ at 75° F for 2 weeks. They were then placed quickly in the working chamber and successively brought to equilibrium at a series of increasing relative-humidity values.

IV. "DRY" WEIGHT OF THE FIBERS

The "dry" weights of the samples used in the desorption experiments were obtained after the completion of the series of experiments by heating the samples in an air oven at 212° F overnight.

The "dry" weights of the samples used for the adsorption experiments were obtained prior to the experiments in the working chamber.

Since heating in an air oven at 212° F might have rendered the samples unfit for tests at lower temperatures, they were dried by suspending them from a wire passing through narrow glass tubing in the stopper of the bottle containing the drier. This made it possible to weigh the sample without removing it from the air over the drier. The samples required 2 weeks to reach constant weight.

The samples thus dried had a "dry" weight a little lower than those dried in the air oven at 212° F (the relative humidity in the oven was from 1.5 to 2.0 percent). The differences for the various

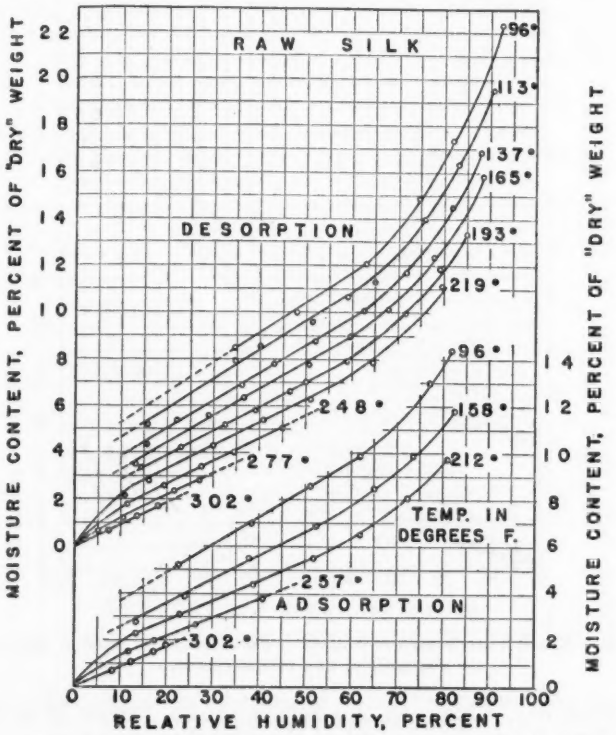

FIGURE 8.—*Equilibrium moisture content of raw silk yarn at different relative humidities and temperatures.*

fibers averaged: For raw and "purified" cotton, 0.15 percent; for clothing wool, carpet wool, viscose rayon, and cuprammonium rayon, 0.30 percent; for mercerized cotton and raw silk, 0.20 percent; and for degummed silk and acetate, 0.10 percent. All desorption data were corrected by these amounts. Thus the moisture contents given in this report are based upon the weight of the material as dried over the chemical drier. They are expressed as percentage of the dry weight of the material. In the textile industry this is termed "regain."

No attempt is made here to differentiate between "free" and "bound" water in textiles or to discuss the merits of such a differen-

tiation. It is realized that the term "dry" may have several connotations, varying from the exceedingly dry condition achieved by keeping materials in sealed tubes over an efficient drying agent for periods of several years, to a superficial drying, commonly described as "bone-dry", achieved by drying in an air oven maintained at or slightly above the boiling point of water, but open to the prevailing atmos-

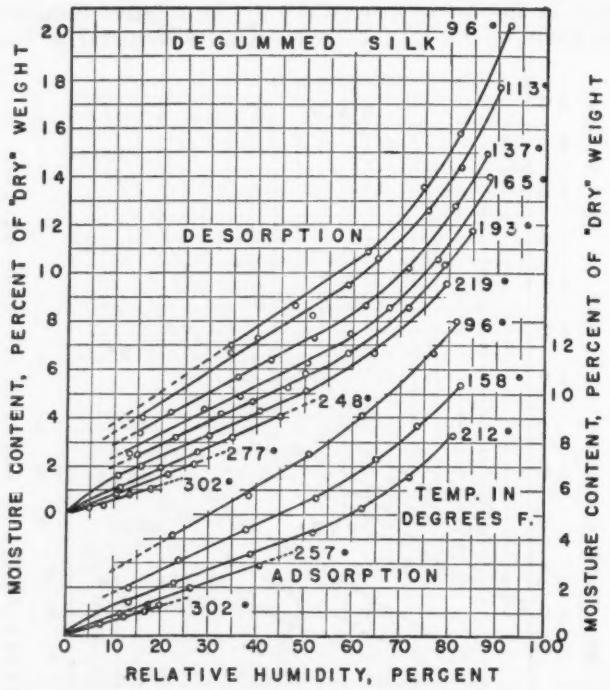

FIGURE 9.—*Equilibrium moisture content of degummed silk yarn at different relative humidities and temperatures.*

pheric humidity, which, as this report shows, results in a failure to remove from 0.1 to 0.3 percent of the adsorbed moisture.

V. RESULTS AND CONCLUSIONS

In the figures 1 to 10 are curves of the familiar form expressing the relation between percentage moisture content and percentage relative humidity for each temperature and each material. Each point on the curves is the average of two determinations. The broken lines show extrapolated values. This extrapolation is quite justifiable, since the relation between percentage moisture content and percentage relative humidity is linear in the range 10- to 60-percent relative humidity.

These curves indicate the limits in moisture content which may be expected in any of the textile fibers if the atmosphere in contact

with the fiber during drying is maintained at any desired temperature and relative humidity. The "desorption" curve for the given temperature is to be used if the fiber is initially wet, and the "adsorption" curve is to be used if the fiber is initially dry. It should be emphasized that the curves apply, of course, only to the samples examined. Further work is necessary to determine what variation

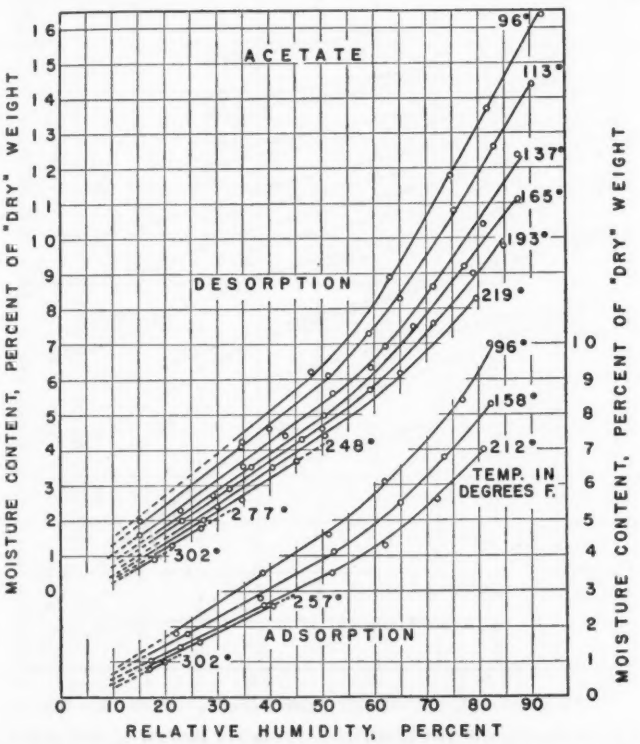

FIGURE 10.—*Equilibrium moisture content of cellulose acetate yarn at different relative humidities and temperatures.*

is to be expected in different lots of the same fiber, or when the fibers contain impurities, such as oils, sizing materials, and dyes.

A study of these data revealed that if the logarithms of the moisture contents at any fixed relative humidity are plotted against the reciprocals of the corresponding absolute temperatures ($1/T$), straight-line relationships are obtained with changes in the slopes of the lines between 200° and 220° F. The slope of the "desorption" line thus obtained gives the rate of *decrease* in equilibrium moisture content of a textile, with *increasing* temperature, at constant relative humidity. The slope of the "adsorption" line gives the rate of *increase* in equilibrium moisture content, with *decreasing* temperature, at constant relative humidity. Thus a series of such linear relations may be prepared, one for each relative humidity, from which it is possible to ascertain the moisture content for any humidity at any tempera-

ture within the range investigated. Since Urquhart and Williams[4] obtained similar data on cotton, including temperatures as low as 50° F, and since the relation holds for their data as well as for those

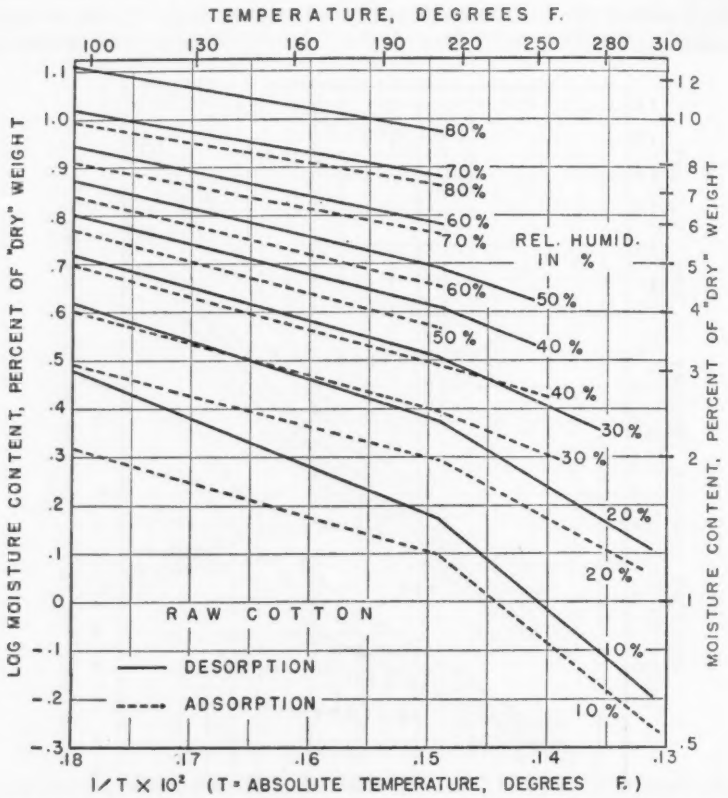

FIGURE 11.—*Logarithm of the equilibrium moisture content of raw cotton yarn in relation to the reciprocal of the absolute temperature (1/T).*

presented here, it seems reasonable to assume that the linear relation may be extrapolated down to temperatures somewhat below room temperature, if desired.

[4] Urquhart and Williams, J. Text. Inst. 15, T559-572 (1924).

Figures 11 to 20 show these relations for humidities at 10-percent intervals between 10- and 80-percent relative humidity. The unbroken lines give this relationship for the desorption data, the broken

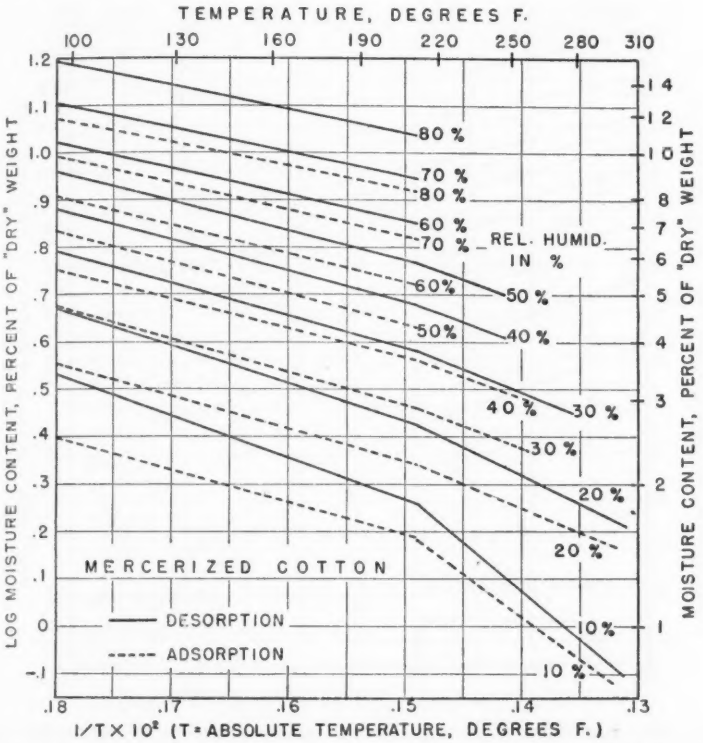

FIGURE 12.—*Logarithm of the equilibrium moisture content of "purified" cotton yarn in relation to the reciprocal of the absolute temperature* $(1/T)$.

lines for the adsorption data. The data for these graphs were taken from the curves given in figures 1 to 10 and are not represented as points on these graphs in order to avoid confusion between the ad-

sorption and desorption curves. An average example of how closely the logarithms of the moisture contents follow a linear relationship

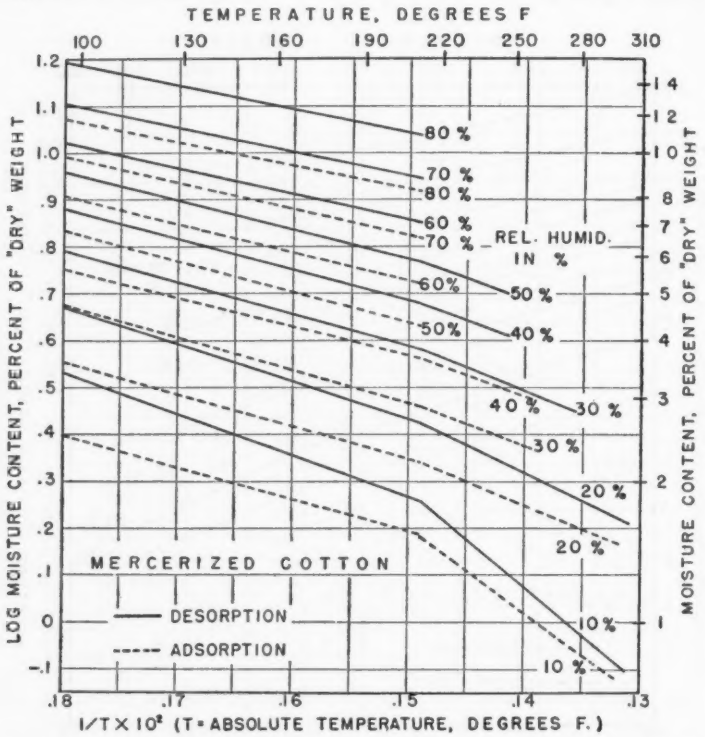

FIGURE 13.—*Logarithm of the equilibrium moisture content of mercerized cotton yarn in relation to the reciprocal of the absolute temperature (1/T).*

with the reciprocals of the corresponding absolute temperatures is shown by figure 21, which gives the desorption data for viscose rayon.

Examination of figures 11 to 20 shows that the linear relationships obtained give changes in the slopes of the lines between 200° and

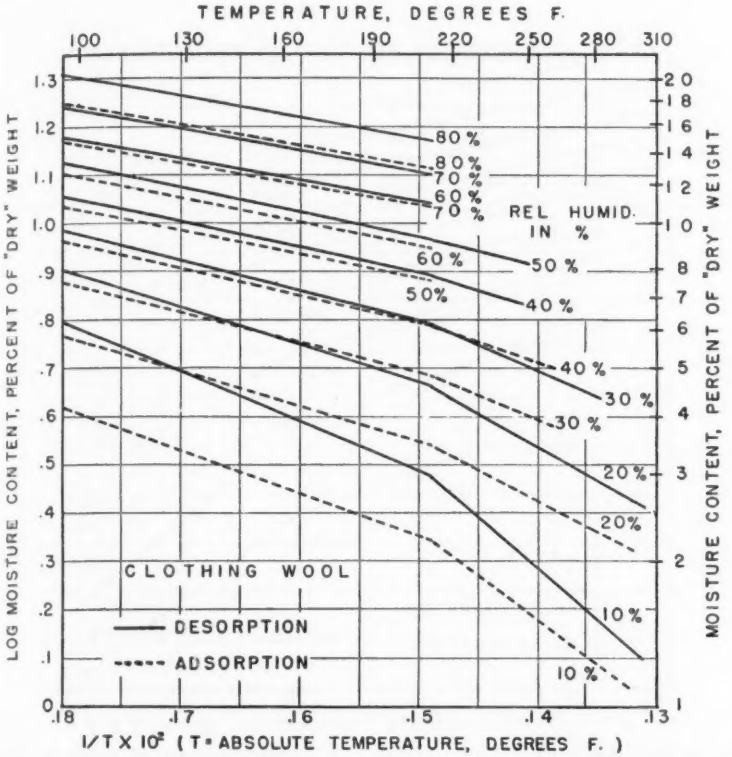

FIGURE 14.—*Logarithm of the equilibrium moisture content of clothing wool yarn in relation to the reciprocal of the absolute temperature (1/T).*

220° F. The data are represented for convenience by straight lines but could be better fitted by a smooth curve. The bending of these

curves is of significance in connection with heats of swelling, but the theoretical analysis has not yet been carried out.

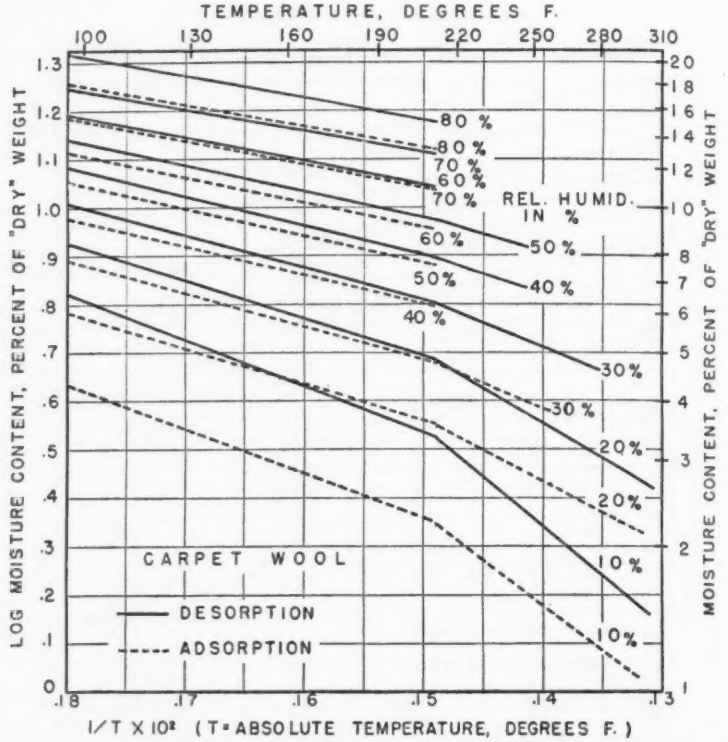

FIGURE 15.—*Logarithm of the equilibrium moisture content of carpet wool yarn in relation to the reciprocal of the absolute temperature (1/T).*

Certain generalizations may be made for all the textiles examined. Above 30-percent relative humidity the slope of the linear relation

changes very little with increasing humidity, in the range between 100° to 200° F. Below 30-percent relative humidity the slope in-

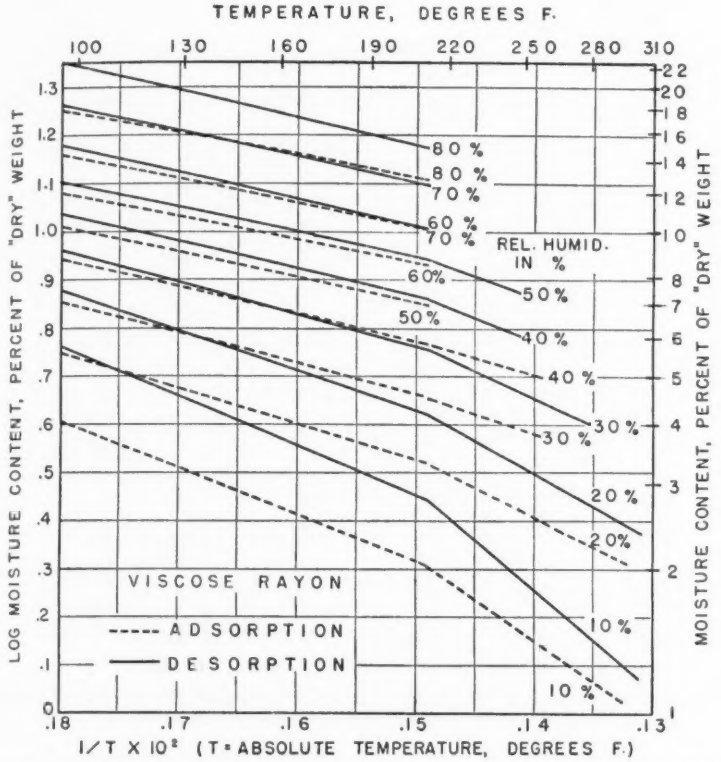

FIGURE 16.—*Logarithm of the equilibrium moisture content of viscose rayon yarn in relation to the reciprocal of the absolute temperature (1/T).*

creases appreciably with decreasing humidity. Above 200° F the slopes change for all relative humidities investigated up to 50 percent.

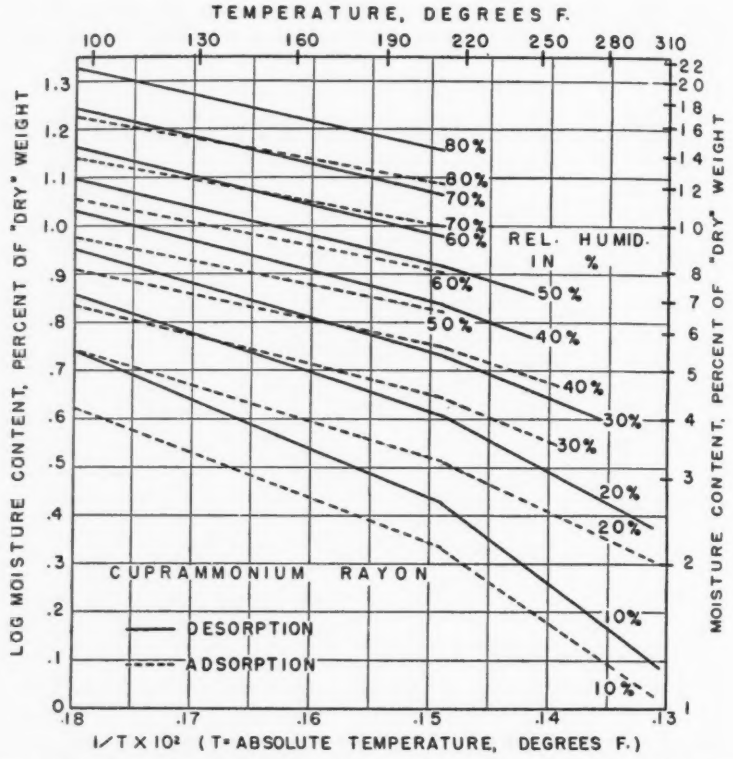

FIGURE 17.—*Logarithm of the equilibrium moisture content of cuprammonium rayon yarn in relation to the reciprocal of the absolute temperature (1/T).*

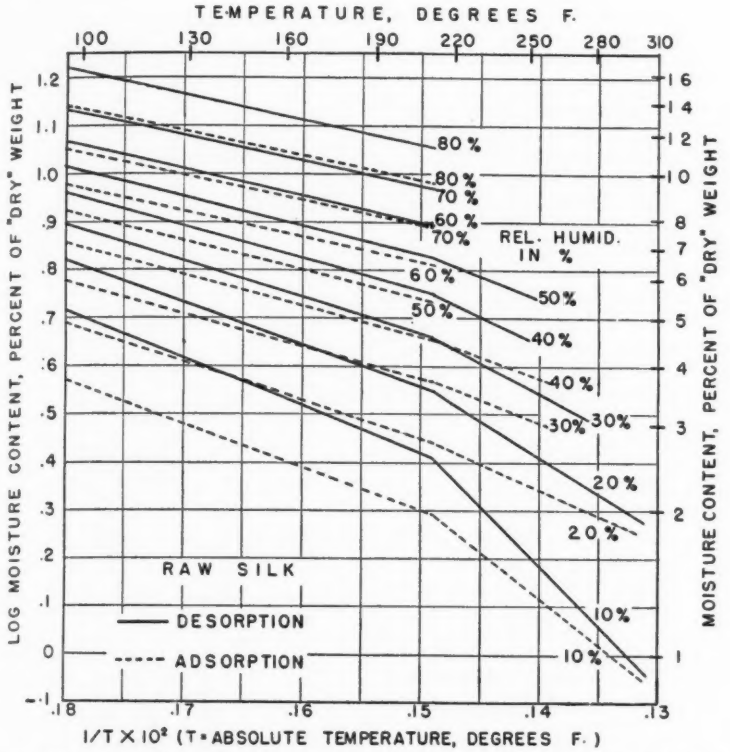

FIGURE 18.—*Logarithm of the equilibrium moisture content of raw silk yarn in relation to the reciprocal of the absolute temperature (1/T).*

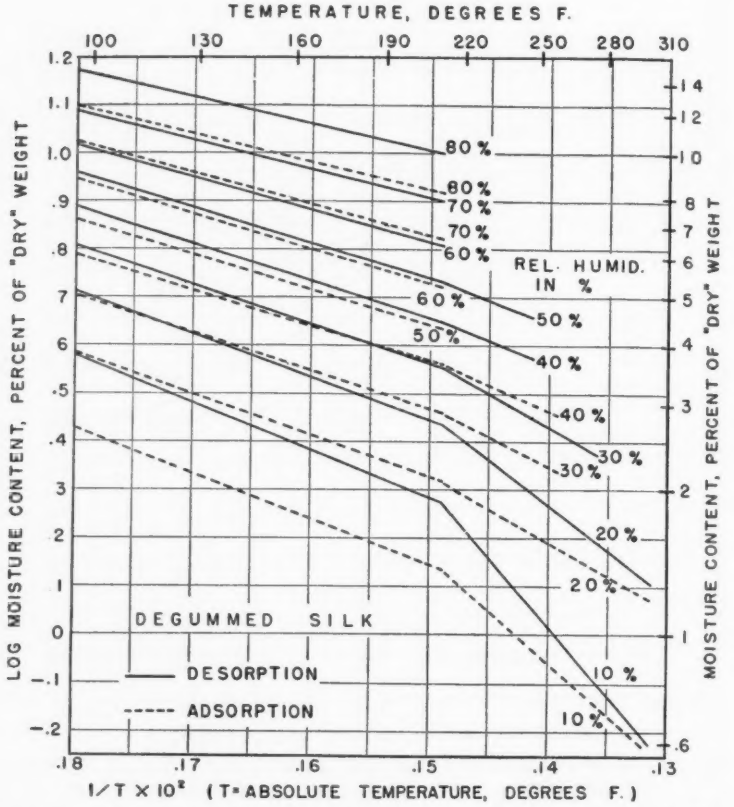

FIGURE 19.—*Logarithm of the equilibrium moisture content of degummed silk yarn in relation to the reciprocal of the absolute temperature (1/T).*

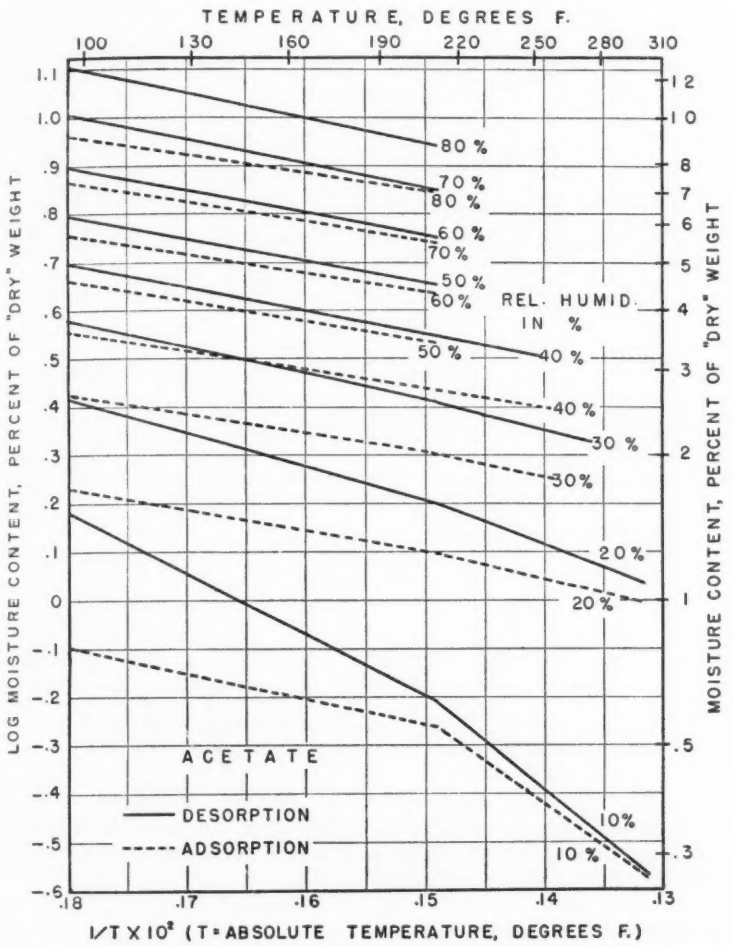

FIGURE 20.—*Logarithm of the equilibrium moisture content of cellulose acetate yarn in relation to the reciprocal of the absolute temperature (1/T).*

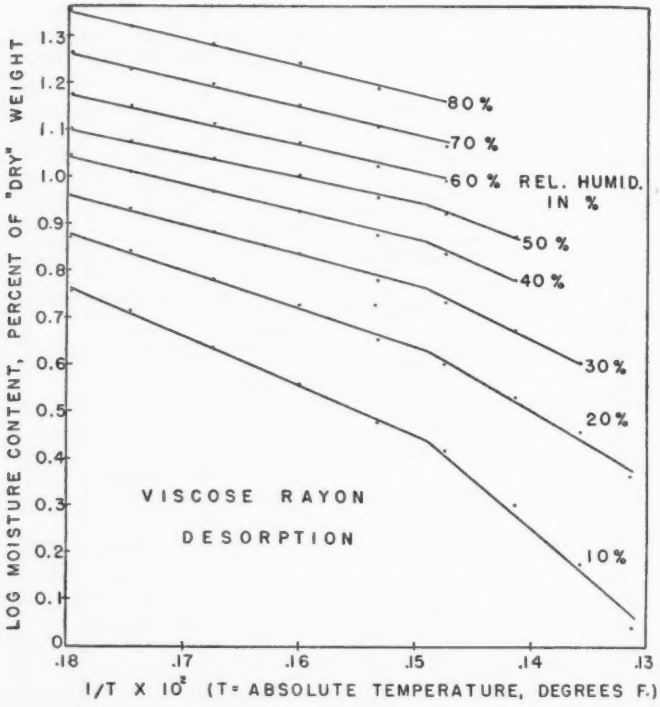

FIGURE 21.—*Logarithm of the equilibrium moisture content of viscose rayon yarn in relation to the reciprocal of the absolute temperature* (*1/T*).

Acknowledgment is made to A. C. Walker, chairman of the Administration Committee for Drying Research, United States Institute for Textile Research, for suggesting the treatment of the data used in this report and other valuable advice.

WASHINGTON, March 21, 1940.

U. S. DEPARTMENT OF COMMERCE NATIONAL BUREAU OF STANDARDS

RESEARCH PAPER RP1305

Part of Journal of Research of the National Bureau of Standards, Volume 24, June 1940

TESTS OF CORROSION INHIBITORS FOR WATER TREATMENT IN AIR-CONDITIONING EQUIPMENT

By James H. Wilson and Edward C. Groesbeck

ABSTRACT

Treatment of the circulating water used in air-conditioning equipment with small amounts of certain chemicals and control of the pH of this water greatly reduce the losses resulting from corrosion. The order of decreasing efficiency of the inhibitors studied was (a) chromates, (b) silicates, (c) phosphates, and (d) carbonates. The differences in the corrosion resistance of the various kinds of iron and steel used were slight in comparison with the effect of a change of inhibitor or condition of test.

CONTENTS

	Page
I. Introduction	665
II. Scope of the investigation	666
III. Apparatus	667
IV. Procedure	669
V. Results	670
1. Total immersion and spray	670
2. Corrosion in crevices	673
VI. Summary	675

I. INTRODUCTION

With the increasing use of air conditioning during recent years, the protection of the equipment against corrosion is becoming increasingly important. If suitable precautions are not taken to guard against the losses from corrosion, parts of the system become badly corroded and require replacement in a very short time. This is especially true in industrial regions, where the normal contamination of the air with acid-forming gases, as oxides of sulfur and carbon, is relatively high. The presence of chlorides in the atmosphere of some localities is also conductive to corrosion.

Painting the equipment to prevent its deterioration is often resorted to, but this is not entirely satisfactory, since corrosion occurs at breaks in the paint film and serious damage to the metal parts may result before it is visible to one inspecting the setup. There are also parts which it is not feasible to paint, such as the interior of the pipes or other inaccessible parts.

A brief outline of the operation of an air-conditioning system may assist the reader in understanding the corrosive conditions encountered therein. For operation during the summer, it is necessary to cool and dehumidify the air as it is drawn from the outside. This is accomplished by blowing the incoming air through a spray of refrigerated

water. By this treatment most of the dust particles and certain gases that are present are removed. The gases, sulfur dioxide and carbon dioxide, in uniting with the water form sulfurous acid and carbonic acid. The former, on oxidation, yields sulfuric acid. In air-conditioning systems it is not economical to use fresh water continuously. After leaving the sprays, the water flows to a recirculating pump and is pumped back to the cooling system and thence to the sprays, and the cycle is repeated. Thus the contaminating impurities in the air are continually being built up in the wash water, and at the same time the pH of the water decreases rapidly, unless some alkaline substance is added to neutralize the acid that is formed. In winter operation, the cycle is the same, except that refrigeration of the spray water is omitted.

II. SCOPE OF THE INVESTIGATION

Two possible methods of reducing the losses from corrosion suggest themselves. One of these is the careful selection of the materials of construction to secure maximum resistance to corrosion, the other is the treatment of the water by the addition of suitable chemicals which will inhibit the corrosive attack. The present investigation was directed toward a study of the latter phase of the subject.

It has been known for many years that certain chemicals, when added to water even in small amounts, will retard corrosion of iron immersed therein. The usual explanation for this is that the chemical produces a film on the surface of the iron which prevents the corrosion reaction from proceeding.

None of the ready-made mixtures sold commercially as inhibitors was used in this work nor was any attempt made to simulate commercial inhibitors by making up mixtures of this kind. Instead, the chemicals which form the basis of such inhibitors were used. These chemicals were (1) sodium dichromate, (2) sodium silicate, (3) sodium phosphate, and (4) sodium carbonate.

The concentration of each of the chemicals was varied from 100 to 500 ppm.

The pH in most of the runs was maintained between 8.0 and 9.0, but the effect of drop in the pH to between 4.0 and 5.0 was studied in two of the runs made.

The effect on the inhibiting action of the pick-up of sulfates and chlorides, such as results from the absorption of impurities in the air, was included in the study.

In order to answer the question which may be raised as to whether the effectiveness of an inhibiting treatment varies with the conditions under which the corrosive attack occurs, the tests were carried out in several ways. Some of the specimens were tested by immersion in a stream of the treated water flowing at a constant rate of 5 ft./min. Others were tested with a fine spray of the treated water impinging directly on their surfaces. It is well known that corrosion within a crevice opening out to the surface is usually more severe than the attack on a relatively plane surface of the same specimen. To determine the effectiveness of the inhibiting treatment against "crevice corrosion," some of the test specimens consisted of an assembly of two simpler ones, so as to simulate a crevice. These were subjected to corrosion by simple immersion as well as by spraying.

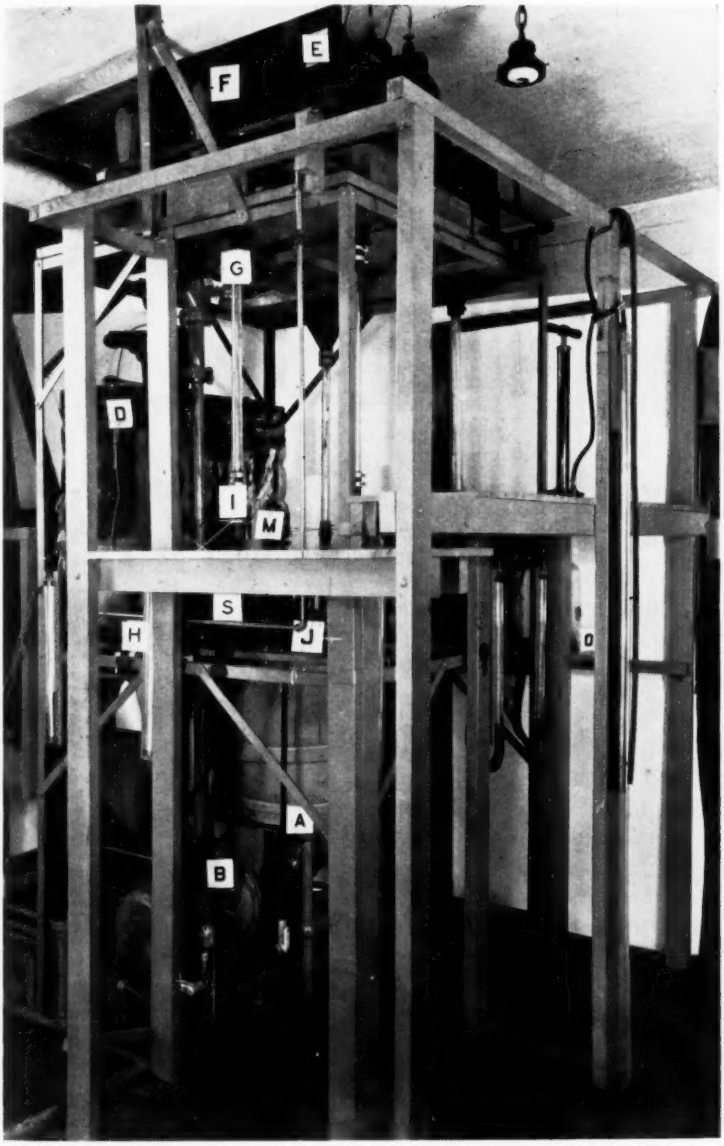

FIGURE 1.—*Apparatus used in the investigation.*

A, lower tank; *B*, pump; *C*, upper tank; *D*, spray chamber; *E*, siphon; *F*, header; *G*, glass tube; *H*, manometer for flow-meter, *I*, orifice; *J*, valve; *K*, pressure gage; *L*, holder for spray specimens; *S*, screw clamp, V_1 and V_2, valves.

UNIV. OF MICH.

Six ferrous sheet materials were used throughout the test. These materials were (1) a copper-bearing steel, (2) an open-hearth iron, (3) an alloyed open-hearth iron, (4) a low-alloy steel, (5) a wrought iron of the new "synthetic" type, and (6) a hand-puddled wrought iron. The results illustrated in figure 4, upon which conclusions were drawn as to the relative merits of the inhibitors used, are the averages for all materials. Although some differences in the behavior of the various materials were observed, they were not considered great or consistent enough to constitute a significant factor affecting these conclusions.

III. APPARATUS

The apparatus used in this investigation is shown in figure 1, and the action is shown diagrammatically in figure 2. The apparatus is

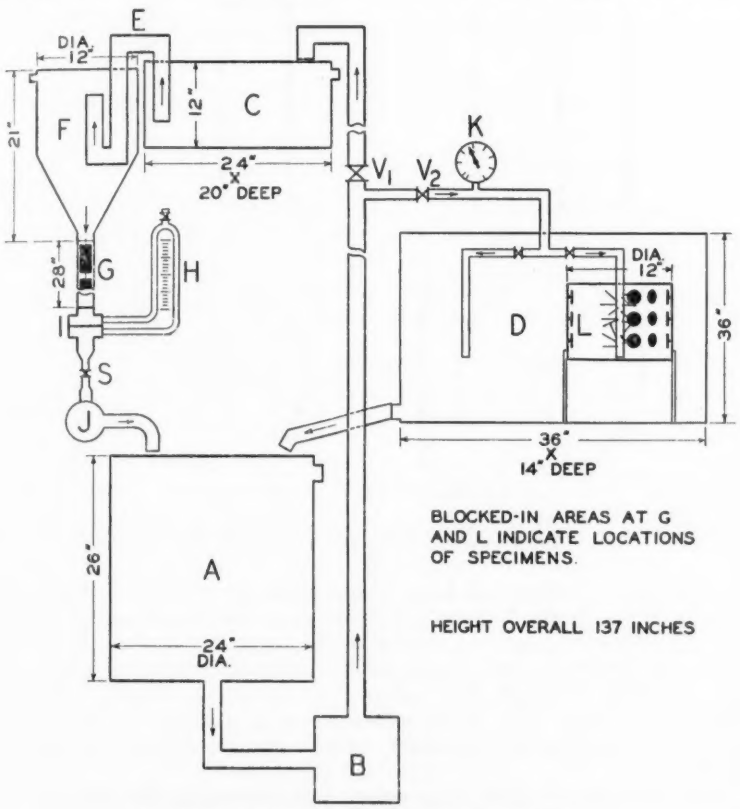

FIGURE 2.—*Diagram of the corrosion apparatus.*
(Significance of letters is the same as in figure 1)

similar in many respects to that used by Rawdon and Waldron.[1] All parts of the apparatus were constructed of hard rubber, with the exception of the flow tubes, which were of Pyrex glass. This made

[1] H. S. Rawdon and L. J. Waldron, *Continuous-flow corrosion tests of steel pipe.* Proc. Am. Soc. Testing Materials, **35**, pt. 2, 233 (1935).

certain that no other metal except those being tested could come in contact with the treated water. The total liquid capacity of the apparatus was approximately 115 gallons.

The course of the liquid through the apparatus is indicated by arrows in figure 2. In conducting the test run, the solution was pumped from the lower tank (*A*) to the upper tank (*C*) by the acid-resisting rubber-lined pump (*B*). From here it was siphoned into a group of headers (*F*) and allowed to flow by gravity down the tubes (*G*) in which the specimens were suspended, and from here the liquid returned to the lower tank and the cycle was repeated. The rate of flow was regulated by the screw clamp (*S*) and was measured by the flow meter (*H*). The specimens used in this part of the test were 3- by 1-inch rectangles cut from 19-gage sheet. This type of speci-

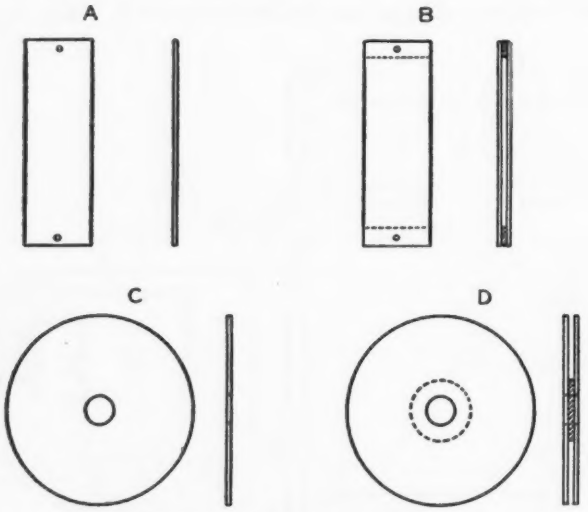

FIGURE 3.—*Types of specimens.*

A, total-immersion specimen, 1- by 3-inch, in flow tubes; *B*, crevice specimen in flow tubes; *C*, spray specimen, 2¾-inch diameter; *D*, crevice specimen in spray chamber.

men is shown in figure 3 (*A*). Fine waterproofed cord (fishing line) passing through the holes near the ends of the specimen was used to support the specimens vertically in the tubes.

In the spray system a part of the treated water being circulated was diverted through the valve (V_2) into the 1-inch spray tube. The wall of this tube was perforated with a large number of holes of 0.5-mm (0.02-inch) diameter, evenly spaced approximately 8 mm apart.

The pressure head of this spray was measured by the gage (*K*). The force of the spray was kept constant by maintaining a pressure of 9 lb/in.^{2} The spray specimens were supported in a hard-rubber cylindrical holder encircling the spray tube. This holder, 12 inches in diameter and 10 inches high, accommodated three rows of specimens, 10 in each row. Each specimen, 2¾ inches in diameter with a ⅜-inch central hole (fig. 3, *C*), was mounted on a hard-rubber rod

about 1 inch long and ⅝ inch in diameter which had been turned down to ⅜ inch in diameter on one end for a distance of about ⅜ inch and threaded. The threaded end was inserted through the hole so as to hold the specimen securely against the shoulder of the rod when a hard-rubber nut of ⅝-inch outside diameter was screwed on to the rod. This rod, carrying the specimen, was then screwed into the holder.

The lower tank was provided with an immersion electric heater and temperature regulator for maintaining a constant temperature of 35° C ±0.2°.

IV. PROCEDURE

A preliminary study was made of the method of preparing the surfaces of the specimens prior to placing them in the apparatus. Wet surface grinding gave results which could be repeated most closely.

The following procedure was therefore adopted in the preparation of the specimens:

1. Both sides were ground on the surface grinder, using a 3860–H8B Norton wheel, and care being taken to remove all the mill scale.
2. The specimens were degreased with trichloroethylene in a vapor degreaser.
3. They were then weighed on an analytical balance.
4. The backs of those specimens of which only one surface was to be exposed to the liquid were coated with a mixture of gutta-percha and ozokerite wax in approximate proportions, 1:2. These specimens included those in the spray test and those in which the effect of a crevice was being studied.
5. The types of specimens to be used for studying crevice corrosion were assembled so that the bare surfaces faced each other as shown in figure 3(*B*) and 3(*D*). Type *B* was used for the totally immersed samples and type *D* for those in the spray. The specimens were separated by means of waxed-paper or waxed-cloth spacers, the width of the resulting crevice being approximately 0.03 inch. This was measured by means of a feeler gage.

All specimens were placed in the apparatus as previously described, and, at the end of the run of 14 days' duration, were removed and photographed. The rust was then removed electrolytically by making the specimens the cathode in a 10-percent ammonium-citrate solution, carbon anodes and a current density of 2 or 3 amp/dm^2 being used. After washing and drying, the specimens were again weighed and the loss was calculated in grams per square decimeter for a period of 14 days.

A blank to determine the loss produced by the cathodic cleaning operations was run for each of the materials tested. The loss was found to be nearly negligible, if the procedure described was followed and all mill scale was removed before starting. However, if this were not done, this cleaning removed the oxides in the scale. The measured losses in certain cases amounted to several times the actual corrosion loss.

The solutions were prepared by dissolving a weighed amount of the appropriate chemical in Washington city water. In many of the preliminary tests, distilled water was used in making up the solutions. The differences in the results obtained in the two cases were not considered significant. In actual practice, tap water is always used.

The results [2] of an average analysis of the raw water used in this investigation are as follows:

Silica	2 ppm.
Calcium	27 ppm.
Magnesium	3 ppm.
Chloride	6 ppm.
Sulfate	30 ppm.
Bicarbonate	60 ppm.

The amount of chemical added was calculated to correspond in concentration to the anhydrous salts, $Na_2Cr_2O_7$, Na_2SiO_3, Na_3PO_4, and Na_2CO_3, respectively. The chemicals used in the actual preparation of the solutions are as follows:

Sodium chromate and dichromate.	$Na_2Cr_2O_7.2H_2O$.
Water glass	$Na_2Si_4O_9.xH_2O$ (sodium silicate, 40° Bé solution).
Sodium metasilicate	$Na_2SiO_3.5H_2O$.
Sodium disilicate	$Na_2O.2SiO_2.2H_2O$.
Sodium phosphate	Approximately equal parts of $Na_3PO_4.12H_2O$ and $Na_2HPO_4.12H_2O$.
Sodium hexametaphosphate	$(NaPO_3)_6$.
Sodium carbonate	Approximately equal parts of Na_2CO_3 and $NaHCO_3$.
Sulfate	Sulfate ions were supplied by Na_2SO_4 for pH of 8 to 9, and by H_2SO_4 for pH of 4 to 5.
Chloride	Chloride ions were supplied by NaCl for pH of 8 to 9, and by HCl for pH of 4 to 5.

The acidity of the solutions as they were prepared was slightly higher than that planned to be used in the test. After the chemicals had been dissolved and thoroughly mixed, the pH of the bath was adjusted to the desired value by the addition of sodium hydroxide. In order to maintain the pH at the desired value during the run, it was necessary to make small additions of sodium hydroxide for runs in which a pH of 8 to 9 was desired and of sulfuric acid for a desired pH of 4 to 5. In those cases in which the composition of the inhibiting chemical was uncertain, as in water glass, a chemical analysis of the bath served as a check on this composition, and the necessary adjustment was made accordingly.

V. RESULTS

1. TOTAL IMMERSION AND SPRAY

The compositions of the solutions used in 14 different corrosion-inhibiting treatments are given in table 1. The average loss in weight obtained in each of these water treatments is shown graphically in figure 4. The loss in weight in each case is the average of duplicate determinations for each of the six ferrous sheet materials used, with the exception of runs 2, 12, and 14, in which cases triplicate determina-

[2] Data supplied by C. J. Lauter, chief chemist, Dalecarlia Filter Plant, Washington, D. C.

tions were made of each material. The height of the solid blocked-in areas in figure 4 represents the loss in weight occurring in the specimens which were totally immersed in the liquid flowing at the rate of 5 linear feet per minute. The height of the cross-hatched areas represents the average loss in weight of the specimens exposed to the spray for the different runs indicated.

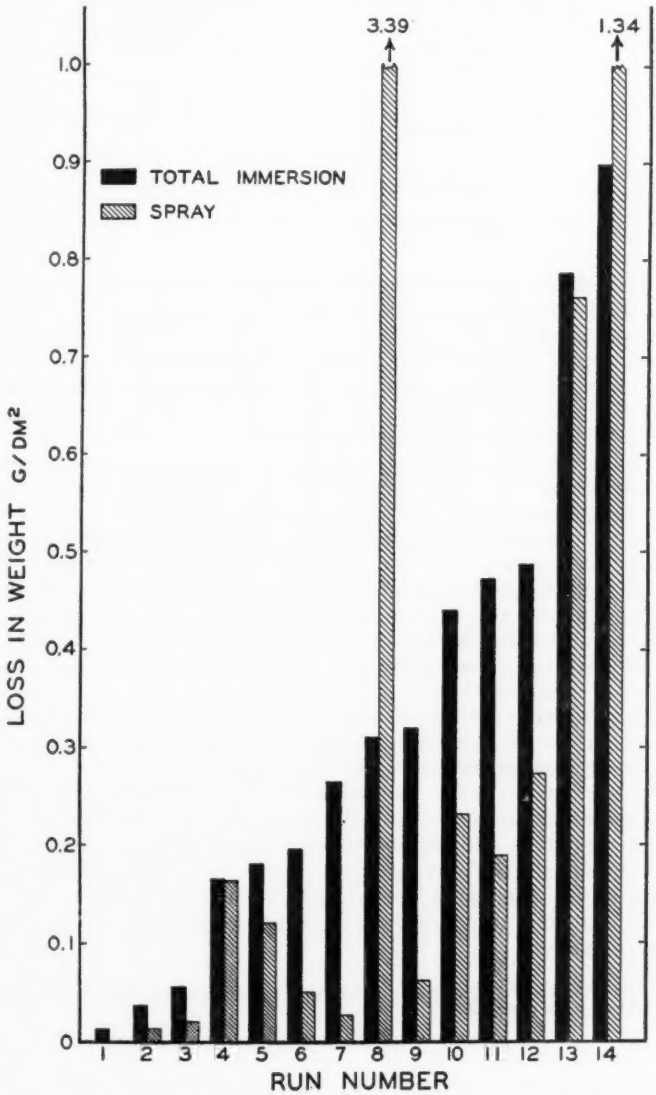

FIGURE 4.—*Chart showing the average loss in weight for the period of 14 days of the six materials tested, using the water treatments listed in table 1.*

TABLE 1.—*Summary showing concentration of inhibitors and* pH *of solutions in the various water treatments used*

Run No.	Concentration of inhibitor	pH	Run No.	Concentration of inhibitor	pH
1	200 ppm of sodium chromate [a]; 100 ppm of sulfate; 50 ppm of chloride [b].	8 to 9	8	500 ppm of water glass; 100 ppm of sulfate; 50 ppm of chloride [b].	4 to 5
2	100 ppm of sodium chromate [a]	8 to 9	9	100 ppm of water glass	8 to 9
3	500 ppm of water glass	8 to 9	10	100 ppm of sodium metasilicate	8 to 9
4	500 ppm of sodium metasilicate	8 to 9	11	500 ppm of water glass; 100 ppm of sulfate; 50 ppm of chloride [b].	8 to 9
5	200 ppm of sodium dichromate [a]; 100 ppm of sulfate; 50 ppm of chloride [b].	4 to 5	12	100 ppm of sodium phosphate	8 to 9
6	500 ppm of sodium disilicate	8 to 9	13	Untreated water	8 to 9
7	500 ppm of sodium phosphate; 50 ppm of sodium hexametaphosphate.	8 to 9	14	100 ppm of sodium carbonate	8 to 9

[a] An alkaline solution has been designated as chromate and the same solution in an acid solution as dichromate.

[b] The chloride and sulfate additions were made to simulate contamination of the water as it occurs in service.

Sodium hexametaphosphate was added in run 7 to prevent the precipitation of large calcium and magnesium phosphate crystals. The addition of hexametaphosphate prevented the formation of any precipitate in the freshly prepared solution. After several hours (overnight run in the apparatus), a precipitate formed but was in so fine a physical state that it did not clog the fine holes of the spray, as was the case when the hexametaphosphate was not used.

The following data (table 1 and fig. 4) support certain generalizations concerning the effectiveness of the inhibitors tested and the relative initial corrosion resistance of the materials:

1. The treatments may be arranged in the following order of decreasing ability to prevent corrosion of ferrous metals under the conditions used: (a) sodium chromate (or dichromate), (b) sodium silicate, (c) sodium phosphate, and (d) sodium carbonate. The last-named chemical was without value in the concentration of 100 ppm. These results are in substantial agreement with those reported by Sterne [3] in the operation of air-conditioning equipment.

2. The inhibiting action of the sodium silicates appeared to increase with an increase of the ratio of SiO_2 to Na_2O. This tendency was especially noticeable for the spray specimens.

3. Contamination of the treated water with 100 ppm of sulfates and 50 ppm of chlorides increased the corrosion in the sodium silicate treated water, even though the pH was maintained at the value of 8 to 9, whereas in the sodium chromate solution, no appreciable corrosion occurred under the same conditions. When the pH value of the chromate solution was lowered to approximately 4 to 5, corrosion resulted, however.

[3] C. M. Sterne, *The control of corrosion in air conditioning equipment by chemical methods*, Proc. Am. Soc. Testing Materials **35**, pt. 2, 261 (1935).

4. A striking difference in the rate of corrosion of specimens exposed in total immersion as compared with those subjected to the spray occurred in run 8, in which the inhibitor consisted of 500 ppm of water glass in a solution with a pH of 4 to 5 and contaminated by sulfate and chloride impurities. The explanation of this apparent disagreement was that under the total immersion conditions a gelatinous coating, evidently insoluble silicic acid, covered the specimens and protected them from corrosion. This coating was from 1/16 to 1/8 in. thick and was easily visible on the specimens. Formation of this coating was prevented on the spray specimens, so that corrosion proceeded normally.

The effect of this coating on the corrosion also accounts for the greater loss in weight of the totally immersed specimens of run 11 than of those of run 8.

However, in most of the runs, the loss in weight was greater for the specimens immersed in the slowly moving liquid than for those specimens exposed to the spray. It is thought that the reason for this difference was that the spray washed off all loose corrosion products, so that most of the surface was maintained approximately in its original condition. This action tended to keep the anodic areas at a minimum. On the other hand, in the flow tubes the motion of the liquid was so slow that the corrosion products were not removed rapidly but were slowly carried down the surface of the specimen, thereby stimulating corrosion at a point immediately below that at which it started. As this process continued, the anodic areas increased in extent. Thus, at the end of a run, the corrosion on the immersed specimens was in the form of long narrow streaks, whereas that on the spray specimens occurred at individual points on the surface as pits.

Some variation was noted in the initial corrosion resistance of the six materials used in the investigation. This variation, however, was of minor significance when compared with the variations resulting from a change in the inhibitor. In other words, corrosion was prevented from occurring on all materials under certain conditions, whereas under other conditions it took place on all the materials. No conditions were found in which corrosion was present on some of the materials and absent on others. Since the runs were of only 14 days' duration, the slight differences in loss in weight of the various materials were not sufficient to draw conclusions as to the superiority or inferiority of these materials.

2. CORROSION IN CREVICES

Corrosion is often more severe within small crevices than on flat surfaces of the same piece. Observations on the corrosion in crevices were therefore included in each run to determine whether serious corrosion might develop from this cause. The specimens were assembled as shown in figures 3 (*B* and *D*), and the results are given in table 2.

TABLE 2.—*Comparative merits of inhibitors in crevice corrosion, with an approximate width of crevice of 0.03 inch*

[Average loss of weight determined on 6 types of ferrous sheet materials in test runs of 14 days' duration, arranged in the same order as in table 1]

Run No.	Concentration of inhibitor	pH	Average loss in weight for 14 days	
			Total immersion (flow, 5 ft/min)	Spray
			mg/dm²	*mg/dm²*
1	200 ppm of sodium chromate 100 ppm of sulfate; 50 ppm of chloride [a]	8 to 9	54	
2	100 ppm of sodium chromate	8 to 9	51	21
3	500 ppm of water glass	8 to 9	88	52
4	500 ppm of sodium metasilicate	8 to 9	133	260
5	200 ppm of sodium dichromate 100 ppm of sulfate; 50 ppm of chloride [a]	4 to 5	239	109
6	500 ppm of sodium disilicate	8 to 1	183	125
7	500 ppm of sodium phosphate 50 ppm of sodium hexametaphosphate	8 to 9	63	137
8	500 ppm of water glass 100 ppm of sulfate; 50 ppm of chloride [a]	4 to 5	221	537
9	100 ppm of water glass	8 to 9	129	289
10	100 ppm of sodium metasilicate	8 to 9	246	323
11	500 ppm of water glass 100 ppm of sulfate; 50 ppm of chloride [a]	8 to 9	150	293
12	100 ppm of sodium phosphate	8 to 9	327	431
13	Untreated water	8 to 9	309	730
14	100 ppm of sodium carbonate	8 to 9	262	598

[a] The chloride and sulfate additions were made to simulate contamination of the water as it occurs in service.

It will be observed that the order of relative merit in which the inhibitors were placed by loss in weight resulting from crevice corrosion was, with a few exceptions, similar to that in which they were placed by the simple immersion or spray tests. Some corrosion occurred in the crevices of all the specimens as compared with a practically complete absence of corrosion in the total immersion and spray specimens of runs 1 and 2. On the other hand, in those cases in which the inhibitor was not especially efficient and a comparatively large amount of corrosion normally would occur on an exposed surface, the resulting corrosion products soon filled the crevice and further corrosion was arrested.

In several of the runs the width of the crevice was varied from a few thousandths of an inch to approximately 0.05 inch. The material used in these special tests was a plain carbon steel, and a glass microscope slide was placed on each side of the specimen. It was found that the corrosion loss was approximately proportional to the width of crevice, as shown in figure 5. The corrosion occurring in these crevices started along the medial longitudinal line of the specimen, this being the most inaccessible region for the replenishment of the solution and its dissolved oxygen. However, on continuing the run, this crevice slowly became filled with corrosion products, so that the total loss was a function of the available space within the crevice. The deficiency of oxygen in the inaccessible regions of the crevice was plainly revealed by the color of the corrosion products. Greenish ferrous compounds formed at the center of the specimens, and reddish-brown ferric compounds formed along the edges where the supply of dissolved oxygen was more abundant. Some of the variation of the results given in table 2 may be attributable to nonuniformity of the width of the

crevice, despite the fact that attempts were made in most of the runs to keep this width constant. It also appears that the greatest amount of corrosion may occur with one width of crevice under one set of conditions of inhibitor, pH, etc., and a different width of crevice

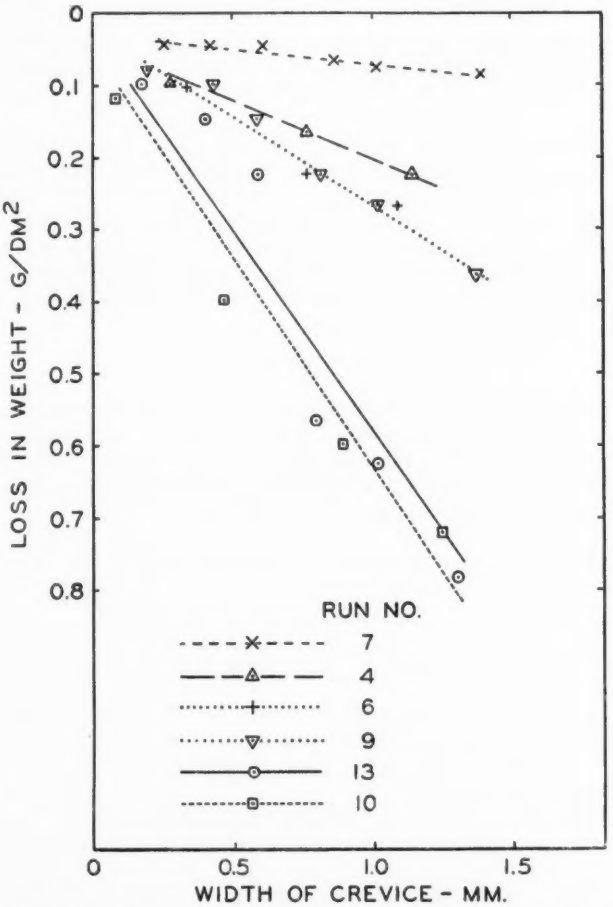

FIGURE 5.—*Effect of the width of crevice on the degree of corrosion occurring therein.*

The conditions for the different runs were the same as those listed in tables 1 and 2.

is conducive to the maximum corrosion under a different set of conditions.

VI. SUMMARY

This study has disclosed a number of generalizations on the corrosive properties of water which has been treated with small amounts of corrosion-inhibiting chemicals. Some of the more important of these trends are listed in the following summary:

1. All of the inhibitors tested, with the exception of 100 ppm of sodium carbonate, decreased the rusting of iron or steel.

229032—40——6

2. The order of decreasing efficiency of the inhibitors studied in the concentrations used, was (a) chromates, (b) silicates, (c) phosphates, and (d) carbonates.

3. In the case of the sodium silicates tested, the results indicated that the higher the ratio of SiO_2 to Na_2O, the greater was the inhibiting action.

4. Although some differences were noted in the initial corrosion resistance of the various kinds of iron and steel used, in most cases this was slight in comparison with that produced by a change in the inhibitor.

5. The distribution of corrosion, especially in the spray, was more uniform in the presence of an inhibitor than it was in its absence.

6. In the case of all the inhibitors used, corrosion to some extent occurred in crevices but it failed to occur on flat, uniformly exposed, metal surfaces in two instances. However, with inefficient inhibitors, the rusting was less in the crevices than on the fully exposed surface. In this case, the amount of corrosion appeared to be a function of the available space within the crevice.

This investigation was started by E. C. Groesbeck under the supervision of H. S. Rawdon. Credit for the design and building of the apparatus is due to Mr. Groesbeck. Later, circumstances involving impairment of physical ability made it necessary for Mr. Groesbeck to take only a minor part in the investigation.

WASHINGTON, March 7, 1940.

U. S. Department of Commerce National Bureau of Standards

RESEARCH PAPER RP1306

Part of Journal of Research of the National Bureau of Standards, Volume 24, June 1940

PREPARATION AND SOME PHYSICAL PROPERTIES OF 2,2,4,4-TETRAMETHYLPENTANE

By Frank L. Howard

ABSTRACT

Over 2 liters of purified 2,2,4,4-tetramethylpentane was prepared synthetically. Physical constants determined on the purest fraction included freezing point, boiling point and its variation with pressure, and refractive index and density and their variations with temperature.

CONTENTS

	Page
I. Introduction	677
II. Preparation of 2,2,4,4-tetramethylpentane	677
1. 2,2,4-Trimethyl-4-chloropentane	678
2. Zinc-copper couple	679
3. Dimethyl zinc	679
4. 2,2,4,4-Tetramethylpentane	681
5. Remarks	682
III. Physical properties	683
IV. References	684

I. INTRODUCTION

In connection with an investigation of paraffin hydrocarbons being conducted by the National Bureau of Standards for the National Advisory Committee for Aeronautics, the Navy Bureau of Aeronautics, and the Army Air Corps, 2,2,4,4-tetramethylpentane was prepared synthetically, and was purified by fractional distillation in an automatically controlled 6-m helix-packed column.

II. PREPARATION OF 2,2,4,4-TETRAMETHYLPENTANE

The method of Whitmore and Southgate [1][1] was used to prepare 2,2,4,4-tetramethylpentane and consists in reacting dimethyl zinc with 2,2,4-trimethyl 4-chloropentane. The yield was increased and the various manipulations were expedited by certain alterations in the procedure, which is therefore given in full.

[1] Figures in brackets refer to the literature references at the end of this paper.

The reactions involved are shown in the following diagram:

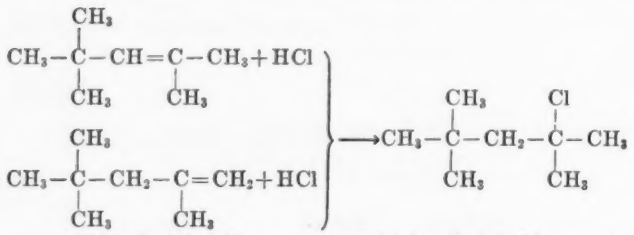

$$Zn\ (Cu)_x + CH_3I \longrightarrow CH_3ZnI$$

$$2CH_3ZnI \longrightarrow (CH_3)_2Zn + ZnI_2$$

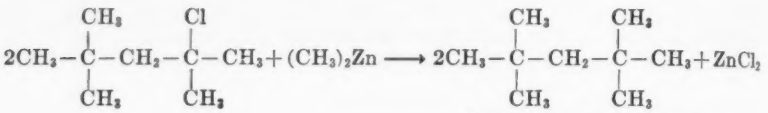

1. 2,2,4-TRIMETHYL-4-CHLOROPENTANE

This compound was prepared by the action of hydrogen chloride on "diisobutylene." The apparatus is shown in figure 1. The two

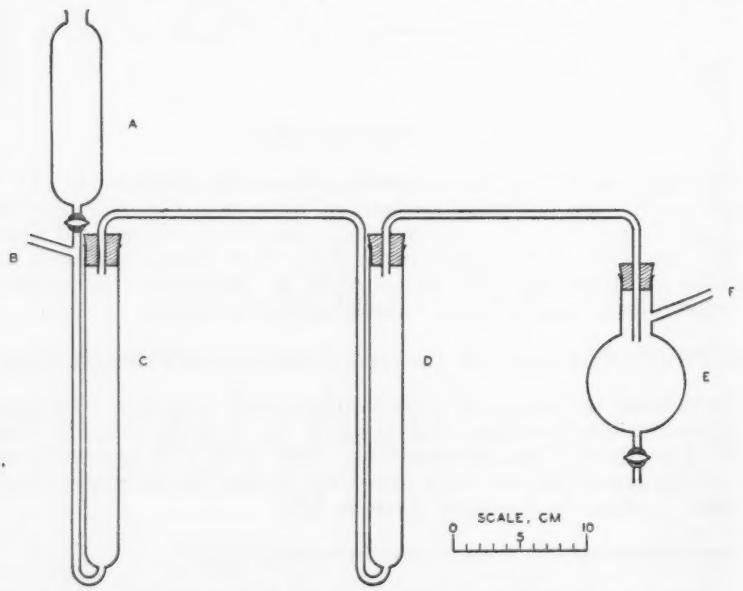

FIGURE 1.—*Apparatus used in the preparation of 2,2,4-trimethyl-4-chloropentane.*

tubes (*C* and *D*) were filled with glass helices admixed with fused zinc chloride. Diisobutylene from a 500-ml separatory funnel (*A*) was added to a stream of dry hydrogen chloride, through *B*, which flowed

to the bottom of the first test tube. The resulting liquid plus gas was forced from the top of the first test tube into the bottom of the second. The product from this second reaction chamber flowed from the top and collected in a separatory funnel (*E*) from which the slight excess of hydrogen chloride was allowed to flow through *F* to a suitable absorber. The two chambers were immersed in a bath of chloroform-carbon tetrachloride, kept between −20° and −25° C by addition of carbon dioxide.

The product was the same as that formed by saturating diisobutylene with hydrogen chloride at 0° C in the absence of a catalyst, but was formed about 12 to 15 times as fast by the technique described. The absorption of hydrogen chloride was much faster at lower temperatures, but the apparatus became clogged with crystalline product.

The melting point of nearly pure alkyl chloride was found to be −26° C, whereas the product from the reactor melted around −30° C. The melting point was raised when the product was purified by crystallization, and excess hydrogen chloride removed by bubbling carbon dioxide through the liquid at 0° C. It was not distilled (save for a small sample), because of the ease with which it decomposed to hydrogen chloride and the corresponding olefins.

2. ZINC-COPPER COUPLE

An intimate mixture of 480 g of technical zinc dust and 60 g of cupric oxide, reagent quality, was introduced into a 150- by 2.7-cm Pyrex tube placed horizontally and plugged with asbestos 15 cm from one end, and was spread evenly in the bottom half of the tube with a scraper. A loose plug of asbestos was inserted into the tube, and a stream of hydrogen, washed with sulfuric acid, was introduced. After the tube was thoroughly swept with hydrogen, it was placed in a 15-in. tube furnace. Heating was started first at the hydrogen-entrance end of the tube, where, after 5 to 10 min, reduction became apparent. The furnace temperature at this time was in the vicinity of 550° C. The tube was left in its original position until minute shining pellets were imbedded in the metal. Then the tube was moved so that the next section of zinc-copper oxide mixture was heated. At this time a faint red glow was observed to progress along the mixture, leaving in its wake a matrix of pellets of very small size, while the upper part of the tube became clouded with a film of condensed zinc. Overheating, evidenced by a yellow to green color, was avoided by moving the tube steadily through the furnace, so that the glow caused by reduction remained in the forward half of the furnace. Overheating caused the pellets to sinter together and resulted in a less active couple. When all the material was reduced and the water driven from the tube, the latter was allowed to cool. The product was removed and used as soon as possible. The entire process consumed about a half hour. Throughout the reduction, hydrogen was passed through the tube at about 40 to 50 ml/min.

3. DIMETHYL ZINC

Two batches of zinc-copper alloy, together with 500 ml (8 moles) of methyl iodide, were placed in a 2-liter round-bottom flask (fig. 2, *A*). The flask was fitted with a cork, through which a hole was bored at 30°

to the vertical. Through the hole was inserted the end of a 40-cm condenser (*B*) which was bent through 90°. The other end of the condenser was fitted with a 120° bend, on which was placed a No. 14 cork, ready for insertion into a side neck of a 5-liter 3-necked flask. By rotating the 2-liter flask and stopper about the vertical axis, the condenser could be lowered for downward distillation. To the upper end of the condenser was attached, beyond the cork, a short rubber tube carrying a T-tube (*C*). The other two sides of the T were connected to a source of carbon dioxide, and to a mercury trap, through

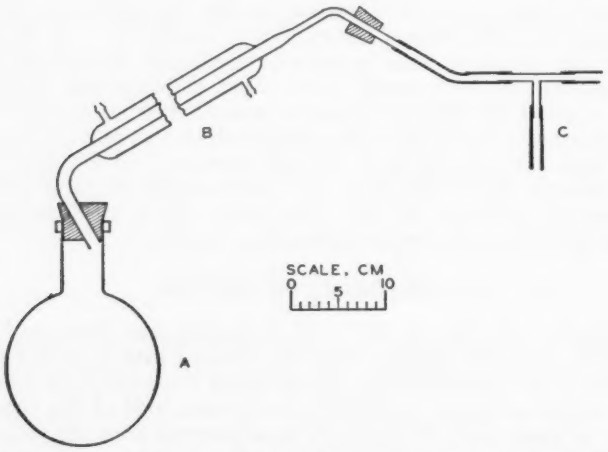

FIGURE 2.—*Apparatus used in the preparation of dimethyl zinc.*

70 cm of Pyrex tubing. All the corks in this apparatus were select, tight-fitting, and well shellacked.

The rubber tube connecting the T-tube with the carbon dioxide supply was closed with a screw clamp. The flask was warmed in an oil bath at 60° C until reaction started, which was evidenced by an increase in reflux rate, then the flame was removed from the bath. Reflux continued smoothly for 24 to 36 hr, after which the flask was again heated at 60° C until reflux ceased (2 to 7 hr) and then allowed to cool. After the flask had cooled, the screw clamp on the carbon dioxide line was opened and the system was filled with carbon dioxide. Then the rubber connection was removed from the end of the condenser and a small cork placed in the opening. Dimethyl zinc was distilled immediately from this apparatus directly into the vessel used for the next step in this synthesis.

A 5-liter 3-necked flask was fitted with a mercury-sealed stirrer and a reflux condenser. The top of the condenser was fitted with a T-tube, one arm of which was connected to a vent, the other arm to a cylinder of carbon dioxide. A slow stream of carbon dioxide was passed across this T to prevent air being sucked back into the flask. Five-hundred millimeters of dry tetrahydronaphthalene (tetralin) was placed in the flask, after which it was swept thoroughly with carbon dioxide.

The condenser on the dimethyl zinc apparatus was lowered, the small cork in the end of the condenser quickly removed, and the end of the condenser inserted into the free neck of the 5-liter flask.

The oil bath was heated to about 90° C, which caused a steady distillation of dimethyl zinc. The temperature was then gradually raised to 200° C and held there as long as distillation took place. When all the dimethyl zinc was distilled, the oil bath was removed, the flask allowed to cool, and the condenser raised. A cork carrying a separatory funnel was quickly placed in the small neck which held the condenser. This operation of removing the condenser and inserting the separatory funnel was carried out while a steady stream of carbon dioxide was played on the apparatus.

4. 2,2,4,4-TETRAMETHYLPENTANE

The 5-liter flask assembly was placed in a small galvanized tub. Water was added until the flask was half immersed. Cooling was effected by conducting water at 5° C through 25 feet of 5/16-inch copper tubing made into a coil around the flask.

The stirrer was started and a mixture of 1,500 ml of tetralin and 1,190 g (8 moles) of 2,2,4-trimethyl-4-chloropentane added to the dimethyl zinc already in the flask, during 6 to 8 hours, with the bath temperature kept below 7° C. After about one-fourth of the alkyl chloride was added, crystals of zinc chloride began to form. As addition was continued, the reaction mixture attained the appearance of a creamy sludge. No difficulty was encountered in stirring, unless the alkyl chloride was added too fast, which caused the formation of curds. When all the alkyl chloride had been added, the mixture was allowed to stand overnight in the cold bath. Then 500 ml of water was added, followed by 500 ml of 15-percent hydrochloric acid. A very clean, uncolored organic layer was thereby obtained.

This layer was separated, washed with water, then with 5-percent aqueous sodium bicarbonate, followed by three more washings with water. It was then dried over calcium chloride and distilled through a 150-by 2-cm helix-packed column [2]. After a forerun of diisobutylene (150 to 450 ml), there was obtained 595 to 687 ml of crude 2,2,4,4-tetramethylpentane (boiling range 119° to 124° C). This is equivalent to a yield of 42 to 48 percent, based on the amount of methyl iodide. Whitmore and Southgate [1] reported a yield of 18 percent.

Twenty-eight hundred milliliters of crude 2,2,4,4-tetramethylpentane prepared as described above was purified by subjecting it to the following treatment: Ten washings with concentrated sulfuric acid; two washings with water; one washing with 5-percent aqueous sodium bicarbonate; one washing with water, drying with calcium chloride, refluxing over sodium, distillation, passing through a column (100 by 2 cm) of silica gel; five washings with sulfuric acid; one washing with water; one washing of bicarbonate; one washing with water, drying with calcium chloride, refluxing over sodium, and distillation through a 150-by 2-cm column [2]. The fraction which boiled at 122° to 123° C was collected, and amounted to 2,210 ml. This purified material was distilled in an automatically controlled helix-packed column in the manner briefly described earlier [3]. The data on the distillation are given in table 1.

TABLE 1.—*Data on distillation of 2,2,4,4-tetramethylpentane*

Fraction number	Reflux time	n_D^{20} (uncorrected)
	hr.	
1	19.0	1.4067
2	21.5	1.4068
3	33.5	1.4067
4	11.5	1.4068
5	26.0	1.4068
6	24.0	1.4066
7	6.0	1.4066
8	6.0	1.4065
9	6.0	1.4067
10	6.0	1.4067
11	12.0	1.4067
12	12.0	1.4067
13	6.0	1.4067
14	6.0	1.4068
15	4.0	1.4067
16	4.0	1.4069
17	4.0	1.4068
18	12.0	1.4069
19	0.3	1.4067
20	.3	1.4069
21	.3	1.4069
22	.2	1.4068
23	.2	1.4066
24	.1	1.4069
25	.1	1.4069
26	.1	1.4069
27	.1	1.4070
28	.1	1.4071
29	.1	1.4085

5. REMARKS

An attempt was made to prepare dimethyl zinc by conducting methyl chloride over the zinc-copper alloy in the same tube in which the alloy was made. Some dimethyl zinc formed, but the reaction was slow and difficulty was experienced in getting reaction below the surface of the metal. It is the opinion of the author that a satisfactory method could be devised to carry out this reaction.

An attempt was made to prepare 2,2,4,4-tetramethylpentane by the action of 2,2,4-trimethyl-4-chloropentane on the mixture of methyl aluminum chlorides obtained by the action of methyl chloride on duralumin turnings. The addition was carried out at a bath temperature of −40° C, with carbon bisulfide as a solvent. The mixture was decomposed by adding dilute hydrochloric acid at −30°C, and worked up in the usual manner.

The product was distilled in a 10- by 900-mm column packed with glass helices [2]. The temperature steadily rose during distillation, and four fractions were obtained. the data being given in table 2. All the fractions had the very disagreeable odor of sulfur-containing compounds. The results indicate that there was probably considerable rearrangement and polymerization, due to the aluminum chloride by-product of the reaction, along with interaction with the solvent.

TABLE 2.—*Distillation data on products from methyl aluminum chlorides and 2, 2, 4-trimethyl 4-chloropentane*

Fraction	Boiling range	n_D^{20}	Volume
	°C		ml
1	up to 82	1.55351	70
2	82 to 120	1.40407	10
3	120 to 136	1.40835	10
4	136 to 161	1.41880	15
5 res			90

Only one trial was made; but the reaction may be worth while, if the proper choice of solvent, time of reaction, temperature, and concentrations are found.

III. PHYSICAL PROPERTIES

Fractions 12, 13, and 14 were combined, and physical properties were determined on this material by the methods described in previous papers [3 and 4]. The distillation curve, figure 3, shows the material to be of high purity. The data plotted in figure 4 were obtained by

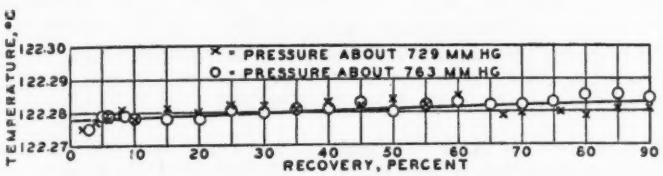

FIGURE 3.—*Distillation curve of 2,2,4,4-tetramethylpentane.*

Points represent values measured at the pressures indicated, and corrected to 760 mm Hg.

slowly cooling the solution until crystallization occurred, then slowly warming it until liquefaction was complete. The average of the temperatures at A and B is taken as the initial freezing point ("liquidus temperature"). The difference between A or B and the liquidus temperature, amounting to a few thousandths of a degree, is believed to result from the influence of external environment on the reading of the thermometer.

Table 3 shows the data obtained on all the physical constants determined, together with those obtained by Whitmore and Southgate [1]

TABLE 3.—*Properties of 2,2,4,4-tetramethylpentane*

Reference	Freezing point	Boiling point at 760 mm Hg	$\frac{dT}{dP}$	Refractive index		$\frac{dn}{dt}$	Density		$\frac{d\rho}{dT}$
				n_D^{20}	n_D^{21}		ρ^{20}	ρ^{25}	
	°C	°C	deg/mm Hg			per deg	g/ml	g/ml	g/ml deg
Whitmore and Southgate [1]	−66.9 to −67.1	122.30		1.40695			0.7185		
Present work [a]	−66.600	122.281	0.0492	1.40677	1.40451	−0.000453	.71957	0.71566	−0.000782

[a] The uncertainty of each value is believed not to exceed a few units in the last decimal place given.

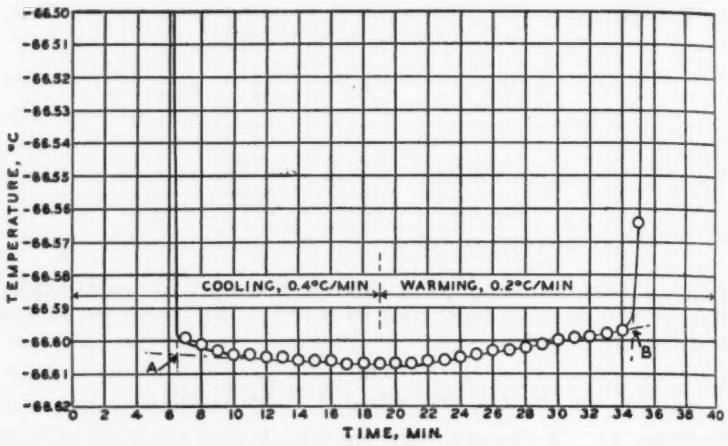

FIGURE 4.—*Freezing and melting curves of 2,2,4,4-tetramethylpentane.*

The author is indebted to Donald B. Brooks for the determination of physical properties, to H. C. Crafton, Jr. for the preparation of 2,2,4-trimethyl-4-chloropentane, and to Thomas W. Mears for aid rendered in carrying out some of the steps in the synthesis.

IV. REFERENCES

[1] F. C. Whitmore and H. A. Southgate, J. Am. Chem. Soc. **60**, 2571 (1938).
[2] F. C. Whitmore and A. R. Lux, J. Am. Chem. Soc. **54**, 3451 (1932).
[3] Donald B. Brooks, Frank L. Howard, and Hugh C. Crafton, Jr., J. Research NBS **23**, 637 (1939) RP1259.
[4] Donald B. Brooks, Frank L. Howard, and Hugh C. Crafton, Jr., J. Research NBS **24**, 33 (1940) RP1271.

WASHINGTON, March 29, 1940.

U. S. DEPARTMENT OF COMMERCE NATIONAL BUREAU OF STANDARDS

RESEARCH PAPER RP1307

Part of Journal of Research of the National Bureau of Standards, Volume 24, June 1940

INFLUENCE OF CYCLIC STRESS ON CORROSION PITTING OF STEELS IN FRESH WATER, AND INFLUENCE OF STRESS CORROSION ON FATIGUE LIMIT

By Dunlap J. McAdam, Jr. and Glenn W. Geil

ABSTRACT

By examination of surfaces and longitudinal sections of specimens of steel after stress corrosion, information has been obtained about the influence of cyclic stress (during corrosion) on the form and size of corrosion pits. A discussion is given of the theoretical stress concentration due to corrosion pits, and of the influence of size on the effective stress concentration.

By comparison of typical views of corrosion pits with curves representing the decrease of the fatigue limit with corrosion time, the forms and sizes of corrosion pits are correlated with the resultant lowering of the fatigue limit.

The stress corrosion process is discussed in terms of the general theory of corrosion of metals. With increase in cyclic stress and cycle frequency, the corrosion process is shifted from a cathodically controlled process toward an anodically controlled process.

CONTENTS

	Page
I. Introduction	686
II. Materials and method of investigation	686
1. Steels	686
2. Specimens	687
3. Corrosion stage	687
4. Determination of the fatigue limit and evaluation of the damage caused by the corrosion	687
5. Method of investigation of forms and sizes of the corrosion pits	688
III. Influence of stress corrosion on the fatigue limit, and the stress-time-cycle relationship for constant net damage	689
1. General description of diagrams representing the influence of both stressless corrosion and stress corrosion on the fatigue limit	689
2. Influence of stressless corrosion on the fatigue limit	689
3. Lowering of the fatigue limit by simultaneous corrosion and cyclic stress	689
4. Diagrams representing the stress-time-cycle relationship for constant net damage	690
IV. Pits formed by stressless corrosion	692
1. Surface views of specimens after stressless corrosion	692
2. Longitudinal sections showing pits caused by stressless corrosion	692
V. Influence of form, size, and distribution of corrosion pits on effective stress concentration	694
1. Factors involved in effective stress concentration	694
2. Theoretical stress concentration due to corrosion pits	695
3. Influence of size, and of the steepness of the stress gradient, on effective stress concentration	697
4. Effective stress-concentration factor for specimens previously corroded without stress	698

Page
VI. Pitting under simultaneous corrosion and cyclic stress, and its action with net damage ... 699
1. Pitting with frequency of 1,450 cycles per minute ... 699
2. Pitting with frequency of 500 cycles per minute ... 702
3. Pitting with frequency of 100 cycles per minute ... 703
4. Pitting with frequency of 50 cycles per minute ... 704
5. Pitting with frequency of 10 cycles per minute ... 706
6. Pitting with frequency of 1.5 cycles per minute ... 707
7. Pitting with frequencies of 0.5 cycle per minute and 5 cycles per hour ... 709
8. Summary of results of examination of specimens ... 710
VII. Stress-corrosion process ... 710
VIII. References ... 715

I. INTRODUCTION

The influence of simultaneous cyclic stress and corrosion on the fatigue limit, and the influence of cyclic stress on corrosion, have been discussed by the senior author in previous papers [10 to 23].[1] In the first five of these papers, the cyclic stress conditions were such as to cause failure by fatigue (corrosion fatigue). In the later papers [15 to 23], each experiment involved two stages. In the first stage, the specimen (with or without cyclic stress) was corroded by water for a definite time, then removed from the water, dried, and oiled. In the second stage, the fatigue limit of the specimen was determined by subjecting it to cyclic stress in air. The decrease in the fatigue limit was used as a measure of the damage resulting from the prior corrosion.

The damage caused by simultaneous corrosion and cyclic stress (stress corrosion) tends to be greater than the damage caused in the same time by stressless corrosion. The greater the stress, cycle frequency, and time in the corrosion stage, the greater is the difference between the resultant damage and the corresponding damage caused by stressless corrosion. The difference in damage (net damage) thus is a measure of the influence of cyclic stress on corrosion.

Opportunity was not then available for study of the forms and sizes of the corrosion pits and their correlation with the cyclic stresses applied during corrosion. Later, however, through the courtesy of the Director of the United States Naval Engineering Experiment Station, Annapolis, Md., the specimens that had been used were made available for such investigation. The results of this examination are used in this paper to correlate the forms and sizes of the corrosion pits with the net damage.

The previous papers were devoted mainly to presentation of data obtained with a great variety of metals, corroded in several different kinds of water. They presented a gradually broadening view of the subject, with no adequate summarizing paper. This paper, therefore, includes a brief summary of the results previously obtained with steels in fresh water, so that these results may be correlated with the results of examination of the corroded specimens.

II. MATERIALS AND METHOD OF INVESTIGATION

1. STEELS

The steels used in the investigation of the influence of cyclic stress on corrosion include carbon steels, ordinary alloy steels, and stainless steels. Only five of the steels, however, were used in the investigation

[1] Figures in brackets indicate the literature references at the end of this paper.

of the influence of cyclic stress on the form and size of corrosion pits: carbon steel JR–W–10, nickel steels IW–W–10 and LQ–W–10, and chromium-nickel steels BC–W–10 and AX–W–10. The compositions of these steels are given in table 1, details of heat treatment are given in table 2, and tensile properties are given in table 3.

2. SPECIMENS

The specimens used were fatigue-test specimens of the rotating cantilever type described in previous papers [9]. The specimens were conically tapered, and were so designed that the maximum stress was ¾ in. out from the inner fillet, and that the stress varied only about 1½ percent over a length of 1½ in. The diameter at the inner fillet was ½ in. With this specimen, therefore, a comparatively large region could be subjected to simultaneous corrosion and cyclic stress.

Each specimen used in the two-stage experiments was machined to within about 0.01 in. of the final diameter. The finishing tool had a radius of ½ in., the speed of the lathe was 90 rpm, and the feed was 130 threads per inch. The specimen, while rotating in the lathe, was then subjected to alternate circumferential and nearly longitudinal polishing. Circumferential polishing was done by the edge of a cloth-covered, relatively thin, rapidly revolving disk, which was moved slowly along the specimen. Nearly longitudinal polishing was done by a rapidly revolving cloth-covered cylinder with the axis in a plane perpendicular to the specimen. Polishing was done by means of a series of powders of increasing fineness, as in ordinary metallographic polishing, the last powder being levigated alumina. By this method, the surface was made sufficiently smooth to permit examination of the microstructure at a magnification of $\times 100$.

3. CORROSION STAGE

In the corrosion stage, water was applied to each specimen in a small stream, which was directed diagonally to the revolving cantilever specimen, so that the entire tapered portion was covered by a thin moving layer of water. The size of the water stream, within wide limits, had no apparent effect on the damage, as measured by the lowering of the fatigue limit. Some specimens were corroded without stress; other specimens, during corrosion, were subjected to various cyclic stresses and cycle frequencies. After corrosion for the desired time, the specimen was removed from the machine, dried and oiled. It was then ready for insertion in another machine in order to determine its fatigue limit in air.

The water used in the experiments considered in this paper was a well water, whose composition is given in table 4. Like many well waters, this water consisted essentially of a solution of calcium and magnesium bicarbonates, calcium sulfate, and chlorides. The chloride content, however, is unusually high for a well water.

4. DETERMINATION OF THE FATIGUE LIMIT AND EVALUATION OF THE DAMAGE CAUSED BY THE CORROSION

In the second stage, the fatigue limit of each corroded specimen was determined by a rotating cantilever test. In the early experiments, it was necessary to use several similarly corroded specimens in order

to determine the fatigue limit corresponding to a given time, stress, and cycle frequency in the corrosion stage. These specimens were tested at different cyclic stresses, and determination was made of the numbers of cycles necessary to cause fatigue failure. A stress-cycle curve could then be plotted, and an estimate could be made of the fatigue limit. Later, however, it was generally found possible to make a satisfactory estimate of the fatigue limit by use of only one specimen for a given corrosion condition. Such a result could be attained by selection of a stress that would cause failure at not much less than 1 million cycles. The fatigue limit was then estimated by extrapolation to 10 million cycles. Decrease in the accuracy owing to the use of only one specimen was slight, and was greatly outweighed by the increase in number of stress-corrosion experiments thus made possible.

The fatigue limits obtained with these specimens have been used in constructing diagrams of three types to represent the influence of cyclic stress, cycle frequency, and corrosion time on total and net damage. These diagrams are shown in figures 1 to 6.

5. METHOD OF INVESTIGATION OF FORMS AND SIZES OF THE CORROSION PITS

The specimens were examined visually on the outer surfaces and photographed at low magnification, about ×4. The pits were also viewed in longitudinal sections cut approximately through the axes of the specimens. Examination was made at magnifications of ×100 and ×500. Typical micrographs, originally at ×100, have been reduced to ×50; other micrographs, originally at ×500, have been reduced to ×250.

The photographs of the surfaces were made after removal of enough of the general rust layer to reveal the corrosion pits, without removal of the corrosion products from the pits. In some instances, photographs were made after each of several stages of removal of the rust layer.

To insure a correct sectional view of the pits, the polishing of the sections must be done in such a way as to avoid removal of corrosion products. (Removal of part of the corrosion products sometimes cannot be prevented.) The specimens, therefore, were prepared by dry polishing. At an early stage in the polishing, the specimen was mounted in Wood's metal. Each section was ground on a series of emery papers of increasing fineness, and finally with Aloxite 400 paper. It was then rubbed on 00 emery paper (previously somewhat worn) lubricated with graphite from a brush block. It was next polished by means of a revolving disk covered with a good grade of chamois skin, with smooth (hair) side outward. A small quantity of No. 600 emery powder was used on this wheel. The specimen was then transferred to an automatic polishing machine and polished on a disk covered with chamois skin. The polishing powder used in this final stage was magnesium oxide. Practice is necessary to determine the proper length of time in each polishing stage and the proper amount of polishing powder.

III. INFLUENCE OF STRESS CORROSION ON THE FATIGUE LIMIT, AND THE STRESS-TIME-CYCLE RELATIONSHIP FOR CONSTANT NET DAMAGE

1. GENERAL DESCRIPTION OF DIAGRAMS REPRESENTING THE INFLUENCE OF BOTH STRESSLESS CORROSION AND STRESS CORROSION ON THE FATIGUE LIMIT

The influence of both stressless corrosion and stress corrosion on the fatigue limit may be represented by diagrams of the type shown in figures 1 to 4. Abscissas in these diagrams represent durations of corrosion, and ordinates represent the resultant fatigue limits. Most of the experimental points on which the curves are based represent results obtained with the same specimens that have been used in the investigation of the forms and sizes of corrosion pits (sections IV and VI). The upper curve in each diagram represents the influence of stressless corrosion; the other curves represent the influence of simultaneous corrosion and cyclic stress. The numbers adjacent to each curve, and to some of the experimental points, represent the cyclic stress, in thousands of pounds per square inch.

2. INFLUENCE OF STRESSLESS CORROSION ON THE FATIGUE LIMIT

In figures 1 to 3 are curves representing the decrease of the fatigue limits of three steels with duration of stressless corrosion. The curve for each of these steels descends at a decreasing rate and eventually becomes nearly horizontal. Curves of this form, called "retarded damage" curves, have been obtained [10 to 23] with a great variety of carbon steels and ordinary alloy steels in well water, in salt water, and in distilled water. They have also been obtained with aluminum alloys.

Curves of very different form, however, were obtained by stressless corrosion of stainless steels. The curves for stainless steels in well water are horizontal at first, and remain horizontal throughout a long corrosion period (100 to 200 days). Eventually, however, the curves begin to descend, and the slope gradually increases. Curves of this form, called "accelerated damage" curves, were also obtained with monel metal and aluminum bronze. A number of curves of each form have been assembled in a previous paper by the senior author [22] and in a paper by McAdam and Clyne [24].

3. LOWERING OF THE FATIGUE LIMIT BY SIMULTANEOUS CORROSION AND CYCLIC STRESS

Under simultaneous corrosion and cyclic stress, as shown in figures 1 to 3, the lowering of the fatigue limit is more rapid than under stressless corrosion. For a given cycle frequency, the rapidity of descent of a curve increases with the cyclic stress. At 1,450 c/min (fig. 1), stress of only 3,000 lb/in.^{2} causes the curve to descend considerably below the curve representing stressless corrosion; even lower stress (2,000 lb/in.^{2}), as shown in a previous paper [22], has appreciable effect. The effect of these small stresses becomes apparent only after a long corrosion time. The rapidity of the descent is much greater at a stress of

4,000 lb/in.^{2}, and increases greatly with further increase in the cyclic stress.

The influence of cycle frequency on the rate of decrease of the fatigue limit during corrosion may be observed by comparing curves (in figs. 1, 2, 3) obtained with different cycle frequencies but with the same cyclic stress. An example of such comparison is given in figure 4. The curves in this figure represent frequencies ranging from 1,450 to 10 c/min with cycle stress 13,000 lb/in.^{2} Two experimental points, through which no curve is drawn, were obtained with frequency of 1.5 cycle per minute, but with cyclic stresses 20,000 and 25,000 lb/in.^{2}

Comparison of the curves shows that the rapidity of descent below the curve representing stressless corrosion increases greatly with the cycle frequency. A similar relationship may be observed by comparing the curve representing 10 c/min with the positions of the experimental points representing 1.5 c/min. Although the stress was much greater at 1.5 c/min, the decrease in the fatigue limit was more rapid at 10 c/min.

The nearly horizontal portion of the curve representing 1,450 c/min must be attributed to a hardening influence of the cyclic stress on the metal around the growing corrosion pits. Because of increasing "effective stress concentration" (section V), the actual stress around the corrosion pits rises and approaches the fatigue limit from below. Such an approach tends to elevate the fatigue limit of the specimen, and thus opposes the tendency to lowering of the fatigue limit by the growing corrosion pits. At lower cycle frequencies (at this stress), the hardening effect is less rapid, and the removal of metal by growth of the pits tends to keep pace with the local hardening. The curve representing 500 c/min, however, shows some evidence of delayed descent.

4. DIAGRAMS REPRESENTING THE STRESS-TIME-CYCLE RELATIONSHIP FOR CONSTANT NET DAMAGE

From diagrams of the type shown in figures 1, 2, and 3 may be derived diagrams to represent the interrelationship between cyclic stress, cycle frequency, corrosion time, and the resultant net damage. In previous papers by the senior author [16 to 23], numerous diagrams of two types are used to represent this interrelationship, for constant net damage. The constant value of net damage, on which these diagrams are based, is 15 percent. The method of deriving such diagrams is illustrated in figures 1, 2, and 3. The broken line below each curve representing stressless corrosion is drawn so that its ordinates are 85 percent of the corresponding ordinates of the curve representing stressless corrosion. Each broken line, therefore, is the locus of all points representing 15-percent net damage. The coordinates of the intersections of this line with the lines representing stress corrosion consequently may be used in deriving diagrams to represent the relationship between cyclic stress, cycle frequency, and corrosion time, for constant net damage.

In representing this interrelationship in a two-dimensional diagram, one variable in addition to the net damage must be held constant. By this means, two types of two-dimensional diagrams have been derived and utilized in previous papers. In one of these types, cycle

frequency is held constant (in each curve); in the other type, cyclic stress is held constant. Diagrams of these types were obtained with a variety of steels and nonferrous metals. It was found possible [18, 23] to combine all the diagrams of each type for carbon steels and ordinary alloy steels corroded in fresh water, and thus to form a composite diagram of each type. Such diagrams, based on data presented in previous papers, are shown in figures 5 and 6.

In figure 5, ordinates represent cyclic stresses; in figure 6, ordinates represent numbers of cycles. In both figures, abscissas represent corrosion times. The abscissa scales in these figures, however, extend in opposite directions. This arrangement is used so that these diagrams may represent two views of a three-dimensional diagram, in which the vertical coordinates represent cyclic stresses and the horizontal coordinates represent corrosion times and numbers of cycles. Figure 6 thus represents the plan view of the three-dimensional diagram, and figure 5 represents a view in the direction indicated by the arrow in figure 6. The curves in figure 6, consequently, may be viewed as contour lines, and the graphs in figure 5 may be viewed as sloping lines, on the surface of a three-dimensional diagram.

Each of the experimental points in figure 5 represents a result obtained with one of the steels indicated in the legend. To avoid too much crowding, the graphs have been separated in figures 5 (*A*) and 5 (*B*) by shifting the abscissa scales as indicated. The graphs thus established have been assembled to form the diagram in figure 5 (*C*).

In the absence of cyclic stress, corrosion pitting is known to be about the same for all steels of these types in fresh water [24]. The fact that a single diagram can be used to represent constant net damage for all these steels (fig. 5) suggests that the influence of cyclic stress on corrosion pitting in fresh water is practically unaffected by variations in composition, heat treatment, or mechanical properties.[2]

The relationship between cyclic stress and corrosion time for constant net damage, as illustrated by the graphs in figure 5 and in previous papers [18 to 23], is approximately a straight-line logarithmic relationship. The slope of a graph evidently decreases slightly with decrease in cycle frequency. The straight-line logarithmic relationship means that the corrosion time required for constant net damage varies inversely as a power of the cyclic stress. As the average rate of net damage varies inversely as the total corrosion time, the average rate evidently varies directly as a power of the stress. This relationship may be represented by the following equation, which has been discussed in previous papers [19 to 23]:

$$R = CS^n.$$

In this equation, R represents the (average) rate of net damage, S represents the cyclic stress, and n represents the cotangent of the angle of slope of the graph (fig. 5). The coefficient C represents the horizontal position of the graph in the diagram (the abscissa at a given ordinate); it depends on the intensity of the corrosion and on the cycle frequency.

[2] Provided that alloying elements are not present in sufficient percentages to cause important increase in corrosion resistance.

For steels in well water with free access of air, as illustrated by the graphs in figure 5, n ranges from about 2.8 to 3.5. A different kind of water, such as distilled water [23], or a different kind of metal [21], may give a diagram very different from those in figures 5 and 6.

IV. PITS FORMED BY STRESSLESS CORROSION

1. SURFACE VIEWS OF SPECIMENS AFTER STRESSLESS CORROSION

Photographs of the surfaces of specimens were made at magnification of about ×4. The size of the photographic prints, 8 by 10 in., was sufficient to include all of the tapered part of each specimen. Typical portions of many of these photographs have been included in this paper. Figures 7 and 8 show surfaces of specimens that have been corroded without stress. Each photograph includes practically the entire width of a specimen. The vertical direction in each photograph represents the longitudinal direction on the surface of a specimen. As the photograph shows a curved surface, the view is oblique except at the center, and the obliquity increases from the center toward the right and left edges. This should be kept in mind in studying the forms, sizes, and distribution of corrosion pits.

The views in figures 7 and 8 are arranged in the order of increasing corrosion time, and without regard for the composition of the steel. After 2 days' corrosion (fig. 7, *A*), the pits are just beginning to appear as small round spots. After 4.7 and 5.8 days (fig. 7, *B* and *C*), the pits have grown considerably and are still round.[3] After 10 days (fig. 7, *D*), the pits are much larger; some of the pits now are slightly elongated, and a few adjacent pits have grown together. After 50 and 59 days (fig. 7, *E* and *F*), the pits have increased greatly in size, and occupy a large proportion of the surface. The pitting now appears in two shades, depending on the depth of pitting. The darker shade is in round pits, either on the surface or within the boundaries of larger pits of lighter shade. Several of the dark round spots can be seen within many of the lighter areas; these spots are larger than those found after corrosion for only 10 days (fig. 7, *D*). The pits evidently have grown by lateral extension, involving the merging of many of the originally round pits. The depth of the pits will be considered later.

With further increase in corrosion time, as shown in figure 8 (69 to 300 days), the pits continued to grow, but much less rapidly than during the first 50 days. Although the growth was largely by lateral extension, involving the merging of originally round pits, a few round pits are still visible both on the surface and within the larger, lighter pits. These relatively deep, round pits are conspicuous in figure 8 (*A*, *D*, and *F*) They are generally larger than the round pits found after 50 and 59 days (fig. 7, *E* and *F*).

2 LONGITUDINAL SECTIONS SHOWING PITS CAUSED BY STRESSLESS CORROSION

In figures 9 and 10 at a magnification of ×50, and in figure 33 at a magnification of ×250, are micrographs of longitudinal sections showing pits caused by stressless corrosion. The Wood's metal in which the specimen is mounted appears at the left of each photograph.

[3] The word "round" here refers to the surface view, not to the three-dimensional form.

Corrosion products appear in all the pits. Although part of the corrosion products has been detached from some of the pits during examination of the outer surface, enough of these products are present to ensure that the photographs give the true forms of the pits. In each figure the photographs are arranged in order of increasing corrosion time and without regard to the composition of the steel.

It should be kept in mind that the sections shown in these micrographs do not pass through the centers of all the visible corrosion pits. An attempt has been made, however, to make each section pass approximately through the center of at least one pit. The micrographs shown have been selected from several micrographs (often five or more) of each section, and each section is represented (figs. 9 and 10) by either two separate micrographs or by a longer continuous micrograph. In studying the forms and sizes of the corrosion pits, frequent reference should be made to the surface views (figs. 7 and 8). Not all the specimens represented in figures 9 and 10, however, are shown in figures 7 and 8, and one specimen shown in a surface view (fig. 7, *C*) is not shown in a sectional view. Nevertheless, comparison can be made between complementary views of specimens corroded for approximately equal times.

Sections through many of the pits that appear roughly circular in the surface views (figs. 7 and 8) appear roughly semicircular in figures 9 and 10. Examples of this may be seen by comparing the micrographs listed below.

	Appearance	
Corrosion time	Circular	Semicircular
Days		
2	7 (*A*)	9 (*A*)
4. 7	7 (*B*)	9 (*C*)
47 to 50	7 (*E*)	9 (*E*), 9 (*F*)
100	8 (*C*)	10 (*B*)

This evidence, supplemented by evidence found in other surface and sectional views still to be discussed, indicates that a large proportion of the pits are roughly hemispherical. Some roughly hemispherical pits are found even after other pits in the same specimen have extended laterally and merged. (Compare figs. 7, *E*, and 8, *C*, with figs. 9, *E* and *F*, and 10, *B*.) Even in early stages of corrosion, however, some of the pits are saucerlike rather than hemispherical. This is illustrated in micrographs *B*, *C*, and *D* of figure 9. In later stages, owing to the lateral extension of the pits, the saucerlike form predominates. Even after the merging of the pits, as illustrated in micrographs *G* and *H* of figure 9 and micrographs *A*, *E*, and *F* of figure 10, the bottoms of the merged pits generally consist of numerous saucers. The shape of the saucers changes little with increase in corrosion time from about 50 to 300 days.

After corrosion for 50 days or more, small salients are visible, projecting into the metal from many of the corrosion pits (figs. 9 and 10). Even after 10 days' corrosion, smaller projections are visible at a magnification of ×250 (fig. 33, *C*). These rootlike projections are due to the influence of oxygen concentration cells, which will be discussed later.

The size of the pits increases greatly during the first few days of corrosion. This is seen both in the surface views (*A* to *D*, inclusive, of fig. 7) and in the longitudinal sections (micrographs *A* to *D* of fig. 9).[4] With increase in corrosion time beyond 10 days, the increase in (relative) size of the corrosion pits is slower; nevertheless, the growth is considerable between about 50 and 100 days. (Compare figs. 9, *E* and *F*, with fig. 10, *B*). Beyond 100 days, the depth evidently increases little, but the breadth increases, largely by the merging of adjacent pits. Under stressless corrosion in well water, therefore, the increase in breadth eventually tends to be greater than the increase in depth.

No evidence is found that the differences in composition have had any important effect on the form or size of the corrosion pits. This relationship confirms the previously mentioned evidence (section III–4) that pitting under stressless corrosion is practically unaffected by variations in the composition or mechanical properties of the steels.

V. INFLUENCE OF FORM, SIZE, AND DISTRIBUTION OF CORROSION PITS ON EFFECTIVE STRESS CONCENTRATION

1. FACTORS INVOLVED IN EFFECTIVE STRESS CONCENTRATION

The lowering of the fatigue limit, represented by a curve in figures 1, 2, and 3, must be attributed to stress concentration around corrosion pits. Because of stress concentration, the actual stress around a pit may be above the fatigue limit, when the nominal stress (estimated from the applied load and the dimensions of the specimen) is much less. Stress concentration, therefore, must be considered in any attempt to correlate the forms and sizes of corrosion pits with the lowering of the fatigue limit.

The effective stress-concentration factor due to a corrosion pit or other notch may be denoted by the ratio of the fatigue limit of an unnotched specimen to the fatigue limit of the notched specimen. The effective stress-concentration factor (K_F) depends on the metal, on the theoretical stress-concentration factor (K), and on the size of the notch. The theoretical stress-concentration factor, however, depends entirely on the form and relative size of the notch (size of the notch in relation to the size of the specimen). When the notch is small in relation to the size of the specimen, the theoretical stress concentration depends almost entirely on the form of the notch.

Theoretical stress-concentration factors are based on the mathematical theory of elasticity.

---

[4] After 4 days' corrosion, the pits in figure 9 appear only slightly larger than in the section made after 2 days (fig. 9, *A*) and much smaller than in the section made after 4.7 days (fig. 9, *C*). The section made after 4 days, however, probably either does not pass through the centers of the pits or does not show representative pits.

2. THEORETICAL STRESS CONCENTRATION DUE TO CORROSION PITS

Although the theoretical stress-concentration factor (K) due to corrosion pits cannot be estimated exactly, an approximate estimate can be made of the minimum value, and of the probable range of significant values. In such estimation, attention will be confined to values obtainable with pits caused by prior stressless corrosion. As the pits during the first few days of stressless corrosion are approximately hemispherical, the simplest approach to a study of the theoretical stress concentration is made by assuming that all the pits are modifications of smooth hemispherical cavities.

No investigation apparently has been made of the theoretical stress-concentration factor due to a hemispherical cavity. The stress-concentration factor for such a cavity, however, probably is about the same as the factor for a spherical cavity. This conclusion is based on analogous relationship for other forms of notch. The theoretical stress-concentration factor for a semicircular notch at the edge of a plate, or for a semicircular groove in a cylinder, has been found to be practically the same as the stress-concentration factor for a circular hole in a plate. Information as to the stress-concentration factor for a hemispherical cavity, therefore, can be derived from results of investigation of the theoretical stress concentration around a spherical cavity.

Leon [8] found that the maximum stress concentration around a spherical cavity, in a solid subjected to one principal stress, is at the equator. (The polar axis is assumed to be in the direction of the principal tensile or compressive stress.) The stress-concentration factor, for a range of Poisson's ratio (σ) between 1/4 and 1/3, was found to range between 2.02 and 2.08. Southwell and Gough [26] obtained numerical values in good agreement with those of Leon [8], with whose work they evidently were unacquainted. Their formula for the stress-concentration factor is $(27-15\sigma)/(14-10\sigma)$. For values of σ ranging between 1/4 and 1/3, this formula gives stress-concentration factors ranging between 2.02 and 2.06.

Goodier [2] obtained the same formula that was obtained by Southwell and Gough. He also studied mathematically the general problem of the stress concentration due to spherical inclusions, as affected by variation of Poisson's ratio and the modulus of elasticity. When a spherical inclusion is less rigid than the surrounding metal, the stress distribution is qualitatively similar to that around a spherical cavity. Around a slag inclusion, the stress concentration was found to be only about 20 percent less than that around a spherical cavity. As the corrosion products in a pit are porous enough to permit diffusion of the aqueous solution during corrosion, the stress-concentration factor due to a hemispherical pit containing corrosion products probably is not appreciably less than that due to a hemispherical cavity. The theoretical stress-concentration factor for a hemispherical corrosion pit, therefore, probably is about 2.

For a pitted specimen, however, the theoretical stress-concentration factor is not the mean of the stress-concentration factors for the individual pits, but is the factor for the pit whose size and form cause the highest effective stress concentration (K_p). Although many of the pits are not far from hemispherical, the pit giving the highest

theoretical stress-concentration factor probably has less resemblance to a hemisphere than to an oblate hemispheroid or to a hemiellipsoid of revolution, whose axis of revolution is the minor axis of an ellipse and is in the direction of the principal stress. Consideration, therefore, must be given to the theoretical-stress concentration around pits of this form.

The stress concentration due to ellipsoids of revolution has been investigated by Neuber [25]. His results may be represented by a curve, with abscissas denoting the eccentricity (a/b) of the ellipsoid, and with ordinates denoting the corresponding values of K. In the ratio a/b, a and b represent the major and minor semiaxes, respectively, of the elemental ellipse. When a/b is 1.0, the cavity is spherical, and Neuber's value for K is about the same as the value obtained by Leon [8], Southwell and Gough [26], and Goodier [2]. When the eccentricity ratio is 1.7, which probably is about the maximum for pits formed during the first days of corrosion, K is about 3. With further increase in the eccentricity, K continues to increase rapidly; values of 3 and 5 for a/b give values of about 5 and 7, respectively, for K. Some of the pits formed under stress corrosion (section VI), have eccentricity ratios even higher than these.

Even in the early stages of stressless corrosion, however, the pits are not entirely smooth. With growth of the pits, projections appear on the boundaries. Some of these are blunt, others are root-like or roughly conical. Consideration, therefore, must be given to the influence of these projections on the theoretical stress concentration. Although no direct investigation has been made of the effect of such projections, an idea of the effect may be obtained from results of investigation of an analogous relationship for a hole in an infinite plate. Inglis [7] has shown that the theoretical stress-concentration factor for a circular hole with a semicircular notch at its edge is the product of the separate factors for the hole and notch. Although such a relationship may not apply quantitatively to the three-dimensional stress concentration caused by a spherical or conical projection at the bottom of a hemispherical pit, it probably applies at least qualitatively. For a hemispherical pit with a much smaller hemispherical projection, consequently, the theoretical stress-concentration factor may be about 4. For a sharp conical projection, the theoretical stress-concentration factor may be somewhat higher.

Multiplication of the two separate factors to obtain the factor for the combination, as shown by Inglis [7], applies only when the projection is small enough to be contained within the very small region of high stress concentration around the larger notch or hole. With increase in the relative size of the projection, the theoretical stress-concentration factor for the combination falls rapidly.

With the first appearance of nearly hemispherical corrosion pits, therefore, the theoretical stress-concentration factor probably is not less than 2, and may become about 3 during the first few days of stressless corrosion. The factor tends to become still higher, with the appearance and growth of projections on the boundaries of the pits. This tendency, however, is opposed by the tendency of the stress-concentration factor to decrease with increase in the relative size of the projections. It is also opposed by the tendency of the pits to change from hemispherical to saucer-like form.

The stress concentration around a pit may also be influenced by the nearness of another pit. If the line of centers of two pits (near together) is in the direction of the principal stress, each pit has a shielding effect on the other and the stress concentration is less than if the pits were far apart. If the line of centers is in the transverse direction, the stress concentration is greater than if the pits were far apart. Instances of this effect of distribution of pits will be mentioned in section VI.

3. INFLUENCE OF SIZE, AND OF THE STEEPNESS OF THE STRESS GRADIENT, ON EFFECTIVE STRESS CONCENTRATION

That the size of a notch has great influence on the effective stress-concentration factor (K_F) has been established by a number of investigations. It is possible to mention only one of these. The influence of small, relatively deep scratches and other small grooves has been investigated by Thomas [28]. The grooves were classified in two series, differing in size and in the method of formation. The smaller grooves ranged in depth from 0.00058 to 0.00244 in.; the larger grooves ranged from 0.0050 to 0.0448 in. The depth of each groove and the root radius were determined by microscopical examination of sections of gelatin casts. For each groove, therefore, an estimate could be made of the value of K.

The values of K, with allowance for the influence of the relative depth, ranged from 3.2 to 6.3 for the smaller grooves, and from 3.2 to 4.05 for the larger grooves. The corresponding values for the effective stress-concentration factor (K_F) ranged from 1.16 to 1.41 for the smaller grooves, and from 1.37 to 2.07 for the larger grooves. The discrepancy between corresponding values of K and K_F evidently increased with the decrease in the size of the groove. This discrepancy, therefore, must be attributed mainly to the influence of absolute size. The lowest value (1.16) of K_F differs little from the value (1.0) for an unnotched specimen. Results obtained by Thomas [28] with scratches caused by emery led him to the conclusion that the effect of even a sharp groove is negligible, if the depth is no more than about 0.0001 in.

In previous discussion, the influence of the theoretical stress concentration and of the size of the notch on the fatigue limit have been treated (in the conventional way) as if they were independent. Evidence obtained by a number of investigators, however, indicates that the effect of size on the fatigue limit increases with the theoretical stress-concentration factor. It has already been shown, moreover, that the effect of the theoretical stress-concentration factor decreases with the size of the notch. This interrelationship is due to the combined influence of the theoretical stress-concentration factor and absolute size on the steepness of the stress gradient.

The theoretical stress gradient around a circular hole is invariant with size, if distances from the hole are expressed in terms of the radius. If distances are expressed in absolute units, however, the steepness of the gradient evidently increases with decrease in the absolute size of the hole. The steepness of the stress gradient, therefore, varies directly with K and inversely with the size of the notch. A suitable index of steepness of the gradient, consequently, would have as numerator an index of the range of stress in the gradient,

and as denominator an index of notch size. An index proposed by the authors is derived by representing the approximate stress range of the gradient by $K-1$, and the size of the notch by the root radius (r). This index, therefore, is $(K-1)/r$.

The available evidence indicates that the discrepancy between K and K_F tends to increase with the steepness of the stress gradient. The fracture of a metal, either by single or repeated loading, apparently is not determined by the highest stress in the theoretical gradient (at a geometrical line), but by the mean stress over an appreciable width of the gradient. The steeper the gradient, therefore, the greater is the difference between this mean stress and the highest stress of the theoretical gradient, and the greater is the difference between K and K_F. The gradient may even be so steep and narrow that the stress peak has practically no effect on the fatigue limit. (Space is not available for discussing the reasons for this behavior of metals.)

Although a sharp projection on a corrosion pit may cause a very high value of K, this value is associated with a very low value of r. Such a projection, therefore, gives a very high value of $(K-1)/r$, the index of steepness of the stress gradient. The sharp projection evidently superposes a very steep, narrow gradient on the broader, less steep gradient induced by the general form of the pit. The stress peaks at such projections may be so sharp that they have no important effect on the fatigue limit. Consequently, when a projection is very small in relation to the size of a corrosion pit, the only significant value of the theoretical stress-concentration factor is that based on the general form of the pit.

4. EFFECTIVE STRESS-CONCENTRATION FACTOR FOR SPECIMENS PREVIOUSLY CORRODED WITHOUT STRESS

The influence of prior corrosion time on the effective stress-concentration factor may be studied by means of the values of K_F obtained from the stressless corrosion curves in figures 1, 2, and 3. With increase in prior corrosion time, K_F evidently increases rapidly during the first few days of corrosion. The rate of increase of K_F, however, decreases with time, and eventually becomes small. The course of each curve appears to indicate that K_F approaches an asymptotic value of about 2. As shown in a paper by McAdam and Clyne [24], however, K_F tends to increase with the hardness of the steel. The curves presented in that paper suggest that, with increase in the hardness of the steel and with increase in corrosion time, K_F approaches an asymptotic value of 3 or 4.

As the theoretical stress-concentration factor for the pits formed during the first few days of corrosion may be as high as 3, and as the asymptotic value of K_F apparently is not much higher, the evidence indicates that the course of the stressless corrosion curves in figures 1, 2, and 3 is due chiefly to increase in the size of the corrosion pits. The tendency toward increase of K due to the formation of projections on corrosion pits probably is nearly counterbalanced by the tendency toward decrease of K with change of pits from roughly hemispherical to saucer-like form.

VI. PITTING UNDER SIMULTANEOUS CORROSION AND CYCLIC STRESS, AND ITS CORRELATION WITH NET DAMAGE

1. PITTING WITH FREQUENCY OF 1,450 CYCLES PER MINUTE

In studying the influence of cyclic stress (during corrosion) on the forms and sizes of corrosion pits, comparison will be made between surface views and longitudinal sections of corroded specimens, and between specimens corroded with and without cyclic stress. Attention will be given first to specimens that have been subjected to stress corrosion with frequency of 1,450 cycles per minute. Typical portions of the surfaces of these specimens, at a magnification of $\times 4$, are shown in figures 11 and 12; typical sectional views are shown in figures 13 and 14. In each of these figures are views of specimens that have been corroded at 1,450 c/min but under different cyclic stresses and for different times. Comparison of the views in each figure, therefore, reveals the influence of both cyclic stress and corrosion time, with constant cycle frequency. The views in each figure are arranged primarily in the order of decreasing cyclic stress, secondarily in the order of increasing corrosion time, and without regard to the composition of the steel. The vertical direction in each view represents the longitudinal direction of the specimen. Below each figure are listed, for each view, the cyclic stress, the corrosion time, and the symbol for the steel.

In the surface views (figs. 11 and 12), some pits appear round, like the pits caused by stressless corrosion. Other pits consist of round or broad irregular cavities apparently crossed by transverse cracks.[5] The corresponding sectional views at higher magnification (figs. 13 and 14), however, show that these are not cracks but are sharp, deep corrosion pits; they are filled with corrosion products similar to those found in round pits. The sharp, deep pits are found at the high-stress end of the series of views (figs. 11, 12, 13, and 14); at the low-stress end of the series, the pits are entirely of the rounded form. The magnitude of the stress, therefore, is one of the factors determining whether or not the sharp projections shall be formed. Another factor, as will be shown, is the corrosion time.

The first stages of development of projections of this form, however, cannot be determined by examination of surface views, especially at low magnification. Even when such projections do not appear on the surface, an examination of a longitudinal section may reveal sharp, wedge-shaped projections extending inward from rounded pits. Instances of this kind will be mentioned in detailed discussion of the photographs. In future discussion, the sharp, transversely extended pits visible in surface views will be called fissures. The less advanced, wedge-shaped pits not visible on the surface will be called crevices. A crevice and a fissure thus differ only in degree.

To show clearly the influence of stress on the development of fissures, the effect of varying stress should be studied with constant corrosion time. Such a study may be made by comparing the six surface views (figs. 11 and 12) representing the effects of different cyclic stresses acting during the same corrosion time, 10 days. These

[5] Transverse to the direction of principal tensile stress in the specimen.

six views (*A*, *C*, *E*, and *F* of fig. 11 and *A* and *B* of fig. 12) represent the effects of cyclic stresses ranging from 15,000 to 8,000 lb/in.^{2} In the view representing stress of 8,000 lb/in.^{2} (fig. 12, *B*), the corrosion pits appear round, like pits caused by stressless corrosion. In the other five views, representing stresses ranging from 15,000 to 9,000 lb/in.^{2}, round or irregularly extended pits are traversed by fissures. Fissures evidently do not appear during 10 days' corrosion at 1,450 c/min, when the cyclic stress is less than about 9,000 lb/in.^{2}

The influence of cyclic stress on the development of fissures and crevices is similarly revealed by comparison of nine sectional views (figs. 13 and 14), most of which correspond to surface views in figures 11 and 12. These sectional views (*A*, *D*, *F*, *G*, and *I* of fig. 13 and *C*, *E*, *G*, and *I* of fig. 14) represent specimens that have been corroded under stresses ranging from 15,000 to 5,000 lb/in.^{2}, with constant corrosion time, 10 days.[6] The sectional views of specimens corroded under cyclic stresses of 9,000 lb/in.^{2} or more show sharp, wedge-shaped pits, which evidently are sections of fissures such as those seen in surface views (figs. 11 and 12). The sectional views of specimens corroded at 8,000 lb/in.^{2} or less show only rounded pits, like those caused by stressless corrosion. Comparison of both surface views and sectional views, therefore, leads to the conclusion that the limiting stress above which fissures develop (during 10 days' corrosion at 1,450 c/min) is 8,000 lb/in.^{2}

There is evidence, however, that some crevices may have appeared during 10 days' corrosion at 8,000 lb/in.^{2} Although the specimen corroded for 10 days at this stress shows no crevices (fig. 14, *C*), another specimen corroded at the same stress for only 4 days (fig. 14, *B*) shows sharp inward projections from rounded corrosion pits. As these projections are filled with adherent corrosion products, they evidently are sections of crevices. Similar crevices, therefore, may have formed beneath some of the rounded pits in the specimen that was corroded at the same stress for 10 days. Another specimen corroded at the same stress for 24 days (fig. 14, *D*) shows typical sections of transverse fissures. In specimens corroded at stresses less than 8,000 lb/in.^{2}, no fissures or crevices are visible in either surface views or longitudinal sections, even after corrosion for much longer than 10 days (views *C* to *F*, inclusive, of fig. 12 and views *E* to *K*, inclusive, of fig. 14).

At sufficiently high stress, tranverses fissures appear after corrosion for much less than 10 days. This is illustrated by surface views *B* and *D* of figure 11 and by sectional views *B* and *C* of figure 13. After corrosion at 11,000 lb/in.^{2} for 3 days, the surface view (fig. 11, *D*) shows short transverse fissures extending from a few of the rounded pits. The longitudinal section (fig. 13, *E*), however, does not cut any of these fissures but shows only rounded pits.

Although some of the sectional views of fissures (figs. 13 and 14) show the rounded pits from which the fissures started, a few sections of fissures do not show rounded origins. Absence of rounded pits in sections of fissures, however, does not mean that the fissures started inward directly from the surface. All the fissures, as shown in the surface views, have started at rounded corrosion pits and have

[6] In specimens that had been subjected to fatigue test after the corrosion stage, the pits did not differ in appearance from those in specimens that had not been subjected to fatigue test.

extended both transversely and inward. Some of the sections in figures 13 and 14 are nearly at the centers, and some are at the edges of the rounded origins of fissures. Others are at a distance from these origins.

The influence of corrosion time on the forms of corrosion pits is revealed also by comparison of views obtained after corrosion at 9,000 lb/in.^{2} for 4, 10, and 50 days. After corrosion for 4 days, only round pits are visible on the surface (not shown) and no fissures or crevices are found in a sectional view (view *H* of fig. 13). Corrosion for 10 days, as already shown (view *A* of fig. 12 and view *I* of fig. 13), has caused long, deep fissures. After 50 days at the same stress (view *A* of fig. 14), the fissures are deeper and have broadened greatly at the surface.

The evidence in figures 11, 12, 13, and 14, therefore, indicates that stress-corrosion pits in steel corroded in fresh water are merely modifications of pits formed by stressless corrosion. The number of pits per unit area and their distribution, consequently, are determined by the same uncontrollable variables that determine the number and distribution of pits formed by stressless corrosion. Great differences may be found in the number and distribution of these anodic regions after apparently identical corrosion conditions. The size of the pits, moreover, generally varies inversely with the number. Occasional mention will be made of typical instances of such variation in number, size, and distribution of pits.

The fissured pits (figs. 11, 12, 13, and 14) generally are much larger than pits formed in corresponding times by stressless corrosion (figs. 7, 8, 9, and 10). Cyclic stress evidently tends to increase the size of corrosion pits. This effect of cyclic stress on the rate of corrosion, moreover, evidently tends to be greatest at the equator of a roughly hemispherical corrosion pit. The tendency to form sharp equatorial fissures may be attributed to the fact, mentioned by Southwell and Gough [26], that nearly all the concentration of stress is in a narrow equatorial ring. With development of a fissure, this stress concentration is intensified. The influence of stress concentration on the rate of corrosion is discussed further in section VII.

To facilitate comparison between the corrosion pits (shown in figs. 11, 12, and following figures) and the corresponding net damage, the forms of the corrosion pits are classified by means of the symbols used to designate the experimental points in figures 1 to 4. Different symbols are used to designate fissures, crevices, and rounded pits. The fissures caused by corrosion for 10 days at stresses ranging from 13,000 to 9,000 lb/in.^{2} (views *C*, *E*, and *F* of fig. 11, and *A* of fig. 12) have lowered the fatigue limit from 64,000 lb/in.^{2} to values ranging between 24,000 and 26,000 lb/in.^{2} These values are far below the fatigue limit (44,000 lb/in.^{2}) that would be found after 10 days' corrosion without stress. The net damage caused by crevices tends to be intermediate between the damage caused by fissures and that caused by rounded pits. Considerable net damage may be caused by stress corrosion even in the absence of fissures or crevices. This is illustrated by the positions of the points representing effects of corrosion for 10 days at stresses less than 8,000 lb/in.^{2}

2. PITTING WITH FREQUENCY OF 500 CYCLES PER MINUTE

Surface views of specimens corroded with frequency of 500 cycles per minute are shown in figure 15, and sectional views are shown in figures 16 and 33.

This series, unlike the series obtained at 1,450 c/min, is not well adapted to reveal the effect of varying the cyclic stress with constant corrosion time. The limiting stress above which fissures appear within a given corrosion time, however, evidently is higher at 500 than at 1,450 c/min. Whereas corrosion at 1,450 c/min at 9,000 lb/in.^{2} for 10 days (fig. 12, *A*) has caused long transverse fissures, corrosion at 500 c/min at 9,000 lb/in.^{2} for 9 days has caused rounded pits with no evidence of fissures or crevices (figs. 15, *E*, and 16, *E*). Corrosion at 13,000 lb/in.^{2} for 15 days at 500 c/min, moreover, has caused only a few short fissures (fig. 15, *B*).

After corrosion at 14,000 lb/in.^{2} for 4 days (fig. 15, *A*), nearly all the pits appear round. Some of the pits, however, have merged so as to form rounded transversely elongated pits. Short transverse fissures, moreover, have started at a few of the rounded pits. A sectional view of typical fissured pits is shown in figure 16 (*A*). The theoretical stress-concentration factor for these sharp fissures is very high. Because of their small size, however, the effective stress-concentration factor (obtained from fig. 3) is only about 2.

The influence of corrosion time on the development of transverse fissures is revealed by a comparison of the surface views of specimens corroded at 13,000 lb/in.^{2} for 15 days and 45 days, respectively (views *B* and *C* of fig. 15). With increase in the corrosion time from 15 to 45 days, the fissures have increased greatly in number and length and have broadened at the surface. The increase of net damage with the development of these fissures is represented by the corresponding curve in figure 1.

Corrosion at 12,000 lb/in.^{2} for 4 days, at 10,000 lb/in.^{2} for 6 days, at 9,000 lb/in.^{2} for 9 days, and at 8,000 lb/in.^{2} for 10 days, as shown in figures 15, 16, and 33, has caused neither fissures nor crevices. (Some of these specimens are not shown in both surface and sectional views.) After corrosion at 8,000 lb/in.^{2} for 25 days, the surface view (not shown) reveals only rounded pits, some of them surrounded by shallower, broad corroded areas. The sectional view (fig 16, *G*), however, shows sharp crevices extending inward from some of the rounded pits. After corrosion at the same stress for 33 days, the surface view (fig. 15, *F*) shows no evidence of transverse fissures, and a longitudinal section (fig. 33, *E*) shows no crevices. The sectional view shows a tendency of corrosion pits to extend by burrowing along the surface. Such salients may appear whether or not the specimen is under cyclic stress. The considerable net damage caused by the pitting of this specimen probably is due to one or more large pits, such as those shown in figure 15 (*F*).

After corrosion at 7,000 lb/in.^{2} for 19 days, no fissures are visible in the surface view (not shown) but a sectional view (fig. 16, *H*) reveals a crevice extending inward from a rounded pit. Crevices such as this may account for the net damage shown in figure 1.

Considerable net damage, as shown in figures 1 and 3, is caused by the rounded stress-corrosion pits. Reasons for this may be found by comparing surface views in figure 15 with surface views of speci-

mens corroded for corresponding times without stress (figs. 7, and 8). Cyclic stress (during corrosion) evidently tends to increase the size of the rounded pits, especially of a few of the pits in each specimen. This is illustrated by views *B* and *F* of figure 15. Cyclic stress thus tends to increase not only the mean size but also the range of size of corrosion pits.

3. PITTING WITH FREQUENCY OF 100 CYCLES PER MINUTE

Surface views of specimens corroded with frequency of 100 cycles per minute are shown in figure 17, and longitudinal sections are shown in figures 18 and 33. Photographs of surface views corresponding to sectional views *H* to *K*, inclusive, of figure 18 are not included in this paper.

At the high-stress end of the series of views, fissures have started from some of the rounded pits. These fissures are shown in views *A*, *B*, *D*, and *E* of figure 17 and in views *A*, *B*, *C*, and *F* of figure 18. The limiting stress below which fissures or crevices do not appear during a given corrosion time is much higher at 100 c/min than at 500 or 1,450 c/min. The limiting stress for about 10 days' corrosion time may be found by comparing view *F* of figure 17 with views *G* and *H* of figure 18. After corrosion at 13,000 lb/in.^{2} for 9 days, the surface view (fig. 17, F) shows no clear evidence of fissures, although the contour of a few of the pits (as seen with a lens) suggests that fissures may be starting. The sectional view (fig. 18, *G*), however, shows deep crevices. After corrosion at 12,000 lb/in.^{2} for 11 days, no fissures appear in the surface view (not shown) and no crevices appear in the sectional view (fig. 18, *H*). During about 10 days' corrosion at 100 c/min, therefore, transverse fissures or crevices evidently do not appear unless the stress is more than about 12,000 lb/in.^{2} This limiting stress is about 50 percent greater than the corresponding stress for 10 days' corrosion at 1,450 c/min (sec. VI–1).

The influence of corrosion time on the development of fissures is illustrated by views *C* and *D* of figure 17, view *D* of figure 18, and view *F* of figure 33. After corrosion for 3.5 days at 20,000 lb/in.^{2} (figs. 17, *C* and 18, *D*), no fissures or crevices are visible. After 4.5 days at the same stress, the surface view (fig. 17, *D*) shows short transverse fissures traversing a few of the rounded pits and a longitudinal section (fig. 33, *F*) shows a crevice. The corresponding curve in figure 1 shows a rapid increase of net damage with corrosion at this stress.

As no crevices were found after corrosion at 12,000 lb/in.^{2} for 11 days (fig. 18, *H*),no crevices would be expected after corrosion at 11,000 lb./in.^{2} for only 3 days longer. Although the surface view of the specimen corroded at 11,000 lb/in.^{2} for 14 days shows only rounded pits, however, a sectional view (fig. 18, *I*) shows a thin crevice. The early development of crevices in this specimen, and the resultant disproportionally rapid net damage represented by the corresponding curve in figure 1, probably are due to the previously mentioned uncontrollable variables affecting the number and distribution of corrosion pits. Another instance of the influence of these variables may be found by comparing the number of corrosion pits in view *E* of figure 17 with the numbers in the other views of this figure. Because of the relatively small number and consequent relatively large size

of the pits shown in view *E*, the net damage (fig. 1) is disproportionally large.

The influence of crevices on net damage, as shown in figure 1, tends to be intermediate between the influences of fissures and rounded stress-corrosion pits. This fact indicates that thin inward projections from pits in figure 18 are sections of crevices and not of root-like projections, which sometimes are formed under the influence of oxygen concentration cells. Sharp root-like projections cause much less net damage than thin transverse crevices.

Considerable net damage, as shown in figures 1 and 3, may be caused by rounded stress-corrosion pits. Probable reasons for this may be found in figures 17 and 18. In views *A*, *B*, *C*, and *D*, which show results of corrosion at high stresses for a few days, the size of at least a few of the rounded pits is much greater than that of pits caused by corrosion for corresponding times without stress. The evidence indicates that cyclic stress tends to increase the size of both fissured and rounded pits. This influence of cyclic stress on the size of pits probably accounts for the net damage caused by the rounded stress-corrosion pits. This effect, however, may be accentuated by the transverse merging of rounded pits.

4. PITTING WITH FREQUENCY OF 50 CYCLES PER MINUTE

Surface views of specimens corroded with frequency of 50 cycles per minute are shown in figures 19, 20, and 21; sectional views are shown in figures 22, 23, and 34.

Transverse fissures, some just starting and others far advanced, are visible in the surface views of specimens corroded under cyclic stresses of 15,000 lb/in.^{2} or higher. They are visible in all the views of figure 19 and in all the views of figure 20 except view *E*, which represents results of corrosion at 15,000 lb/in.^{2} for 17 days. Although view *E* shows no clear evidence of fissures, some pits have merged transversely and a few show indications of incipient fissures. After corrosion at the same stress for 24.5 days (fig. 20, *F*), transverse merging has proceeded further than in view *E* and transverse fissures are clearly visible.

In the series of sectional views (figs. 22 and 23), some sections are shown for which no corresponding surface views are shown in figures 19, 20, or 21. Comparison of the series of sectional views with the series of surface views leads to the conclusion that the limiting stress below which no fissures or crevices appear during 10 days' corrosion is about 15,000 lb/in^2. After corrosion at 16,000 lb/in.^{2} for 4 days, no fissures are found in the surface view (not shown) and no crevices are found in a sectional view (fig. 23, *D*). After corrosion at the same stress for 9 days, no fissures are found in the surface view (not shown) but a crevice is found in a longitudinal section (fig. 23, *E*). As fissures have just started after corrosion at 15,000 lb/in.^{2} for 17 days (fig. 20, *E*), and as no crevices are found in the sectional view (fig. 23, *F*), no fissures or crevices probably would appear during 10 days at this stress. No fissures are found in the specimens corroded at stresses less than 15,000 lb/in.^{2}, although the corrosion times were much longer than 10 days. Crevices, however, are found in the specimens corroded at 13,000 lb/in.^{2} for 20 days (fig. 23, *H*) and 34 days (not shown).

The limiting stress (15,000 lb/in.^{2}), therefore, is about 25 percent higher at this frequency than at 100 c/min (12,000 lb/in.^{2}) and is nearly twice as high as at 1,450 c/min (8,000 lb/in.^{2}).

The influence of corrosion time on the development of fissures is illustrated by the surface views of specimens after corrosion at 30,000 lb/in.^{2} for 5, 6, and 8 days (views *C*, *D*, and *E* of fig. 19) and after corrosion at 25,000 lb/in.^{2} for 4, 6, 7, and 9 days (view *F* of fig. 19 and views *A*, *B*, and *C* of fig. 20). In the first view of each of these series, short fissures traverse a few of the rounded pits. With increase in corrosion time, the number of rounded pits so traversed increases, and the fissures increase in length and in breadth at the surface. Within these broadened fissures may be seen the outlines of deeper rounded pits. The corresponding curves of decrease of the fatigue limit with corrosion time are shown in figures 2 and 3.

The net damage caused by specimens that show crevices in sectional views (views *B*, *E*, and *H* of fig. 23) but no fissures in surface views, as shown in the corresponding diagram of figure 2, is intermediate between the net damage caused by fissures and that caused by rounded stress-corrosion pits. The net damage due to the rounded stress-corrosion pits must be attributed to the influence of cyclic stress on the size of these pits, and probably on the form of a few of the larger pits. The influence of cyclic stress on the size of rounded pits is illustrated by a number of views in figures 19, 20, and 21.

The rounded pits caused by corrosion at 35,000 lb/in.^{2} for 3 days (fig. 19, *B*) are about as large as pits caused by stressless corrosion for 10 days (fig. 7, *D*). After corrosion at 25,000 lb/in.^{2} for 4 days (fig. 19, *F*), parts of the surface are occupied by groups of very small pits. Some of the pits, however, have grown as large as those caused by stressless corrosion for 10 days. After corrosion for 6 days at the same stress (fig. 20, *A*), the groups of smaller pits have increased in number without much increase in size. Some of the larger pits, however, have increased greatly in size, and some round pits of intermediate size have merged to form transversely extended pits. After 9 days' corrosion of another specimen of the same steel at the same stress (fig. 20, *C*), very few of the small pits are visible but the larger pits have increased considerably in size.

After corrosion of a specimen of another steel at 20,000 lb/in.^{2} for 10 days (fig. 20, *D*), pits are more numerous, and consequently are smaller, than those caused by stressless corrosion for 10 days (fig. 7, *D*). Some of the pits in figure 20 (*D*) however, have merged to form transversely extended pits, and some of these are traversed by short fissures. The net damage shown by this specimen may be attributed mainly to the influence of cyclic stress on the form of corrosion pits.

C and *D* of figure 21 are views of two specimens of the same steel after corrosion at 10,000 lb/in.^{2} for 27 and 28 days, respectively. These views illustrate the great differences that may be found in the distribution of anodic and cathodic areas after exposure to apparently identical corrosion conditions. In view *C*, the round pits are about as numerous and as large as those in view *B*. In view *D* are a few very large pits, evidently caused by the merging of pits of medium size. Around these large pits are nearly circular areas containing numerous very small pits, and around these areas are nearly uncor-

roded cathodic areas. Early in the process, the anodic areas probably were confined to the large pits. With accumulation of corrosion products around these anodes, new oxygen concentration cells (section VII) evidently were formed, and thus caused the new small anodic areas which now appear as minute corrosion pits.

After corrosion at 8,000 lb/in.^{2} for 95 days (fig. 21, *E*), a large proportion of the surface is covered with broad irregular pits containing some small, relatively deep, round pits. This view should be compared with views *B* and *C* of figure 8, which show specimens that have been corroded for 93 and 100 days, respectively, without stress. Such comparison suggests that the pits caused by corrosion under cyclic stress tend to spread less along the surface and thus tend to be deeper than the pits caused in the same time by stressless corrosion. This may account for the net damage (fig. 2) caused by the pits shown in figure 21 (*E*). Reasons for this effect of cyclic stress are given in section VII.

5. PITTING WITH FREQUENCY OF 10 CYCLES PER MINUTE

Surface views of specimens corroded with frequency of 10 cycles per minute are shown in figures 24 and 25, and sectional views are shown in figure 26.

After corrosion at 45,000 lb/in.^{2} for 2.8 days, no fissures are visible in the surface view (fig. 24, *A*) and no crevices are visible in a sectional view (not shown). After corrosion at 40,000 lb/in.^{2} for 5 days, no fissures are visible in the surface view (fig. 24, *B*). Many of the pits, by growth and merging, have formed transversely extended pits with sharp ends. A sectional view through such pits (not examined) probably would show crevices. After corrosion for 6.5 days at the same stress, a sectional view (fig. 26, *B*) shows sharp inward projections from rounded pits. No surface view was examined.

Effects of corrosion at 35,000 lb/in.^{2} for times ranging from 6.5 to 9 days are shown in surface views *C* and *D* of figure 24 and in sectional views *C* and *D* of figure 26. After corrosion for 6.5 days, a few incipient fissures are visible in the surface view (fig. 24, *C*). No fissures or crevices, however, are found in the sectional view obtained after corrosion for 7 days (fig. 26, *C*). After corrosion for 9 days, fissures have made considerable progress.

After corrosion at 30,000 lb/in.^{2} for 9 and 12 days, no fissures are visible in the surface views (views *E* and *F* of fig. 24). Sharp crevices, however, are revealed by the corresponding sectional views (fig. 26, *E*, and another sectional view, not shown). After corrosion at 25,000 lb/in.^{2} for 11 days, no fissures are visible in the surface view (fig. 25, *A*) and no crevices are found in the sectional view (fig. 26, *F*). The results obtained at 30,000 and 25,000 lb/in.^{2}, therefore, indicate that the limiting stress below which fissures or crevices do not appear during 10 days' corrosion at 10 c/min evidently is between 25,000 and 30,000 lb/in.^{2} The limiting stress is more than 50 percent higher at this cycle frequency than at 50 c/min, and more than three times the corresponding stress at 1,450 c/min.

After corrosion at 22,000 lb/in.^{2} for 15 days, only large rounded pits are visible in the surface view (not shown). The sectional view shows thin curved projections extending inward from rounded pits. The

small size and irregular course of these projections suggest that they probably are rootlike projections rather than transverse crevices.

B to *E*, inclusive, of figure 25 are views of specimens that have been corroded at stresses ranging from 18,000 to 13,000 lb/in.^{2} and for times ranging from 20 to 36 days. Each of these views shows a few large pits, some of them formed by the merging of smaller pits. No fissures are visible in these surface views. Two of the sectional views (*H* and *L* of fig. 26), however, reveal small crevices.

Evidence that cyclic stress (during corrosion) tends to increase the size of rounded pits may be found by comparing the sizes of pits shown in figures 24 and 25 with the sizes of pits caused by stressless corrosion for corresponding times (figs. 7 and 8). In each view of figure 24 and in several views of figure 25, some of the pits are much larger than those caused in corresponding times by stressless corrosion.

After corrosion at 12,000 lb/in.^{2} for 70 days (view *F* of fig. 25), many groups of round pits have merged to form large broad pits, within which relatively deep round pits are still visible. This view should be compared with view *A* of figure 8 representing results of stressless corrosion for 69 days. After the stressless corrosion, the round pits within the broad areas caused by the merging are less distinct than after corrosion for the same time at 12,000 lb/in.^{2} Although this difference may be due largely to difference in the composition of the two steels, it may be due in part to the previously mentioned influence of cyclic stress. Cumulative evidence appears to indicate that the tendency to deepening of pits is greater for stress corrosion than for stressless corrosion. To such a tendency may be attributed the numerous examples, already mentioned, of net damage caused by rounded pits.

6. PITTING WITH FREQUENCY OF 1.5 CYCLES PER MINUTE

Surface views after corrosion at 1.5 c/min are shown in figure 27, and sectional views are shown in figures 28, 29, and 35.

No fissures are visible in the surface views (fig. 27). Sharp inward projections from rounded pits, however, are visible in some of the sectional views (figs. 28 and 29). As the net damage caused by these pits is rather small (fig. 2), it appears possible that these projections are not crevices but are rootlike projections caused by oxygen concentration cells. Such projections may be formed even in the absence of cyclic stress. It is important, therefore, to know the approximate width of the inward projections shown in figures 28 and 29.

To obtain this information, successive layers, each 0.001 in. thick, were removed from some of the sections shown in figures 28 and 29. After removal of each layer, the section was again polished, examined, and photographed. Views *D* to *G*, inclusive, of figure 28 and view *A* of figure 29 show five successive sectional views thus obtained with a specimen corroded at 25,000 lb/in.^{2} for 42 days. The subdivisions of these five views are correspondingly numbered; it is thus possible to follow the changes in each subdivision. Only the smaller of the two pits in view *D–3*, however, is shown in the four subsequent sections.

The pit in subdivision 1 decreases gradually in width from section *D–1* of figure 28 to section *A–1* of figure 29. This change occurred with removal of a total of 0.004 in. from section *D–1*, in which the

maximum width of the rounded pit is about 0.025 in. Section *D–1*, therefore, probably is nearly at the center of the rounded pit. With removal of about 0.008 in. more from section *A–1* of figure 29, the pit probably would disappear. (The repeated grinding and repolishing necessary to obtain these five sections caused gradual removal of corrosion products, so that none remain in section *A–1*.) The pit in subdivision 2 also decreases greatly in size from section *D–2* of figure 28 to section *A–2* of figure 29. (The section of the pit may have been enlarged slightly in polishing after removal of the corrosion products.) The apparently smaller pit in subdivision 3 decreases slightly from section *D–3* to section *E–3*, and then increases greatly from section *E–3* of figure 28 to section *A–3* of figure 29, which probably is nearly at the center. This pit evidently is nearly as large as the pit shown in *D–1*. The pit in subdivision 4 increases slightly from section *D–4* to section *E–4* of figure 28, then increases greatly to section *F–4* and decreases slightly to section *G–4*. With removal of an additional 0.001 in., the pit has disappeared; it is not found, therefore, in view *A* of figure 29. The maximum section of this pit evidently is section *F–4*.

The sharp projection shown in section *D–2* is much smaller in section *E–2*, is still smaller in section *F–2*, and is not found in section *G–2*. Removal of less than 0.003 in. from section *D–2*, therefore, has caused the projection to disappear. As section *D–2* probably is nearly at the center of the round pit and of its projection, the projection probably is not more than 0.005 in. wide (in direction perpendicular to section *D–2*). As the maximum thickness of the projection (section *D–2*) is about 0.0015 in., the width probably is three or four times the maximum thickness. The projection, consequently, is not root-shaped. Cyclic stress evidently has caused the projection to extend transversely as well as inward, and thus has formed a narrow wedge-shaped crevice. The width of the crevice, however, is only about one-fourth the diameter of the rounded pit from which the crevice started.

Corrosion at 20,000 lb/in.^{2} for 96 days has caused the rounded pits seen in the surface view (fig. 27, *F*). Sections through three of the pits are shown in figure 29 (*B*). In section *B–1*, the pit has several small inward projections. After removal of 0.001 in. (*C–1*), one of these projections has become deeper and much thicker. After removal of 0.002 in., the projection has become thinner (*D–1*). With removal of 0.003 and 0.004 in., the projection has decreased in depth and become much blunter. As the width of this projection evidently is not more than about 0.005 in., the maximum thickness is only about one-third the width. This projection, therefore, is a very narrow transverse crevice, only about one-fourth the diameter of the rounded pit from which it started.

In section *B–2* (fig. 29), the pit has a shallow, blunt projection. After removal of 0.001 in. (*C–2*), this projection has been replaced by three smaller projections. After removal of 0.002 in. (*D–2*), a larger, blunt projection has appeared. After removal of another 0.001 in. (*E–2*), this projection has almost disappeared. It therefore was only about 0.002 in. wide and evidently was root-shaped rather than wedge-shaped. The theoretical stress concentration due to this projection, therefore, is much less than that due to the projection seen in subdivision 1.

Although section *B–3* is not at the center of the rounded pit, it probably is not far from the center of the sharp inward projection. After removal of 0.001 in. (*C–3*), the projection has become somewhat larger. After removal of another 0.001 in. (*D–3*), the projection has become very small. Nevertheless, traces of the projection are visible after removal of additional layers (*E–3* and *F–3*). This projection evidently is a narrow transverse crevice, less than one-fourth the breadth of the rounded pit.

The cyclic stress during the 96 days' corrosion, therefore, evidently has caused the sharp inward projections from corrosion pits to be wider (and probably deeper) than they would have been after corrosion for the same time without stress. The increased stress concentration due to these crevices probably accounts for part of the slight net damage shown in figure 2.

The pits seen in surface views *A*, *D*, and *E* of figure 27 are larger than pits caused by stressless corrosion for corresponding times (figs. 7 and 8). Transversely merged pits are seen in views *B* and *D*. After corrosion at 20,000 lb/in.^{2} for 96 days (view *F* of fig. 27), many groups of the round pits have merged to form large broad pits. This view should be compared with views *B* and *C* of figure 8, which show effects of corrosion for about the same time without stress. The round, relatively deep pits within the larger areas are more distinct after corrosion at 20,000 lb/in.^{2} than after corrosion for the same time without stress. This relationship supports previously mentioned evidence that pits tend to spread less and deepen more under stress corrosion than under stressless corrosion.

7. PITTING WITH FREQUENCIES OF 0.5 CYCLE PER MINUTE AND 5 CYCLES PER HOUR

Surface views after corrosion at 0.5 c/min and at 5 c/hr are shown in figure 30; sectional views are shown in figures 31, 32, and 35.

No fissures are visible in the surface views (fig. 30). Sharp inward projections from rounded pits, however, are visible in some of the sectional views (figs. 31, 32, and 35). As the net damage caused by these pits was rather small (figs. 2 and 3), successive layers 0.001 in. thick were removed from one of these specimens in order to determine whether or not the projections are transverse crevices.

The successive sections after removal of these layers are shown in views *B* to *F*, inclusive, of figure 31. The four pits shown in view *B* are shown in views *C*, *D*, and *E*; only two of these pits remain in view *F*. The inward projection from the rounded pit is less deep in view *C–4* than in view *B–4*. After removal of an additional 0.001 in. (*D–4*), this projection has disappeared. No sharp projection appears in views *E–4* and *F–4*. The width of the projection (within the 0.004-in. layer examined), therefore, is less than 0.002 in. and more than 0.001 in. The thickness, as shown in *B–4*, is only about 0.0003 in. The projection, therefore, is a thin narrow crevice; its width is much less than the diameter of the rounded pit from which it projects. This projection probably was due chiefly to an oxygen concentration gradient. The cyclic stress changed it from a rootlike projection to a thin crevice. Because of the small size of such crevices, the resultant net damage generally is small.

The influence of corrosion time is illustrated by views *C* and *D* of figure 30. After corrosion at 35,000 lb/in.^{2} for 19 days (view *C*), many of the pits are large and a few have begun to extend transversely. After corrosion (of another steel) at the same stress for 40 days (view *D*), the pits are much larger and many have merged transversely. To these effects of the cyclic stress, rather than to the small sharp inward projections from rounded pits (fig. 35 *E*), may be attributed the resultant net damage (fig. 2). Corrosion at 5 c/hr. at 40,000 lb/in.^{2} for 146 days (fig. 30 *F*), has caused broad rounded pits, many of which have merged and are surrounded by broad, shallower areas. A sectional view (fig. 32 *E*) reveals no transverse crevices. The appreciable net damage (not shown in a diagram) probably was due chiefly to the influence of cyclic stress on the relative depth of the corrosion pits (compare fig. 30 *F* with view *D* of fig. 8, which shows a specimen corroded for about the same time without stress).

8. SUMMARY OF RESULTS OF EXAMINATION OF SPECIMENS

The results of examination of specimens corroded with and without cyclic stress indicate that cyclic stress tends to increase the size of corrosion pits, to cause transverse extension and merging, and to cause increase in relative depth. When the combined influence of stress, cycle frequency, and corrosion time is sufficiently great, transverse fissures appear at the equators of the rounded corrosion pits. When the combined influence of these three variables is somewhat less, transverse crevices are formed. When the combined influence is still less, the rounded pits may merely extend laterally and deepen, without loss of rounded contour. When the combined influence is small, the chief effect may be an increase in the size and relative depth of the rounded pits.

Cyclic stress, while increasing the size of the pits, apparently decreases the tendency of pits to spread and form shallow saucers. Cyclic stress may have great effect on the size of a few pits, while having little apparent effect on the size of most of the pits. The range of both form and size of the corrosion pits on any one specimen may thus be greatly increased.

VII. STRESS-CORROSION PROCESS

The evidence presented in figures 7 to 35, inclusive, confirms the conclusions expressed in previous papers [14, 15] that pitting under stress corrosion differs only in degree and form from pitting under stressless corrosion. The process of stress corrosion, therefore, must be interpreted in terms of the general theory of corrosion of metals.

When a metal is submerged in a corrosive aqueous solution, metal ions tend to go into solution in some regions (anodic areas), and a corresponding number of hydrogen ions tend to give up their electric charge and leave the solution at other regions (cathodic areas). The cathodic areas thus tend to become covered with hydrogen. Under ordinary corrosion conditions in neutral or alkaline waters, however, very little hydrogen is evolved from the cathodic areas. Removal of hydrogen as gas is so slow that the corrosive action practically ceases because of polarization, unless the hydrogen is continuously removed by chemical action. It can be so removed by combination with

oxygen dissolved in the aqueous solution. Continuous progress of ordinary corrosion thus depends on a continuous supply of dissolved oxygen to the cathodic areas.

Continuous corrosion, however, requires also a continuous removal of metal ions from the anodic areas and a continuous supply of negative ions (such as hydroxyl or chloride ions) to the anodic areas. Obstruction to continuous inward and outward flow of these ions by accumulation of corrosion products causes anodic polarization, just as obstruction to continuous flow of dissolved oxygen to cathodic areas causes cathodic polarization. With some metals in some corrosion conditions, polarization tends to be greater at the anode than at the cathode. At the cathode, under these conditions, the concentration of dissolved oxygen is greater than the concentration of hydrogen. The rate of corrosion, then, is controlled by the rate of reaction at the anode, and depends very little on the rate of supply of oxygen to the cathode. With other metals, or even with the same metal under different corrosion conditions, polarization tends to be much greater at the cathode than at the anode. The concentration of dissolved oxygen at the cathode, then, is much less than the concentration of deposited hydrogen, and the rate of corrosion depends chiefly on the rate of supply of dissolved oxygen. The rate of corrosion, therefore, sometimes is controlled by the rate of depolarization of the anodes, and sometimes by the rate of depolarization of the cathodes. Under other conditions, the concentrations of hydrogen and dissolved oxygen at the cathode do not differ greatly. The rate of corrosion, then, is neither anodically nor cathodically controlled.

The rate of corrosion of carbon steels and ordinary alloy steels in natural waters generally depends chiefly on the rate of arrival of dissolved oxygen at the cathodic areas. To reach these areas, oxygen of the air must dissolve at the surface of the water and be transferred (by diffusion or convection) to the coating on the metal. This coating consists of a layer of primary and secondary corrosion products permeated by water solution. When the steel is some distance below the surface of the water, the rate of arrival of oxygen at the cathodic areas, and hence the rate of corrosion, may depend chiefly on the rate of transfer of dissolved oxygen downward through the water. When the surace of water in contact with air is small in relation to the volume of water, the rate of supply of oxygen to the cathode may depend chiefly on the rate of solution of oxygen in the water. The effects shown in figures 1 to 35, however, were obtained by rotating each specimen in a small stream of water, so that the specimen was surrounded by a thin layer of water previously almost saturated with dissolved oxygen. The initial rate of corrosion under these conditions would depend primarily on the rate of anodic reaction. With accumulation of corrosion products, however, the rate of reaction would depend more and more on the rate of diffusion of oxygen through the cathodic coating.

The previous brief outline of the corrosion process applies primarily to the process of stressless corrosion. The accelerating influence of cyclic stress on corrosion was discussed in previous papers [13, 17] briefly as follows: Cyclic stress may accelerate corrosion, not only by increasing the permeability of the film and layer of corrosion products,

but also by increasing the solution pressure of the metal.[7] The relative importance of these two factors probably varies with the kind of metal, the intensity of the general corrosion, the properties of the corrosion products, the cycle frequency, and the stress. Under moderate or severe general corrosion, the important factor is the influence of cyclic stress (in the metal) on the permeability of the coating. Under slight general corrosion, and especially under relatively high stress, an important factor may be the influence of stress on the solution pressure of the metal. These views are practically unaltered by the evidence presented in figures 1 to 35.

The observed effects of cyclic stress on the corrosion pitting of steel in fresh water (figs. 7 to 35) are explainable on the assumption that cyclic stress increases the permeability of the film and the layer of corrosion products. When the combined influence of stress and cycle frequency is so small that it manifests itself only after a long corrosion time, the acceleration of corrosion pitting probably is due chiefly to the increase in the permeability of the cathodic coating. Stress concentration at the anodes (corrosion pits), under such conditions, would have little influence on the rate of corrosion pitting. Cyclic stress, therefore, would be expected to increase the size of corrosion pits, but to have little effect on their form. Numerous examples have been given of such an effect of cyclic stress when either stress or frequency is sufficiently low.

With increase of the stress or the cycle frequency above certain values (depending on the corrosion time), however, evidence appears that the rate of corrosion has been influenced by the stress concentration at the corrosion pits. The equatorial enlargement of the pits is evidence that corrosion has been most rapid in regions of highest local stress. The acceleration of corrosion, therefore, has been caused by increase in the permeability of both the cathodic and anodic coatings. The higher the stress and cycle frequency, the more is the rate of corrosion influenced by the resultant increase in the permeability of the anodic coating.

This tendency toward an anodically controlled process, due to cyclic stress, manifests itself not only in the equatorial enlargement of the corrosion pits, but also in a decreased tendency of the pits to spread along the metal surface (with increase in the corrosion time beyond about 10 days). The tendency of pits to spread along the surface is due chiefly to the effect of accumulation of secondary corrosion products on the cathodic area around each corrosion pit. The resultant obstruction to the flow of oxygen to these cathodic areas tends to cause new oxygen-concentration cells, and thus tends to cause new anodic areas in what were originally cathodic areas. Cyclic stress, by increasing the permeability of the cathodic coating, tends to prevent the formation of anodes within originally cathodic areas, and thus decreases or delays the spreading of the corrosion pits. Cyclic stress, consequently, opposes the tendency to a decrease in the ratio of cathodic to anodic areas, and thus opposes the approach to a cathodically controlled process.

For the same reason, decrease in the number of anodes per unit area tends to shift the corrosion process toward an anodically con-

[7] This does not necessarily imply that the acceleration is due to the stress itself. The acceleration may be due directly to the plastic strain caused by the stress.

trolled process. Under cyclic stress, as shown in section VI, a few pits often grow much more rapidly than the surrounding pits. The surrounding small pits may even appear no larger than if cyclic stress had been absent. The increased corrosion at a few large pits tends to increase the surrounding cathodic areas, and may thus bring into these areas some of the smaller pits. This tendency of cyclic stress to decrease the number of active anodes is a manifestation of the tendency to shift the corrosion process toward an anodically controlled process.[8]

The rate of the anodic reaction is a function of both the solution pressure of the metal and the permeability of the anodic coating. When the rate of corrosion is controlled by the anodic reaction, cyclic stress may accelerate corrosion not only by increasing the permeability of the anodic coating, but also by increasing the solution pressure of the metal. Such increase of the solution pressure probably is not due directly to the stress or to the elastic strain, but is due to plastic deformation. In regions of plastic deformation, especially at slip planes, the solution pressure probably is higher than in regions free from plastic deformation.[9] Evidence tending to substantiate this view has been given by Gough and coworkers [3 to 6] as a result of their investigation of corrosion fatigue of crystals of aluminum. They report that corrosion-fatigue cracks started at slip planes caused by the cyclic stress.

The equatorial enlargement of corrosion pits, due to the influence of cyclic stress on corrosion, has been mentioned as evidence that the corrosion process has been shifted toward an anodically controlled process. As the rate of anodic reaction is a function of both the solution pressure of the metal and the permeability of the anodic coating, consideration must now be given to the relative importance of these two factors in causing the observed equatorial enlargement of corrosion pits. The solution pressure probably is increased only when the stress is high enough to cause plastic deformation, at least locally. The possibility that corrosion will be accelerated because of enhanced solution pressure, therefore, probably is small when the cyclic stress is small, but increases with the stress, and becomes large when the stress (at least in regions of high stress concentration) exceeds the fatigue limit.

The possibility that corrosion will be accelerated because of enhanced solution pressure also increases as the corrosion process is shifted from a cathodically controlled toward an anodically controlled process. The possibility would thus be expected to increase not only with the stress but also with the cycle frequency. The possibility would be greatest for metals and corrosion conditions such that the corrosion process would be anodically controlled even in the absence of cyclic stress. Other factors being equal, therefore, the possibility would be greater for such metals as aluminum and stainless steel than for carbon steels or ordinary alloy steels in natural waters.[10]

The possibility that increased solution pressure plays an important part in stress corrosion of the steels represented in figures 1 to 35, therefore, need be considered only when the stress is initially high or

[8] The shift of the process with corrosion time is not necessarily in the same direction as the shift with increase in stress or cycle frequency.

[9] Much of the evidence generally given in support of this view, however, is inconclusive. Evans [1] has shown that some of the examples of increased corrosion at plastically deformed regions are due chiefly to breaking of the film during the plastic deformation.

[10] Under some corrosion conditions, enhanced solution pressure possibly affects the rate of corrosion of ordinary steels.

has become locally high because of stress concentration. The influence of increase in solution pressure probably is small in comparison with the influence of increased permeability of the coating, unless the stress (at least locally) is not far below the ordinary fatigue limit. Even if the initial stress is far below the fatigue limit, however, the actual local stress (because of increasing stress concentration) may eventually reach or even exceed the fatigue limit. By reference to curves such as those in figures 1 to 4, it is possible to determine approximately when the stress concentration at corrosion pits has raised the actual stress to the fatigue limit. If the actual fatigue limit of the metal has not been altered even locally by the cyclic stress, the actual stress would reach the fatigue limit when the nominal fatigue limit (represented by ordinates in figs. 1 to 4) has fallen to equality with the nominal cyclic stress (in the corrosion stage).

As shown in figures 1 to 4, the actual stress in some of the experiments eventually exceeded the fatigue limit. The fatigue limit, however, usually was reached long after the appearance of crevices or fissures. Crevices or fissures, therefore, are not evidence of actual fatigue, or that the process has been influenced appreciably by enhancement of solution pressure. Appearance of crevices at actual stresses so far below the fatigue limit suggests that the influence of cyclic stress on the forms of these pits consisted chiefly in increase of the permeability of the anodic coating. Even when the actual stress has risen almost to the fatigue limit, the rate of corrosion (of ordinary steels in fresh water) probably depends much more on the permeability of the cathodic and anodic coatings than on any enhancement of solution pressure.

The evidence presented by Gough and coworkers [3 to 6] that corrosion-fatigue cracks in aluminum crystals started at slip planes is not in conflict with the evidence in figures 1 to 35. Although the cyclic stress used in their experiments was low, it was high enough to cause numerous slip planes in a metal that corrodes with anodic control even in the absence of cyclic stress. Conclusions drawn from those experiments, therefore, cannot be applied without modification to ordinary steels corroded at stresses so far below the fatigue limit that slip planes must have been few. Even in the results of the experiments with aluminum, moreover, evidence may be found that rounded corrosion pits have been increased in size and altered in form by cyclic stress. Mention is made of "local attack" consisting of several large corrosion pits, for which no cause was assigned. A crack had started at one of the larger round pits. Mention is also made of a tendency to merging of small pits. If fatigue failure had not occurred at cracks starting from slip lines, therefore, it probably would have occurred eventually at cracks starting from rounded pits.

The evidence presented in figures 1 to 35 indicates that the accelerating influence of cyclic stress on corrosion, for steels in aerated natural waters, is due to increase in the permeability of the coating. The effect is primarily on the cathodic coating. The influence of permeability of the anodic coating, however, increases with the stress and cycle frequency.

Acknowledgment is made to H. O. Willier for the careful preparation and photographing of the metal specimens.

VIII. REFERENCES

[1] U. R. Evans, Metallic Corrosion, Passivity, and Protection (Edward Arnold & Co., London, 1937).

[2] J. N. Goodier, *Concentration of stress around spherical and cylindrical inclusions and flaws*, Trans. Am. Soc. Mech. Engrs., APM 55, 7 (1933).

[3] H. J. Gough and D. G. Sopwith, *The behavior of a single crystal of aluminum under alternating torsional stresses while immersed in a slow stream of tap water*, Proc. Roy. Soc. (London) [A] **135,** 392–411 (1932).

[4] H. J. Gough and G. Forrest, The Behavior of a Single Crystal of Aluminum Subjected to Stressless Corrosion in Tap Water, Followed by Test to Destruction in Air Under Alternating Torsional Stresses, Aeron. Research Comm. Reports and Memoirs No. 1476 (1932).

[5] H. J. Gough, *Corrosion-fatigue of metals*, Eleventh Autumn Lecture, J. Inst. Metals **49,** 17–92 (1932).

[6] H. J. Gough and D. G. Sopwith, *Corrosion-fatigue characteristics of an aluminum specimen consisting of two crystals*, J. Inst. Metals **52,** 57–72 (1933).

[7] C. E. Inglis, *Stresses in a plate due to the presence of cracks and sharp corners*, Trans. Inst. Naval Arch., pt. 1, **55,** 219 (1913).

[8] A. Leon, *Über die Störungen der Spannungsverteilung die in elastischen Körpern- und Bläsen entstehen*, Österr. Wochschr. öffent. Baudienst **14,** 163 (1908).

[9] D. J. McAdam, Jr., *Endurance properties of steel: Their relation to othe physical properties and to chemical composition*, Proc. Am. Soc. Testing Materials **23,** pt. 2, 56 (1923).

[10] D. J. McAdam, Jr., *Stress-strain-cycle relationship and corrosion fatigue of metals*, Proc. Am. Soc. Testing Materials **26,** pt. 2, 224 (1926).

[11] D. J. McAdam, Jr., *Corrosion-fatigue of metals as affected by chemical composition, heat treatment and cold working*, Trans. Am. Soc. Steel Treating **11,** 355 (1927).

[12] D. J. McAdam, Jr., *Corrosion-fatigue of nonferrous metals*, Proc. Am. Soc. Testing Materials **27,** pt. 2, 102 (1927).

[13] D. J. McAdam, Jr., *Fatigue and corrosion fatigue of metals*, Proc. Int. Cong. Testing Materials **1,** 305 (1927).

[14] D. J. McAdam, Jr., *Fatigue and corrosion fatigue of spring materials*, Trans. Am. Soc. Mech. Engrs., APM **45,** 511 (1929).

[15] D. J. McAdam, Jr., *Corrosion of metals as affected by time and by cyclic stress*, Trans. Am. Inst. Mining Met. Engrs., Inst. Metals Div. 571 (1928).

[16] D. J. McAdam, Jr., *Some factors involved in corrosion and corrosion fatigue of metals*, Proc. Am. Soc. Testing Materials **28,** pt. 2, 117 (1928).

[17] D. J. McAdam, Jr., *Corrosion of metals as affected by stress, time, and number of cycles*, Trans. Am. Inst. Mining Met. Engrs., Inst. Metals Div. 56 (1929).

[18] D. J. McAdam, Jr., *Corrosion of metals under cyclic stress*, Proc. Am. Soc. Testing Materials **29,** pt. 2, 250 (1929).

[19] D. J. McAdam, Jr., *The influence of stress range and cycle frequency on corrosion*, Proc. Am. Soc. Testing Materials **30,** pt. 2, 411–447 (1930).

[20] D. J. McAdam, Jr., *Stress and corrosion*, Third International Congress of Applied Mechanics, Stockholm, **2,** 269–293 (1930).

[21] D. J. McAdam, Jr., *Influence of stress on corrosion*, Trans. Am. Inst. Mining Met. Engrs., Inst. Metals Div. **99,** 282–318 (1932).

[22] D. J. McAdam, Jr., *Stress corrosion of metals*, Proc. Zurich Cong., Int. Assn. Testing Materials, **1,** 228–246 (1931).

[23] D. J. McAdam, Jr., *Influence of water composition on stress corrosion*, Proc. Am. Soc. Testing Materials, **31,** pt. 2, 259–278 (1931).

[24] D. J. McAdam, Jr., and R. W. Clyne, *Influence of chemically and mechanically formed notches on fatigue of metals*, J. Research NBS **13,** 527–572 (1934).

[25] H. Neuber, *Elastischstrenge Lösungen zur Kerbwirkung bei Schreiben-und Umdrehungs Körpern*, Z. Math. Mech. **13,** 13 (1933).

[26] R. V. Southwell and H. J. Gough, On the Concentration of Stress in the Neighborhood of a Small Spherical Flaw, and on the Propagation of Fatigue Fractures in a Statistically Isotropic Material, Brit. Aeron. Research Comm. Reports and Memoirs, No. 1003 (Jan. 1926).

[27] F. N. Speller, Corrosion: Causes and Prevention (McGraw-Hill Book Co., Inc., New York, N. Y., 1926).

[28] W. N. Thomas, The Effect of Scratches and of Various Workshop Finishes Upon the Fatigue Strength of Steel, Brit. Aeron. Research Comm. Reports and Memoirs, No. 860 (March 1923).

TABLE 1.—*Chemical composition*

Material	Designation	C	Mn	Si	Cr	Ni
		%	%	%	%	%
Carbon steel	JR	0.46	0.65	0.016		
Nickel steel	LQ[a]					
Do	IW	.28	.5	.19	0.26	3.7
Chromium-nickel steel	BC	.28	.69	.21	.73	1.51
Do	AX	.36	.48	.22	1.55	3.26

[a] About the same in composition as IW.

TABLE 2.—*Thermal treatment*

Material	Designation	Temperature	Time held	Cooled in—	Temperature	Time held	Cooled in—
		°F	min		°F	min	
0.46 percent C steel	JR–W–10	1,500	60	Water	1,000	120	Furnace.
3.5 percent Ni steel	LQ–W–10	1,450	60	do	1,000	120	Do.
3.7 percent Ni steel	[a]IW–W–10	1,450	60	do	1,000	120	Do.
0.73 percent Cr, 1.51 percent Ni steel.	BC–W–10	1,550	60	do	1,000	120	Do.
1.55 percent Cr, 3.26 percent Ni steel.	AX–W–10	1,550	60	do	1,000	120	Do.

[a] Previously heated to 1,675° F for 60 min, cooled in air.

TABLE 3.—*Tensile properties*

[Usually these values are the average for at least 4 determinations.
"Johnson's limit" is the stress at that point on the stress-strain diagram at which the tangent is 3/5 that at the origin. "Proof stress" is the stress that, after release of load, will cause permanent extension of 0.01 percent. "Elastic limit" is the highest stress that, after release of load, will cause no appreciable permanent extension. "Proportional limit" is the highest stress that will not cause appreciable departure from a linear stress-strain relationship. (The smallest divisions of the extensometer scale were 0.0001 in. but estimate could be made to 0.00002 in. The extensometer was of a type that permitted accurate determination of permanent extension).]

Material	Designation	Tensile strength	Johnson's limit	Proof stress	Elastic limit	Proportional limit	Elongation	Reduction of area
		Lb./in.²	*Lb./in.²*	*Lb./in.²*	*Lb./in.²*	*Lb./in.²*	% *in 2 in.*	%
0.46% C steel	JR–W–10	129,800	100,000	101,400	99,500	92,300	17.5	51.9
3.5% Ni steel	LQ–W–10	133,700	121,300	123,300	121,300	106,400	21.0	63.8
3.7% Ni steel	IW–W–10	128,100	114,000	114,600	110,000	94,300	20.6	61.8
0.73% Cr, 1.51% Ni steel	BC–W–10	135,900	119,100	121,700	119,100	111,500	20.0	62.2
1.55% Cr, 3.26% Ni steel	AX–W–10	157,700	141,000	142,000	139,000	115,000	17.5	50.7

TABLE 4.—*Composition of well water, parts per million*

[pH values ranged from 7.0 to 7.2]

Date	Solids	Organic and volatile matter (O+V)	Alkalinity[a]	Cl	SO_3	CaO	MgO	Al_2O_3 and Fe_2O_3	SiO_2
April 12, 1928	579.4	158.4	111.6	244.5	9.14	151.1	25.5	None	15.4
April 20, 1928	614.0	108.3	97.4	240.8	10.7	70.3	67.8	do	9.8
May 22, 1928	556.2	98.4	104.9	209.0	48.1	148.3	18.6	do	9.6
September 5, 1929	410.5	142.7	98.0	117.0	4.3	51.8	19.3	do	3.9

[a] Alkalinity is expressed in terms of $CaCO_3$.

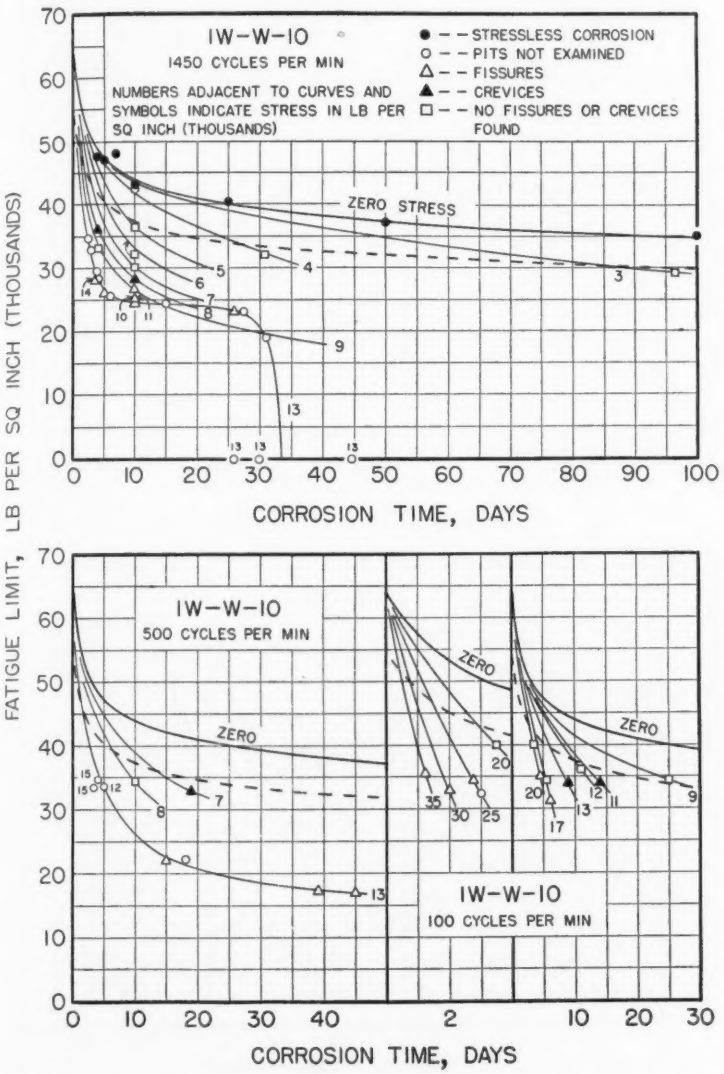
1W-W-10
1450 CYCLES PER MIN
NUMBERS ADJACENT TO CURVES AND SYMBOLS INDICATE STRESS IN LB PER SQ INCH (THOUSANDS)
● - - STRESSLESS CORROSION
○ - - PITS NOT EXAMINED
△ - - FISSURES
▲ - - CREVICES
□ - - NO FISSURES OR CREVICES FOUND
ZERO STRESS
FATIGUE LIMIT, LB PER SQ INCH (THOUSANDS)
CORROSION TIME, DAYS
1W-W-10
500 CYCLES PER MIN
ZERO
1W-W-10
100 CYCLES PER MIN
CORROSION TIME, DAYS

FIGURE 1.—*Influence of corrosion time, at various stresses and cycle frequencies, on the fatigue limit of a nickel steel.*

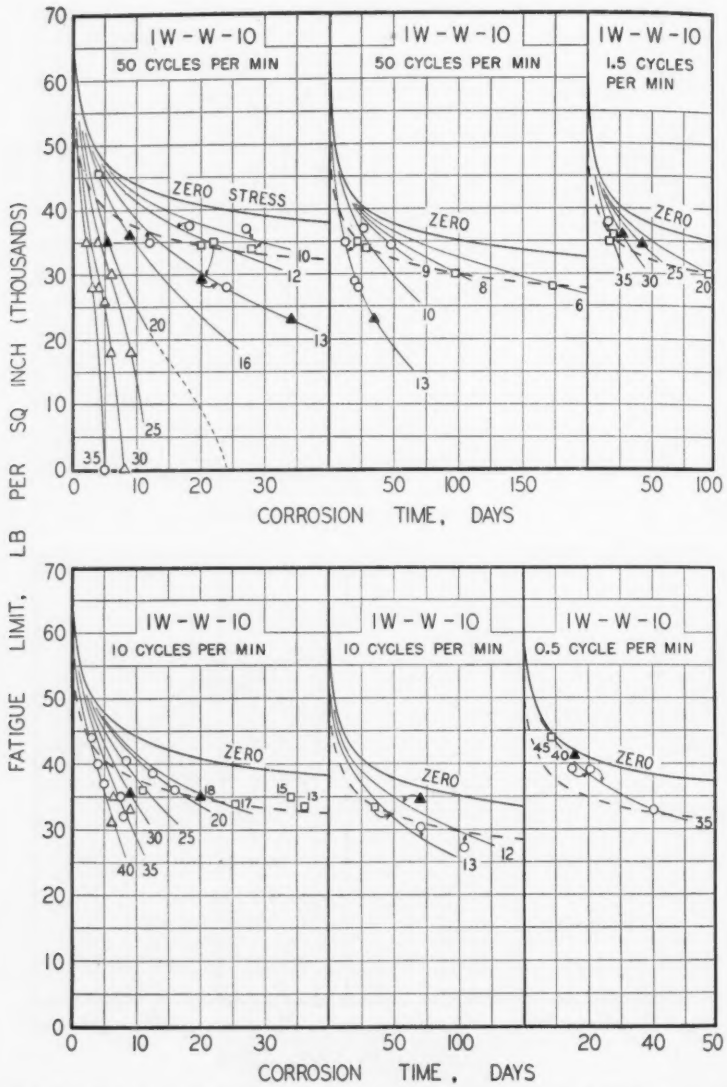

FIGURE 2.—*Influence of corrosion time, at various stresses and cycle frequencies, on the fatigue limit of a nickel steel.*

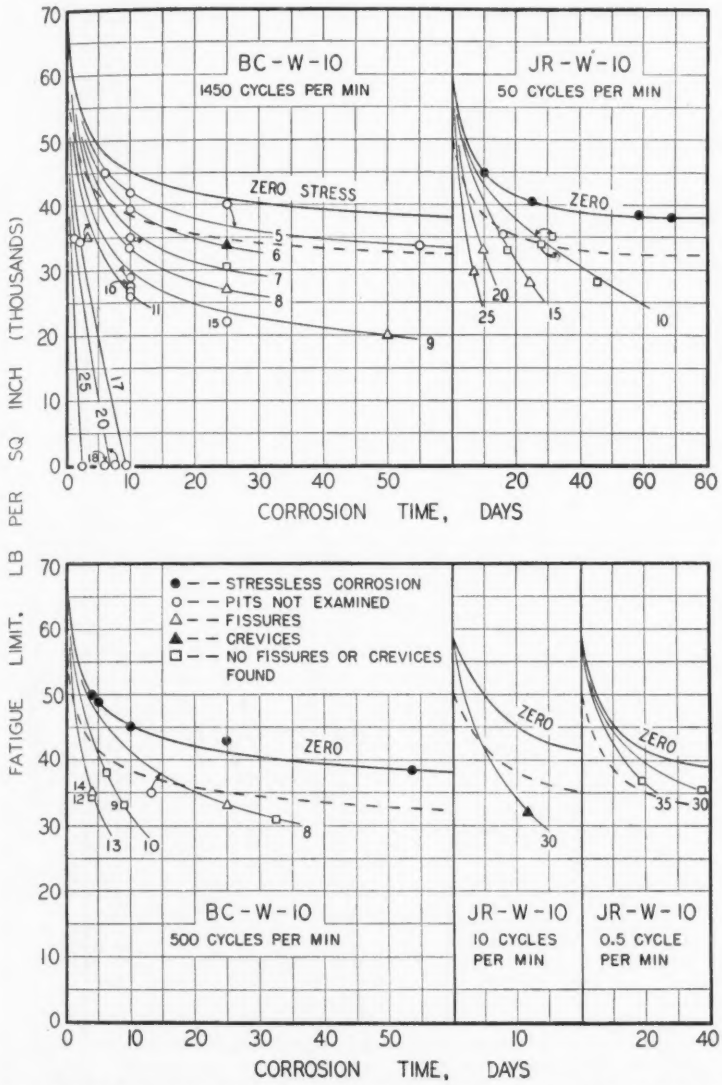

FIGURE 3.—*Influence of corrosion time, at various stresses and cycle frequencies, on the fatigue limit of a carbon steel and a chromium-nickel steel.*

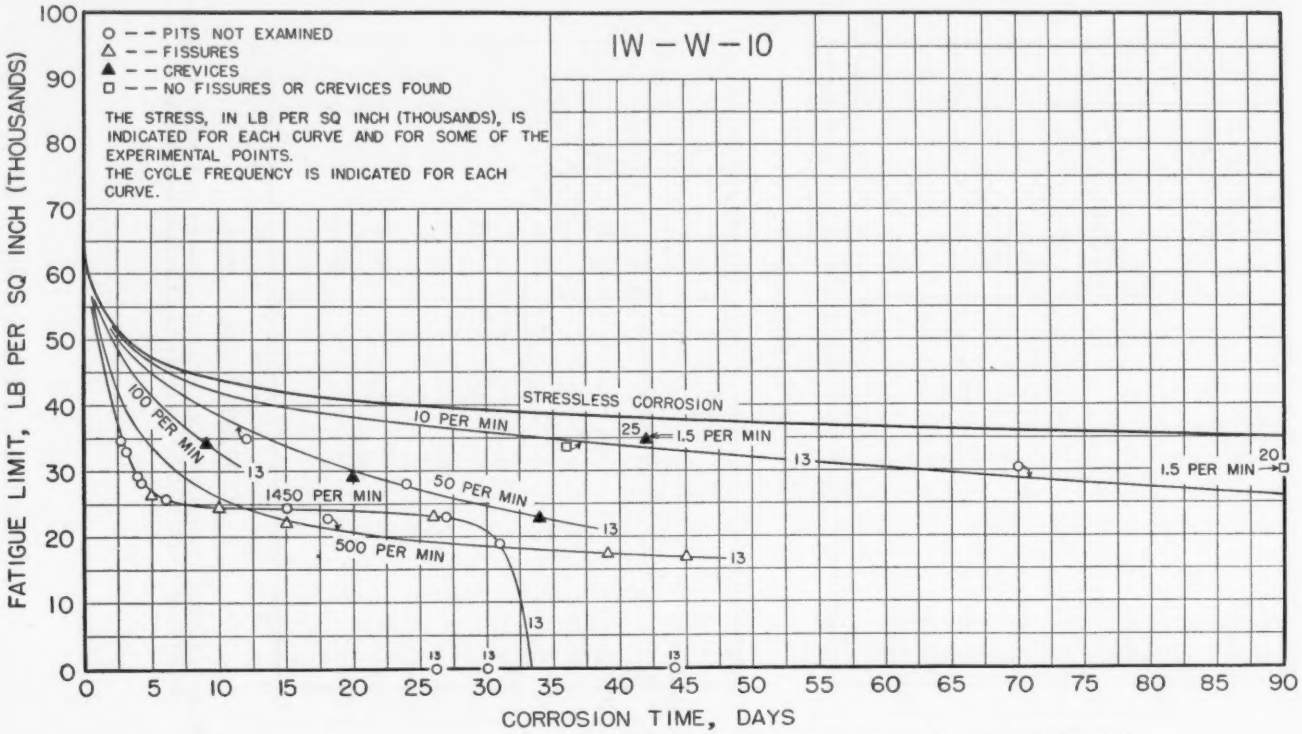
IW – W – 10
○ – – PITS NOT EXAMINED
△ – – FISSURES
▲ – – CREVICES
□ – – NO FISSURES OR CREVICES FOUND
THE STRESS, IN LB PER SQ INCH (THOUSANDS), IS INDICATED FOR EACH CURVE AND FOR SOME OF THE EXPERIMENTAL POINTS.
THE CYCLE FREQUENCY IS INDICATED FOR EACH CURVE.
FATIGUE LIMIT, LB PER SQ INCH (THOUSANDS)
CORROSION TIME, DAYS
STRESSLESS CORROSION
10 PER MIN
100 PER MIN
1450 PER MIN
500 PER MIN
50 PER MIN
1.5 PER MIN
1.5 PER MIN
13
20
25

FIGURE 4.—*Influence of corrosion time and of cycle frequency on the fatigue limit of a nickel steel.*

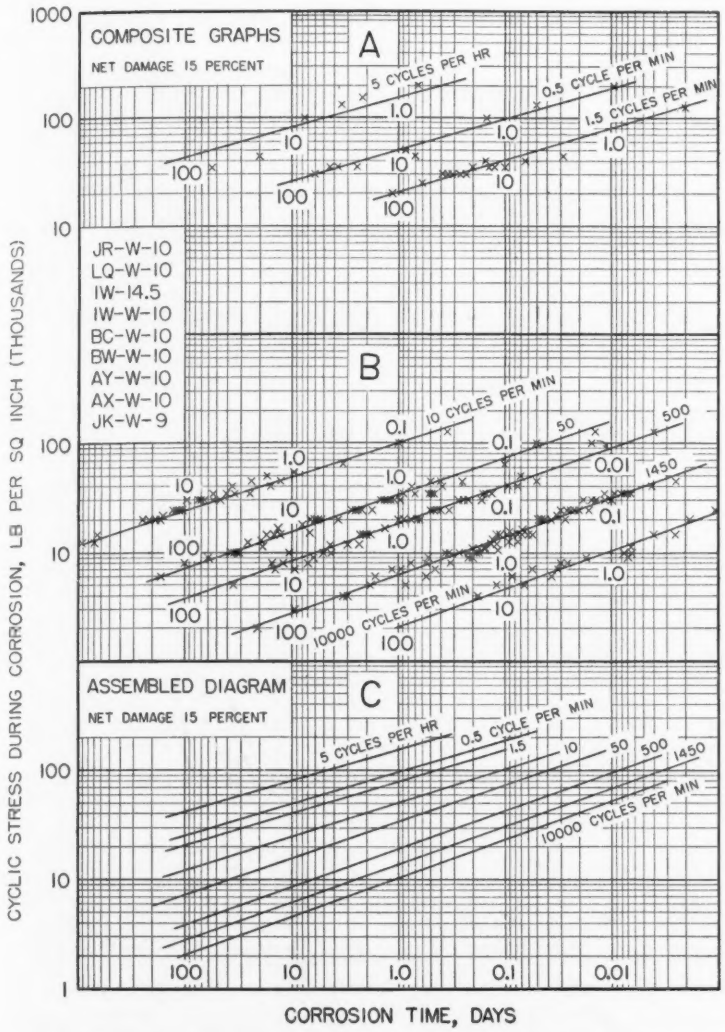

FIGURE 5.—*Composite diagram representing the influence of cyclic stress and cycle frequency on corrosion time, for constant net damage.*

JR-W-10	0.46% C.	BW-W-10	0.92% Cr, 1.83% Ni.
LQ-W-10	3.5% Ni.	AY-W-10	0.95% Cr, 2.16% Ni.
IW-14.5	3.7% Ni.	AX-W-10	1.55% Cr, 3.26% Ni.
IW-W-10	3.7% Ni.	JK-W-10	0.82% Cu.
BC-W-10	0.73% Cr., 1.5% Ni.		

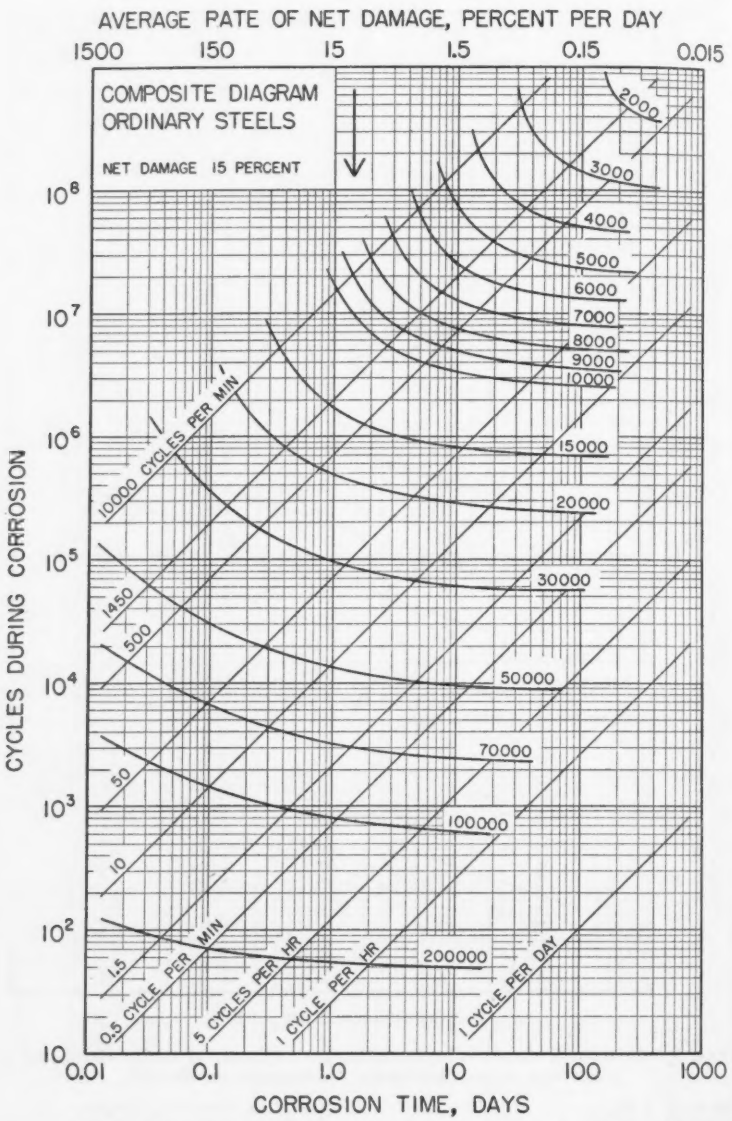

FIGURE 6.—*Composite diagram representing the influence of number of cycles and of cycle frequency on corrosion time, for constant net damage.*

WASHINGTON, March 1, 1940.

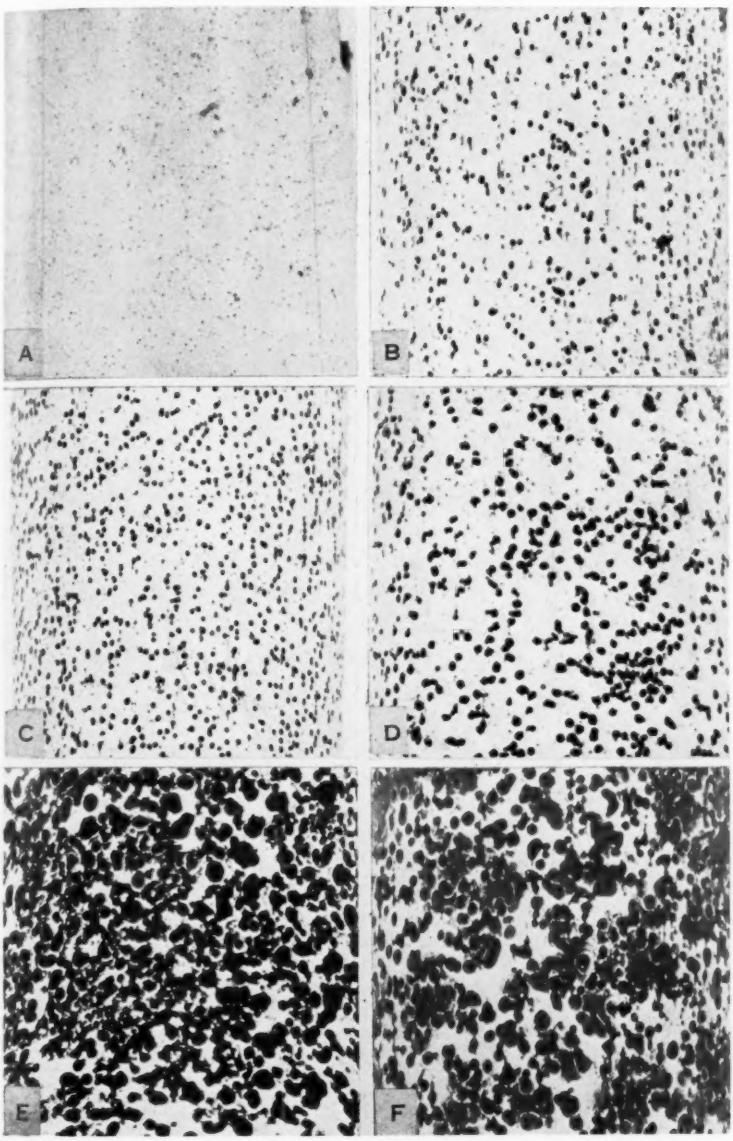

FIGURE 7.—*Stressless corrosion; outer surfaces;* $\times 4$.

A, 2 days, AX–W–10.
B, 4.7 days, IW–W–10.
C, 5.8 days, IW–W–10.
D, 10 days, JR–W–10.
E, 50 days, IW–W–10.
F, 59 days, JR–W–10.

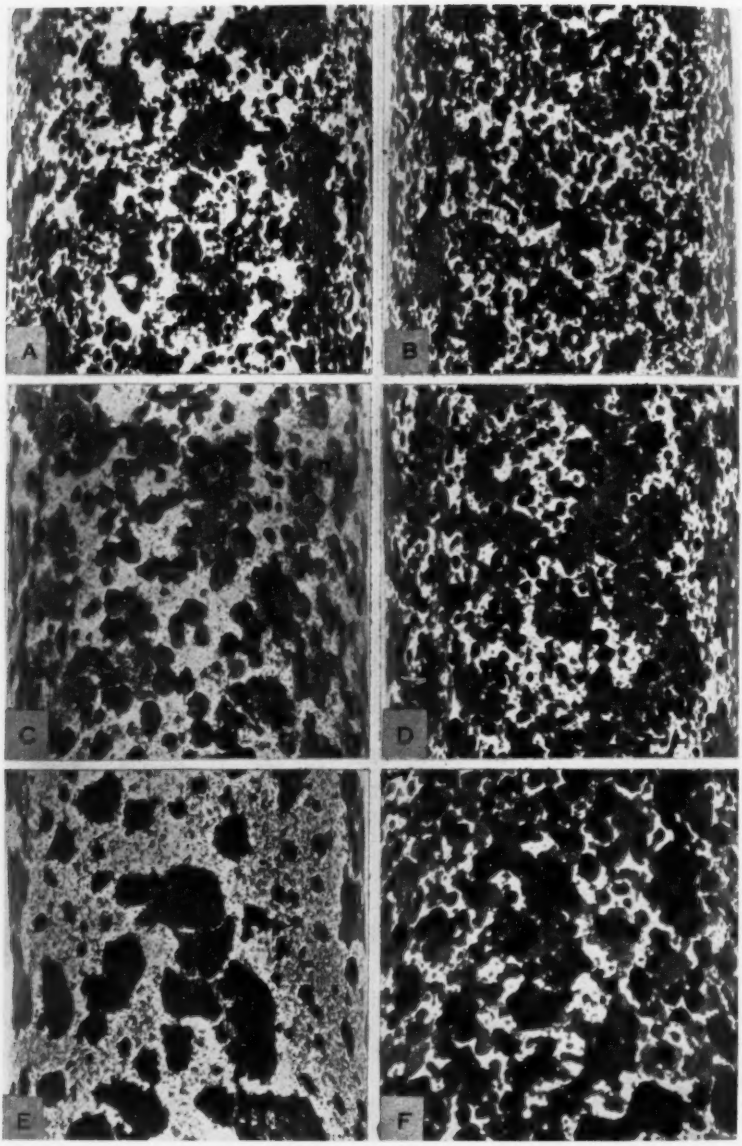

FIGURE 8.—*Stressless corrosion; outer surfaces;* $\times 4$.

A, 69 days, JR–W–10.
B, 93 days, JR–W–10.
C, 100 days, IW–W–10.
D, 150 days, AX–W–10.
E, 220 days, AX–W–10.
F, 300 days, IW–W–10.

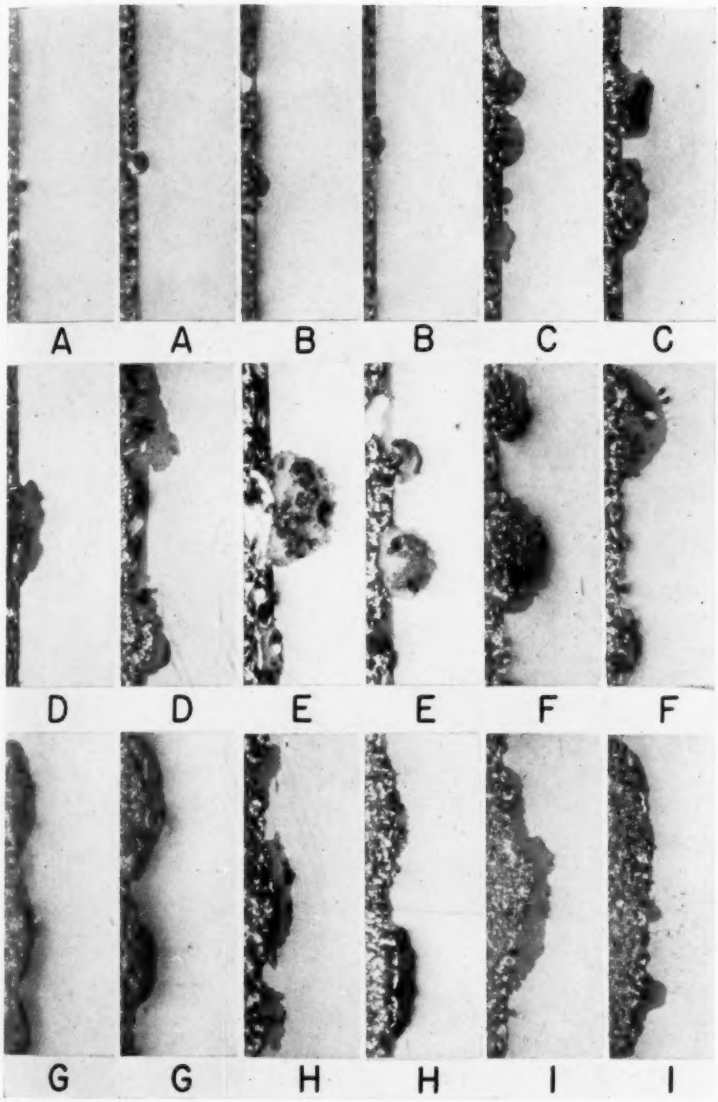

FIGURE 9.—*Stressless corrosion; longitudinal sections;* $\times 50$.

A, 2 days, AX-W-10.
B, 4 days, AX-W-10.
C, 4.7 days, IW-W-10.
D, 10 days, IW-W-10.
E, 47 days, AX-W-10.
F, 50 days, IW-W-10.
G, 59 days, JR-W-10.
H, 69 days, JR-W-10.
I, 84 days, AX-W-10.

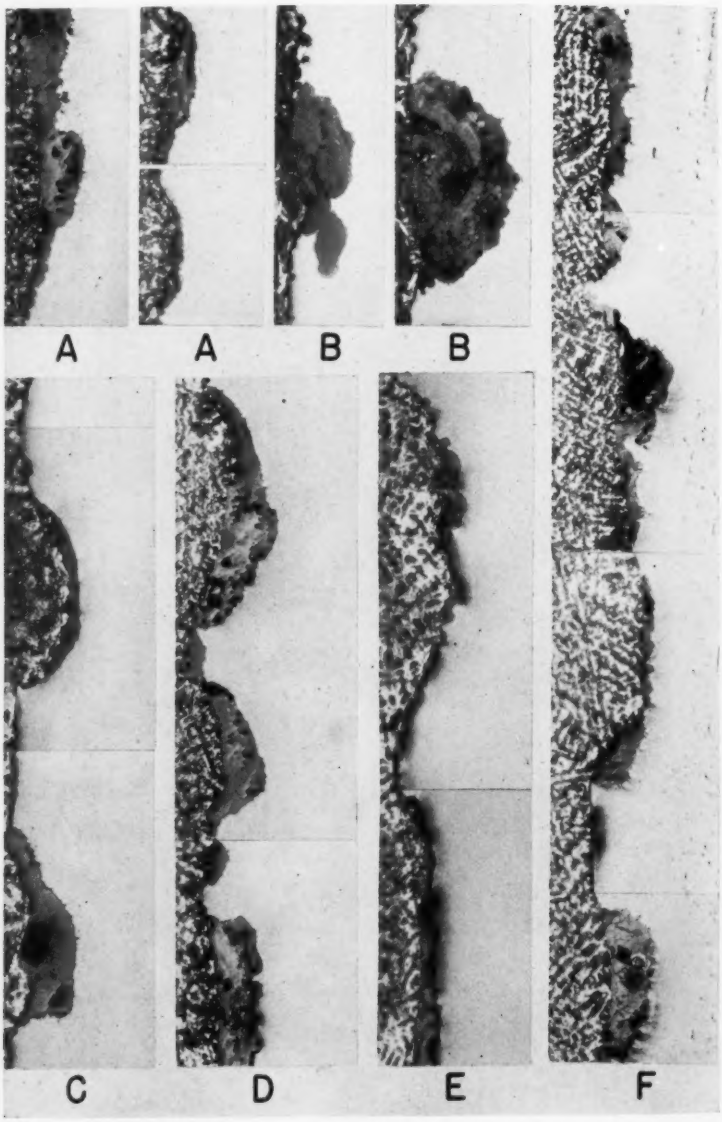

FIGURE 10.—*Stressless corrosion; longitudinal sections;* $\times 50$.

A, 93 days, JR–W–10.
B, 100 days, IW–W–10.
C, 110 days, IW–W–10.
D, 150 days, AX–W–10.
E, 220 days, AX–W–10.
F, 300 days, IW–W–10.

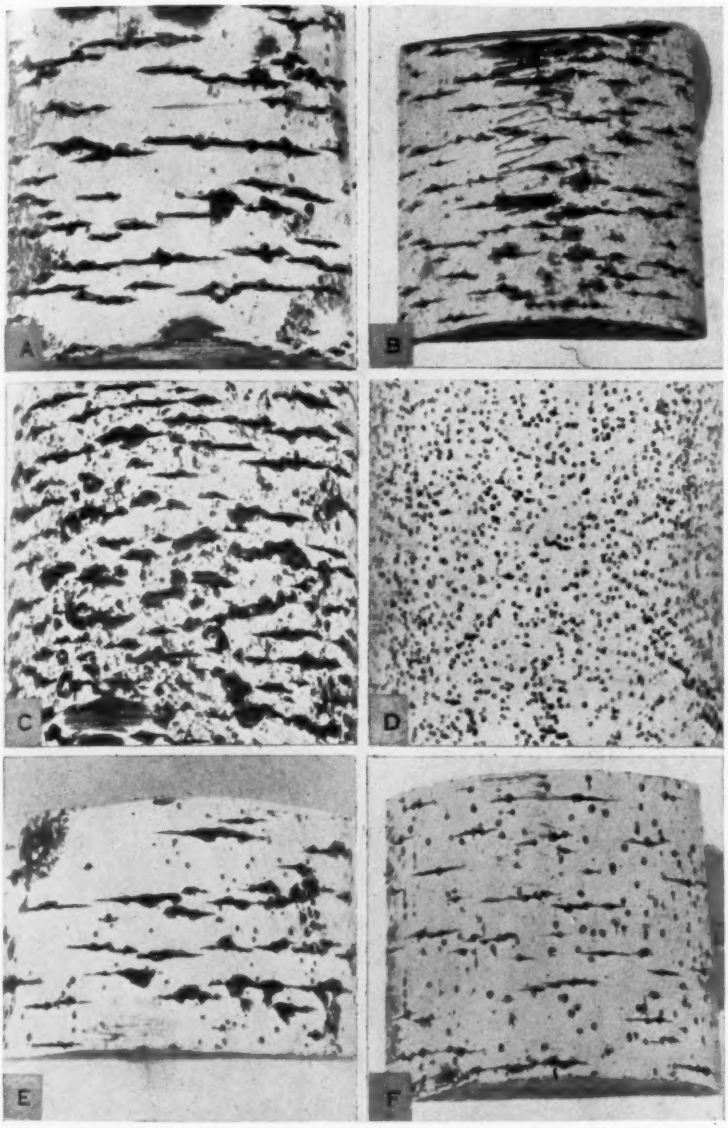

FIGURE 11.—*1,450 c/min; outer surfaces;* $\times 4$.

A, 15,000 lb/in.^{2}, 10 days, IW–W–10.
B, 13,000 lb/in.^{2}, 5 days, IW–W–10.
C, 13,000 lb/in.^{2}, 10 days, IW–W–10.
D, 11,000 lb/in.^{2}, 3 days, BC–W–10.
E, 11,000 lb/in.^{2}, 10 days, IW–W–10.
F, 10,000 lb/in.^{2}, 10 days, IW–W–10.

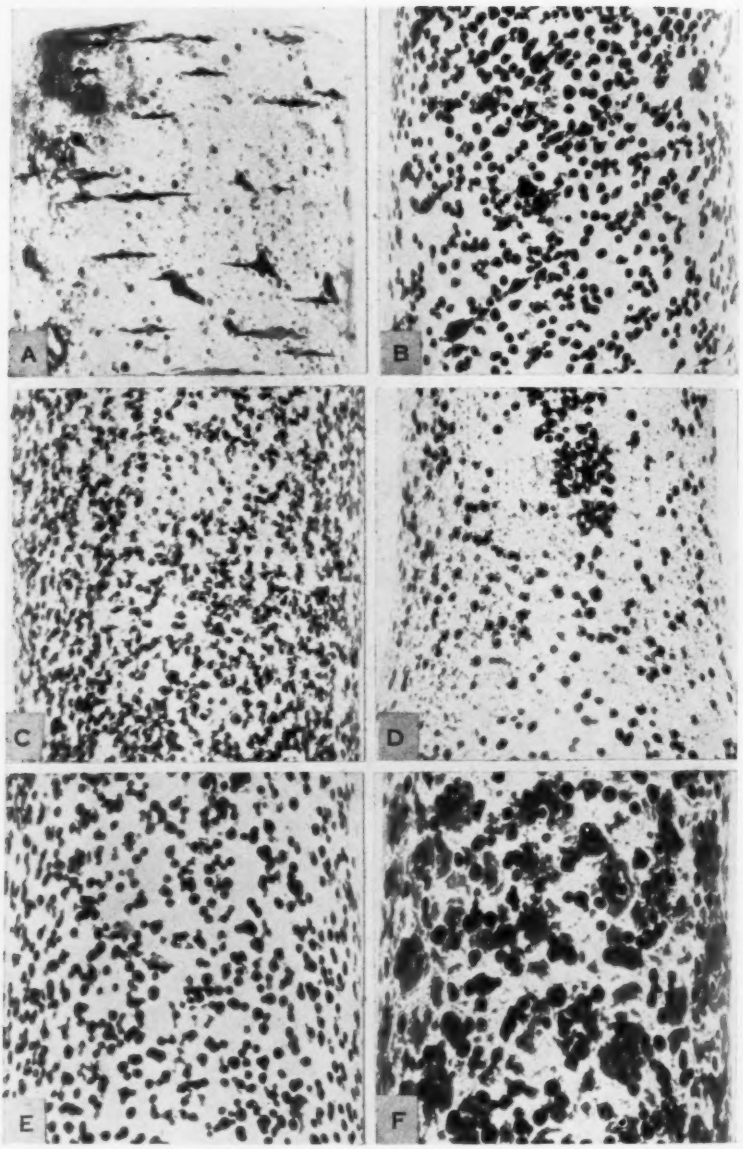

FIGURE 12.—*1,450 c/min; outer surfaces;* $\times 4$.

A, 9,000 lb/in.², 10 days, IW–W–10.
B, 8,000 lb/in.², 10 days, IW–W–10.
C, 7,000 lb/in.², 25 days, BC–W–10.
D, 6,000 lb/in.², 25 days, BC–W–10.
E, 4,000 lb/in.², 31 days, IW–W–10.
F, 3,000 lb/in.², 97 days, IW–W–10.

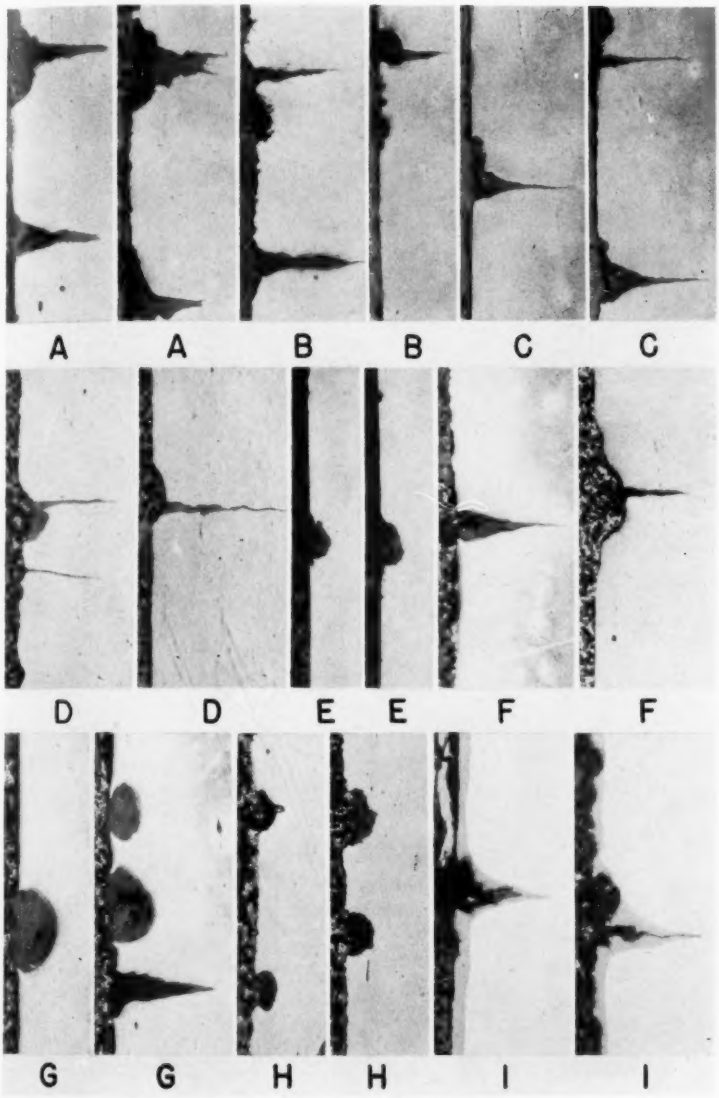

FIGURE 13.—*1,450 c/min; longitudinal sections;* $\times 50$.

A, 15,000 lb/in.², 10 days, IW–W–10.
B, 14,000 lb/in.², 3.2 days, IW–W–10.
C, 13,000 lb/in.², 5 days, IW–W–10.
D, 13,000 lb/in.², 10 days, IW–W–10.
E, 11,000 lb/in.², 3 days, BC–W–10.
F, 11,000 lb/in.², 10 days, IW–W–10.
G, 10,000 lb/in.², 10 days, IW–W–10.
H, 9,000 lb/in.², 4 days, IW–W–10.
I, 9,000 lb/in.², 10 days, IW–W–10.

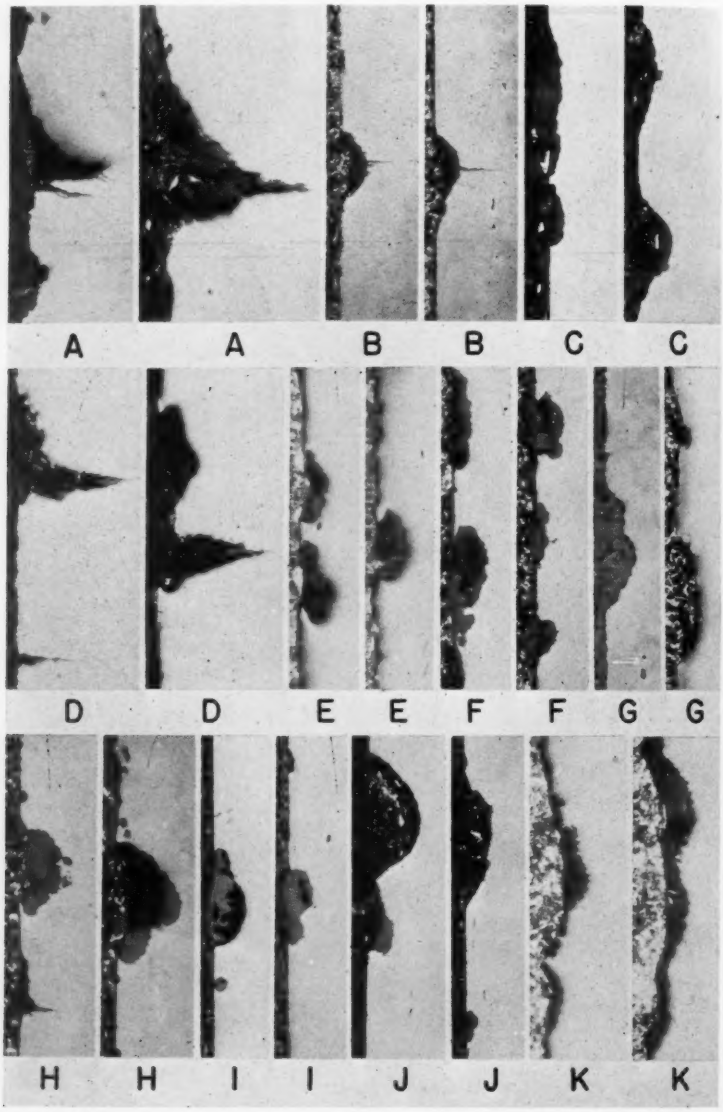

FIGURE 14.—*1,450 c/min; longitudinal sections;* ×*50.*

A, 9,000 lb/in.², 50 days, BC–W–10.
B, 8,000 lb/in.², 4 days, IW–W–10.
C, 8,000 lb/in.², 10 days, IW–W–10.
D, 8,000 lb/in.², 24 days, BC–W–10.
E, 7,000 lb/in.², 10 days, IW–W–10.
F, 7,000 lb/in.², 25 days, BC–W–10.
G, 6,000 lb/in.², 10 days, IW–W–10.
H, 6,000 lb/in.², 25 days, BC–W–10.
I, 5,000 lb/in.², 10 days, IW–W–10.
J, 4,000 lb/in.², 31 days, IW–W–10.
K, 3,000 lb/in.², 97 days, IW–W–10.

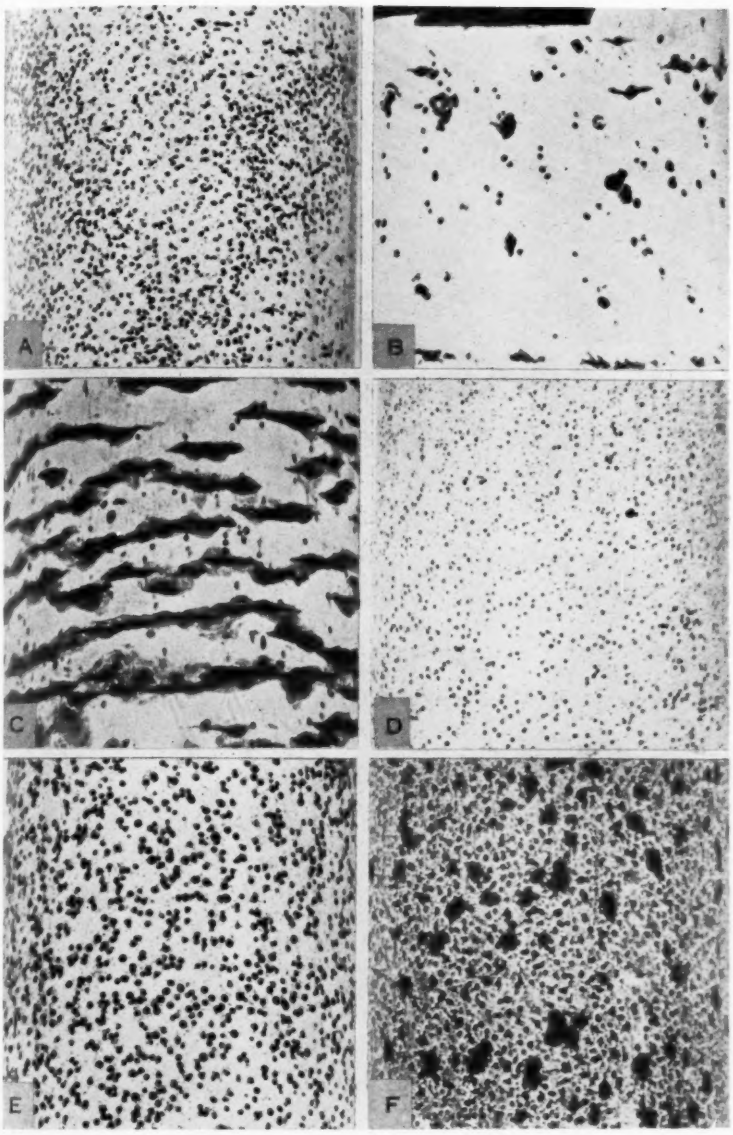

FIGURE 15.—*500 c/min; outer surfaces;* $\times 4$.

A, 14,000 lb/in.², 4 days, BC–W–10.
B, 13,000 lb/in.², 15 days, IW–W–10.
C, 13,000 lb/in.², 45 days, IW–W–10.
D, 12,000 lb/in.², 4 days, BC–W–10.
E, 9,000 lb/in.², 9 days, BC–W–10.
F, 8,000 lb/in.², 33 days, BC–W–10.

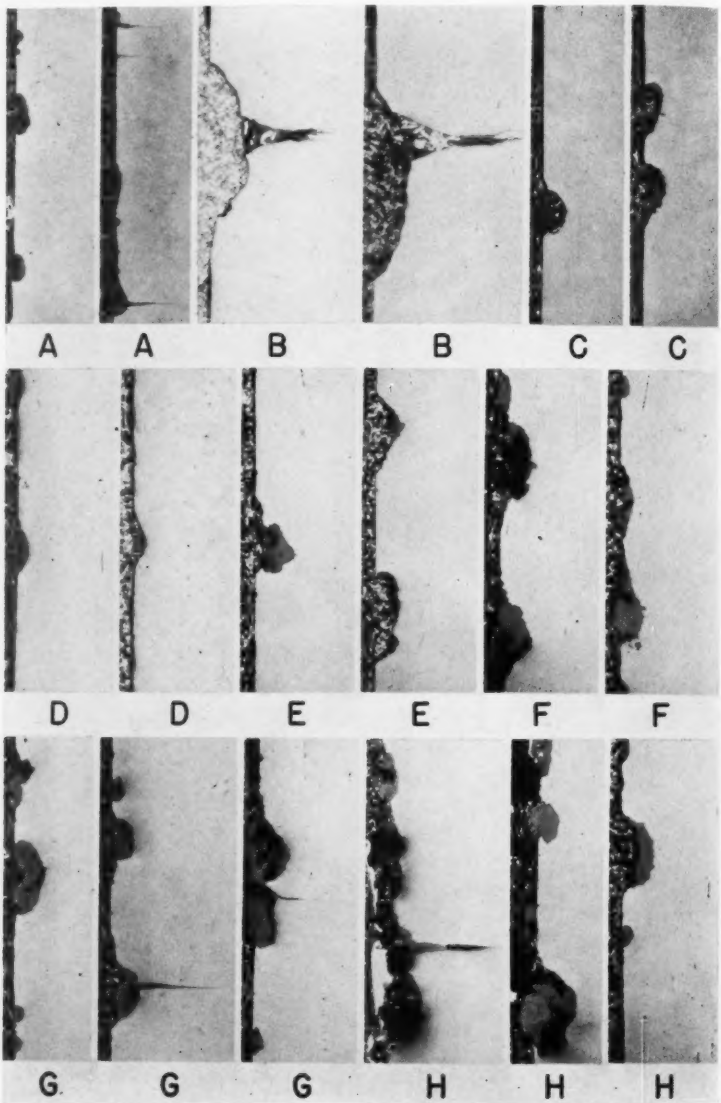

FIGURE 16.—*500 c/min; longitudinal sections;* $\times 50$.

A, 14,000 lb/in.², 4 days, BC–W–10.
B, 13,000 lb/in.² 15 days, IW–W–10.
C, 12,000 lb/in.², 4 days, BC–W–10.
D, 10,000 lb/in.², 6 days, BC–W–10.
E, 9,000 lb/in.², 9 days, BC–W–10.
F, 8,000 lb/in.², 10 days, IW–W–10.
G, 8,000 lb/in.², 25 days, BC–W–10.
H, 7,000 lb/in.², 19 days, IW–W–10.

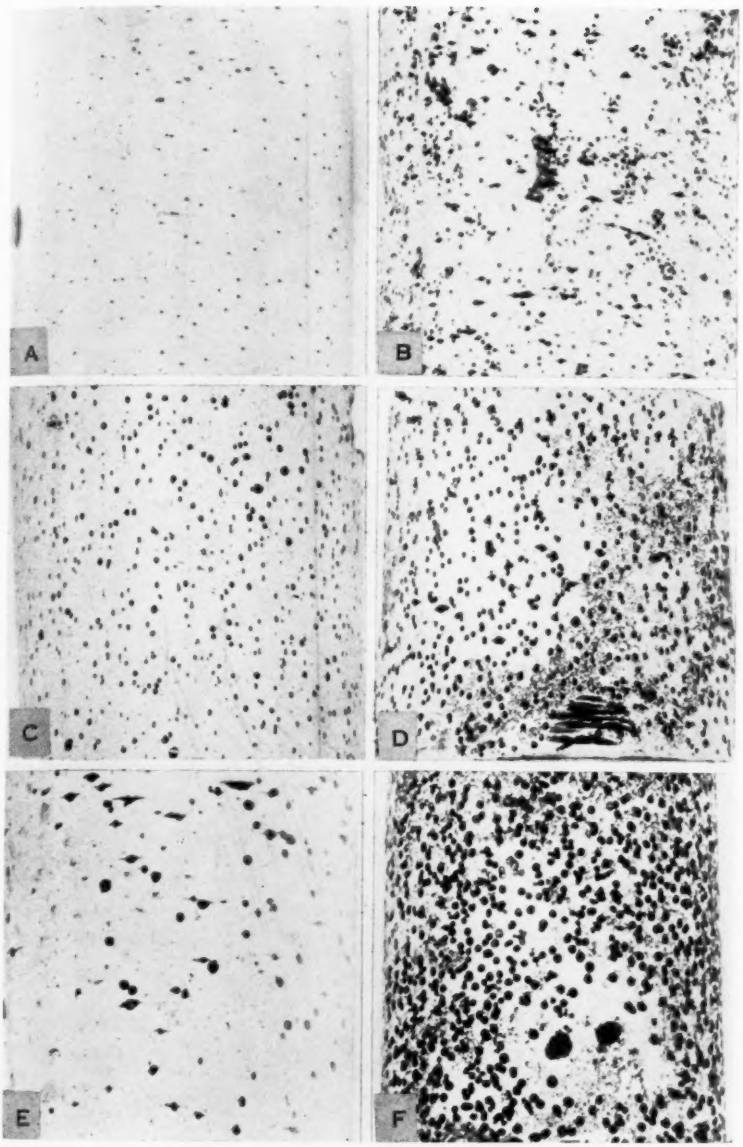

FIGURE 17.—*100 c/min; outer surfaces;* $\times 4$.

A, 35,000 lb/in.², 1.2 days, IW–W–10.
B, 30,000 lb/in.², 2 days, IW–W–10.
C, 20,000 lb/in.², 3.5 days, IW–W–10.
D, 20,000 lb/in.², 4.5 days, IW–W–10.
E, 17,000 lb/in.², 6 days, IW–W–10.
F, 13,000 lb/in.², 9 days, IW–W–10.

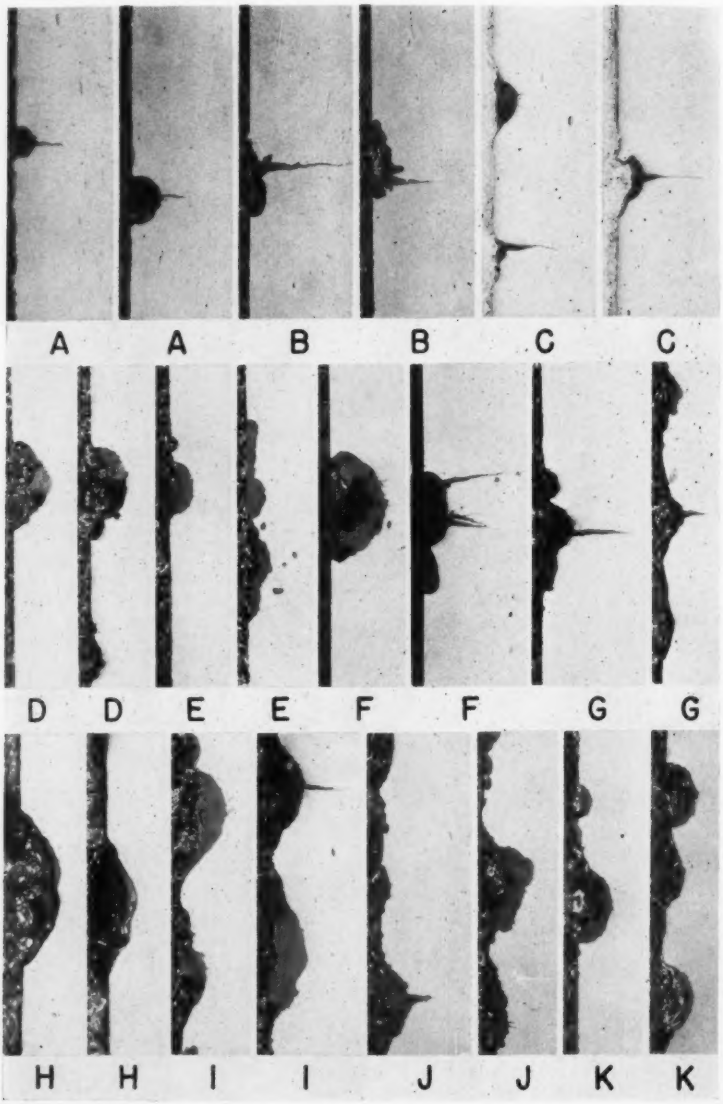

FIGURE 18.—*100 c/min; longitudinal sections; ×50.*

A, 35,000 lb/in.², 1.2 days, IW–W–10.
B, 30,000 lb/in.², 2 days, IW–W–10.
C, 25,000 lb/in.², 2.8 days, IW–W–10.
D, 20,000 lb/in.², 3.5 days, IW–W–10.
E, 17,000 lb/in.², 5.5 days, IW–W–10.
F, 17,000 lb/in.², 6 days, IW–W–10.
G, 13,000 lb/in.², 9 days, IW–W–10.
H, 12,000 lb/in.², 11 days, IW–W–10.
I, 11,000 lb/in.², 14 days, IW–W–10.
J, 10,000 lb/in.², 29 days, JR–W–10.
K, 9,000 lb/in.², 25 days, IW–W–10.

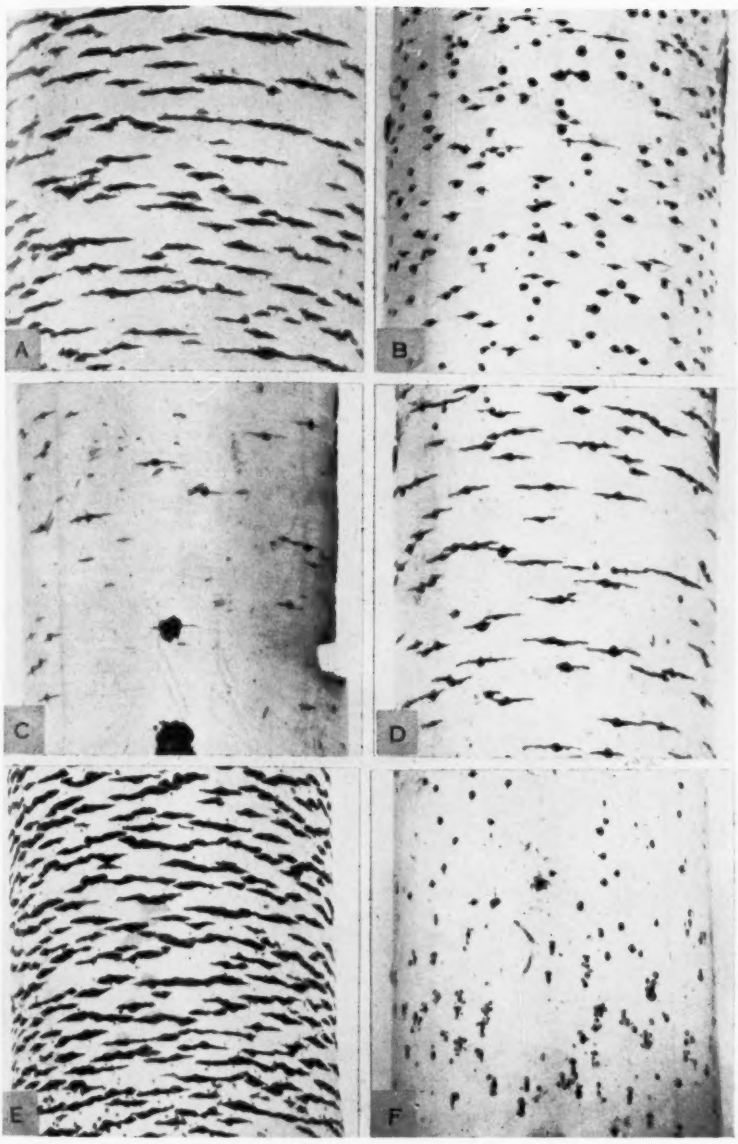

FIGURE 19.—*50 c/min; outer surfaces;* ×4.

A, 68,000 lb/in.², 1.1 days, IW–W–10.
B, 35,000 lb/in.², 3 days, IW–W–10.
C, 30,000 lb/in.², 5 days, IW–W–10.
D, 30,000 lb/in.², 6 days, IW–W–10.
E, 30,000 lb/in.², 8 days, IW–W–10.
F, 25,000 lb/in.², 4 days, IW–W–10.

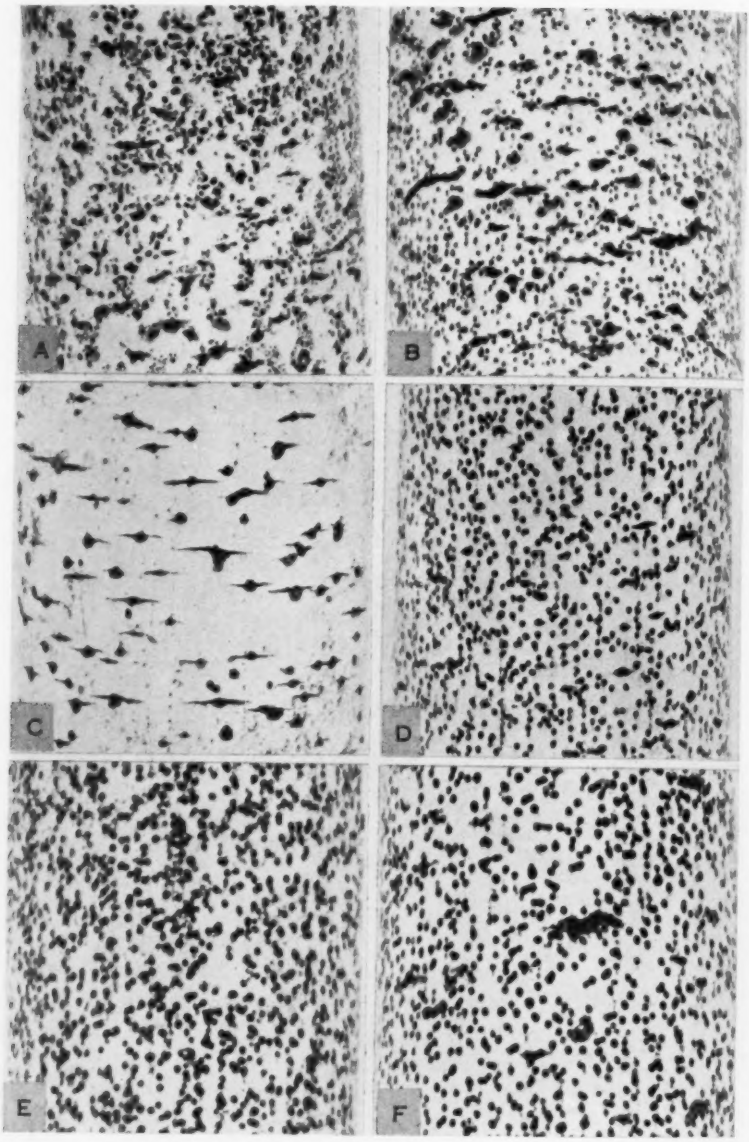

FIGURE 20.—*50 c/min; outer surfaces;* $\times 4$.

A, 25,000 lb/in.², 6 days, IW–W–10.
B, 25,000 lb/in.², 7 days, JR–W–10.
C, 25,000 lb/in.², 9 days, IW–W–10.
D, 20,000 lb/in.², 10 days, JR–W–10.
E, 15,000 lb/in.², 17 days, JR–W–10.
F, 15,000 lb/in.², 24.5 days, JR–W–10.

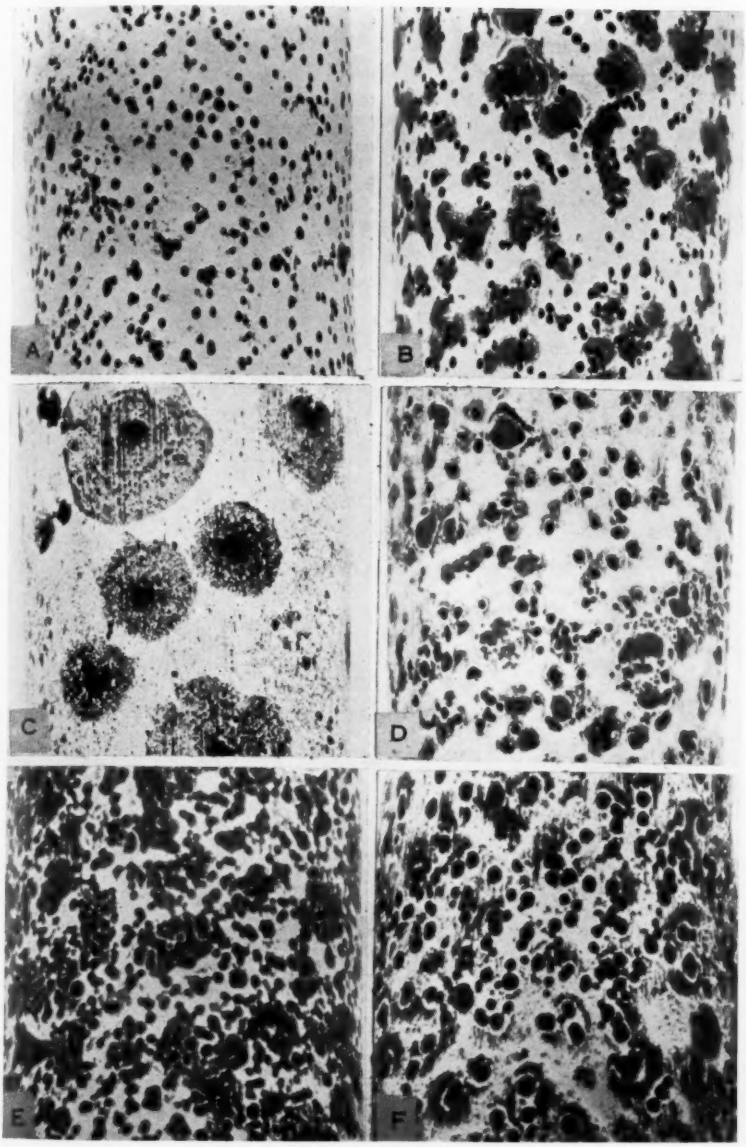

FIGURE 21.—*50 c/min; outer surfaces;* $\times 4$.

A, 13,000 lb/in.², 20 days, IW–W–10.
B, 13,000 lb/in.², 34 days, IW–W–10.
C, 10,000 lb/in.², 27 days, IW–W–10.
D, 10,000 lb/in.², 28 days, IW–W–10.
E, 8,000 lb/in.², 95 days, IW–W–10.
F, 6,000 lb/in.², 173 days, IW–W–10.

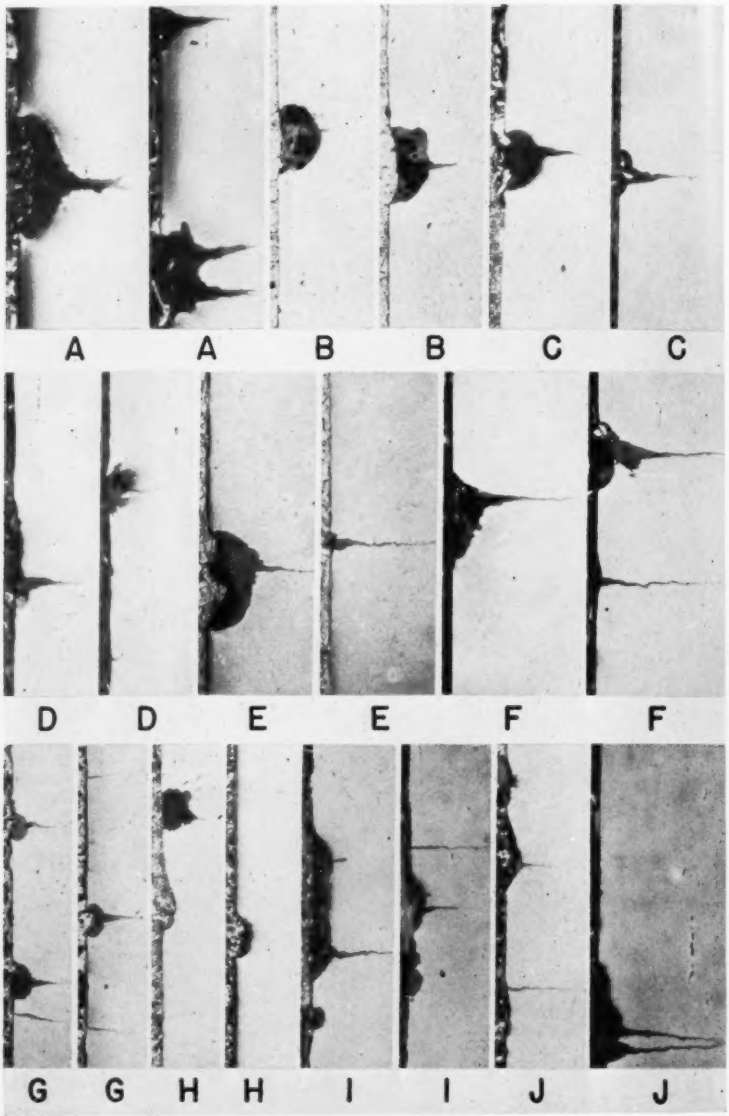

FIGURE 22.—*50 c/min; longitudinal sections;* $\times 50$.

A, 68,000 lb/in.², 1.1 days, IW–W–10.
B, 35,000 lb/in.², 2 days, IW–W–10.
C, 35,000 lb/in.², 3 days, IW–W–10.
D, 30,000 lb/in.², 4 days, IW–W–10.
E, 30,000 lb/in.², 5 days, IW–W–10.
F, 30,000 lb/in.², 6 days, IW–W–10.
G, 30,000 lb/in.², 8 days, IW–W–10.
H, 25,000 lb/in.², 4 days, IW–W–10.
I, 25,000 lb/in.², 6 days, IW–W–10.
J, 25,000 lb/in.², 7 days, JR–W–10.

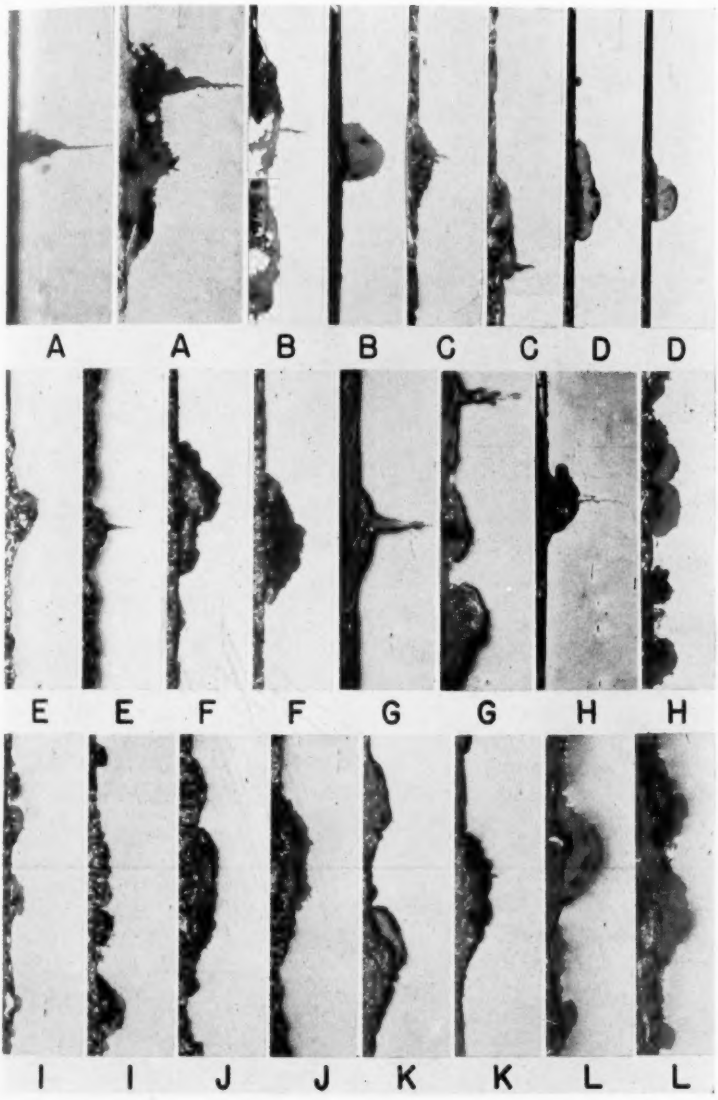

FIGURE 23.—*50 c/min; longitudinal sections;* $\times 50$.

A, 25,000 lb/in.², 9 days, IW–W–10.
B, 20,000 lb/in.², 5.5 days, IW–W–10.
C, 20,000 lb/in.², 10 days, JR–W–10.
D, 16,000 lb/in.², 4 days, IW–W–10.
E, 16,000 lb/in.², 9 days, IW–W–10.
F, 15,000 lb/in.², 17 days, JR–W–10.
G, 15,000 lb/in.², 24.5 days, JR–W–10.
H, 13,000 lb/in.², 20 days, IW–W–10.
I, 12,000 lb/in.², 20 days, IW–W–10.
J, 10,000 lb/in.², 28 days, IW–W–10.
K, 10,000 lb/in.², 45 days, JR–W–10.
L, 6,000 lb/in.², 173 days, IW–W–10.

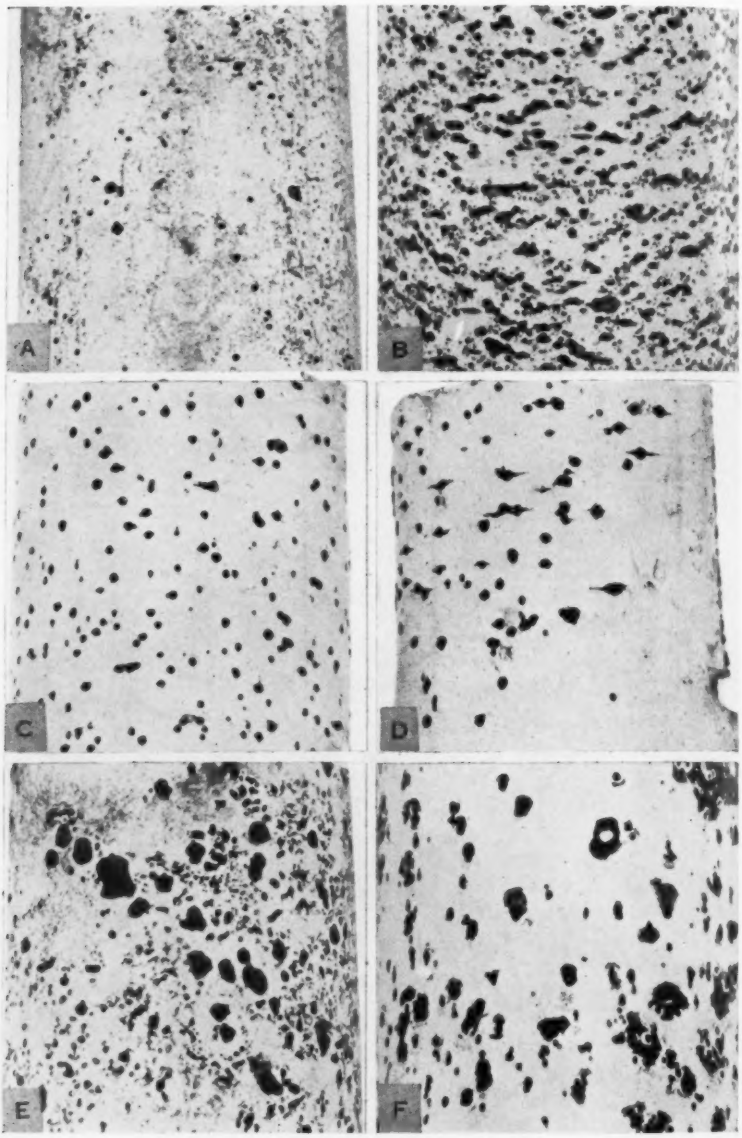

FIGURE 24.—*10 c/min; outer surfaces;* $\times 4$.

A, 45,000 lb/in.^{2}, 2.8 days, IW–W–10.
B, 40,000 lb/in.^{2}, 5 days, IW–W–10.
C, 35,000 lb/in.^{2}, 6.5 days, IW–W–10.
D, 35,000 lb/in.^{2}, 9 days, IW–W–10.
E, 30,000 lb/in.^{2}, 9 days, IW–W–10.
F, 30,000 lb/in.^{2}, 12 days, JR–W–10.

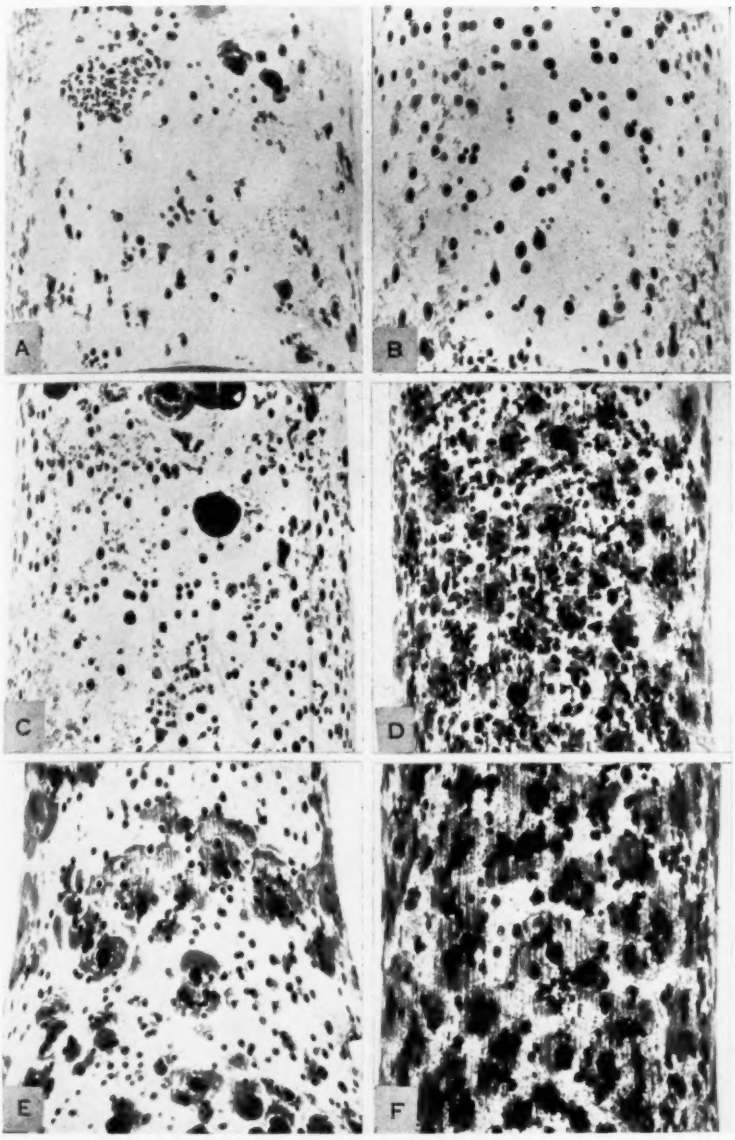

FIGURE 25.—*10 c/min; outer surfaces;* $\times 4$.

A, 25,000 lb/in.², 11 days, IW–W–10.
B, 18,000 lb/in.², 20 days, IW–W–10.
C, 17,000 lb/in.², 25 days, IW–W–10.
D, 15,000 lb/in.², 34 days, IW–W–10.
E, 13,000 lb/in.², 36 days, IW–W–10.
F, 12,000 lb/in.², 70 days, IW–W–10.

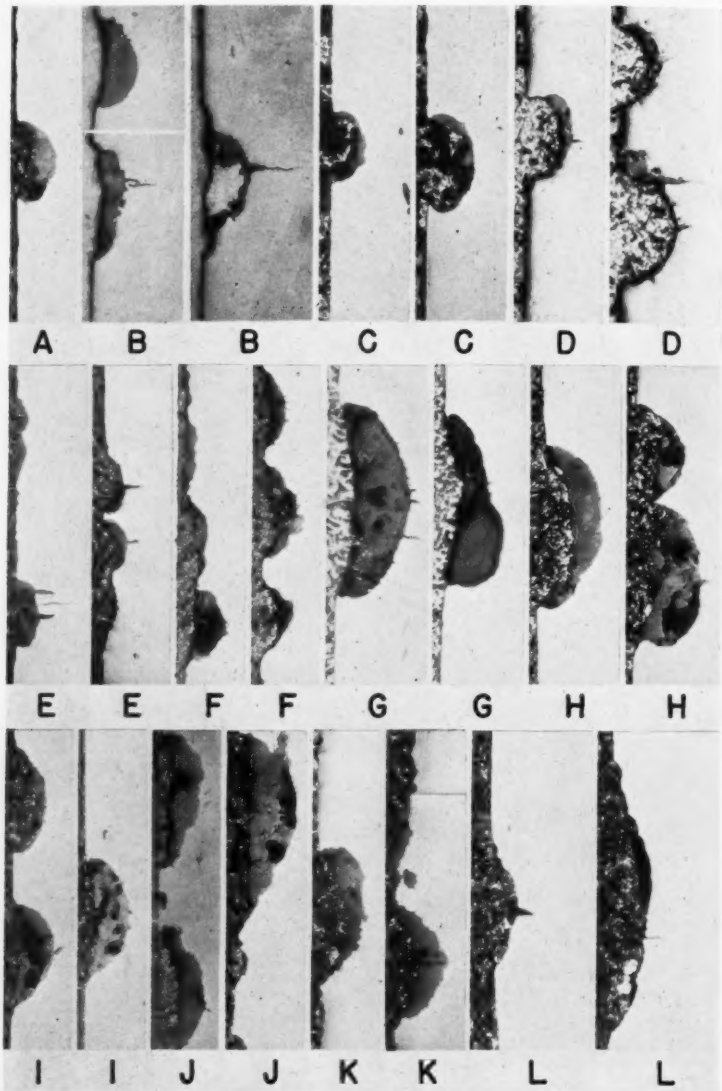

FIGURE 26.—*10 c/min; longitudinal sections; ×50.*

A, 45,000 lb/in.², 2.8 days, IW–W–10.
B, 40,000 lb/in.², 6.5 days, IW–W–10.
C, 35,000 lb/in.², 7 days, IW–W–10.
D, 35,000 lb/in.², 9 days, IW–W–10.
E, 30,000 lb/in.², 9 days, IW–W–10.
F, 25,000 lb/in.², 11 days, IW–W–10.
G, 22,000 lb/in.², 15 days, IW–W–10.
H, 18,000 lb/in.², 20 days, IW–W–10.
I, 17,000 lb/in.², 25 days, IW–W–10.
J, 15,000 lb/in.², 34 days, IW–W–10.
K, 13,000 lb/in.², 36 days, IW–W–10.
L, 12,000 lb/in.², 70 days, IW–W–10.

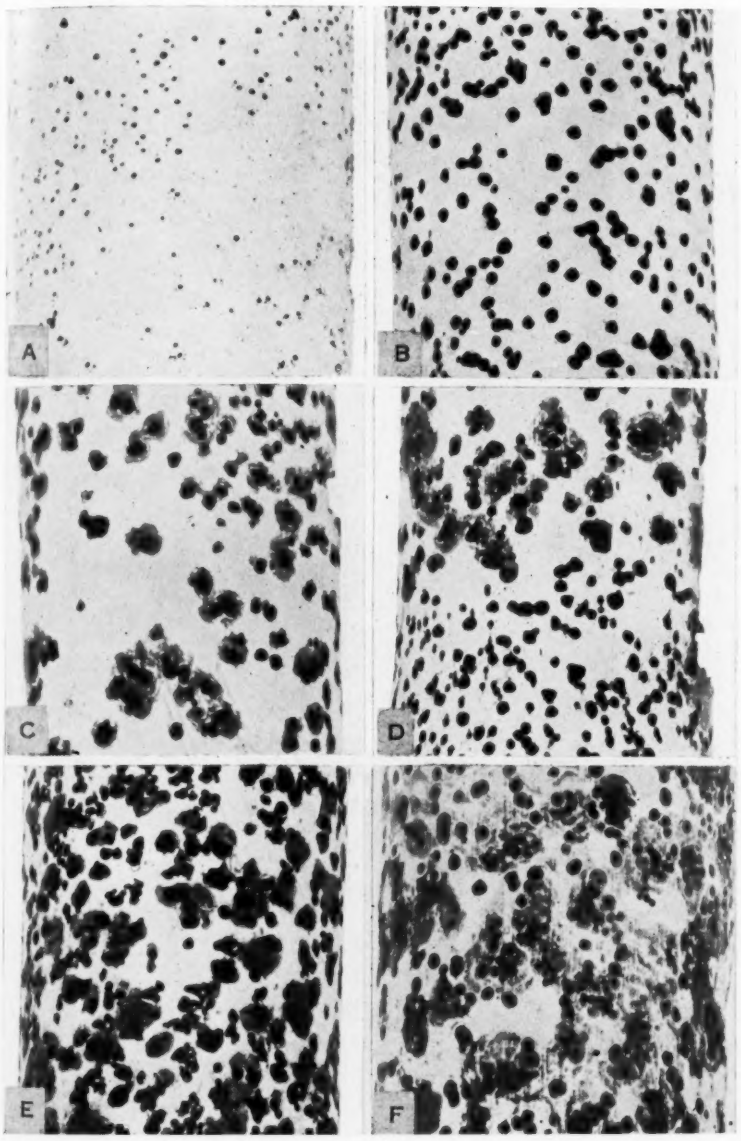

FIGURE 27.—*1.5 c/min; outer surfaces;* $\times 4$.

A, 55,000 lb/in.², 1.2 days, IW–W–10.
B, 35,000 lb/in.², 17 days, IW–W–10.
C, 35,000 lb/in.², 20 days, IW–W–10.
D, 30,000 lb/in.², 23 days, IW–W–10.
E, 30,000 lb/in.², 26 days, IW–W–10.
F, 20,000 lb/in.², 96 days, IW–W–10.

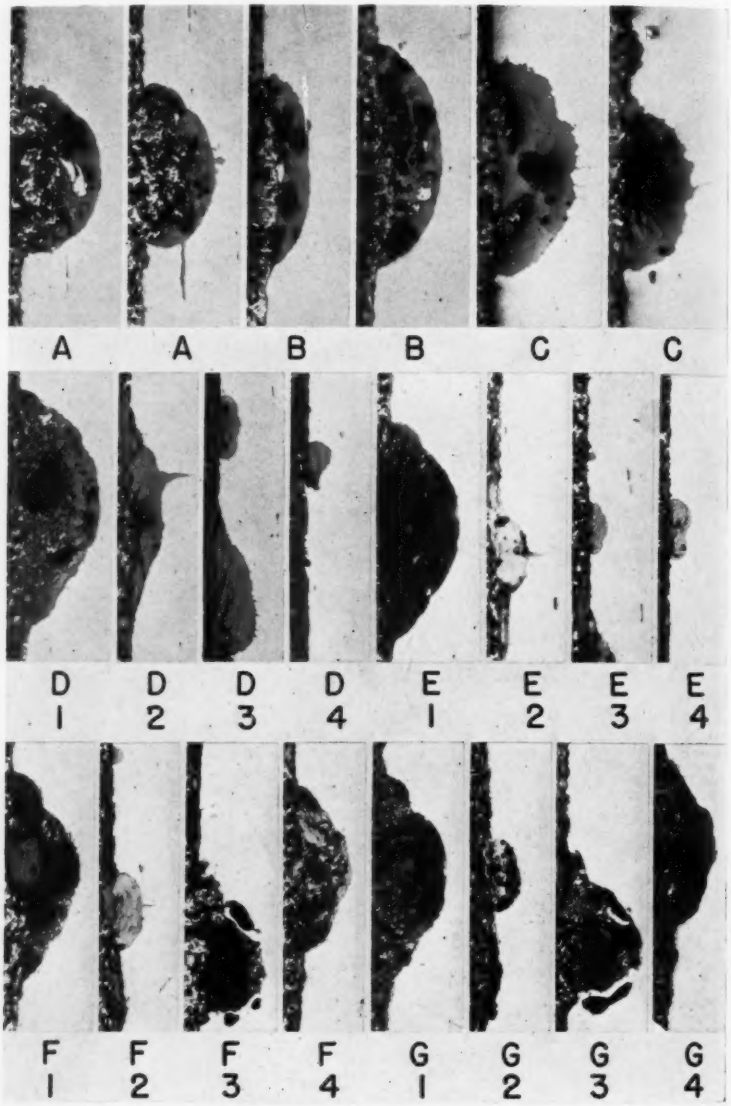

FIGURE 28.—*1.5 c/min; longitudinal sections;* $\times 50$.

A, 35,000 lb/in.², 17 days, IW–W–10.
B, 35,000 lb/in.², 20 days, IW–W–10.
C, 30,000 lb/in.², 23 days, IW–W–10.
D, 25,000 lb/in.², 42 days, IW–W–10.
E, Same as *D*, with 0.001 in. removed.
F, Same as *D*, with 0.002 in. removed.
G, Same as *D*, with 0.003 in. removed.

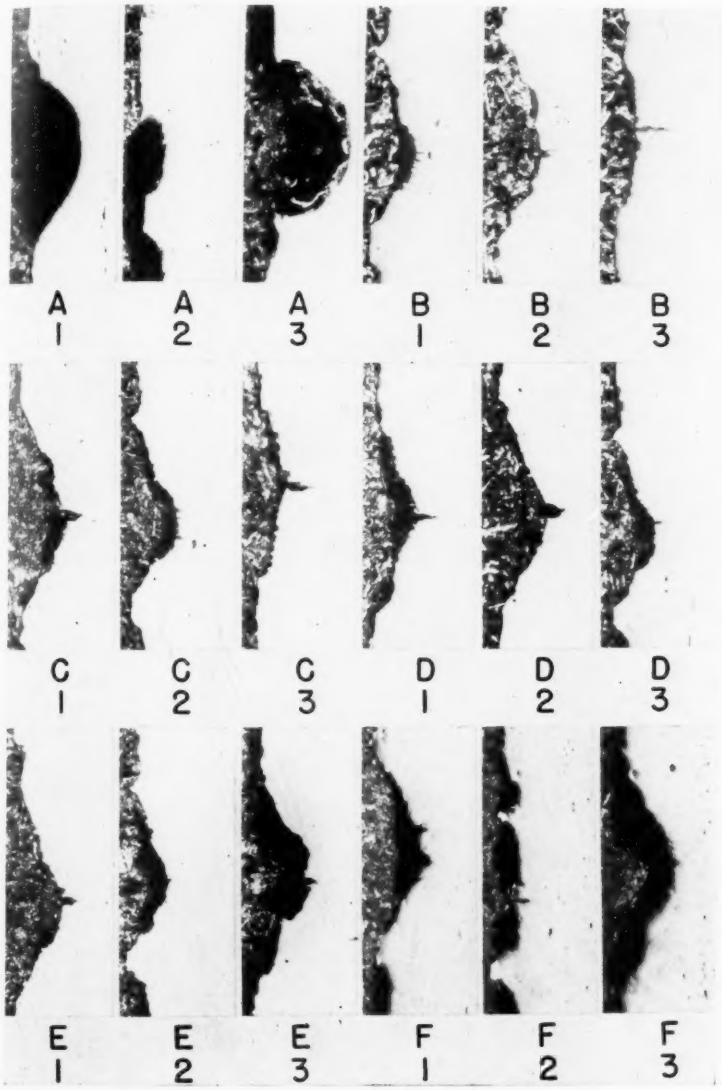

FIGURE 29.—*1.5 c/min; longitudinal sections;* $\times 50$.

A, Same as *D* of figure 29, with 0.004 inch removed.
B, 20,000 lb/in.², 96 days, IW–W–10.
C, Same as *B*, with 0.001 in. removed.
D, Same as *B*, with 0.002 in. removed.
E, Same as *B*, with 0.003 in. removed.
F, Same as *B*, with 0.004 in. removed.

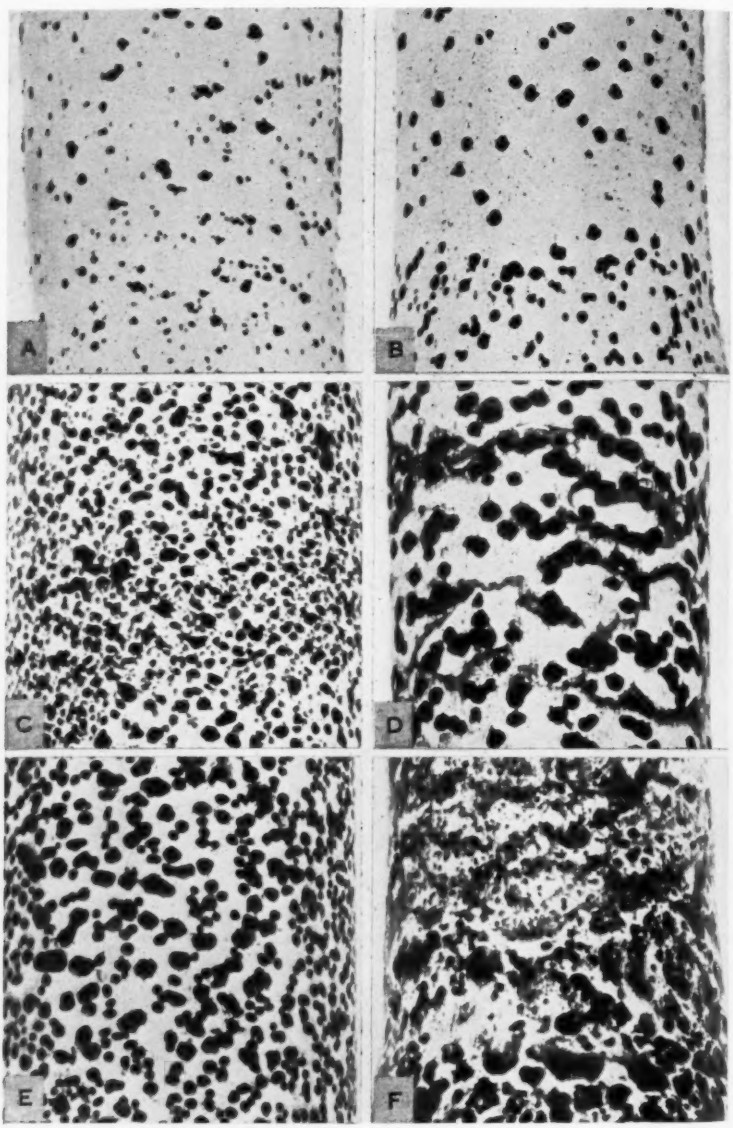

FIGURE 30.—*0.5 c/min, and 5 c/hr; outer surfaces;* $\times 4$

A, 45,000 lb/in.², 8.8 days, 0.5 c/min, IW–W–10.
B, 40,000 lb/in.², 16 days, 0.5 c/min, IW–W–10.
C, 35,000 lb/in.², 19 days, 0.5 c/min, JR–W–10.
D, 35,000 lb/in.², 40 days, 0.5 c/min, IW–W–10.
E, 30,000 lb/in.², 38 days, 0.5 c/min, JR–W–10.
F, 40,000 lb/in.², 146 days, 5 c/hr, LQ–W–10.

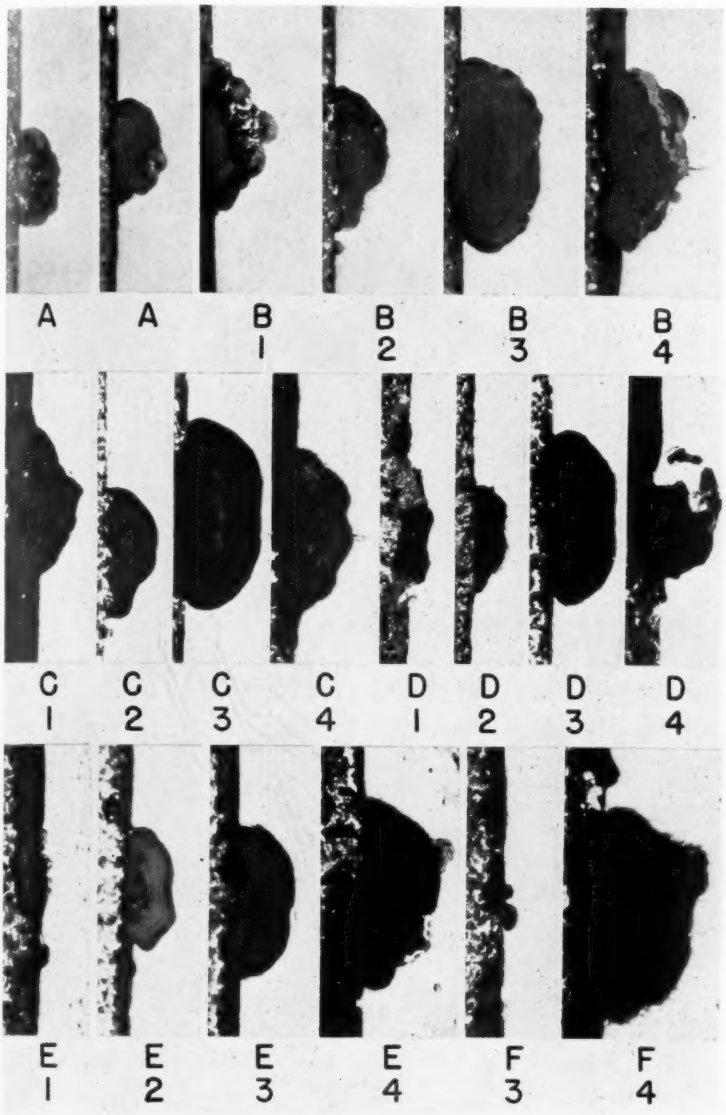

FIGURE 31.—*0.5 c/min; longitudinal sections;* $\times 50$.

A, 45,000 lb/in.², 8.8 days, IW–W–10.
B, 40,000 lb/in.², 16 days, IW–W–10.
C, Same as *B*, with 0.001 in. removed.
D, Same as *B*, with 0.002 in. removed.
E, Same as *B*, with 0.003 in. removed.
F, Same as *B*, with 0.004 in. removed.

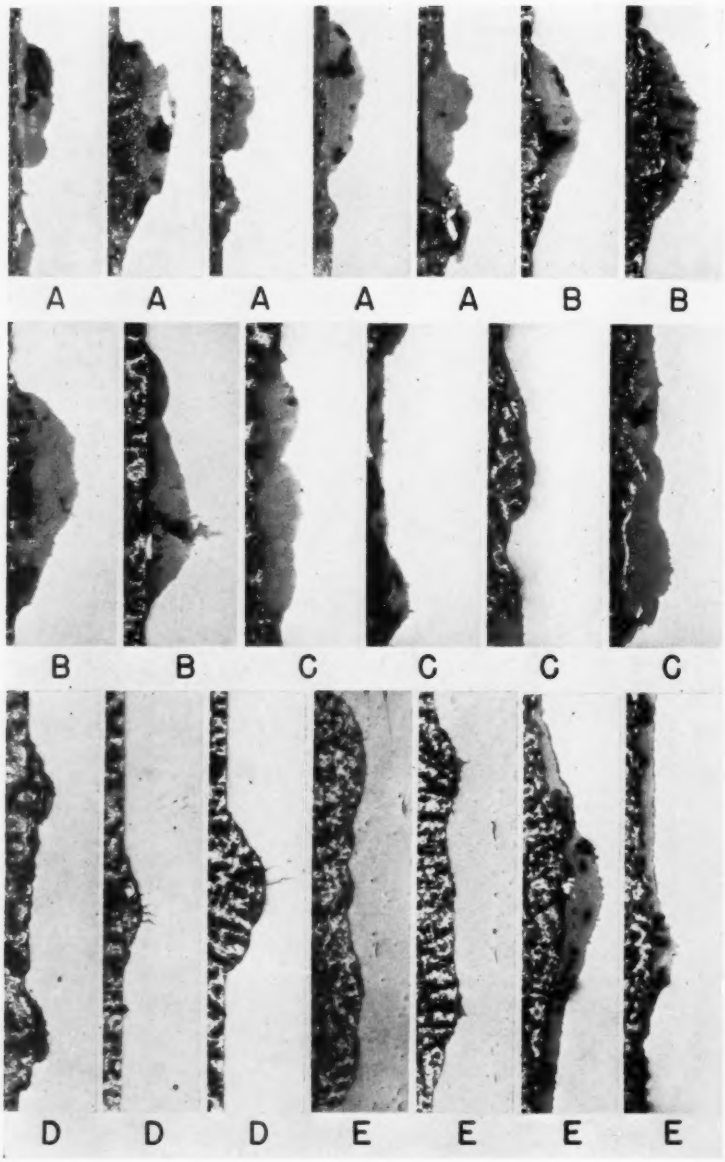

FIGURE 32.—*0.5 c/min and 5 c/hr; longitudinal sections;* $\times 50$

A, 35,000 lb/in.², 19 days, JR–W–10, 0.5 c/min.
B, 35,000 lb/in.², 40 days, IW–W–10, 0.5 c/min.
C, 30,000 lb/in.², 38 days, JR–W–10, 0.5 c/min.
D, 25,000 lb/in.², 15 days, IW–W–10, 0.5 c/min.
E, 40,000 lb/in.², 146 days, LQ–W–10, 5 c/hr.

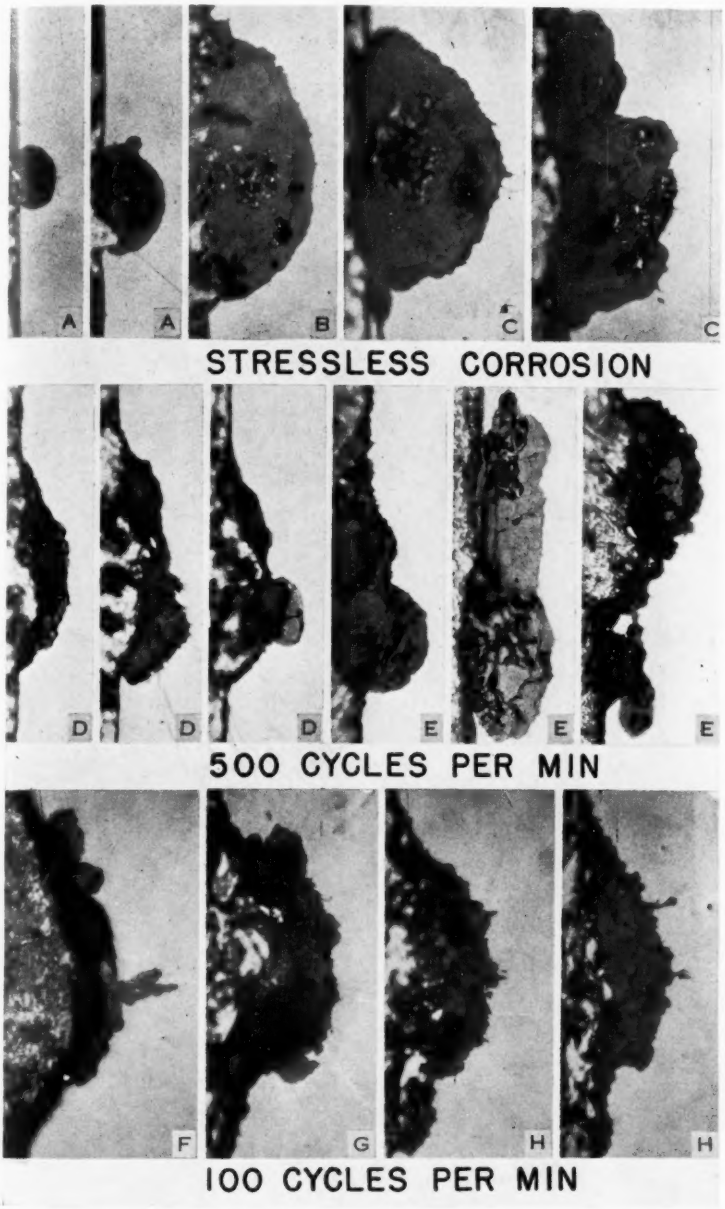

FIGURE 33.—*Stressless corrosion; stress corrosion at 500 c/min and 100 c/min; longitudinal sections;* $\times 250$.

Stressless corrosion

A, 2 days, AX–W–10.
B, 4.7 days, IW–W–10.
C, 10 days, JR–W–10.

Stress corrosion

D, 10,000 lb/in.^{2}, 6 days, BC–W–10.
E, 8,000 lb/in.^{2}, 32.5 days, BC–W–10.
F, 20,000 lb/in.^{2}, 4.5 days, IW–W–10.
G, 12,000 lb/in.^{2}, 11 days, IW–W–10.
H, 9,000 lb/in.^{2}, 25 days, IW–W–10.

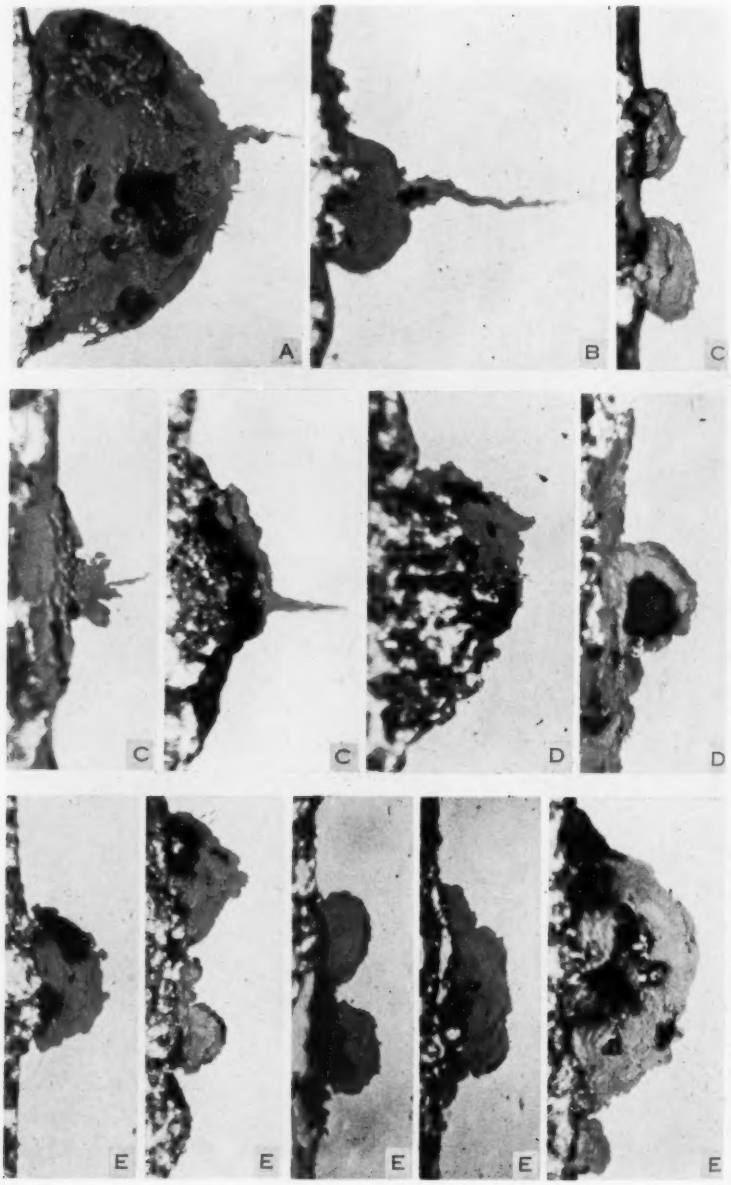

FIGURE 34.—*50 c/min; longitudinal sections;* ×*250.*

A, 35,000 lb/in.², 2 days, IW–W–10.
B, 30,000 lb/in.², 8 days, IW–W–10.
C, 25,000 lb/in.², 7 days, JR–W–10.
D, 16,000 lb/in.², 9 days, IW–W–10.
E, 12,000 lb/in.², 20 days, IW–W–10.

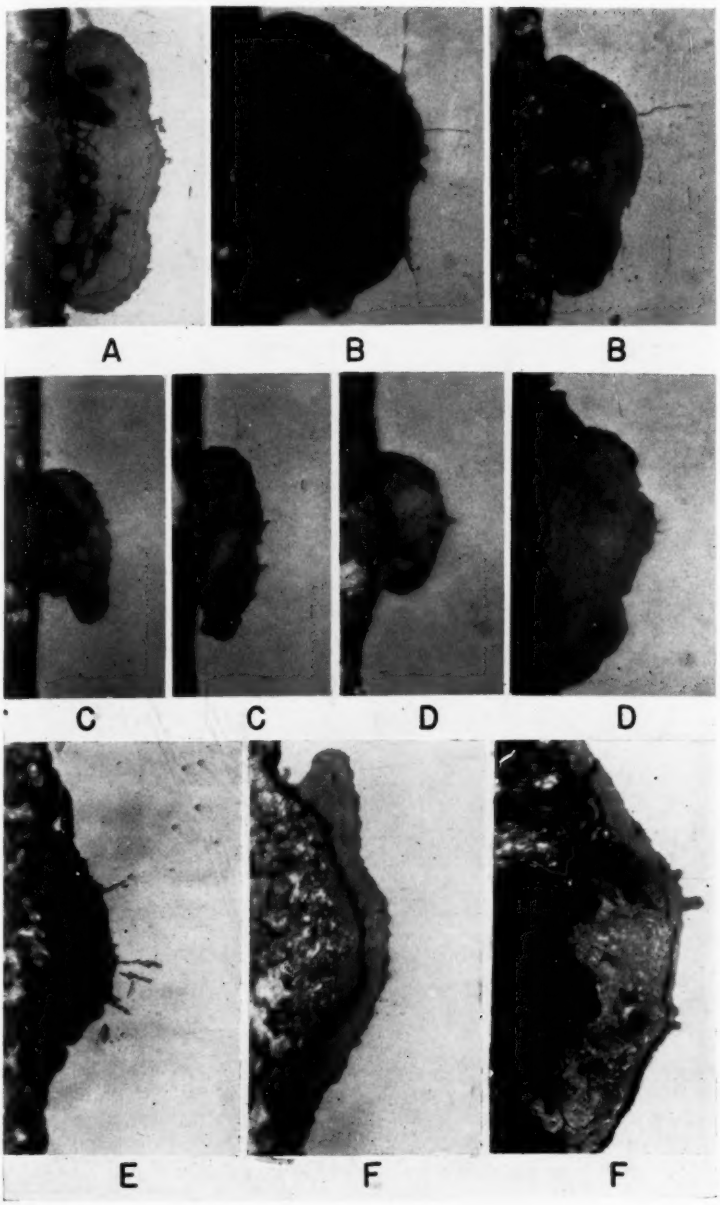

FIGURE 35.—*1.5 c/min and 0.5 c/min; longitudinal sections;* $\times 250$.

A, 25,000 lb/in.², 42 days, IW–W–10, 1.5 c/min.
B, 45,000 lb/in.², 8.8 days, IW–W–10, 0.5 c/min.
C, 40,000 lb/in.², 16 days, IW–W–10, 0.5 c/min.
D, 35,000 lb/in.², 19 days, JR–W–10, 0.5 c/min.
E, 35,000 lb/in.², 40 days, IW–W–10, 0.5 c/min.
F, 30,000 lb/in.², 38 days, JR–W–10, 0.5 c/min.

UNIV. OF MICH.

U. S. DEPARTMENT OF COMMERCE NATIONAL BUREAU OF STANDARDS

RESEARCH PAPER RP1308

Part of Journal of Research of the National Bureau of Standards, Volume 24, June 1940

INFLUENCE OF AUSTENITIC GRAIN SIZE ON THE CRITICAL COOLING RATE OF HIGH-PURITY IRON-CARBON ALLOYS

By Thomas G. Digges

ABSTRACT

A method is described for heating small specimens in vacuo and in an atmosphere of dry nitrogen to different temperatures and quenching directly in hydrogen. Determinations were made of the austenitic grain size and critical cooling rate of high-purity iron-carbon alloys ranging in carbon from 0.23 to 1.21 percent. These data show how carbon influences the austenitic grain size and critical cooling rate of the alloys and make possible a direct comparison of the relation of austenitic grain size to critical cooling rate, or hardenability.

CONTENTS

		Page
I.	Introduction	723
II.	Alloys studied	724
III.	Experimental procedure	724
IV.	Austenitic grain size	728
	1. Previous investigations	728
	2. Effect of rate of heating through the transformation range	729
	3. Effect of temperature	729
V.	Critical cooling rate	730
VI.	Influence of austenitic grain size and carbon content on the critical cooling rate	736
VII.	Surface hardness	738
VIII.	Summary	740
IX.	References	742

I. INTRODUCTION

The critical cooling rate, or hardenability, of a steel at the time of quenching depends primarily upon three factors, namely (1) chemical composition, (2) chemical homogeneity, and (3) grain size. The effect of carbon content on the rate of transformation of austenite in high-purity iron-carbon alloys and in plain carbon steels [1],[1] and the influence of variations in chemical homogeneity on the mode and rate of transformation of austenite on quenching high-purity iron-carbon alloys [2], were discussed in previous reports. The present study was made to determine quantitatively the influence of grain size of the austenite on the critical cooling rate of the iron-carbon alloys.

[1] Figures in brackets indicate the literature references at the end of this paper.

II. ALLOYS STUDIED

The high-purity iron-carbon alloys used in the present study ranged in carbon from 0.23 to 1.21 percent. The alloys were the same as those used in previous investigations, and their preparation was described in detail in a previous report [1]. Essentially, the procedure for preparing these alloys consisted in carburizing hot- and cold-worked specimens of high-purity iron in a mixture of hydrogen and benzene vapor and subsequently homogenizing by heating in vacuo at 1,700° F. Cooling from the temperature used in homogenizing was sufficiently rapid to produce sorbite (fine pearlite) in all of the alloys. Specimens subsequently used for the determination of the austenitic grain size and critical cooling rate had this initial structure of sorbite. The method used in preparing the alloys eliminated the quality factor and variables other than carbon in composition.

The results of spectrochemical and chemical analyses, and the gas content as determined by the vacuum-fusion method for the iron-carbon alloys, are given in table 1. Sulfur, nickel, cobalt, and oxygen were the major impurities contained in the alloys. These elements amounted to about 0.021 percent, whereas the total percentage (by weight) of all impurities determined was about 0.030.

TABLE 1.—*Impurities determined in the iron-carbon alloys*

Element	Method of analysis [1]		
	Spectrochemical [2]	Chemical	Vacuum fusion
	Percent (by weight)	*Percent (by weight)*	*Percent (by weight)*
Manganese		0.002	
Phosphorus		<.001	
Sulfur		.004	
Silicon	0.001	.002	
Copper	<.001	Not detected	
Nickel	.006	.007	
Cobalt		.007	
Calcium			
Lead	<.001		
Magnesium	Probably <.001		
Oxygen	<.001		
Nitrogen			0.003
Hydrogen			.001
			.0002

[1] Determinations were made on specimens from the bars after carburizing and heat treatment for homogeneity, except as follows: Values of nickel, cobalt, and copper by chemical analysis were obtained from the electrolytic iron prior to melting and the values of manganese and phosphorus by chemical analysis were obtained from the bars as carburized. Spectrochemical analyses were made by B. F. Scribner, chemical analyses by W. H. Jukkola and J. L. Hague, and vacuum-fusion analyses by V. C. F. Holm, all members of the staff of the National Bureau of Standards.

[2] Spectrum lines of cobalt and manganese were also found.

III. EXPERIMENTAL PROCEDURE

All the specimens used in the present investigation were approximately 0.10 inch square by 0.040 inch thick. One wire of a 32-gage Chromel-Alumel thermocouple was spot-welded to the center of one flat face of the specimen, and the other wire was spot-welded to the center of the opposite face. The specimens were heated in vacuo or in an atmosphere of dry nitrogen within a Chromel coil to the desired

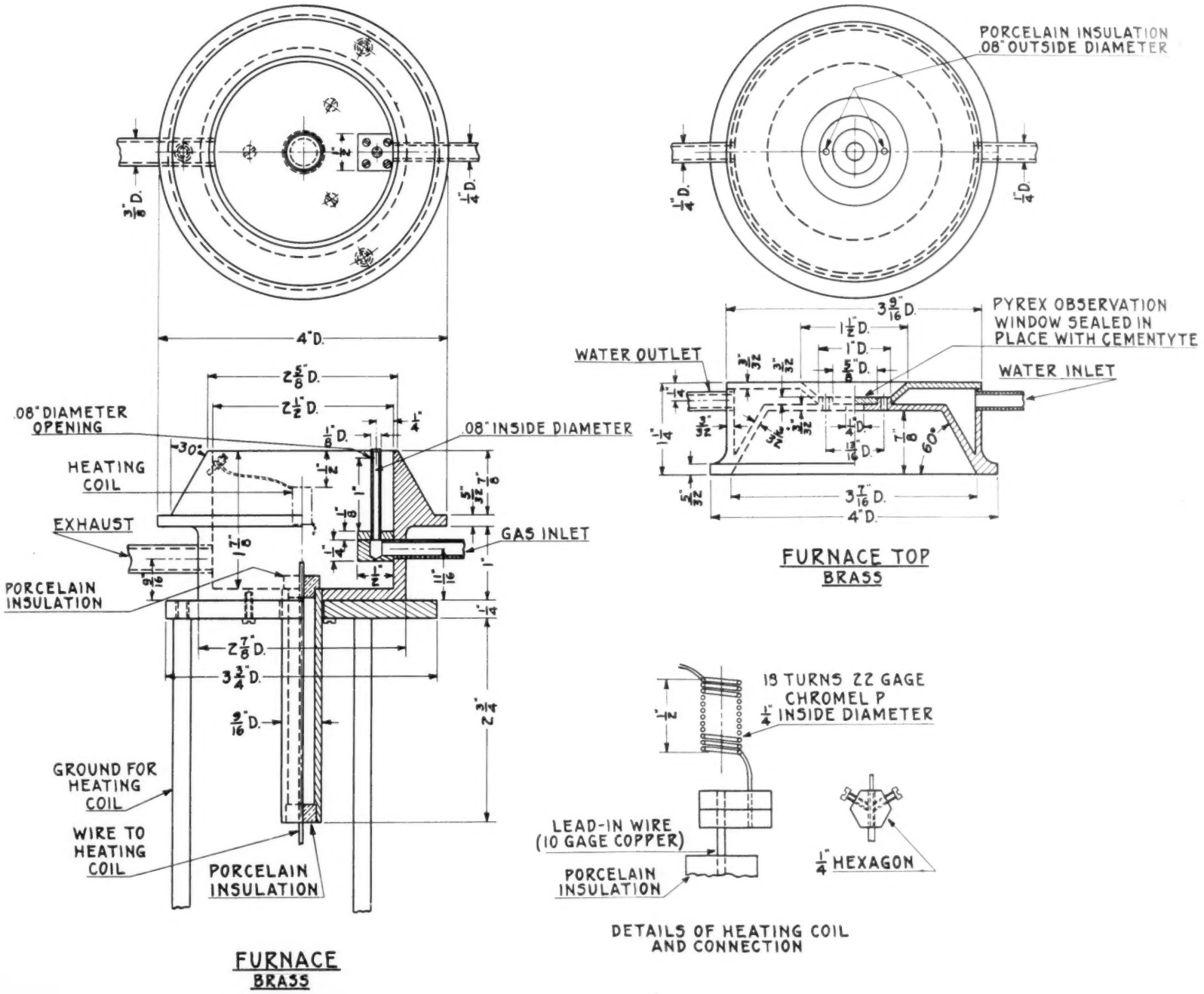

FIGURE 1.—*Details of the construction of the furnace and heating coil for heating specimens in vacuo or in gas.*

Test specimen is supported by 32-gage Chromel-Alumel thermocouple wires passing through porcelain insulation in top of furnace and is so adjusted as to be located in center of heating coil when furnace is assembled. Thermocouples and heating-coil wires are sealed in porcelain insulation with Cementyte.

229032—40 (Face p. 724)

UNIV. OF MICH.

temperature, and were held at that temperature for 15 minutes before cooling.

The specimens used in the determination of the austenitic grain size were cooled from the temperature establishing the grain size in a manner suitable for outlining the grains with proeutectoid ferrite or cementite, or troostite (fine pearlite). Grain-size measurements were made by the method described by Jeffries [3]. The specimens used in the determination of the critical cooling rate were quenched directly from the high temperatures in hydrogen. For correlating the critical cooling rate with microstructure, microscopic examination was made of the quenched specimens on the cross section of the 0.040-inch-thick sheet a short distance from the point of contact of the thermocouple wires.

Figure 1 shows the details of the construction of the furnace, and figure 2 shows the assembly of the apparatus used for heating the specimens either in vacuo or in dry nitrogen and quenching directly in hydrogen. The chamber (*E*) containing the heating coil and the specimen was evacuated before heating the specimen. For heating the specimen in vacuo, the stopcocks (*C*) to the hydrogen tank and (*B*) to the nitrogen train were closed, and the stopcock (*D*) to the vacuum pump was opened. For heating the specimen in nitrogen, the stopcock (*C*) was closed, stopcock (*D*) was opened only until the chamber was evacuated, and nitrogen was admitted into the evacuated chamber until the pressure within the chamber was slightly in excess of that of the atmosphere as shown by the mercury seal. The nitrogen was bubbled through butyl phthalate and over copper heated to 750° to 800° F., and dried by passing through Ascarite, magnesium perchlorate, and phosphorus pentoxide. The stopcock (*B*) to the nitrogen train was closed prior to heating the specimen. At the time of quenching the specimen heated either in vacuo or nitrogen, the stopcocks (*D*) and (*B*) were closed, and the switch (*A*) was opened and the stopcock (*C*) turned to permit passage of hydrogen into the heating chamber. The hydrogen, after passing around the specimen, was exhausted into the air through the mercury seal. The desired cooling rates were obtained by regulating the flow of gas with reducing and needle valves attached to the hydrogen tank, and by changing the position of a gas nozzle within the chamber. With a selected rate of flow of hydrogen, higher cooling rates were obtained when the outlet of the nozzle was directly below the heating coil containing the specimen than when the nozzle was in the side position, shown in figure 1. After the heating chamber was partially evacuated, three "C" clamps (not shown in figs. 1 and 2) were used to clamp together the top and bottom sections of the furnace. This procedure aided in obtaining a tight seal with the stopcock grease used along the tapered surfaces of the furnace, and also prevented the furnace top from lifting during the time of quenching. Stopcocks *B*, *C*, and *D* were specially ground to prevent leakage, and a liquid air trap was used between the furnace and the mercury-diffusion pump.

With the present equipment and with the use of gases as the quenching media, it was possible to heat the specimens in vacuo or dry nitrogen at various rates to different temperatures and to quench directly from these temperatures without moving the specimens.

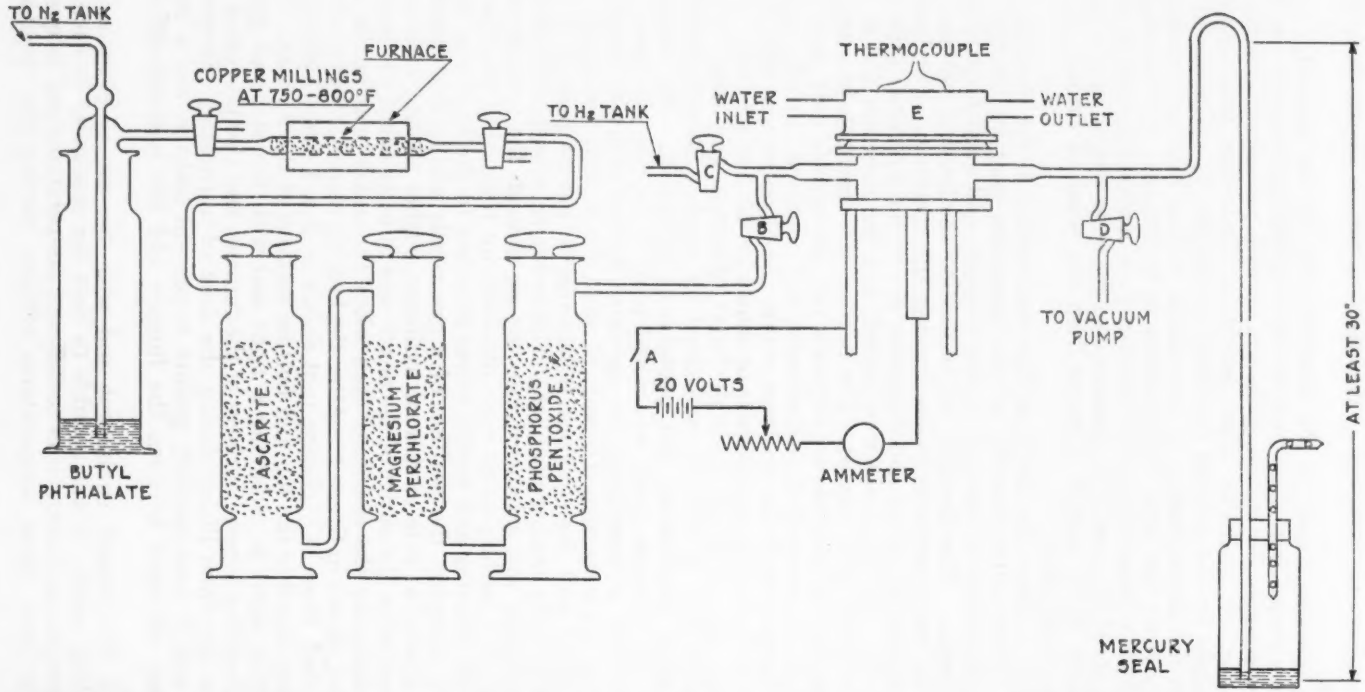

FIGURE 2.—*Assembly of apparatus for heating specimens in vacuo or in an atmosphere of dry nitrogen and quenching directly in hydrogen.*

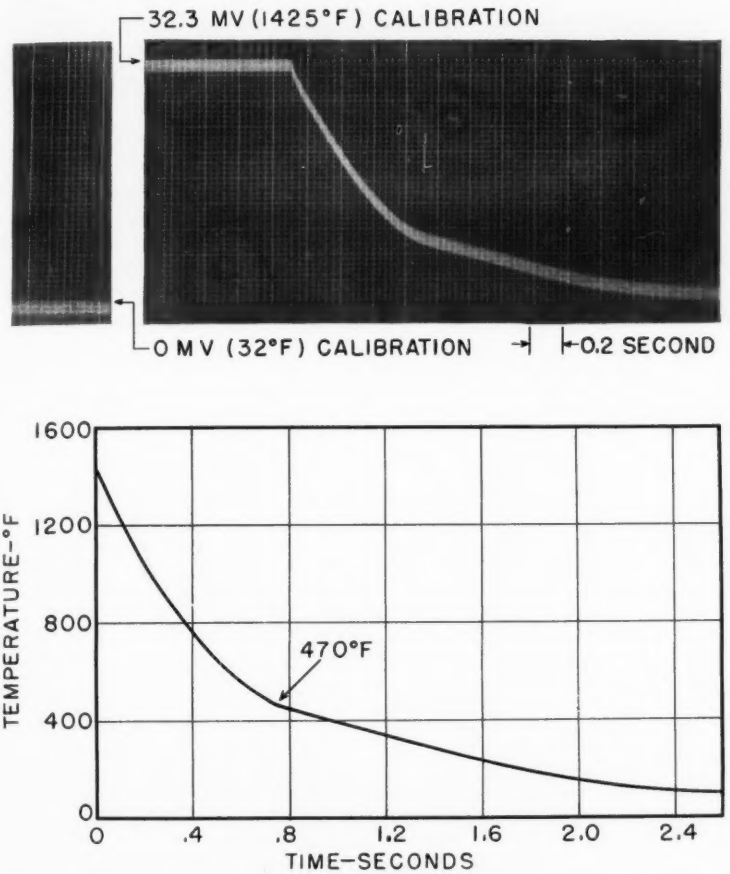

FIGURE 3.—*Photographic record obtained with the string galvanometer apparatus and plotted time-temperature cooling curve.*

Specimen of the alloy containing 0.85 percent of carbon heated in an atmosphere of dry nitrogen and quenched directly in hydrogen at about its critical cooling rate.

FIGURE 2.—*Assembly of apparatus for heating specimens in vacuo or in an atmosphere of dry nitrogen and quenching directly in hydrogen.*

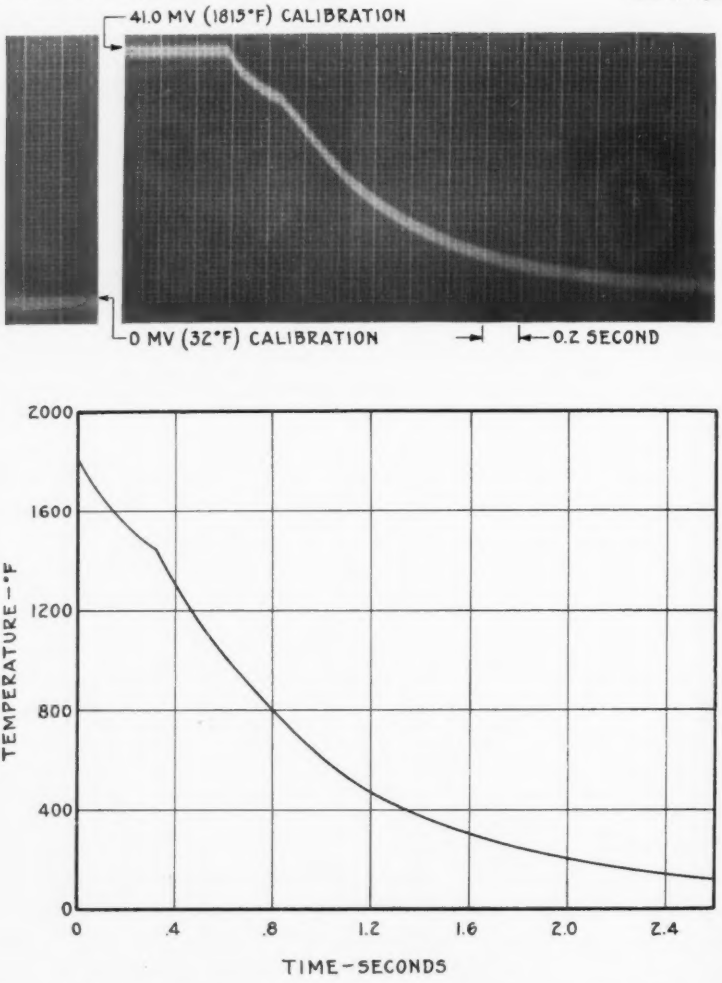

FIGURE 4.—*Photographic record obtained with the string galvanometer apparatus and plotted time-temperature cooling curve.*

Platinum specimen heated in vacuo and quenched directly in hydrogen.

Oxidation of the specimen during the time of heating and quenching was eliminated, and progressive changes in cooling rates were obtainable over the wide range required in the present experiments. The structure produced in the quenched specimens indicated that they were cooled uniformly over the entire surface.

Preliminary tests were carried out to determine whether specimens of high-purity iron were contaminated with aluminum, chromium, and nickel in the process of spot-welding the Chromel-Alumel thermocouple, or during the time of heating the specimens to high temperatures in contact with this couple within a Chromel coil in vacuo. Spectrochemical analysis made on these specimens after removing 0.002 to 0.003 inch from the original surfaces showed no indication of aluminum or chromium, and only a small increase in nickel incident to these treatments.

For the determination of the critical cooling rates, a photographic time-temperature cooling curve was obtained during the quench by means of a string-galvanometer apparatus, in the manner previously described by French & Klopsch [4]. The string galvanometer used consisted of a fine tungsten wire suspended in a strong magnetic field. When this galvanometer is connected to a source of electromotive force, which in this case is a thermocouple, a deflection of the string is obtained which is proportional to the current in the string circuit. Provided the resistance of the string circuit and the strength of the magnetic field remain constant, deflections of the string are directly proportional to the electromotive force and these deflections may be converted into temperature equivalents. The shadow of the string is projected, at about 500 magnification, upon a moving photographic film of bromide paper, 2⅜ inches wide, thus giving a continuous record of variations in temperature during the quench. Time intervals are recorded on the film by interrupting the beam of light with a slotted disk rotated at a constant speed by means of a synchronous motor operated from a tuning fork. A continuous time-temperature cooling curve could be plotted from the data recorded on the film.

Calibration of this apparatus was carried out before each quench by recording on the film the zero position of the string, corresponding to open circuit of the thermocouple (zero emf), and the position of the string when the known emf of the thermocouple corresponding to the quenching temperature was applied (figs. 3 and 4). The emf of the thermocouple corresponding to the quenching temperature was determined with a potentiometer indicator. Change in resistance of the galvanometer circuit resulting from cooling a short length of the thermocouple wires during the time of quenching was relatively small in comparison with the total resistance of the circuit. This variation in resistance was well within the limit of experimental error and could be neglected.

Figure 3 shows a photographic record and plot of a time-temperature cooling curve obtained on a specimen of the 0.85-percent-carbon alloy heated in an atmosphere of dry nitrogen to 1,425° F and quenched directly in hydrogen at about its critical cooling rate. No arrest appeared in the cooling curve until the temperature of the specimen had fallen to about 470° F. At approximately this temperature the austenite started to transform to martensite (Ar''). The Ar'' transformation, however, was not clearly shown in the photographic records

obtained on quenching the relatively stable austenite of the hypereutectoid alloys. With the hypereutectoid alloys, the Ar'' occurred at temperatures below the arrest shown in figure 3, a factor that made difficult its detection.

A photographic record and a plot of the time-temperature curve obtained on a platinum specimen heated in vacuo to 1,800° F and quenched directly in hydrogen are shown in figure 4. There was an arrest in the cooling curve at about 1,450° F, or about 350° F below the temperature at the start of the quench. The arrest, obviously, was not due to a heat evolution caused by a structural change in the platinum specimen. This high-temperature arrest was observed in the cooling curves of all the specimens heated in vacuo and rapidly quenched directly in hydrogen, but it was not observed in the specimen heated in an atmosphere of nitrogen and similarly quenched. The arrest was therefore characteristic of the procedure used in heating in vacuo and quenching directly in hydrogen, and was probably due to the variation in rate of flow of the quenching gas around the specimen during a short interval at the start of the quench. Such an arrest in the cooling of specimens by heating in vacuo and quenching directly in hydrogen has no appreciable effect on the rate of transformation of austenite, provided the quenching temperature is sufficiently high for the lag to occur above or in the vicinity of Ae_1. With quenching temperatures just above Ae_1, the arrest may occur in the upper range in which austenite is least stable (1,110° to 930° F) and thus have an influence in the formation of the decomposition products of austenite of high transformation rate. To eliminate this factor in the determination of the critical cooling rate, the specimens quenched directly from temperatures just above Ae_1 were heated in an atmosphere of dry nitrogen.

As shown in figure 4, no arrest occurred on cooling the platinum specimen through the temperature range below 950° F. With high-purity iron-carbon alloys containing carbon in excess of 0.20 percent, the transformation of austenite to martensite begins at temperatures below 950° F.

IV. AUSTENITIC GRAIN SIZE

1. PREVIOUS INVESTIGATIONS

Reviews of some of the most important works on the subject of austenitic grain size have recently been prepared by Shapiro [5] and by Ward and Dorn [6]. Shapiro states that "The final austenitic grain size of any steel is influenced by: (1) prior structure or initial grain size, (2) mechanical deformation (hot and cold work) which remains or is conferred upon it during austenitizing, (3) the rate of heating to the austenitic condition, (4) time and temperature of heating (T^{max}), (5) method of deoxidation, and (6) the type of inhibitors resulting from the deoxidization process. These factors may either intensify or minimize one another's effects and thereby may either refine or increase the austenitic grain size, depending on whether they act in a like or opposite manner."

Derge, Kommel, and Mehl [7] have investigated some of the factors influencing austenitic grain size in high-purity steels. They conclude that "Al_2O_3 and SiO_2 inhibit grain growth; whereas aluminum and silicon in solid solution do not, and that the degree of inhibition is closely related to the type of dispersion of the oxides." Grossmann

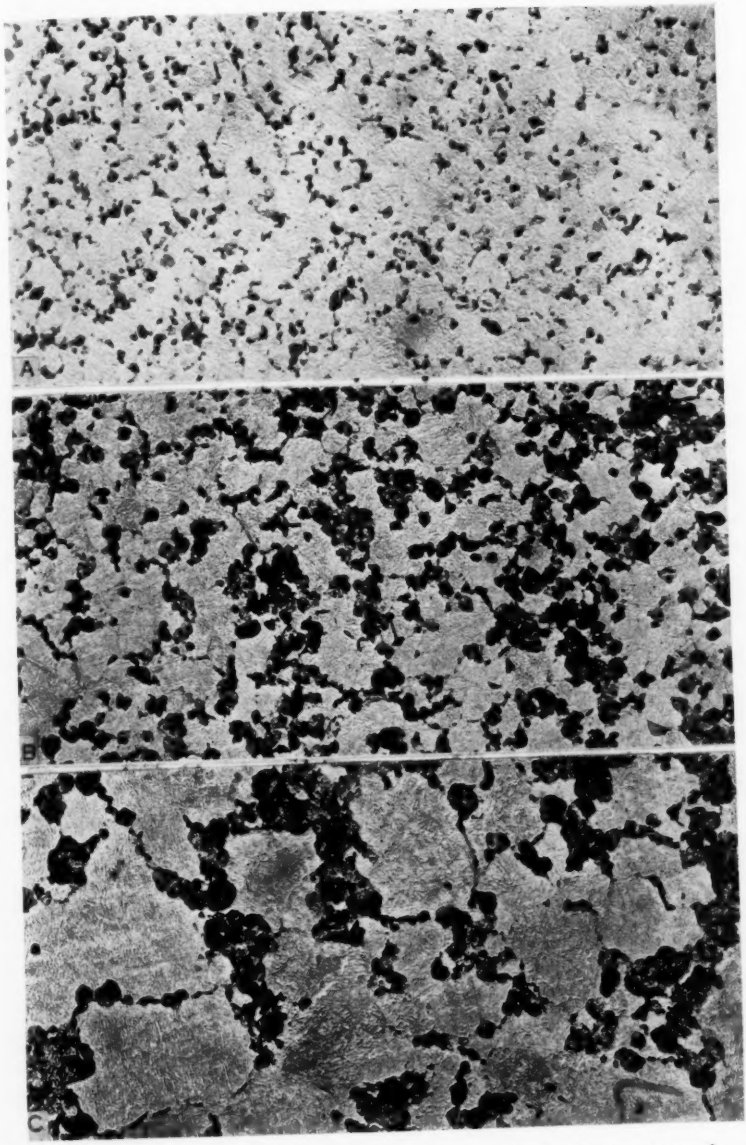

FIGURE 5.—*Effect of rate of heating through the transformation range on the grain size at 1,425° F of iron-carbon alloy containing 0.73 percent of carbon.*

A, Heated rapidly in lead bath at 1,425° F; approximately 40 grains per square inch at 100 diameters. *B*, Heated from 70° to 1,400° F in 1 minute; approximately 20 grains per square inch at 100 diameters. *C*, Heated from 70° to 1,415° F in 2½ minutes; approximately 5 grains per square inch at 100 diameters. Etched with 1-percent nital. ×100.

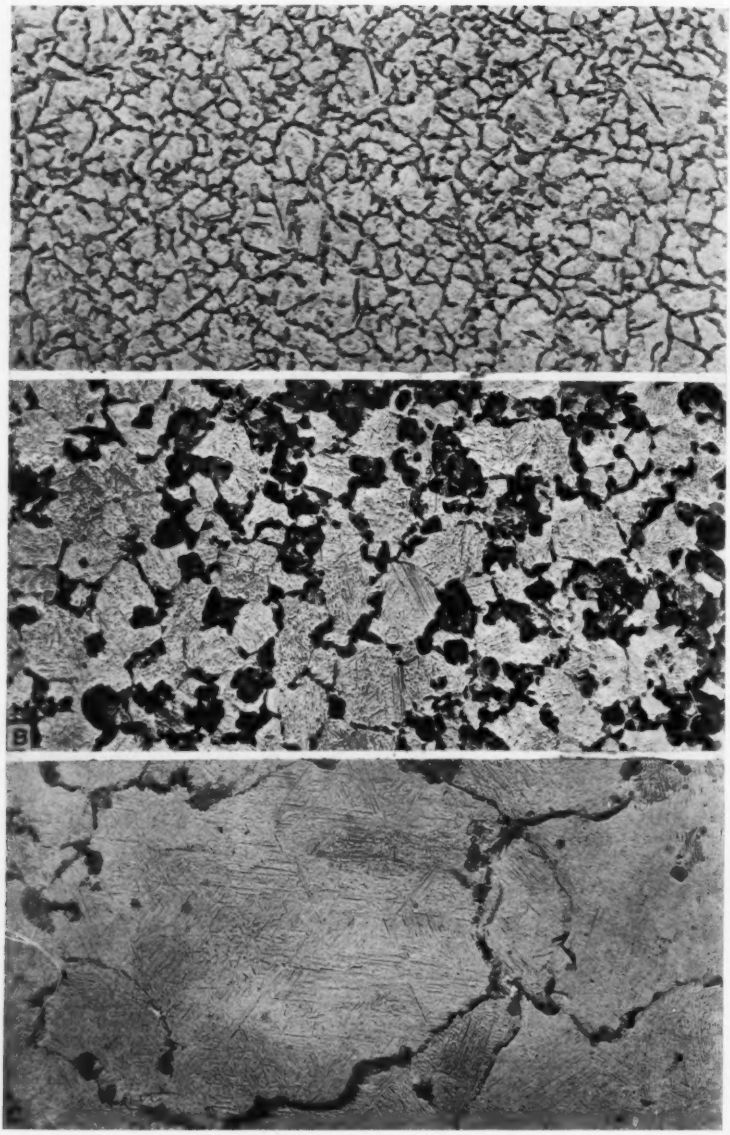

FIGURE 6.—*Effect of rate of heating through the transformation range on the grain size at 1,600° F of iron-carbon alloy containing 0.50 percent of carbon.*

A, Heated rapidly in lead bath at 1,600° F; approximately 50 grains per square inch at 100 diameters. *B*, Heated from 70° to 1,500° F in 51 seconds; approximately 15 grains per square inch at 100 diameters. *C*, Heated from 70° to 1,415° F in 2½ minutes; approximately 1 grain per square inch at 100 diameters. Etched with 1-percent nital. ×100.

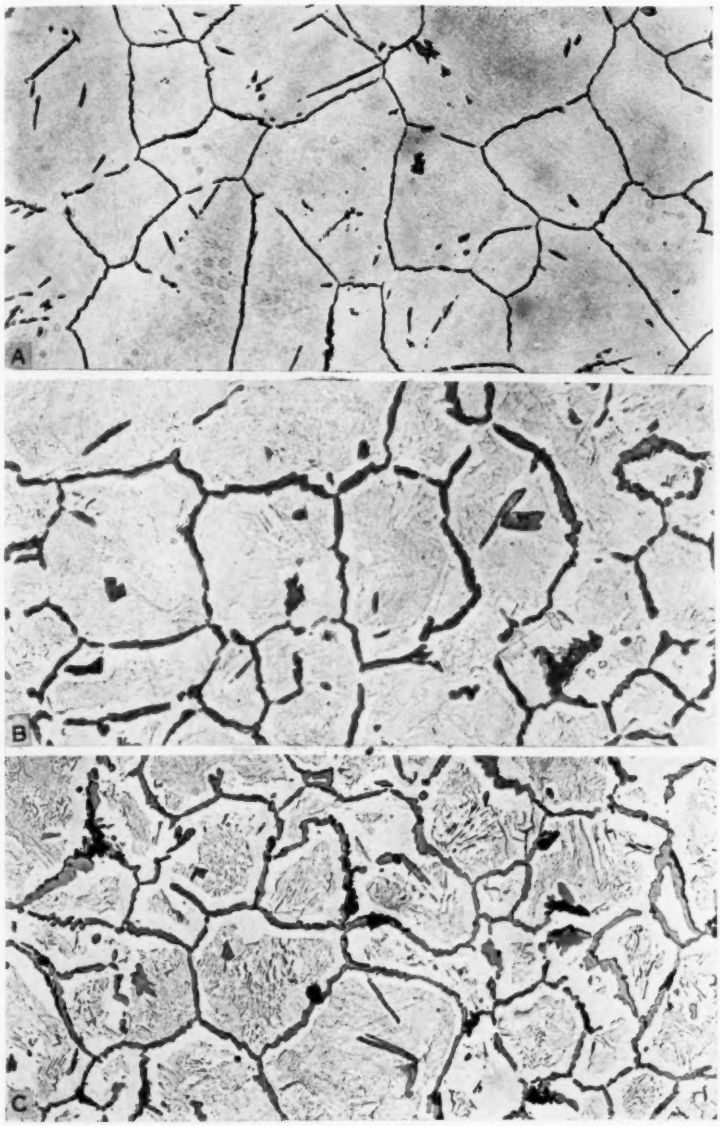

FIGURE 7.—*Effect of rate of heating through the transformation range on the grain size at 1,800° F of iron-carbon alloy containing 1.21 percent of carbon.*

A, Heated from 70° to 1,750° F in 1 minute; approximately 2.2 grains per square inch at 100 diameters. *B*, Heated from 1,330° to 1,370° F in 24 minutes; approximately 2.3 grains per square inch at 100 diameters. *C*, Heated from 1,330° to 1,370° F in 38½ minutes; approximately 3.2 grains per square inch at 100 diameters. Etched with boiling sodium picrate. ×100.

[8] has discussed the mechanism of grain growth in low-carbon steels during carburization. He shows that upon heating a low-carbon steel, the first austenite appears at the interfaces of the ferrite and carbide. As the temperature of heating is increased, the austenite begins to encroach on the ferrite grains and proceeds until the steel is completely transformed to austenite.

2. EFFECT OF RATE OF HEATING THROUGH THE TRANSFORMATION RANGE

Specimens of the high-purity iron-carbon alloys were heated at various rates through the transformation range to temperatures ranging from 1,425° to 1,800° F. The grain sizes obtained with the different rates of heating for the 0.73-percent-carbon alloy at 1,425° F are shown in figure 5, for the 0.50-percent-carbon alloy at 1,600° F in figure 6, and for the 1.21-percent-carbon alloy at 1,800° F in figure 7. The grain size established at temperatures ranging from 1,425° to 1,600° F increased markedly with decrease in rate of heating these high-purity alloys, whereas the grain size at 1,800° F was not so noticeably dependent upon the rate of heating. Additional data on this subject will be presented in a subsequent report.

3. EFFECT OF TEMPERATURE

The grain sizes at temperatures ranging from 1,425° to 2,100° F were determined for the alloys, and the results are summarized in table 2. Although the specimens were heated at a rapid rate through the transformation range, this rate was not precisely the same for all the specimens. With the heating rate employed and with complete solution of carbon, all the alloys had approximately the same average grain size at any selected temperature within the range of 1,600° to 2,100° F. At temperatures of 1,425° and 1,500° F, some variations were observed in the average grain size of the different alloys, which were probably due to small differences in rate of heating or to masking of some of the smaller size grains by coalescence of the constituent used in outlining the parent austenite grain.

TABLE 2.—*Austenitic grain size of the iron-carbon alloys*

[The specimens, 1/10 inch square by 0.040 inch thick, were heated rapidly in vacuo or in an atmosphere of dry nitrogen to temperatures indicated, held at temperature for 15 minutes, and then cooled in a manner suitable for outlining the grains. In general, each grain-size value reported is the average of four determinations made on one specimen]

Carbon	Average number of grains per square inch at 100 diameters at various temperatures, °F											
	1,425	1,500	1,550	1,600	1,650	1,700	1,750	1,800	1,900	2,000	2,050	2,100
%												
0.23	------	------	------	------	------	[a](8)	------	2.2, 2.2	------	1.1	------	0.8
.40	------	------	------	------	------	------	------	2.3, 2.7	------	------	------	------
.50	------	12	------	12, 9, 7	------	------	------	2.3, 3.0	------	------	------	------
.62	13, 15	10, 8	------	9	------	8, (8), (8)	------	2.5, 3.2, 3.7, 3.5	------	------	------	1.5
.73	23	17	------	13, 12	------	------	------	2.0, 2.5, 2.7, 3.5, 3.5, 3.0.	------	------	1.6	------
.80	------	25	14	11	------	------	------	3.0, 2.7	------	------	------	------
.85	------	17	------	------	------	8	------	2.8	------	.8	------	------
1.01	------	------	------	16, 15, 10	------	6, (8)	------	3.1	2.1	1.6	------	------
1.14	------	------	------	------	9	6, 7, (9), (8).	4	3.1	2.1	1.9	------	------
1.21	------	------	------	------	------	9, (9)	------	2.8, 1.9, 2.3, 2.7, 3.5, 3.1, 3.7.	------	------	------	------

[a] The values appearing in parentheses were obtained in a previous investigation [1] on specimens ¼ inch square by 0.040 inch thick, heated rapidly in dry nitrogen.

Carbon was the only element present in these alloys in a sufficient amount that might be considered in the class of grain-growth inhibitors. At temperatures required for complete solution in austenite (that is, above Ac_3 or Ac_m), carbon evidently is not effective in inhibiting grain growth in high-purity iron-carbon alloys. For example, at 1,700° F each of the alloys ranging in carbon from 0.23 to 1.21 percent had an average grain size of about 6 to 9 grains per square inch at 100 diameters. This temperature is only slightly above the A_{cm} for the 1.21-percent-carbon alloy, whereas it is approximately 370° F in excess of the temperature required for complete solution of carbon in the alloy of eutectoid composition. The actual temperature (T_{max}) and the rate of heating through the transformation range were the dominant factors in controlling the austenitic grain size of these alloys.

V. CRITICAL COOLING RATE

Davenport and Bain [9], and coworkers [10], in their studies of the process and results of the transformation of austenite at constant temperatures, showed that the structure and hardness of a quenched steel depend primarily on the particular temperature at which the austenite decomposes during quenching. The general form of the transformation temperature-time curve (the so-called S-curve when temperature is plotted on Cartesian and time on a logarithmic basis) was the same for all steels investigated, but there were significant differences in the position of the S-curve on the time scale and minor differences on the temperature scale. Their results showed that the hardenability of a steel depends upon the stability of the quenched austenite in the temperature range of about 1,110° to 930° F, the upper bend of the S-curve, figure 8. This is the upper range in which austenite is most likely to decompose and in which its decomposition products are relatively soft. If by a continuous quench to room temperature the austenite is cooled through this temperature range without decomposing (figure 8, curve *A*), it transforms only in the temperature range below about 300° F and the product of decomposition is martensite. If the austenite is cooled at a slower rate through this upper temperature range (curve *C*), part of the austenite transforms in this temperature range to troostite (fine pearlite) and the remaining austenite is cooled unchanged to the temperature favorable for its decomposition to martensite. At some cooling rate, called the critical cooling rate, the austenite just begins to decompose (curve *B*), in the range 1,110° to 930° F. Obviously, the critical cooling rate of a steel is an index to the stability of its austenite in this temperature range. The slower the critical cooling rate the more stable is its austenite in the temperature range 1,110° to 930° F and the deeper is the hardening.

In the present experiments, the critical cooling rate was taken as the average cooling rate between 1,110° and 930° F, which produced in the quenched specimens a structure of martensite with nodular troostite in amounts estimated to be between 1 and 3 percent.

As shown in previous experiments [2] in which specimens of the alloys were quenched directly from 1,800° F, the Ar'' transformation commenced in some of the alloys at temperatures appreciably higher than in the plain carbon steels used in the interrupted quench experiments of Davenport and Bain. Data on the isothermal transformation of austenite in high-purity iron-carbon alloys would be of particu-

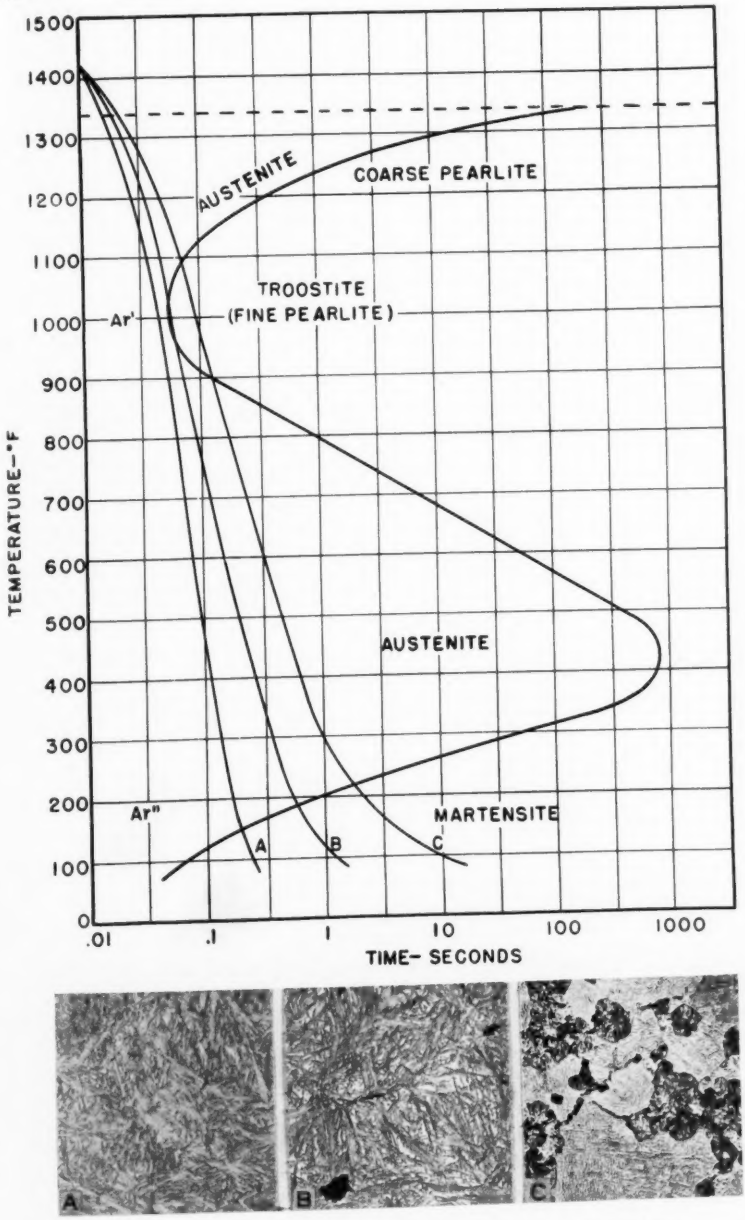

FIGURE 8.—*Decomposition of austenite at various temperatures.*

The diagram illustrates the method of determining the critical cooling rate and the structures obtained with different cooling rates. *A*, Martensite; ×250. *B*, Martensite with small amount of troostite (critical cooling rate); ×250. *C*, Martensite and troostite; ×100. All specimens etched with 1-percent nital.

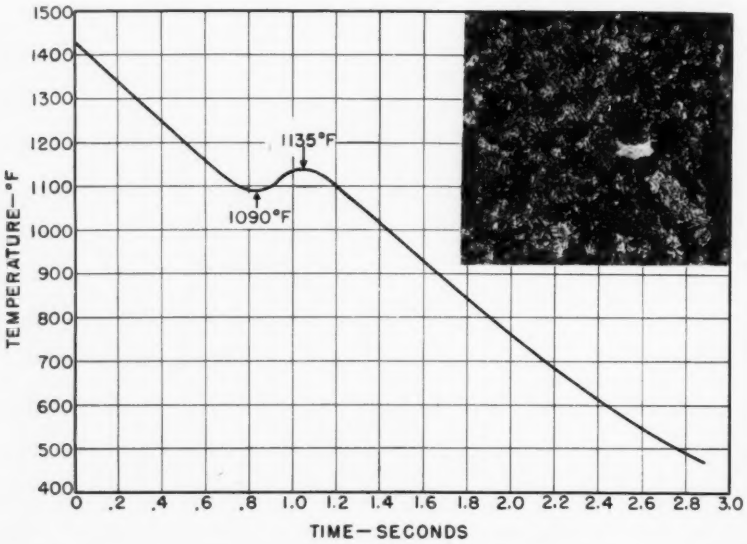

FIGURE 9.—*Time-temperature cooling curve and structure of iron-carbon alloy containing 0.80 percent of carbon.*

Quenched structure consisted of troostite with a trace of martensite. Etched with 1-percent nital. ×100.

lar assistance in the determination of the critical cooling rates by definitely establishing the upper range in which the austenite is most likely to decompose. Accurate data on this subject would be difficult to obtain because of the relatively high transformation rates of austenite in high-purity iron-carbon alloys, especially those of the lower carbon contents.

Although the transformation rates of austenite at constant temperature levels were not determined for the alloys, some data obtained in the continuous quench experiments throw light upon the temperatures of the *Ar'* and *Ar''* transformations. These data for the alloys, ranging in carbon from 0.62 to 1.01 percent, are summarized in table 3 and in figures 9 and 10. In general, the start of the *Ar'* occurred within the temperature range of about 1,110° to 930° F, provided the specimens were cooled at the most rapid rate possible for the austenite to transform completely to troostite. This fact is shown by the cooling curve and microstructure, reproduced in figure 9, for a specimen of the 0.80-percent-carbon alloy quenched directly

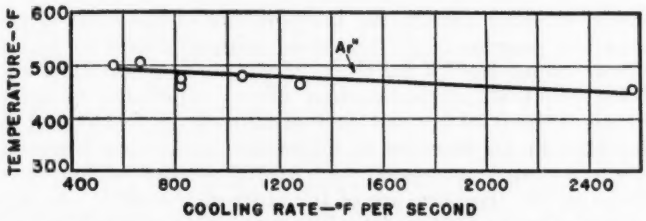

FIGURE 10.—*Relation of cooling rate to temperature of the start of Ar'' for iron-carbon alloy containing 0.80 percent of carbon quenched from 1,425° F.*

Except for the cooling rate of 560° F per second, where a correction was made for the heat effect due to the *Ar'* transformation, all cooling rates are based on the average rate required for the specimen to cool through the temperature range of 1,110° to 930° F.

from 1,425° F. The austenite was cooled unchanged to a temperature of about 1,090° F, which is in the upper portion of the range 1,110° to 930° F. At this temperature the austenite started to decompose, as shown by the inflection in the cooling curve, the evolution of heat accompanying the transformation causing a 45° F rise in temperature to a maximum of 1,135° F in 0.2 second. The transformation of the austenite continued at approximately this temperature for about 0.1 second, and additional transformation of austenite to troostite undoubtedly occurred while the specimen cooled through the *Ar'* temperature range. A small proportion of the austenite was cooled to the temperature (*Ar''*) favorable for its transformation to martensite. This is shown by the microstructure of the quenched specimen, which consisted of a trace of martensite in a matrix of troostite. If the cooling rate of the alloy were progressively increased, the proportion of the austenite that transforms in the *Ar'* temperature range would be decreased, the heat effect from the *Ar'* transformation would be diminished in intensity, and the temperature of the start of *Ar'* would be lowered. With a cooling rate that produced 5 to 10 percent of troostite in the 0.80-percent-carbon alloy, the *Ar'* started at approximately 1,040° F. With rates in excess of the critical cooling rate, all the austenite is cooled unchanged through the *Ar'* to the *Ar''* temperature range.

TABLE 3.—*Temperature of the start of the Ar′ and Ar″ transformations in the iron-carbon alloys*

Carbon	Quenching temperature	Transformation			Structure
		Ar′		*Ar″* Start	
		Start	Maximum		
%	°F	°F	°F	°F	
0.62	1,800	1,130	1,130	----------	Troostite+martensite.
.73	1,425	1,130	1,155	----------	Troostite+trace martensite.
.73	1,425	1,075	1,100	----------	Do.
.73	1,425	1,020	1,020	----------	Troostite+martensite.
.73	1,800	1,075	1,075	----------	Do.
.80	1,425	1,040	1,060	----------	Do.
.80	1,425	1,040	1,040	500	Do.
.80	1,425	1,090	1,135	----------	Troostite+trace martensite.
.80	1,500	1,120	1,190	----------	Troostite.
.80	1,500	1,075	1,075	480	Troostite+martensite.
.80	1,550	1,020	1,020	----------	Do.
.85	1,425	1,030	1,030	----------	Do.
.85	1,800	1,120	1,120	----------	Do.
1.01	1,425	1,105	1,210	----------	Troostite+free carbides.

As already pointed out [2], the temperature at the start of the *Ar″* transformation progressively decreased with increase in the carbon content from about 900° F for the 0.23-percent-carbon alloy to about 500° F for the 0.80-percent-carbon alloy. Increase in quenching temperature of the 0.80-percent-carbon alloy from 1,425° to 1,800° F, which resulted in an increase in austenitic grain size from approximately 20 to 3 grains per square inch at 100 diameters, had no appreciable effect on the temperature of the start of the *Ar″*. As shown in figure 10, variation in observed cooling rates from about 550° to 2,600° F per second had no appreciable influence on the temperature range of the start of the *Ar″* transformation in the 0.80-percent-carbon alloy.

The difficulty of accurate measurements of the isothermal transformation of austenite in the alloys is well illustrated by the cooling curve of figure 9. The specimen, containing 0.80 percent of carbon, was cooled from the quenching temperature of 1,425° F to below 1,000° F in less than 1.5 seconds. This elapsed time was sufficient for the austenite to decompose to troostite. With austenite of lower carbon content, or smaller grain size, the reaction time is less than that shown for the 0.80-percent-carbon alloy.

The position of the bend in the S-curve (at 1,110° to 930° F) for the alloys is not accurately defined by these data (table 3, figs. 9 and 10). Although desirable, it is not entirely essential that the location of this temperature range be known for use in the determination of the critical cooling rate of the alloys because of the exponential type of cooling curve obtained by quenching the specimens in a gas. In any event, the relation of the critical cooling rate to the several variables studied would have been similar if some other temperature interval within the limits of approximately 1,150° to 900° F had been selected for the determination of the critical cooling rate of the alloys.

The influence of variations in quenching rate on the rate of transformation of austenite, and on the hardness of the alloy containing 0.80 percent of carbon, are summarized in figure 11. At the quenching temperature of 1,425° F, all the specimens had approximately the same average grain size and the carbon was completely dissolved. With a cooling rate of 450° F per second, the austenite transformed in the *Ar′* temperature range, whereas with a rate of 560° F per second, less than 10 percent of the austenite decomposed at *Ar′*. With further

progressive increase in cooling rate, the estimated proportion of the austenite that transformed in the *Ar'* temperature range progressively decreased until none of the austenite transformed in this temperature range. Thus, there is a narrow range in quenching rates in which the austenite of high-purity iron-carbon alloys transforms at *Ar'* and a wide range in quenching rates in which the larger portion of the austenite transforms at *Ar''*. Critical-cooling-rate values, by definition, are restricted to the latter range in cooling rates. As shown by the slope of the transformation–cooling-rate curve for the upper range of cooling rates, wide changes in cooling rates result in only minor changes in the proportion of troostite. For example, an increase in quenching rate from about 1,000 to 1,280° F per second decreased the

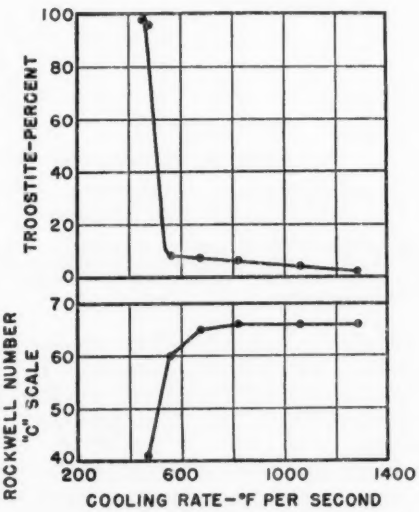

FIGURE 11.—*Effect of cooling rate on structure and hardness of iron-carbon alloy containing 0.80 percent of carbon quenched from 1,425° F.*

Except for cooling rates ranging from 450° to 560° F per second where corrections were made for the heat effect due to the *Ar'* transformation, all cooling rates are based on the average rate required for the specimen to cool through the temperature range of 1,110 to 930° F. Hardness values were obtained on the flat surface of the quenched specimens.

estimated amounts of troostite only from 5 to 2 percent. This fact should be borne in mind when the critical cooling rate is used as the basis for a comparison of the hardenability of the alloys.

The hardness of the quenched specimens increased from Rockwell *C 40* to *65* as the cooling rate was increased from about 450° to 680° F per second. Further increase in quenching rate had no marked effect on the hardness of the alloy. Thus, appreciable proportions of troostite may be produced in the quenched specimens without its presence being indicated by hardness testing. This is shown by the difference in the slope of the two curves in figure 11, for the upper range of quenching rates. The Rockwell test indicated that the alloy was completely hardened when the specimens contained troostite varying in amounts up to approximately 6 percent. A similar relation was also shown in microhardness testing. Obviously the hardness values alone, obtained on the quenched specimens, could not be used as a precise index of the actual cooling rate of the specimens.

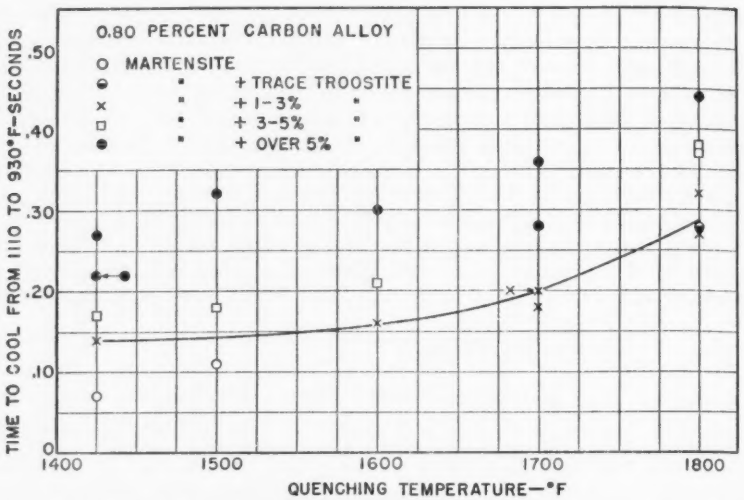

FIGURE 12.—*Effect of cooling time on the structure of the 0.80-percent-carbon alloy quenched from different temperatures.*

Specimens, 0.10 inch square by 0.040 inch thick, were heated rapidly in nitrogen to the temperatures of 1,425°, 1,500°, and 1,600° F, and in vacuo to 1,800° F, and quenched in hydrogen. Specimens, 0.25 inch square by 0.040 inch thick, were heated rapidly in nitrogen to the temperature of 1,700° F and quenched directly in a sodium-silicate-water bath.

The transition from the unhardened to the hardened condition in high-purity iron-carbon alloys is brought about by a small change in cooling rate. This important fact is of particular significance in considering the mechanism of the decomposition of austenite on quenching the alloys.

The critical cooling rate was determined for the 0.80-percent-carbon alloy quenched from temperatures ranging from 1,425° to 1,800° F,

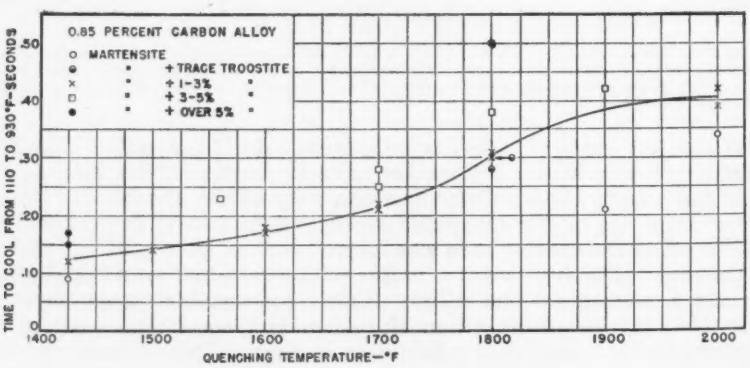

FIGURE 13.—*Effect of cooling time on the structure of the 0.85-percent-carbon alloy quenched from different temperatures.*

Specimens, 0.10 inch square by 0.040 inch thick, were heated rapidly in nitrogen to the temperatures of 1,425°, 1,500°, and 1,600° F, and in vacuo to 1,800°, 1,900°, and 2,000° F, and quenched in hydrogen. Specimens 0.25 inch square by 0.040 inch thick, were heated rapidly in nitrogen to 1,700° F and quenched in a sodium-silicate-water bath.

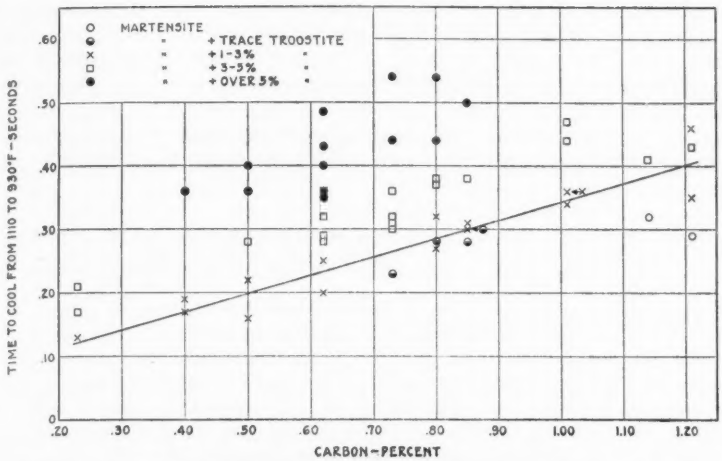

FIGURE 14.—*Effect of cooling time on the structure of iron-carbon alloys.*

Specimens were heated rapidly in vacuo to 1,800° F and quenched directly in hydrogen. At 1,800° F, all the alloys had the same average grain size of 2.9 grains per square inch at 100 diameters (table 2), and the carbon was completely dissolved.

for the 0.85-percent-carbon alloy quenched from temperatures ranging from 1,425° to 2,000° F, and for the other alloys ranging in carbon from 0.23 to 1.21 percent quenched from 1,800° F.

The effect of the time to cool from 1,110° to 930° F on the structure of the 0.80-percent-carbon alloy quenched from various temperatures is shown in figure 12, and on the 0.85-percent-carbon alloy in figure 13. The effect of time to cool from 1,110° to 930° F on the structure of the alloys, varying in carbon content, quenched from 1,800° F is shown in figure 14. The relation of critical cooling time (resulting in 1 to 3 percent of troostite) to quenching temperature is represented by the curves in figures 12 and 13, and to carbon content in figure 14.

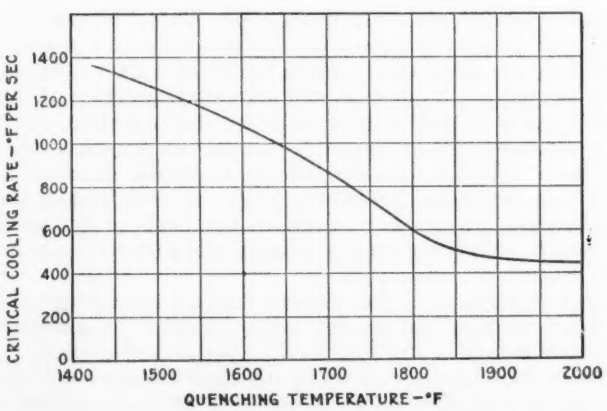

FIGURE 15.—*Relation of critical cooling rate to quenching temperature of iron-carbon alloys containing 0.80 to 0.85 percent of carbon.*

The austenitic grain size ranged from approximately 20 to 1½ grains per square inch at 100 diameters.

The relation of critical cooling rate to quenching temperature for the alloys containing 0.80 to 0.85 percent of carbon is summarized in figure 15. These alloys were quenched from temperatures sufficiently high to insure complete solution of carbon and the time at these temperatures was sufficient for the carbon to be uniformly distributed. The decrease in critical cooling rate with increase in quenching temperature was due solely to variation in austenitic grain size.

VI. INFLUENCE OF AUSTENITIC GRAIN SIZE AND CARBON CONTENT ON THE CRITICAL COOLING RATE

The data from figure 15 and table 2 are assembled in figure 16 to show quantitatively the effect of variation in austenitic grain size on the critical cooling rate of the 0.80- to 0.85-percent-carbon alloys. The rate of heating through the transformation range to any selected temperature was of the same order of magnitude for specimens used in the determination of the critical cooling rate as that for specimens used in the measurement of the austenitic grain size. In some cases, the grain size was determined on the specimens used in the critical-

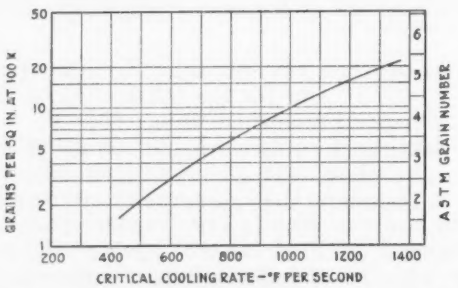

FIGURE 16.—*Relation of critical cooling rate to austenitic grain size of iron-carbon alloys containing 0.80 to 0.85 percent of carbon.*

cooling-rate experiments. On quenching these alloys, the initial transformation of austenite to troostite occurred at the grain boundaries of the parent austenite. Some variations always existed in the size of the austenitic grains, and only a small proportion of the austenite transformed to troostite on quenching at the critical cooling rate. It is obvious that precisely the same critical-cooling-rate values would not have been obtained had the alloys contained grains of only one size at each quenching temperature used. Correlation of the critical cooling rate with grain size is made on the basis of the average size of the austenite grains for each condition and not on the minimum or maximum values.

As shown in figure 16, the critical cooling rate progressively decreased (hardenability increased) with increase in austenitic grain size of the alloys containing 0.80 to 0.85 percent of carbon. For constant carbon content and uniform distribution and solution of all carbon in austenite, the relation between critical cooling rate and austenitic grain size may be represented approximately by the empirical equation

$$R = \text{constant } (N)^n, \tag{1}$$

where R is the critical cooling rate in °F per second, N is the number of austenitic grains per square inch at 100 diameters, and n is constant and equals approximately 0.4.

The basis for this equation is the fact that graphs of relationship between grain size and critical cooling rate, on logarithmic scale, are approximately straight lines.

The relation of critical cooling rate to carbon content of the alloys for two different austenitic grain sizes is shown in figure 17. The results summarized in curve A were obtained in previous experiments [1] by quenching specimens directly from 1,700° F, the temperature

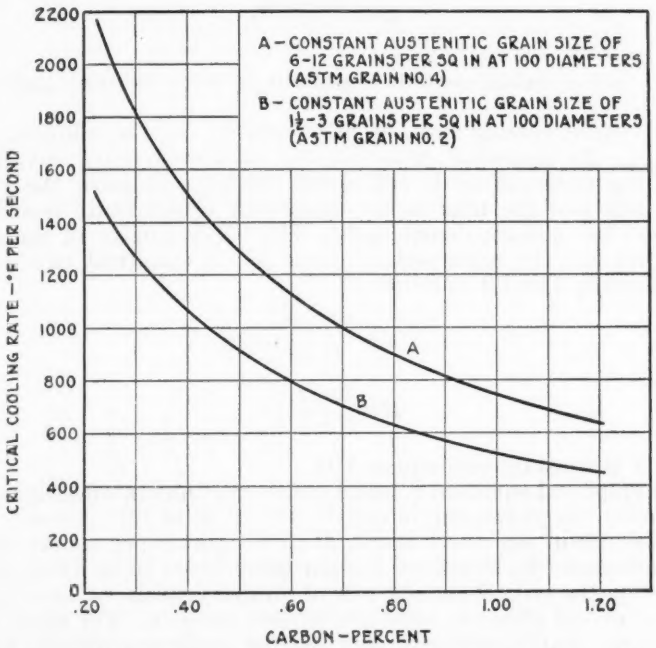

FIGURE 17.—*Relation of critical cooling rate to carbon content of iron-carbon alloys.*

establishing an average constant grain size of approximately 7.5 grains per square inch at 100 diameters with all carbon in solution. The results summarized in curve B were obtained in the present experiments (fig. 14) by quenching specimens directly from 1,800° F, the temperature establishing an average constant austenitic grain size of approximately 2.9 grains per square inch at 100 diameters with all carbon in solution (see table 2 for grain size of the alloys at 1,700° and 1,800° F).

The influence of austenitic grain size on the hardenability of the alloys is also shown by a comparison of the results summarized in curves A and B. With any selected carbon content within the range of 0.23 to 1.21 percent, the ratio of the critical cooling rate for an average austenitic grain size of 7.5 grains per square inch at 100 diameters to that for an average austenitic grain size of 2.9 grains per square inch at 100 diameters was approximately constant and was of the

order of 1.43 to 1.0. That is, in order to attain complete hardening, an alloy with the smaller austenitic grains must be cooled approximately 1.5 times as fast as the same alloy with the larger grains.

For each austenitic grain size investigated (fig. 17), the critical cooling rate decreased continuously with increase in carbon content of the alloys. For constant austenitic grain size and uniform distribution and solution of all carbon in austenite, the relation between critical cooling rate and carbon content of the alloys may be approximately represented by the empirical equation

$$R=\frac{\text{constant}}{C+c}, \tag{2}$$

where C is the carbon content in percent, and c is constant and equals 0.2.

The critical cooling rate, or hardenability, of the alloys depends only upon the austenitic grain size and carbon content, provided the quenching temperature is sufficiently high to dissolve the carbon completely and the time at the quenching temperature is sufficient to insure its uniform distribution. The hardenability of the alloys, therefore, may be expressed in terms of an empirical equation by combining eq 1 and 2 as follows:

$$R=\frac{K(N)^n}{C+c}, \text{ and} \tag{3}$$

$$R=\frac{410N^{\cdot 4}}{C+0.2}, \tag{4}$$

where K is constant and equals 410.

This empirical equation is based upon experiments with high-purity iron-carbon alloys ranging in carbon from 0.23 to 1.21 percent and in austenitic grain size from about 20 to 1½ grains per square inch at 100 diameters. It, therefore, has not been shown to be applicable for computing the critical cooling rate of ordinary steels, or for computations involving alloys of very low carbon content. For example, eq 4 indicates that high-purity iron can be made martensitic by fast quenching, obviously a condition that is impossible. It should be pointed out that the determinations for carbon were made with considerably more precision than was possible in the determinations of the austenitic grain size of the alloys.

VII. SURFACE HARDNESS

French and Klopsch [4] reported the results of Rockwell hardness tests made on specimens of carbon steels varying in carbon content and quenched at different rates. For specimens quenched at the critical cooling rate, hardness increased rapidly with carbon content up to about 0.70 percent but thereafter remained constant with increase in carbon. With steels containing 0.75 to 1.25 percent of carbon, practically identical hardness values were obtained on the quenched specimens containing appreciable proportions of troostite and on the completely martensitic specimens. In 1938, Burns, Moore, and Archer [11] showed that the maximum hardness attainable by quenching the

plain carbon and common alloy steels depends alone on the carbon content. The hardness values (Rockwell *C*) increased with carbon up to about 0.55 percent and thereafter remained constant with increase in carbon (for the range in carbon investigated).

In the present investigation, readings for hardness were made with the Rockwell Superficial tester (30-kg load) on most of the specimens used in the determination of the critical cooling rate of the alloys. For comparison purposes, the readings were converted to the *C* scale in accordance with the conversion tables supplied by the manufacturer of the instrument. The flat surfaces of the quenched specimens were cleaned with *1 G* emery paper before testing.

The results of the hardness tests made on specimens of the alloys quenched directly from 1,800° F at various rates are summarized in figure 18. The estimated amounts of troostite formed (1 to 3 percent for critical cooling rate) are also shown, together with the curve

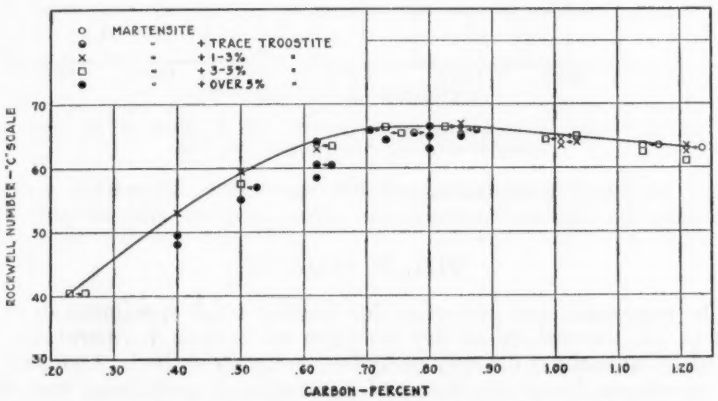

FIGURE 18.—*Effect of carbon content on the hardness of iron-carbon alloys.*

representing the relation of maximum values obtained for hardness to carbon content.

The alloys had the same average grain size of 2.9 grains per square inch at 100 diameters and all carbon was in solution at the time of quenching, but not all the specimens were completely martensitic after the quench as evidenced by the presence of troostite. The latter specimens, with troostite estimated up to 5 percent, had Rockwell hardness values of the same order of magnitude as the fully martensitic specimens of similar carbon content. The maximum hardness values obtained increased with increase in carbon up to about 0.70 percent, remained constant for alloys ranging in carbon from 0.70 to 0.85 percent, and decreased slightly with further increase in carbon. The decrease in hardness with increase in carbon of the alloys in the high-carbon range is believed to be due to the retention of some austenite after the quench. The maximum hardness values obtained for the alloys in the low-carbon range are considerably lower than those reported by Burns, Moore, and Archer [11] for steels of similar carbon content, whereas in the high-carbon range the alloys had approximately the same hardness values as the steels.

As is shown in figure 19, the maximum hardness value for the 0.85-percent-carbon alloy was not affected by variation in quenching temperatures from 1,425° to 2,000° F. This range in quenching temperatures produced austenitic grain sizes ranging from approximately 20 to 1½ grains per square inch at 100 diameters (table 2). The maximum hardness value obtained for this alloy, therefore, was not influenced by wide variations in the grain size at the time of quenching.

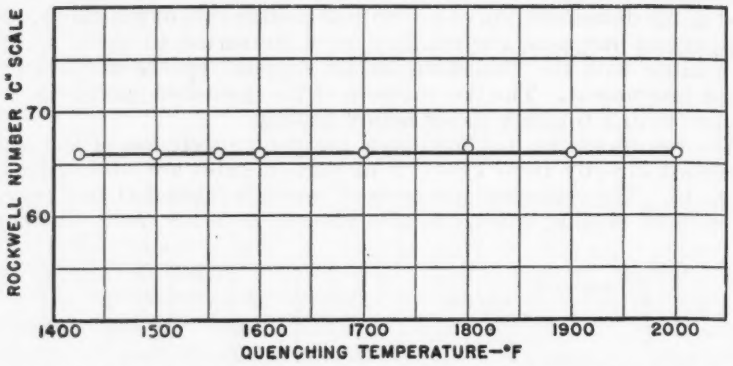

FIGURE 19.—*Effect of quenching temperature on the hardness of the iron-carbon alloy containing 0.85 percent of carbon.*

VIII. SUMMARY

The apparatus and procedure for heating small specimens in vacuo and in an atmosphere of dry nitrogen to various temperatures followed by quenching directly in hydrogen are described. Oxidation of the specimen during the time of heating and quenching was eliminated, and it was possible to obtain progressive changes in cooling rates over the wide range required in the present experiments. Specimens quenched in hydrogen were cooled uniformly over the entire surface, as shown by the microstructure in the cross section.

The string-galvanometer apparatus and the procedure used for obtaining photographic records of the time-temperature cooling curves are also described in some detail. Examples are given of typical cooling curves obtained on specimens heated in vacuo and in an atmosphere of dry nitrogen and quenched directly in hydrogen.

The high-purity iron-carbon alloys used in the present study ranged in carbon from 0.23 to 1.21 percent. The specimens were from the same alloys as those used and described in previous investigations [1, 2].

The grain size established at temperatures ranging from 1,425° to 1,600° F increased markedly with decrease in rate of heating through the transformation range, whereas the grain size at 1,800° F was not so noticeably dependent upon the rate of heating. The grain sizes at temperatures ranging from 1,425° to 2,100° F was determined for the alloys. For any selected temperatures within the range from 1,600° to 2,100° F and with the heating rate employed, all the alloys were found to have approximately the same average grain size provided the carbon was completely dissolved at that temperature. Carbon in solution, therefore, was not effective in inhibiting grain growth of

the austenite in the high-purity iron-carbon alloys. The actual temperatures and the rate of heating through the transformation range were the dominant factors in controlling the austenitic grain size of these alloys.

There is a narrow range in cooling rates in which the austenite transforms at Ar' and a wide range in quenching rates in which the larger portion of the austenite transforms at Ar''. Thus, the transition from the unhardened to the hardened condition in high-purity iron-carbon alloys is brought about by a small change in cooling rate.

The critical cooling rate was determined for the 0.80-percent-carbon alloy quenched directly from temperatures ranging from 1,425° to 1,800° F, for the 0.85-percent-carbon alloy quenched from temperatures ranging from 1,425° to 2,000° F, and for the alloys varying in carbon from 0.23 to 1.21 percent quenched from 1,800° F.

The critical cooling rate was taken as the average cooling rate, between 1,110° and 930° F, which produced in the quenched specimen a structure of martensite with nodular troostite (fine pearlite) in amounts estimated to be between 1 and 3 percent.

The critical cooling rate progressively decreased (hardenability increased) as the austenitic grain size increased in the alloys containing 0.80 to 0.85 percent of carbon. For each austenitic grain size investigated, the critical cooling rate decreased continuously with increase in carbon content of the alloys.

For complete solution and uniform distribution of carbon at the time of quenching, the critical cooling rate (R in °F per second) or hardenability of the alloys may be approximately represented by the equation

$$R=\frac{410\,N^{.4}}{C+0.2},$$

where N is the number of austenitic grains per square inch at 100 diameters and C is the carbon content in percent.

Hardness values obtained on the quenched specimens could not alone be used as a precise index to the actual cooling rates of the alloys.

The maximum hardness values obtained on specimens of each alloy quenched from 1,800° F increased with increase in carbon up to about 0.70 percent, remained constant for alloys ranging from 0.70 to 0.85 percent, and decreased slightly with further increase in carbon. The maximum hardness value for the 0.85-percent-carbon alloy was not affected by variation in quenching temperatures from 1,425° to 2,000° F. This range in quenching temperatures produced in the alloy austenitic grain sizes ranging from approximately 20 to 1½ grains per square inch at 100 diameters.

Variation in observed cooling rates from about 550° to 2,600° F per second with austenitic grain size of approximately 20 grains per square inch at 100 diameters had no appreciable influence on the temperature range of the start of the Ar'' transformation in the 0.80-percent-carbon alloy. Variation in austenitic grain size ranging from approximately 20 to 3 grains per square inch at 100 diameters

had no detectable effect on the temperature of the start of the Ar'' in this alloy.

Grateful acknowledgment is made to N. L. Carwile and S. J. Rosenberg for assistance in this work.

IX. REFERENCES

[1] Thomas G. Digges, *Effect of carbon on the critical cooling rate of high-purity iron-carbon alloys and plain carbon steels*, J. Research NBS **20,** 571 (1938) RP1092. Also, *Effect of carbon on the hardenability of high-purity iron-carbon alloys*, Trans. Am. Soc. Metals **26,** 408 (1938).

[2] Thomas G. Digges, *Transformation of austenite on quenching high-purity iron-carbon alloys*, J. Research NBS **23,** 151 (1939) RP1225. Also, Preprint 24. Paper presented at twenty-first annual convention of the Am. Soc. Metals (Oct. 23–27, 1939).

[3] Zay Jeffries, Am. Soc. Testing Materials, Standards, pt. 1, Metals, Designation E2–36 (Note 2) p. 763 (1936).

[4] H. J. French and O. Z. Klopsch, *Quenching diagrams for carbon steels in relation to some quenching media for heat treatment*, Trans. Am. Soc. Steel Treating **6,** 251 (1924).

[5] Carl L. Shapiro, *What about grain size?* Iron Age **143,** 25, March 16; 23, March 30; 33, April 6 (1939).

[6] N. F. Ward and J. E. Dorn, *Grain size of steel*, Metals & Alloys **10,** 74, 115, 212, 246 (1939).

[7] G. Derge, A. R. Kommel, and R. F. Mehl, *Some factors influencing austenitic grain size in high-purity steels*, Trans. Am. Soc. Metals **26,** 153 (1938).

[8] M. A. Grossmann, *On grain size and grain growth*, Trans. Am. Soc. Steel Treating **21,** 1079 (1933).

[9] E. S. Davenport and E. C. Bain, *Transformation of austenite at constant subcritical temperatures*, Trans. Am. Inst. Min. & Met. Engrs., Iron & Steel Div. **90,** 117 (1930).

[10] A contribution form the Research Laboratory, United States Steel Corporation, *The process and results of austenite transformation at constant temperature*, Metals & Alloys, **8,** 22 (1937).

[11] J. L. Burns, T. L. Moore, and R. S. Archer, *Quantitative hardenability*, Trans. Am. Soc. for Metals **26,** 1 (1938).

WASHINGTON, February 13, 1940.

U. S. DEPARTMENT OF COMMERCE NATIONAL BUREAU OF STANDARDS

RESEARCH PAPER RP1309

Part of Journal of Research of the National Bureau of Standards, Volume 24, June 1940

MICROSCOPIC EXAMINATION OF COTTON FIBERS IN CUPRAMMONIUM HYDROXIDE SOLUTIONS *

By Charles W. Hock and Milton Harris [1]

ABSTRACT

During treatment of cotton with cuprammonium hydroxide solutions, the cellulose dissolves, leaving residues which vary in amount and in structure, depending upon the degree of purification of the fibers. The undissolved residue from raw and from dewaxed fibers consists principally of fragmented shells that formed the outer surface of the fibers, and, to a lesser extent, of material from the lumen. Both of these residues are isotropic and stain deeply with ruthenium red. Fibers from which both wax and pectic substance have been removed dissolve in cuprammonium reagent, leaving only a very small amount of isotropic residue which exhibits no definite cytological structure.

When a steady flow of cuprammonium hydroxide solution is applied to fibers mounted on a slide, the initial swelling of the fibers is followed by the appearance of small ellipsoidal particles which range from 1 to 2μ in size, appear bright between crossed nicols, and become dark in color when stained with iodine and sulfuric acid. Identical particles appear, however, when cuprammonium hydroxide solution is drawn under the cover glass, in the absence of fibers. These particles are formed both in the presence and absence of cotton, and result from the exposure of the cuprammonium hydroxide reagent to air. They are washed under the cover glass by the flow of cuprammonium hydroxide and become associated with any fiber residue on the slide. Formation of these particles may be prevented by using a specially constructed cell which prevents exposure of the reagent. Under these conditions, no particles were observed during the slow passage, even for prolonged periods, of the cuprammonium reagent over the cotton fibers.

Two cuprammonium hydroxide solutions, one prepared according to ACS specification, and the other higher in ammonia content, were used in this investigation. It was found that particles formed much more quickly in the former, and accordingly make it less desirable for microscopic studies of the behavior of cotton fibers in cuprammonium reagent.

CONTENTS

		Page
I.	Introduction	743
II.	Materials	744
III.	Experimental procedure and results	745
IV.	References	748

I. INTRODUCTION

The viscosity of cuprammonium hydroxide solutions of cotton has frequently been related to the quality of the fiber, especially as regards tensile strength. It has been shown, for example, that chemical treatments which modify the properties of the fibers in such a way as

* This paper was presented before the Cellulose Division of the 99th meeting of the American Chemical Society, Cincinnati, Ohio.

[1] Research Associates at the National Bureau of Standards, representing the Textile Foundation.

to impair their tensile strength also bring about a lowering of the viscosity in cuprammonium hydroxide solutions [1, 2].[2] On the basis of the molecular chain theory for the structure of cellulose, this decrease in tensile strength and the accompanying increase in cuprammonium hydroxide fluidity may be regarded as having resulted from a shortening in chain-length of the cellulose molecule. Recently, Farr and her collaborators [3, 4, 5] have brought forth a new explanation based principally on microscopic observations. According to these investigators, the cellulose component of cotton fibers does not dissolve in cuprammonium solution but maintains a visible state of aggregation in the form of diminutive cellulose particles, each of which is surrounded by cementing material which swells in cuprammonium solutions, thereby giving rise to a gel-like structure upon which many of the characteristic properties of the dispersion depend. On the basis of this interpretation, it follows that the reduction of viscosity through processing or deterioration of the fibers may be regarded as the result of a direct effect upon the viscosity-producing power of the cementing material.

Since measurements of the viscosity of cuprammonium hydroxide solutions of cotton are widely used to evaluate some of the characteristics of the fiber, and since the above concepts lead to widely different interpretations of the behavior of cotton in this solution, it appeared advisable to undertake a new investigation of the microscopically observable changes which cotton fibers undergo in this reagent.

II. MATERIALS

The cotton used in these experiments was *Gossypium hirsutum* L, Missdel–7 variety, grown at the Delta Experiment Station at Stoneville, Miss., and furnished by the Bureau of Agricultural Economics, United States Department of Agriculture. It had been ginned and twice carded, but had received no chemical treatments. In the present paper these fibers are designated as *raw fibers*. The natural waxes were removed from the raw fibers by extraction with alcohol and ether for 24 hours each. These fibers are termed *dewaxed fibers*. A portion of the dewaxed material was further purified by extraction for 6 hours with a boiling 1-percent solution of sodium hydroxide, according to the method recommended for the preparation of standard cellulose. The procedure was essentially the same as that described by Corey and Gray [6], except that the apparatus of Worner and Mease [7] was employed. Fibers treated in this way were shown by the method of Whistler, Martin, and Harris [8] to be free of pectic substance. These fibers, from which both wax and pectic substance were removed, are designated *depectinized fibers*.

Two solutions of cuprammonium hydroxide were used in the experiments. One, made according to the recommendations of Mease [9], is essentially the same as that set forth by the Fabrics Research Committee (London) [10], except that the higher concentration of ammonia originally recommended by Clibbens and Geake [11] was used. This solution contained 240 ± 5 g of ammonia (NH_3), 15 ± 0.1 g of copper, and 1.0 g of sucrose, per liter. The concentration of nitrite was less than 0.5 percent. In the present paper this solution will hereafter be

[2] Figures in brackets indicate the literature references at the end of this paper.

referred to as *cuprammonium hydroxide solution A*. A second cuprammonium hydroxide solution, prepared according to the specification of the Division of Cellulose Chemistry of the American Chemical Society [12] was also used. It contained 30 ±2 g of copper, 165 ±2 g of ammonia, and 10 g of sucrose, per liter. In the present paper this solution will hereafter be referred to as *cuprammonium hydroxide solution B*. When not in actual use, all solutions of cuprammonium hydroxide were kept under nitrogen in tightly stoppered bottles in the refrigerator. Unless stated otherwise, both solutions *A* and *B* were used in each of the experiments in this investigation.

III. EXPERIMENTAL PROCEDURE AND RESULTS

Raw, dewaxed, and depectinized fibers were placed, without any mounting medium, on microscope slides, and then examined microscopically as cuprammonium hydroxide solution was drawn under the cover glass. In other cases the fibers were mounted in distilled water, or in ammonium hydroxide, and the cuprammonium solution was added as above. The water and ammonium hydroxide appeared to act merely as diluents, thereby retarding the solvent action of the cuprammonium hydroxide solution. The behavior of the fibers in the cuprammonium reagent was observed microscopically, using ordinary and dark-field illumination and crossed nicols.

Raw cotton fibers, upon addition of the reagent, immediately began to swell and twist, often forming balloon-like structures (fig. 1, *A* and *B*). After a few minutes, the inner portion of the fiber appeared to be completely dissolved, leaving transparent shells which originally formed the outer surface of the fibers (fig. 1, *C*). Likewise, a small amount of material from the lumen did not dissolve (fig. 1, *B*). This behavior was especially striking when observed with crossed nicols. The fibers, originally bright against a black background, became dimmer as the cellulose was dissolved by the reagent. After a few minutes, the field was black, which indicated that all birefringent material had disappeared. When the same preparation was then examined in ordinary light, it was found to contain many of the shells described above.

Dewaxed cotton fibers presented essentially the same picture as raw fibers. Dissolution of the inner part of the fiber took place in a few minutes, leaving residues (fig. 2) similar to those of the raw fibers (fig. 1, *C*), but less dense and bulky, and often more torn and fragmented than the latter. With crossed nicols the results were the same as with raw cotton; that is, the strongly birefringent cellulose was dissolved rapidly, leaving an insoluble, isotropic material.

Depectinized cotton fibers dissolved in cuprammonium hydroxide solution, leaving only a very small amount of isotropic residue which consisted of small irregular bits of material (fig. 3). This residue exhibited no definite cytological structure, such as that shown by the shells of raw and of dewaxed fibers. (Compare with fig. 1, *C* and fig. 2.)

The isotropic shells of raw and of dewaxed fibers and the isotropic material from the lumen did not stain blue when given the iodine-sulfuric acid test for cellulose, but they stained deeply with ruthenium red [13]. Although ruthenium red is not a specific stain for pectic

substance, native pectic compounds invariably take a red color in the presence of this dye [14].

In the above experiments the effects of cuprammonium reagent on the different samples of cotton could be observed for only relatively short periods. In order to make observations over longer periods, samples of raw, dewaxed, and depectinized cotton fibers were placed in separate vials of cuprammonium hydroxide solution. At intervals thereafter, samples from each of the vials were removed and viewed microscopically, using ordinary and dark-field illumination and crossed nicols. During the first day, the preparations were examined every few hours; during the remainder of the first week, examinations were made once each day; and thereafter, once each week for a period of 6 weeks. After the initial dissolution of cellulose, which appeared to be complete in a few minutes, there was no further change in microscopic appearance of the undissolved material. The solutions of raw and of dewaxed cotton showed nothing but isotropic residues, whereas the samples containing depectinized cotton were practically free of residue.

These experiments indicate that pectic substance is a constituent of the insoluble shells which remain when cotton fibers are treated with cuprammonium hydroxide solutions. This conclusion is substantiated by direct chemical evidence presented elsewhere [2]. It also appeared from these experiments that the cellulose portion of the fibers dissolved in cuprammonium reagent, leaving no microscopically resolvable particles of the type described by Farr [3], who has stated, however, that the particles are not visible as ordinarily observed, since they are obscured to the point of invisibility by a matrix of colloidal cementing material which surrounds them. It is stated further that by maintaining a steady flow of cuprammonium hydroxide over the fibers the matrix may be removed, thereby rendering the particles visible. It might have been expected, however, that the particles would have been visible in the depectinized fibers, since these fibers left an almost negligible amount of visible colloidal material after treatment with cuprammonium reagent.

Since particles were not observed, it appeared advisable to repeat Farr's experiments exactly as they are described. Raw cotton fibers were mounted in distilled water. The water was then gradually replaced with cuprammonium hydroxide solution by the following procedure: Small drops of the reagent were applied to one edge of the cover glass. The solution was then drawn under the cover glass by means of very narrow strips of filter paper placed at the opposite side. Swelling of the fibers ensued, resulting in the formation of some "balloons" (fig. 1, *A* and *B*) which eventually disappeared, leaving residues like those described earlier. However, as the flow of fresh reagent was continued, small particles appeared (fig. 4, *A*).

The same technique was then applied to depectinized cotton fibers. As previously described, the cellulose appeared to dissolve upon addition of the cuprammonium hydroxide, leaving only a very small amount of insoluble residue. Nevertheless, as with raw fibers, particles became evident when a steady flow of the reagent was maintained.

It was noted, however, that identical particles appeared, even in the absence of fibers, when the steady flow of cuprammonium hydroxide was continued. The results were the same whether cuprammonium

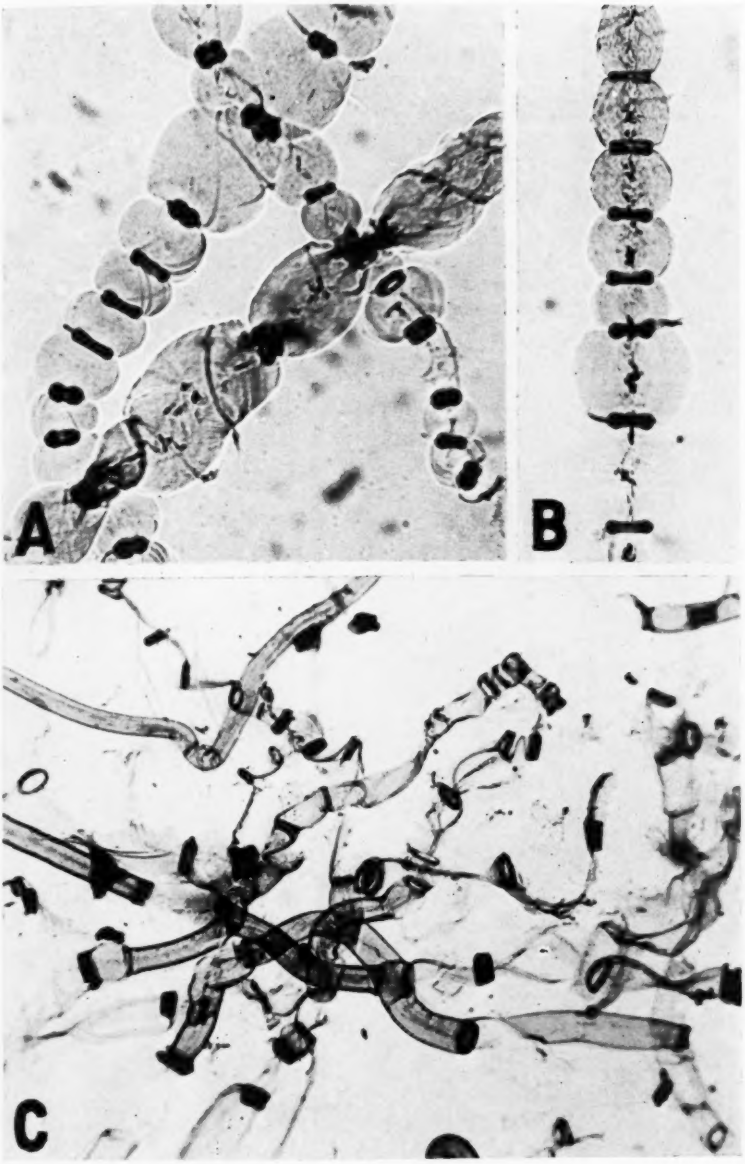

FIGURE 1.—*Raw cotton fibers in cuprammonium hydroxide solution.*

A, fibers swollen to form "balloons"; *B*, typical string of "balloons," showing deeply stained material in the lumen and at the constrictions between the swellings; *C*, residue which remains after the cellulose of the fibers has dissolved in the reagent.
Fibers stained with ruthenium red. Magnification ×120.

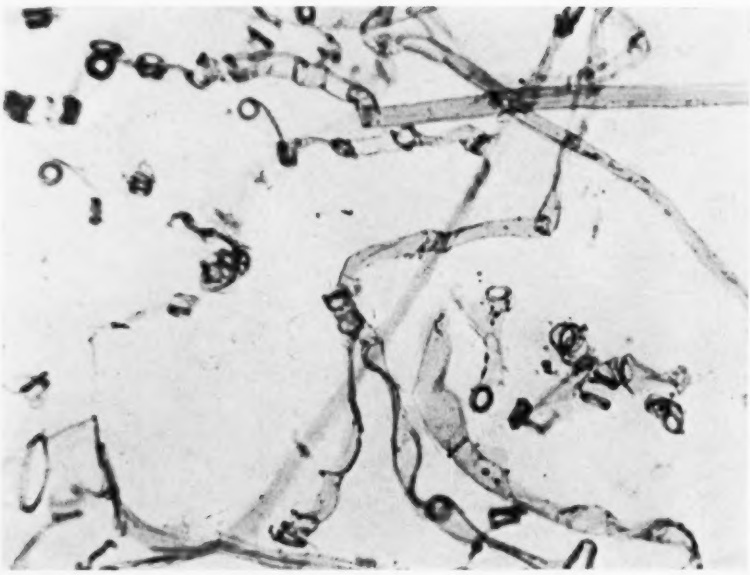

FIGURE 2.—*Dewaxed cotton fibers in cuprammonium hydroxide solution.*

Residue which remains after the cellulose of the fibers has dissolved in the reagent. Fibers stained with ruthenium red. Magnification ×120.

FIGURE 3.—*Depectinized cotton fibers in cuprammonium hydroxide solution.*
Residue which remains after the cellulose of the fibers has dissolved in the reagent. Magnification ×120.

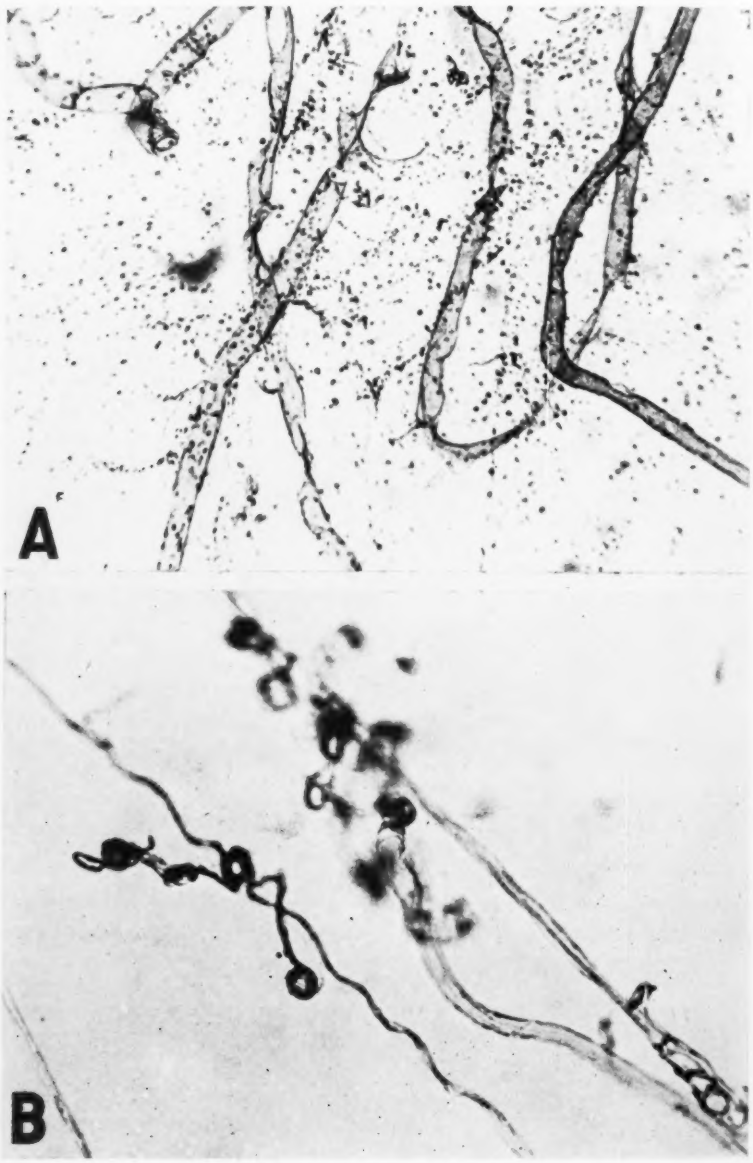

FIGURE 4.—*Fibers treated with a steady flow of cuprammonium hydroxide solution.*

A, residue of raw fibers after a continuous flow of the reagent was maintained over them. Particles, formed from the cuprammonium solution, are seen among the residue. *B*, raw cotton fibers after treatment with cuprammonium solution for 1 hour, under conditions which prevented exposure of the reagent. Magnification ×120.

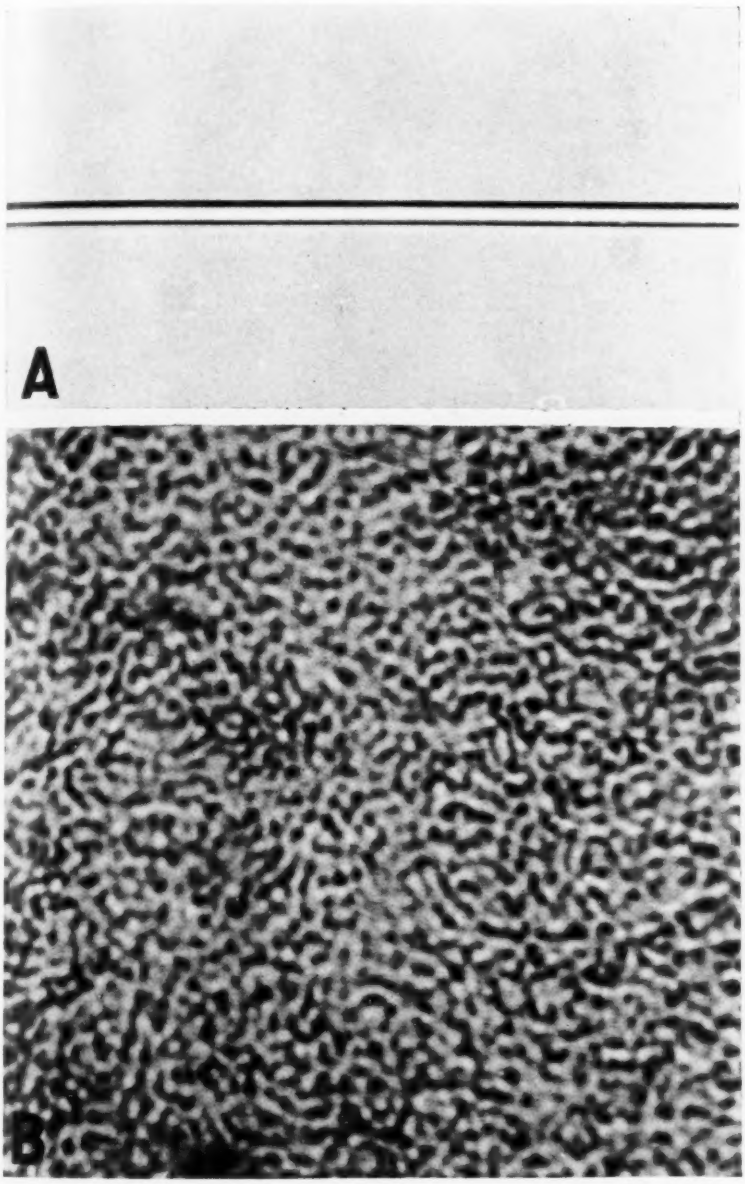

FIGURE 5.—*Cuprammonium hydroxide solution: no cellulose present.*

A, fine strand of glass rod in focus in the solution. The latter has not been exposed to allow formation of particles. Magnification ×500. *B*, particles formed upon exposure of the reagent to air. Magnification ×1500.

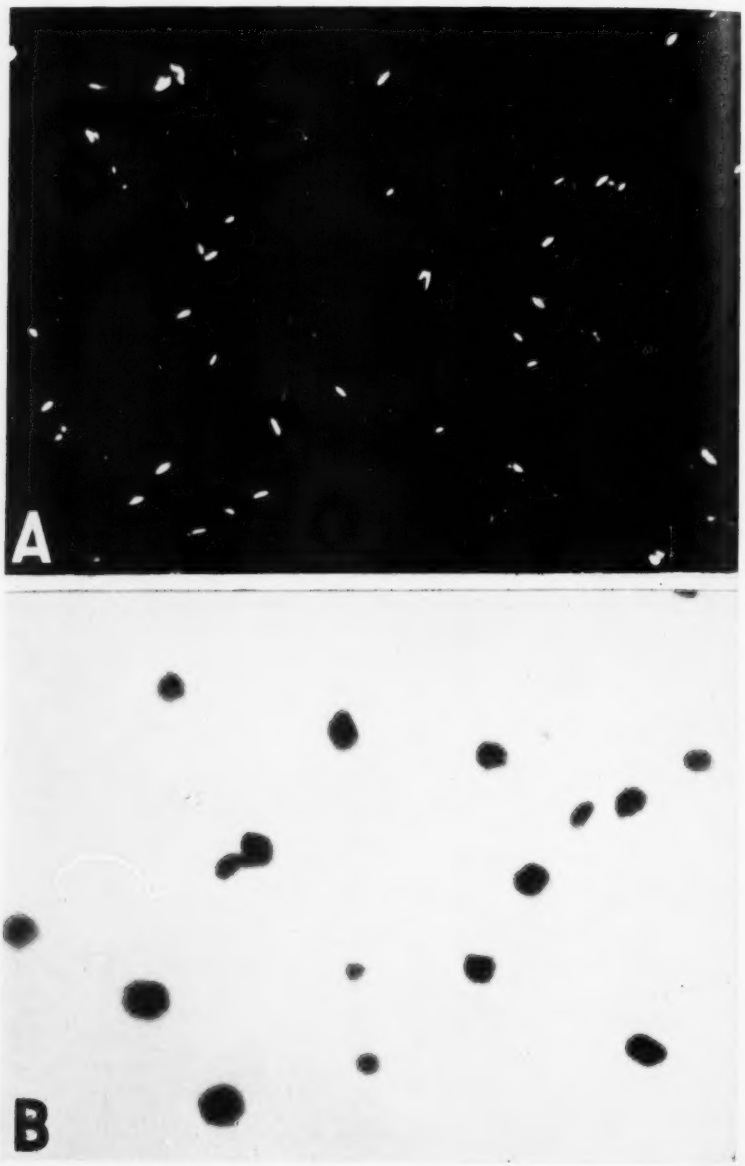

FIGURE 6.—*Particles formed in cuprammonium hydroxide solution, in the absence of cellulose.*

A, particles as viewed between crossed nicols. *B*, Particles which appear after the addition of iodine and sulfuric acid. Magnification ×1500.

solution *A* or *B* was used. In both cases, the particles appeared to be ellipsoidal and ranged from 1 to 2 μ in size. They were birefringent and showed extinction when rotated between crossed nicols. When given the iodine-sulfuric acid test for cellulose, dark particles, somewhat larger than the original ones, were observed. The photomicrographs (figs. 5 *B*, 6 *A*, 6 *B*) of these particles greatly resemble those shown by Farr [3]. All of these photomicrographs are of cuprammonium hydroxide solutions *which contained no cotton fibers*. In all cases the original solutions were clear (fig. 5, *A*), and particles appeared only after the solution was exposed to the air, as in drawing it under the cover glass.

Further examination of the cuprammonium solutions showed that a precipitate was always formed when this reagent was exposed. Farr [3] has stated that a steady flow of the solution had to be maintained in order to prevent crystallization of the copper salt. In the present investigation, it was found that regardless of the care exercised in this experiment, particles were always obtained when the cuprammonium solution was allowed to flow under the cover glass according to the described technique.

The experiments in which a continuous flow of cuprammonium reagent was maintained over the fibers were then repeated under conditions which prevented exposure of the reagent to air. In order to do this a sealed mount, constructed as follows, was employed. A ring consisting of a mixture of paraffin and vaseline was made in the center of a microscope slide, and a few cotton fibers were then placed in the enclosure. A hypodermic syringe was arranged in such a way that the tip of the needle extended just inside the ring, on the opposite side of which a small opening was made. A cover glass was then placed over the fibers and the ring, and further sealed to the slide by applying a viscous solution of methyl methacrylate in acetone, to the edges of the cover glass. The microscope slide and syringe were fastened to a sheet of stiff cardboard so that the whole apparatus could be placed on the stage of the microscope.

The syringe was filled with cuprammonium hydroxide solution. By applying pressure to the plunger of the syringe, the solution was passed slowly over the fibers, which were mounted either dry or in distilled water. The liquid was allowed to flow through the cell and out the small opening in the ring. During this process the behavior of the fibers was continuously observed with the microscope.

Using this specially constructed cell, which prevented exposure of the reagent, fibers were treated with cuprammonium hydroxide solutions *A* and *B*. It was found that a steady flow of solution *A* could be passed over the fibers for more than an hour without the appearance of particles (fig. 4, *B*). As the reagent started to flow through the cell, the frequently observed reaction took place. The fibers began to swell, thereby giving rise to typical balloon-like structures, which eventually appeared to be optically clear. Moreover, as the flow of cuprammonium hydroxide was continued, no particles appeared, even after prolonged passage of the reagent.

When solution *B* was used, some particles always appeared, even in control mounts which contained no fibers. In all cases in which the solutions were exposed to the air, particles formed more readily with solution *B* than with *A*, probably because of the higher copper and lower ammonia concentrations of the former. Because of this

fact, solution *A* was found to be much more desirable for microscopic studies of the behavior of cotton fibers in cuprammonium reagent.

The results of this investigation indicate that microscopically resolvable particles of cellulose do not persist when cotton fibers are dispersed in cuprammonium hydroxide solutions. Particles are obtained, however, even in the absence of fibers, upon exposure of the reagent to air.

IV. REFERENCES

[1] D. A. Clibbens and B. P. Ridge, J. Textile Inst. **19,** T394 (1928).
[2] R. L. Whistler, A. R. Martin, and M. Harris, J. Research NBS **24,** 555 (1940) RP 1299.
[3] W. K. Farr, Contrib. Boyce Thompson Institute **10,** 71 (1938).
[4] W. A. Sisson, Contrib. Boyce Thompson Institute **10,** 113 (1938).
[5] J. Compton, Contrib. Boyce Thompson Institute **10,** 57 (1938).
[6] A. B. Corey and H. L. Gray, Ind. Eng. Chem. **16,** 853, 1130 (1924).
[7] R. K. Worner and R. T. Mease, J. Research NBS **21,** 609 (1938) RP1146.
[8] R. L. Whistler, A. R. Martin, and M. Harris, J. Research NBS **24,** 13 (1940) RP1268.
[9] R. T. Mease, J. Research NBS **22,** 271 (1939) RP1179.
[10] Report of the Fabrics Research Committee, Department of Scientific and Industrial Research, His Majesty's Stationery Office, London (1933).
[11] D. A. Clibbens and A. Geake, J. Textile Inst. **19,** T77 (1928).
[12] American Chemical Society. Committee on the Viscosity of Cellulose of the Division of Cellulose Chemistry. Ind. Eng. Chem., Anal. Ed. **1,** 49 (1929).
[13] L. Mangin, Compt. rend. **116,** 653 (1893).
[14] D. B. Anderson and T. Kerr, Ind. Eng. Chem. **30,** 48 (1938).

WASHINGTON, March 1, 1940.

INDEX TO VOLUME 24

A

Page

Acoustic materials, effect of paint on the sound absorption, RP1298 ... 547
Acree, S. F., John O. Burton, Walter J. Hamer and, Second ionization constant and related thermodynamic quantities for malonic acid from 0° to 60° C, RP1284 ... 269
——, *Elizabeth E. Hughes and,* Reaction of bromine with furfural and related compounds, RP 1276 ... 175
After images, effect on surface color in chromatic illumination, RP1285 ... 293
Air-conditioning equipment, prevention of corrosion, RP1305 ... 665
Air permeability measurements, determing pore size, RP1292 ... 435
Air voids in mortars, RP1273 ... 103
Aliphatic hydrocarbons, properties {RP1271 ... 33 / RP1306 ... 677
Alkaline cyanide copper plating baths, measurement of pH, RP1291 ... 423
Alloys, cooling rate of high-purity iron-carbon, influence of austenitic grain size, RP1308 ... 723
Alloys, determination of arsenic in ferrous and nonferrous, RP1267 ... 7
Alloys, high-purity iron-carbon, influence of austenitic grain size on the critical cooling rate, RP1308 ... 723
Ambient temperature, as affecting safe operation of journal bearings, RP1295 ... 491
Aneroid diaphragm capsule, RP1270 ... 31
Arc spectrum of germanium, RP1266 ... 1
Arsenic, colorimetric determination, in ferrous and nonferrous alloys, RP1267 ... 7
Atmospheric pressure, diaphragm capsule for measurement, RP1270 ... 31
Austenitic grain size, influence on the critical cooling rate of high-purity iron-carbon alloys, RP1308 ... 723
Azeotropic distillation with methyl alcohol, separation of naphthenes from paraffins, RP1296 ... 509

B

Barium bromide, effect on reducing powers of sugars, RP1282 ... 241
Barograph diaphragm capsule, RP1270 ... 31
Base metal thermocouples, stability, RP1278 ... 205
Batteries, electromotive force and heat of reaction, RP1294 ... 475
Bearings, journal, friction, RP1295 ... 491
Bezold-Brücke phenomenon, RP1285 ... 293
Bifilar inductor, theory, RP1302 ... 597
Blaine, Raymond L. and John Tucker, Jr., Application of vibrators for measuring mortar consistency and fabricating mortar cubes, RP1273 ... 103
Blum, William, and P. W. C. Strausser, Outdoor exposure tests of electroplated nickel and chromium coatings on steel and nonferrous metals, RP1293 ... 443
Boiling points and vapor pressures of *n*-heptane and 2,2,4-trimethylpentane, RP1280 ... 229
Brake lining, small inertia-type machine for testing, RP1297 ... 531
Brombacher, W. G., V. H. Goerke, and F. Cordero, Sensitive aneroid diaphragm capsule with no deflection above a selected pressure, RP1270 ... 31
Bromine, reaction with furfural and related compounds, RP1276 ... 175
Brooks, Donald B., Frank L. Howard, and Hugh C. Crafton, Jr., Physical properties of some purified aliphatic hydrocarbons, RP1271 ... 33
Burton, John O., S. F. Acree, Walter J. Hamer and, Second ionization constant and related thermodynamic quantities for malonic acid from 0° to 60° C, RP1284 ... 269

C

Page

Carson, Frederick T., Some observations on determining the size of pores in paper, RP1292 ... 435
Cellophane, apparatus for photochemical study, RP1300 ... 567
Cellulose acetate, apparatus for photochemical study, RP1300 ... 567
Cellulose, behavior in cuprammonium solutions: RP1299 ... 555 / RP1309 ... 743
Cellulosic materials, determination of uronic acids, RP1268 ... 13
Christer, V. L., Effect of painting on the sound absorption of acoustic materials, RP1298 ... 547
Chromates as corrosion inhibitors, RP1305 ... 665
Chromatic illumination, surface colors under, RP1285 ... 293
Chromel-Alumel thermocouples, RP1278 ... 205
Chromium plating, exposure tests, RP1293 ... 443
Chromium-vanadium steels, thermal expansion, RP1269 ... 25
Closest distance of approach for the ionic species in solutions of sodium malonate and sodium chloride, RP1284 ... 269
Color constancy, RP1285 ... 293
Colorimetric determination of arsenic in alloys, RP1267 ... 7
Colorimetric method of pH measurement of cyanide plating baths, RP1291 ... 423
Constancy of surface colors, RP1285 ... 293
Cooling rate of high-purity iron-carbon alloys, influence of austenitic grain size, RP1308 ... 723
Copper, methods of pH measurement of cyanide plating baths of, RP1291 ... 423
Copper citrate reagent for determination of sugars, RP1282 ... 241
Copper tartrate reagent, method of preparation, RP1301 ... 579
Cordero, F., V. H. Goerke, W. G. Brombacher and, Sensitive aneroid diaphragm capsule with no deflection above a selected pressure, RP1270 ... 31
Corrosion inhibitors in air-conditioning equipment, RP1305 ... 665
Corrosion of steels, influence of cyclic stress, RP1307 ... 685
Cotton, solubility in cuprammonium hydroxide solutions {RP1299 ... 555 / RP1309 ... 743
Cotton, uronic-acid content, RP1268 ... 13
Crafton, Hugh C., Jr., Frank L. Howard, Donald B. Brooks and, Physical properties of some purified aliphatic hydrocarbons, RP1271 ... 33
Craig, D. Norman, and George W. Vinal, Thermodynamic properties of sulfuric-acid solutions and their relation to the electromotive force and heat of reaction of the lead storage battery, RP1294 ... 475
Cuprammonium solutions, solubility of cotton fibers in {RP1299 ... 555 / RP1309 ... 743
Cuprous oxide as a measure of reducing sugar, RP1301 ... 579
Cyanide plating baths, measuring pH of, RP1291 ... 423

D

Dahl, Andrew I., Stability of base-metal thermocouples in air from 800° to 2,200° F, RP1278 ... 205
Deuterium oxide, heat and free energy of formation, RP1287 ... 369
Dextrose, gravimetric determination, RP1301 ... 579
Diaphragm capsule, sensitive, RP1270 ... 31
Dielectric constant, power factor, and resistivity of marble, RP1281 ... 235
Difructose anhydride III, methylated, preparation, RP1277 ... 181

Page

Difructose anhydride III, structure of, RP1277 .. 181
Digges, Thomas S., Influence of austenitic grain size on the critical cooling rate of high-purity iron-carbon alloys, RP1308 .. 723
Dimethylbutanes, preparation and properties, RP1271 .. 33
Dimethylbutenes, preparation and properties, RP1271 .. 33
trans-1,2-Dimethylcyclopentane, isolation from petroleum, RP1296 .. 509
trans-1,3-Dimethylcyclopentane, isolation from petroleum, RP1296 .. 509
3,4-Dimethyl fructose, preparation, RP1277 .. 181
Dimethyl zinc, use in preparation of 2,2,4,4-tetramethylpentane, RP1306 .. 677
Disaccharides, reducing powers, RP1282 .. 241
n-Dodecane, isolation from petroleum, RP1289 .. 395
n-Dodecane, physical constants, RP1289 .. 395
Dominant wavelength as an indication of hue, RP1285 .. 293
Dyeing, bearing of titration curve on wool, RP1286 .. 335

E

Eclipses, predictions for solar, RP1279 .. 225
Electrical properties of marble, RP1281 .. 235
Electrometric method, pH measurement of cyanide copper plating baths by, RP1291 .. 423
Electromotive force and heat of reaction of storage batteries, RP1294 .. 475
Electroplating on steel and nonferrous metals, exposure tests, RP1293 .. 443
Entropy changes for the ionization of the acid malonate ion, RP1284 .. 269
Entropy of deuterium oxide (heavy water), RP1287 .. 369
Equations for pH values of sodium malonate solutions, RP1284 .. 269
3-Ethylpentane, properties, RP1271 .. 33
Expansion, thermal, chromium-vanadium steels, RP1269 .. 25
Exposure tests of electroplated coatings, RP1293 .. 443

F

Fatigue limit of steels, influence of stress corrosion, RP1307 .. 685
Fehling reducing-sugar method, RP1301 .. 579
Ferrous and nonferrous alloys, determination of arsenic, RP1267 .. 7
Fibrous materials, determining pore size, RP1292 .. 435
First spectrum of iron, RP1288 .. 389
Flax, uronic acid in, RP1268 .. 13
Fractionation of petroleum {RP1289 .. 395; RP1296 .. 509}
Free-air ionization chamber, measurement of gamma radiation, RP1283 .. 247
Free-energy changes for the ionization of the acid malonate ion, RP1284 .. 269
Free energy of formation of deuterium oxide (heavy water), RP1287 .. 369
Friction, determination of coefficient of, for brake lining, RP1297 .. 531
Friction of journal bearings, RP1295 .. 491
Frush, Harriet L., Horace S. Isbell and, Alpha and beta methyl lyxosides, mannosides, gulosides, and heptosides of like configuration, RP1274 .. 125
——, *William W. Pigman, Horace S. Isbell and*, Reducing powers of various sugars with alkaline copper-citrate reagent, RP1282 .. 241
Furan compounds, reaction of bromine with, RP1276 .. 175
Furoic acid, reaction of bromine with, RP1276 .. 175

G

d-*β*-Galaheptose, methyl glycosides of, RP1274 .. 125
Gamma radiation from radium, measurement, RP1283 .. 247
Geil, Glenn W., Dunlap, J. McAdam, Jr. and, Influence of cyclic stress on the corrosion pitting of steels in fresh water, and the influence of stress corrosion on the fatigue limit, RP1307 .. 685
Germanium wavelengths, RP1266 .. 1

Page

Glasgow, Augustus R., Jr., Isolation of 3-methylhexane, *trans*-1,2-dimethylcyclopentane, and *trans*-1,3-dimethylcyclopentane from petroleum, RP1296 .. 509
Glass electrode, pH measurement of cyanide copper plating baths by, RP1291 .. 423
d-*α*-Glucoheptose, methyl glycosides of, RP1274 .. 125
Glucose, rate of carbon-dioxide evolution from, in HCl, RP1268 .. 13
Goerke, V. H., F. Cordero, W. G. Brombacher and, Sensitive aneroid diaphragm capsule with no deflection above a selected pressure .. 31
Grain size, austenitic, influence on the critical cooling rate of high-purity iron-carbon alloys, RP1308 .. 723
Groesbeck, Edward C., James H. Wilson and, Tests of corrosion inhibitors for water treatment in air-conditioning equipment, RP1305 .. 665
d-Gulose, methyl glycosides of, RP1274 .. 125

H

Hamer, Walter J., John O. Burton, and S. F. Acree, Second ionization constant and related thermodynamic quantities for malonic acid from 0° to 60° C, RP1284 .. 269
Hammond, Lester D., Redetermination of the Munson-Walker reducing-sugar values, RP1301 .. 579
Hardenability of high-purity iron-carbon alloys, influence of austenitic grain size, RP1308 .. 723
Harris, Milton, Charles W. Hock and, Microscopic examination of cotton fibers in cuprammonium hydroxide solutions, RP1309 .. 743
——, *Albert R. Martin, Roy L. Whistler and*, Determination of uronic acids in cellulosic materials, RP1268 .. 13
——, ——, ——, Pectic substance in cotton and its relation to the properties of the fiber, RP1299 .. 555
——, *Henry A. Rutherford and*, Concerning the existence of fractions of the sericin in raw silk, RP1290 .. 415
——, *Jacinto Steinhardt and*, Combination of wool protein with acid and base: Hydrochloric acid and potassium hydroxide, RP1286 .. 335
Heat capacity of sulfuric acid solutions, RP1294 .. 475
Heat dissipation characteristics of journal bearings, RP1295 .. 491
Heat of formation of deuterium oxide (heavy water), RP1287 .. 369
Heats of ionization of the acid malonate ion, RP1284 .. 269
n-Heptane, boiling point and vapor pressure, RP1280 .. 229
n-Heptane, properties, RP1271 .. 33
Heptoses, reducing powers, RP1282 .. 241
Hexoses, reducing powers, RP1282 .. 241
Hidnert, Peter, Thermal expansion of some chromium-vanadium steels, RP1269 .. 25
Hock, Charles W., and Milton Harris, Microscopic examination of cotton fibers in cuprammonium hydroxide solutions, RP1309 .. 743
Holt, William L., Rolla H. Taylor and, Small inertia-type machine for testing brake lining, RP1297 .. 531
Howard, Frank L., Preparation and some physical properties of 2,2,4,4-tetramethylpentane, RP1306 .. 677
——, *Hugh C. Crafton, Jr., Donald B. Brooks and*, Physical properties of some purified aliphatic hydrocarbons, RP1271 .. 33
Hue of surface colors, RP1285 .. 293
Hughes, Elizabeth E. and S. F. Acree, Reaction of bromine with furfural and related compounds, RP1276 .. 175
Humphreys, Curtis J., Note on the effect of pressure on the wavelengths of the international secondary standards in the first spectrum of iron, RP1288 .. 389
Hydraulics, waves in canals, RP1272 .. 47
Hydrocarbons in petroleum {RP1289 .. 395; RP1296 .. 509}
Hydrocarbons, preparation and properties of {RP1271 .. 33; RP1306 .. 677}
Hydrodynamics of gravity waves, RP1272 .. 47
Hydrolysis of methyl glycosides, RP1274 .. 125

I

Page

Illumination, chromatic, surface colors under, RP1285 293
Inductance coil, formula for, RP1302 597
Inductor, mutual, single-layer, bifilar, RP1302 597
Inertia-type machine for testing brake lining, RP1297 531
Infrared germanium spectrum, RP1266 1
Inhibitors of corrosion in air-conditioning equipment, RP1305
Inulin, difructose anhydrides from, RP1277 181
Invert sugar, method of preparation, RP1301 579
Ionization chamber, measurement of gamma radiation from radium, RP1283 247
Ionization potential of tin, RP1275 153
Ionosphere predictions, RP1279 225
Iron-carbon alloys, high-purity, influence of austenitic grain size on the critical cooling rate, RP1308 723
Iron-constantan thermocouples, RP1278 205
Iron spectra, RP1288 389
Irrotational translation waves, mathematical theory, RP1272 47
Isbell, Horace S., and Harriet L. Frush, Alpha and beta methyl lyxosides, mannosides, gulosides, and heptosides of like configuration, RP1274 125
——, *William W. Pigman, and Harriet L. Frush*, Reducing powers of various sugars with alkaline copper-citrate reagent, RP1282 241
Isooctane, properties, RP1271 33

J

Jackson, Richard F., Emma J. McDonald and, Structure of difructose anhydride III (difructofuranose 1,2′, 2,3′-anhydride), RP1277 181
Johnston, Herrick L., John W. Knowlton, Frederick D. Rossini and, Heat and free energy of formation of deuterium oxide, RP1287 369
Journal bearings, friction and temperature, RP1295 491
Judd, Deane B., Hue, saturation, and lightness of surface colors with chromatic illumination, RP1285 293

K

Kennelly-Heaviside, layer, RP1279 225
Ketodihydrofurfural, dihydrazone of, RP1276 175
Keulegan, Garbis H., and George W. Patterson, Mathematical theory of irrotational translation waves, RP1272 47
Kiess, C. C., Infrared arc spectrum of germanium, RP1266 1
Knowlton, John W., Herrick L. Johnston, Frederick D. Rossini and, Heat and free energy of formation of deuterium oxide, RP1287 369

L

Launer, Herbert S., Apparatus for the study of the photochemistry of sheet materials, RP1300 567
Levulose, gravimetric determination, RP1301 579
Lightness of surface colors, RP1285 293
Load-carrying capacity of journal bearings, RP1295 491
d-Lyxose, methyl glycosides of, RP1274 125

M

Mair, Beveridge J., and Anton J. Streiff, Separation of the aromatic hydrocarbons, and the isolation of *n*-dodecane, naphthalene, 1-methylnaphthalene, and 2-methylnaphthalene, from the kerosene fraction of petroleum, RP1289 395
Malonic acid; its ionization, pH values, thermodynamic quantities, its purification, RP1284 269
d-Mannose, methyl glycosides of, RP1274 125
Marble, dielectric constant, power factor, and resistivity, RP1281 235
Martin, Albert R., Milton Harris, Roy L. Whistler and, Determination of uronic acids in cellulosic materials, RP1268 13
——, ——, ——, Pectic substance in cotton and its relation to the properties of the fiber, RP1299 555
Mathematical theory of irrotational translation waves, RP1272 47
Maxwell triangle for surface colors in chromatic illumination, RP1285 293
McAdam, Dunlap J., Jr. and Glenn W. Geil, Influence of cyclic stress on the corrosion pitting of steels in fresh water, and the influence of stress corrosion on the fatigue limit, RP1307 685
McDonald, Emma J., and Richard F. Jackson, Structure of difructose anhydride III (difructofuranose 1,2′, 2,3′-anhydride), RP1277 181
McKee, Samuel A., Friction and temperature as criteria for safe operation of journal bearings, RP1295 491
Meggers, William F., First spectrum of tin, RP1275 153
Metals, determination of arsenic in ferrous and nonferrous alloys, RP1267 7
Metals, steel and nonferrous, exposure tests of nickel and chromium coatings, RP1293 443
4-Methyl fructose, preparation, RP1277 181
6-Methyl fructose, preparation, RP1277 181
Methylfurfural, reaction of bromine with, RP1276 175
Methyl glycosides of lyxose, mannose, and gulose, RP1274 125
3-Methylhexane, isolation from petroleum, RP1296 509
1-Methylnaphthalene, isolation from petroleum, RP1289 395
2-Methylnaphthalene, isolation from petroleum, RP1289 395
1-Methylnaphthalene, physical constants, RP1289 395
2-Methylnaphthalene, physical constants, RP1289 395
Moisture relations of textile fibers at elevated temperatures {RP1303 639, RP1304 645
Mortar, characteristics, RP1273 103
Munson and Walker reducing-sugar method, RP1301 579
Mutual inductance, theory of a single-layer, bifilar, absolute standard, RP1302 597

N

Naphthalene, isolation from petroleum, RP1289 395
Naphthalene, physical constants, RP1289 395
Nickel plating, exposure tests, RP1293 443
Nonferrous metals, exposure tests of nickel and chromium coatings, RP1293 443
Numerical constants for use in potentiometric measurements of hydrogen-ion activities, RP1284 269

O

Olefin hydrocarbons, properties, RP1271 33
Operating characteristics of journal bearings, RP1295 491
Optical rotation of methyl glycosides, RP1274 125
Oxidation of furfural with bromine, RP1276 175

P

Paint, effect on the sound absorption of acoustic materials, RP1298 547
Paper, apparatus for photochemical study, RP1300 567
Paper, determining pore size, RP1292 435
Paraffin hydrocarbons, properties {RP1271 33, RP1306 677
Patterson, George W., Garbis H. Keulegan and, Mathematical theory of irrotational translation waves, RP1272 47
Pectic substance, solubility in cupram- {RP1299 555, monium hydroxide solutions {RP1309 743
Pectin, constituent uronic acids of, in cotton, RP1268 13
Pentane, 2, 2, 4, 4-tetramethyl-, preparation and properties, RP1306 677
Pentoses, reducing powers, RP1282 241
Permeability-pressure method of determining pore size, RP1292 435
Petroleum, fractionation of {RP1289 395, RP1296 509
pH, effect on reactions of bromine with furfural derivatives, RP1276 175

Page

pH, measurement of in alkaline cyanide copper plating baths, RP1291 423
Phosphates as corrosion inhibitors, RP1305 665
Photochemical study of sheet materials, apparatus for, RP1300 567
pH standards—sodium malonate solutions, RP1284 269
pH values of sodium malonate solutions, RP1284 269
Pigman, William W., Harriet L. Frush, Horace S. Isbell and, Reducing powers of various sugars with alkaline copper-citrate reagent, RP1282 241
Pitting of steel, influence of cyclic stress on corrosion, RP1307 685
Plating baths, measuring pH of alkaline cyanide, RP1291 423
Plating on steel and nonferrous metals, exposure tests, RP1293 443
Plating on steel, brass, and zinc; exposure tests, RP1293 443
Polyuronides in cellulosic materials, RP1268 13
Pores, determining size, RP1292 435
Power factor, dielectric constant, and resistivity of marble, RP1281 235
Predictions, radio critical frequency, RP1279 225
Pressure effect in spectra, RP1288 389
Pressure, effect on battery voltage, RP1294 475
Pressure measurements, sensitive aneroid diaphragm for use in, RP1270 31
Pressure-permeability method of determining pore size, RP1292 435
Protective value of plating, exposure tests, RP1293 443
Protein, combination with acid and base, RP1286 335
Purification of malonic acid, RP1284 269

R

Radiation from radium, measurement, RP1283 247
Radio, critical-frequency predictions, RP1279 225
Radio sonde diaphragm capsule, RP1270 31
Radium, measurement of gamma radiation, RP1283 247
Ramie, uronic acid in, RP1268 13
Reaction of furfural with bromine, RP1276 175
Reducing powers of various sugars, RP1282 241
Reducing-sugar, method of formation, RP1301 579
Resistivity, dielectric constant, and power factor of marble, RP1281 235
Rodden, Clement J., Colorimetric determination of arsenic in ferrous and nonferrous alloys, RP1267 7
Rossini, Frederick D., John W. Knowlton, and Herrick L. Johnston, Heat and free energy of formation of deuterium oxide, RP1287 369
Roughness of brake drums, relation to wear, RP1297 531
Rubber, apparatus for photochemical study, RP1300 567
Rutherford, Henry A., and Milton Harris, Concerning the existence of fractions of the sericin in raw silk, RP1290 415

S

SAE chromium-vanadium steels, thermal expansion, RP1269 25
Safe operation of journal bearings, RP1295 491
Salt error of indicators, RP1291 423
Saturation of surface colors, RP1285 293
Scales method for determination of sugars, RP1282 241
Scott, Arnold H.: Dielectric constant, power factor, and resistivity of marble, RP1281 235
Second ionization constant of malonic acid, RP1284 269
Sericin, nature of, in raw silk, RP1290 415
Sheet materials, apparatus for photochemical study, RP1300 567
Silicates as corrosion inhibitors, RP1305 665
Silk, raw, fractions of sericin in, RP1290 415
Singer, George, Lauriston S. Taylor and, Measurement, in roentgens, of the gamma radiation from radium by the free-air ionization chamber, RP1283 247
Size of pores in paper, RP1292 435
Slip-coefficient method of determining pore size, RP1292 435
Smith, Edgar Reynolds, Boiling points of *n*-heptane and 2,2,4-trimethylpentane over the range 100- to 1,500-millimeter pressure, RP1280 229
Smith, Newbern, Predictions of normal radio critical frequencies related to solar eclipses in 1940, RP1279 225
Snow, Chester, Theory of a single-layer, biflar, absolute standard of mutual inductance, RP1302 597
Sodium error of glass electrode, RP1291 423
Sound absorption of acoustic material, effect of paint, RP1298 547
Specific heats for the ionization of the acid malonate ion, RP1284 269
Spectrum of germanium I, RP1266 1
Spectrum of neutral iron, RP1288 389
Spectrum of tin, RP1275 153
Stability of base-metal thermocouples, RP1278 205
Standards, international secondary, in the first spectrum of iron, RP1288 389
Steel, exposure tests of electroplated nickel and chromium coatings, RP1293 443
Steels, chromium-vanadium, thermal expansion, RP1269 25
Steels, influence of cyclic stress on corrosion, RP1307 685
Steinhardt, Jacinto, and Milton Harris, Combination of wool protein with acid and base: Hydrochloric acid and potassium hydroxide, RP1286 335
Storage batteries, electromotive force and heat of reaction, RP1294 475
Strausser, P. W. C., William Blum and, Outdoor exposure tests of electroplated nickel and chromium coatings on steel and nonferrous metals, RP1293 443
Streiff, Anton J., Beveridge J. Mair and, Separation of the aromatic hydrocarbons, and the isolation of *n*-dodecane, naphthalene, 1-methylnaphthalene, and 2-methylnaphthalene, from the kerosene fraction of petroleum, RP1289 393
Strength of vibrated mortars, RP1273 103
Stress corrosion of steels, RP1307 685
Sucrose, effect on reducing-sugar formation, RP1301 579
Sugar derivatives, optical rotation and hydrolysis, RP1274 125
Sugars, reducing powers, RP1282 241
Sulfuric acid, thermodynamic properties, RP1294 475
Surface colors, hue, saturation, and lightness, RP1285 293

T

Table, reducing-sugar, RP1301 579
Taylor, Lauriston S., and George Singer, Measurement, in roentgens, of the gamma radiation from radium by the free-air ionization chamber, RP1283 247
Taylor, Rolla H., and William L. Holt, Small inertia-type machine for testing brake lining, RP1297 531
Temperature coefficient of storage batteries, RP1294 475
Temperature of journal bearings, RP1295 491
Terms of germanium I, RP1266 1
2,2,4,4-Tetramethylpentane, preparation and properties, RP1306 677
Textile fibers, moisture relations at elevated temperatures {RP1303 639 / RP1304 645
Thermal expansion of chromium-vanadium steels, RP1269 25
Thermocouples, stability of base metal, RP1278 205
Thermodynamic properties of sulfuric acid, RP1294 475
Thermodynamic quantities for malonic acid, RP1284 269

Page

Thompson, Maurice R., Methods of measuring pH in alkaline cyanide plating baths, RP1291 423
Tin, first spectrum, RP1275 153
2,2,3-Trimethylbutane, properties, RP1271 33
2,3,3-Trimethylbutene-1, properties, RP1271 33
2,2,4-Trimethylpentane, boiling point and vapor pressure, RP1280 229
2,2,4-Trimethylpentane, properties, RP1271 33
2,3,4-Trimethylpentane, properties, RP1271 33
Trityl derivatives of inulin and difructose anhydride, preparation, RP1277 181
Tucker, John, Jr., Raymond L. Blaine and, Application of vibrators for measuring mortar consistency and fabricating mortar cubes, RP1273 103

U

Uniform-chromaticity-scale triangle applied to surface colors, RP1285 293
Uronic acids in cellulosic materials, RP1268 13

V

Vapor pressures and boiling points of *n*-heptane and 2,2,4-trimethylpentane, RP1280 229
Vibrators for fabricating mortar cubes, RP1273 103
Vinal, George W., D. Norman Craig and, Thermodynamic properties of sulfuric-acid solutions and their relation to the electromotive force and heat of reaction of the lead storage battery, RP1294 475
Viscosity characteristics, as affecting safe operation of journal bearings, RP1295 491
Visual after images, effect on surface color, RP1285 293
Voids in mortars, RP1273 103
Voltage of storage batteries, RP1294 475

Page

W

Water, corrosion pitting of steels in, RP1307 685
Water, heavy, heat and free energy of formation, RP1287 369
Water, sorption of by textile materials at elevated temperatures { RP1303 639 / RP1304 645
Water treatment in air conditioning equipment, RP1305 665
Wavelengths of germanium I, RP1266 1
Wavelengths of tin, RP1275 153
Wavelength standards, RP1288 389
Waves, cnoidal, irrotational translation, and solitary, in canals, RP1272 47
Wear of brake lining, machine for testing, RP1297 531
Whistler, Roy L., Albert R. Martin, and Milton Harris, Determination of uronic acids in cellulosic materials, RP1268 13
——, ——, ——, Pectic substance in cotton and its relation to the properties of the fiber, RP1299 555
Wiegerink, James G., Equipment for conditioning materials at constant humidities and at elevated temperatures, RP1303 639
——, Moisture relations of textile fibers at elevated temperatures, RP1304 645
Wilson, James H., and Edward C. Groesbeck, Tests of corrosion inhibitors for water treatment in air-conditioning equipment, RP1305 665
Wool, combination with acid and base, RP1286 335

X

X-ray dosage measuring instruments, standard for, RP1283 247

Z

Zero-point energies of H_2O and D_2O, RP1287 369

○

eering
ibrary

UNITED STATES DEPARTMENT OF COMMERCE

JUL 2 1940

Journal of Research

of the

National Bureau of Standards

Vol. 24, No. 6 June 1940

CONTENTS

RP	TITLE AND AUTHOR	Page
1302.	Theory of a single-layer, bifilar, absolute standard of mutual inductance. Chester Snow.....[Price 10c]	597
1303.	Equipment for conditioning materials at constant humidities and at elevated temperatures. James G. Wiegerink.....[Price 5c]	639
1304.	Moisture relations of textile fibers at elevated temperatures. James G. Wiegerink.....[Price 5c]	645
1305.	Tests of corrosion inhibitors for water treatment in air-conditioning equipment. James H. Wilson and Edward C. Groesbeck. [Price 5c]	665
1306.	Preparation and some physical properties of 2,2,4,4-tetramethylpentane. Frank L. Howard.....[Price 5c]	677
1307.	Influence of cyclic stress on corrosion pitting of steels in fresh water, and influence of stress corrosion on fatigue limit. Dunlap J. McAdam, Jr., and Glenn W. Geil.....[Price 10c]	685
1308.	Influence of austenitic grain size on the critical cooling rate of high-purity iron-carbon alloys. Thomas G. Digges..[Price 10c]	723
1309.	Microscopic examination of cotton fibers in cuprammonium hydroxide solutions. Charles W. Hock and Milton Harris. [Price 5c]	743
	Index to volume 24 (January 1940 to June 1940) Research Papers (RP1266 to RP1309).....	749

The articles listed may be purchased separately (see cover page II) at the prices stated

A monthly periodical of pure and applied science published by our National Government

Journal of Research

of the

National Bureau of Standards

The January 1940 issue of the JOURNAL OF RESEARCH of the National Bureau of Standards began the twenty-fourth semiannual volume of this periodical. Fundamental researches in progress in the Bureau's laboratories are reported in this JOURNAL. If you are interested in new developments in science and technology, you should receive the JOURNAL. If you are not already a subscriber, you are invited to send in your subscription.

Technical News Bulletin

This is a monthly publication containing short articles reporting progress of work in the Bureau laboratories, abstracts of papers which appear in the JOURNAL OF RESEARCH, accounts of scientific and technical meetings in which the Bureau has taken part, a list of all publications by members of the staff, and other items within the Bureau's fields. The BULLETIN is designed primarily to give a general and timely review of the activities of the Bureau in brief form. It is a prompt and reliable source of official information. If you have not already subscribed for the BULLETIN, you are invited to do so.

ANNUAL SUBSCRIPTION	Prices	
	United States, Canada, Cuba, Mexico, Newfoundland, Republic of Panama	Other countries
JOURNAL OF RESEARCH of the National Bureau of Standards:		
12 monthly issues (2 volumes), paper covers	$3.50	$4.50
Bound volume (year, 1 volume), blue buckram	3.00	3.50
Technical News Bulletin, 12 monthly issues	.50	.70

Research Papers, reprinted individual articles appearing in the JOURNAL OF RESEARCH, are available from the Superintendent of Documents shortly after appearance of monthly issue of the JOURNAL.

Address orders only to
Superintendent of Documents, U. S. Government Printing Office,
Washington, D. C.